Oxygen Dynamics in the High-Temperature Superconductor LSCO+O

PhD Thesis in Physics by

Tim Tejsner

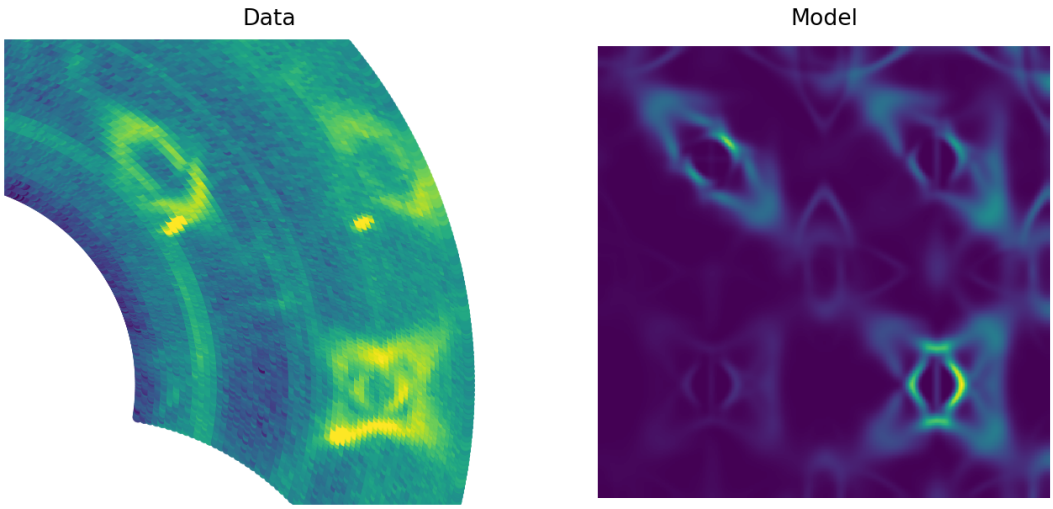

Supervisor
Linda Udby, Niels Bohr Institute

Co-supervisors
Martin Boehm, Institut Laue-Langevin
Andrea Piovano, Institut Laue-Langevin

This thesis has been submitted to
the PhD School of The Faculty of Science,
University of Copenhagen

December, 2019

Abstract

Understanding the mechanisms of high-temperature superconductivity in the cuprates remains one of the great unsolved questions of condensed matter physics. Hole-doping the Mott-insulator La_2CuO_4 with various chemical species creates a superconductor with a transition temperature T_c that depends heavily on the amount and type of doped species. While the amount of hole-doping typically dictates the phase diagram, there are certain situations where superconductivity can be suppressed or enhanced due to structural modifications caused by the dopant species. In this thesis, I investigate these structural modifications and, in particular, related dynamics in order to better understand any possible relationship to superconductivity.

A particular interesting sample in this context is $La_{2-x}Sr_xCuO_{4+\delta}$ (LSCO+O), where doping can be performed with two distinct chemical species, Sr and O. Doping with Sr is 'quenched', meaning that Sr has a fixed, random distribution on La sites. On the other hand, doping with O is performed after crystal growth using electrochemical methods. Oxygen dopants are 'annealed' in the sense that they sit on interstitial sites and are mobile at room temperature. In addition, doping with O creates a superconductor with slightly better T_c that is equipped with a number of unique phenomena such as electronic phase separation and complex superstructures. In this thesis, various aspects of phonon dynamics in LSCO+O are investigated through a combination of theoretical and experimental methods. Density functional theory and molecular dynamics is used to numerically estimate the phonon band structure and density of states. Inelastic neutron scattering is used to probe phonon dynamics and the two methods are compared.

Despite the fact that Density Functional Theory is known to struggle with the electronic structure of the cuprates, excellent agreement between phonon dynamical simulations and experiments are found. An analysis of this relationship reveals unique dynamics of octahedral tilt patterns due to interstitial oxygen. We speculate that these tilt patterns may assist in relieving the inherent frustration between magnetism and superconductivity in LSCO+O. Finally, anomalous features in the Cu-O bond stretching phonon of two different LSCO+O samples is observed with neutron scattering. This 'phonon anomaly' is suspected to be a signature of charge density fluctuations that might be important for superconductivity. While previously observed in Sr-doped $La_{2-x}Sr_xCuO_4$, this result rules out a phonon anomaly caused by structural mechanism related to the specific dopant type.

Resumé

Forståelsen af høj-temperatur superledning i kupraterne er stadig et uløst spørgsmål i faststoffysikken. Ved at huldope det Mott-insulatorende materiale La_2CuO_4 med forskellige kemiske arter, skabes en superleder med en overgangstemperatur T_c der afhænger kraftigt af typen og mængden af denne kemiske 'dopant'. Selvom mængden af huldoping typisk dikterer fasediagrammet, er der situationer hvor superledning kan understrykkes eller forbedres på baggrund af strukturelle modifikationer forudsaget af den kemiske dopant. I denne afhandling undersøges disse strukturelle modifikationer, og især den relaterede dynamik, for bedre at forstå en eventuel relation til superledning.

En særligt interessant prøve i denne sammenhæng er $La_{2-x}Sr_xCuO_{4+\delta}$ (LSCO+O), hvor doping kan udføres med to forskellige kemiske arter, Sr og O. Doping med Sr er 'quenched', hvilket betyder at Sr har en fikseret, tilfældig distribution. På den anden side, udføres doping med O ved brug af elektrokemiske metoder after krystallen er groet. Oxygen doping er derfor 'annealet' i den forstand at O sidder på interstitielle sites og er mobile ved stuetemperatur. Derudover skaber doping med O en superleder med lidt bedre T_c der er udstyret med en række unikke fænomener som elektronisk faseseperation og komplekse superstrukturer. I denne afhandling undersøges diverse aspeketer af fonon-dynamik i LSCO+O gennem en komination af teoretiske og eksperimentelle metoder. Density Functional Theory og molekyledynamik bruges til at estimere fonon båndstrukuter og density-of-states. Inelastisk neutron spredning bruges til at undersøge fonon dynamik eksperimentelt og de to metoder sammenlignes.

Selvom Density Functional Theory ikke kan beskrive den elektroniske struktur af kuprater, finder vi en fremragende overensstemmelse mellem simulering og eksperiment i kontekst af fonondynamik. En analyse af denne overensstemmelse afslører unik dynamik af octahedrale tilt-mønstre som konsekvens af interstitiel oxygen. Vi formoder at disse tilt-mønste kan assistere til at lindre den kendte frustration mellem magnetisme og superledning i LSCO+O. Afslutningsvis undersøger vi en såkaldt fonon-anomali relateret til en Cu-O vibration i to forskellige LSCO+O prøver ved hjælp af neutronspredning. Denne fonon-anomaly mistankes for at være relateret til ladningsfluktationer som igen mistænkes for at være vigtigt for superledning. Selvom denne anomali tidligere er observeret i Sr-dopet $La_{2-x}Sr_xCuO_4$, udelukker dette resultat en fonon-anomali forudsaget af strukturelle mekanismer relatret til den specifikke dopant.

Contents

Chapter 1

Introduction

In this thesis, I explore certain aspects of the so-called high-temperature superconductors. While these materials were discovered fairly recently (1986), they have a rich history with hundreds of thousands of citations and, to this day, a lively debate surrounding the microscopic nature of this mysterious macroscopic quantum state. The purpose of this chapter is to briefly state the 'the story so far' in broad strokes, and then dive deeper into state-of-the-art research relevant for the work performed in this thesis.

1.1 Superconductivity

Superconductivity is a state of matter where a material is able to conduct electricity with *zero* DC resistance below a certain critical temperature T_c. Since we, fortunately, live in a world where the 'spherical cow in a vacuum' model is a very crude approximation to reality, it is remarkable to find *real* materials where electrons can propagate without friction. In fact, experiments have shown, that under the right conditions it is possible to keep a persistent superconducting current running for 100000 years [1]!

Superconductivity was first discovered in 1911 by Heike Kamerlingh Onnes, essentially as a consequence of being able to liquefy helium in 1908 and reach temperatures close to absolute zero (see ref. [2] and references therein for a breakdown of the experiments). His low-temperature measurement of lead revealed a sudden drop in resistivity at 4.2 K, as seen in the historic plot on figure 1.1

Despite this remarkable experimental result, it would take 20 years for the next major milestone to appear. In 1933 the Meissner effect was discovered [4], showing that superconducting materials would completely resist an applied magnetic field by exhibiting perfect diamagnetism as sketched in figure 1.2. In 1935 this effect was phenomenologically explained by the London equations, showing that the Meissner effect is due to superconducting currents on the surface of the material [5]. From their relatively simple set of equations, an observable length scale known as the penetration depth

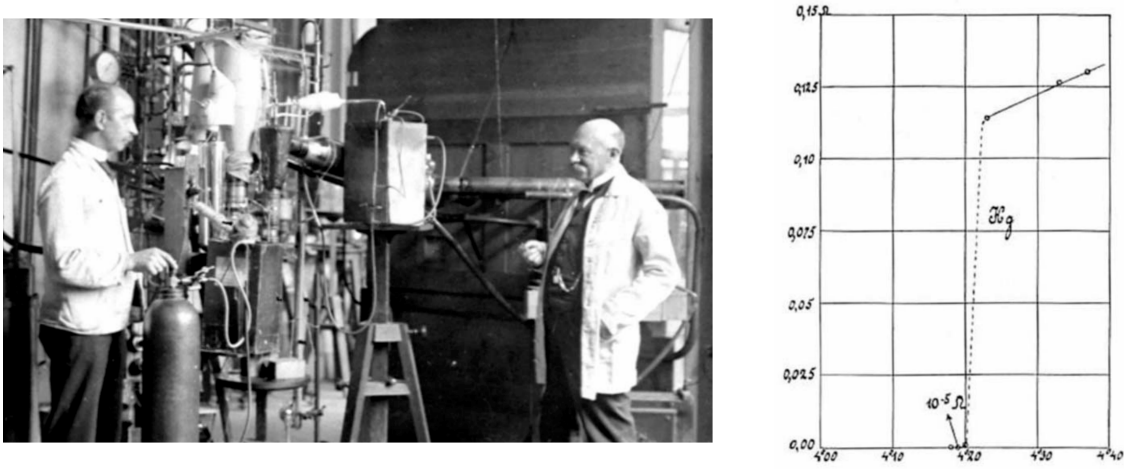

Figure 1.1: **Left**: Kammerling Onnes (right) and his chief engineer (left) in their cryogenics lab. **Right**: Resistivity as a function of temperature in elemental Lead. Both images from ref. [2].

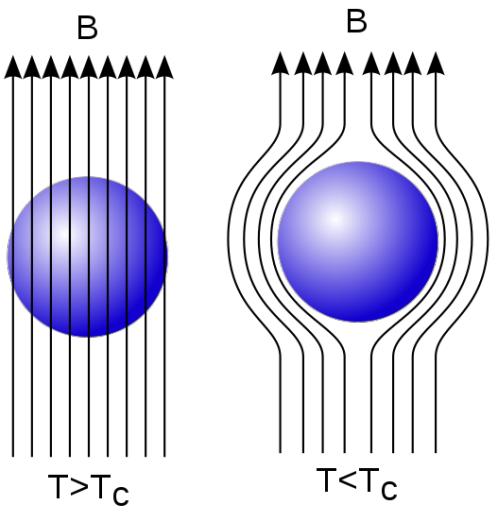

Figure 1.2: The Meissner effect. As a superconducting material is cooled below T_c, the applied magnetic field $\boldsymbol{B}$ is completely expelled due to superconducting currents on the surface. As a consequence there is no magnetic flux inside the superconducting material, in contrast to the same situation for 'normal' conductors. Figure from [3].

was defined

$$\lambda_L = \sqrt{\frac{m}{\mu_0 n q^2}}$$

where μ_0 is the permeability of free space, n the number concentration of the superconducting carriers, m the electron mass and q the electron charge. This length scale determines how an external magnetic field penetrates the superconductor through the relationship $B(x) = B(0)\exp(-x/\lambda)$. λ is typically on the order of 20 nm to 100 nm [6].

Another roughly 20 years would pass until Landau's work on phase transitions paved the way to understanding the superconducting phase transition as a thermodynamic quantity through the Ginzburg-Landau equations in 1950 [7]. I will not repeat the details here, but the idea is to make a polynomial expansion of the free energy as a function of a complex superconducting wavefunction ψ. As the material is cooled below T_c, ψ 'chooses' a phase and breaks gauge symmetry, analogous to how a ferromagnet choses a common direction for the magnetic moment at the magnetic phase transition. This description predicts an new characteristic length scale of the superconductor called the *coherence length* ξ and recasts the penetration depth in terms of ψ:

$$\xi = \sqrt{\frac{\hbar^2}{4m|\alpha|}} \qquad \lambda = \sqrt{\frac{m}{4\mu_0 e^2 \psi_0^2}},$$

where α is a phenomenological parameter of the polynomial expansion. The ratio of these parameters, $\kappa = \lambda/\xi$, are used to classify superconductors into type-I ($\kappa < 1/\sqrt{2}$) and type-II ($\kappa > 1/\sqrt{2}$). The significance of $\kappa > 1/\sqrt{2}$ can be understood as a threshold where the surface tension between normal and superconducting phases becomes negative [8]. Intuitively, the coherence length ξ defines the shortest length within which the superconducting carrier concentration are allowed to change considerably. For elemental metals ξ can be on the nanometre to micrometre scale: 1600 nm in Al and 83 nm in Pb [6]. In the cuprates (which will be discussed in detail in the next section), ξ is typically on the order of a few lattice spacings (1 nm in $YBa_2Cu_3O_{7-\delta}$ [9]).

Based on Ginzburg-Landau theory, Abrikosov predicted the existence of vortices in Type-II superconductors, which showed excellent agreement with the measured magnetization of several lead alloys [8]. These vortices can be pinned by defects and form a lattice that we have been able to image using modern day microscopy techniques (see e.g. [10] for a recent example with beautiful real-space images). The experimental evidence piled up [11, 12], and it quickly became evident that Ginzburg-Landau theory is applicable to most known superconductors, including the cuprates and iron-based varieties.

Despite the descriptive power of Ginzburg-Landau theory, we are left with no recipe on how to construct, even theoretically, 'better' superconductors. In order to manipulate material properties,

it is necessary to understand the microscopic properties that lead to macroscopic behaviour (e.g. how phonons influence thermal properties or how magnetic exchange influences magnetic properties. Inspired by Ginzburg-Landau theory, rapid progress towards a microscopic theory was being made in the mid 1950s, culminating in the famous BCS theory formulated by Bardeen, Cooper and Schrieffer [13].

BCS theory is based on the assumption that an attractive interaction between electrons at the Fermi level can result in so-called 'cooper-pairs', a bosonic quasi-particle consisting of an electron pair with opposite momentum and spin. The bosonic nature of this quasi-particle can, at low temperatures, result in a Bose-Einstein condensate where a large fraction of these electron pairs occupy the lowest energy quantum state. This microscopic theory of superconductivity made several testable predictions, such as the appearance of an energy gap with a temperature-dependent width $\Delta(T)$ in the electronic density of states related to the critical temperature through the relationship

$$2\Delta(T=0) = 3.5 k_{\mathrm{B}} T_{\mathrm{c}} \,,$$

where k_{B} is the Boltzmann constant. A few years later electron tunnelling experiments confirmed this prediction with reasonable accuracy [14, 15]. Additionally, Josephson predicted that superconducting currents could tunnel across an insulating barrier [16], experimentally verified a few years later [17].

While BCS theory predicts an attractive interaction between electrons, the original paper [13] makes no assumption about the nature of this interaction. Some experiments, performed a few years prior, showed that T_{c} of Hg^{198} was higher when compared to that of natural Hg (avg. atomic weight of 200.6) [18, 19]. Since the chemistry of these materials can be assumed identical, this experiment suggests a positive correlation between phonon frequencies and T_{c}, since lighter elements have more energetic vibrations. Assuming an attractive potential due to lattice vibrations, BCS theory could relate the attractive interaction to phonon frequencies and predict a relative relationship between isotopic mass and critical temperature [20]:

$$T_{\mathrm{c}} \propto \frac{1}{\sqrt{m_{\mathrm{ion}}}} \,,$$

where m_{ion} is the isotopic mass of the constituent ionic species. With BCS theory, superconductivity in many elemental metals were believed to be 'solved' with the identification of phonon-mediated superconductivity. Unfortunately, this discovery also set a *practical* upper limit on T_{c}. In order to increase phonon frequencies, and thus critical temperatures, we need materials with low mass atomic species, while still being crystalline. At ambient pressure this practical upper limit is often quoted to be around 30 K. A good demonstration of this principle is the case of H_2S where researchers were able to reach a critical temperature of $T_{\mathrm{c}} = 200\,\mathrm{K}$ by applying a pressure of 155 GPa [21]. This material contains the light atomic species we require, but cannot crystallize at ambient pressures so we can only reach high critical temperatures under extreme conditions. A different example is the highly unusual case of MgB_2, where coincidences add up to an unusually high electron-phonon coupling resulting in a critical temperature of $T_{\mathrm{c}} = 39\,\mathrm{K}$ [22].

While this thesis is about cuprates, which cannot be described within the BCS framework, I believe that the history of conventional superconductivity emphasizes exactly what is desired from a 'solution' to high-temperature superconductivity. It is also a fascinating story due to the fact that the tools to solve the problem were not even close to being developed when the phenomenon was discovered. It took roughly 50 years for a satisfying conclusion and we have only been working on the cuprates for roughly 30 years.

1.2 Cuprates

With this brief introduction to superconductivity, I will proceed with an introduction to cuprate superconductivity. While the previous section contains research results and explanations generally accepted and agreed upon, it is difficult to capture an unbiased view of cuprate research. As such, the following will be somewhat narrowly focused. While this is a reasonable choice for this introduction, it is important to realize just how massive the field is and how impossible it is to know every last detail.

Before we begin, I want to establish some of the nomenclature As the title of this thesis suggests, I am working on the so-called 'high-temperature superconductors'. This definition essentially only concerns itself with the value of the critical temperature (usually above the 'BCS-limit' of 30 K), without saying anything about other physical properties. On the other hand Type-I and Type-II, as seen in the previous section, are rigidly defined with respect to their properties as defined

Table 1.1: list of common cuprate families. In the case of La-214, doping is performed by exchanging La with Re = Sr, Ba or by the introduction of additional oxygen δ. In Y-123, doping is performed by removing a small amount of oxygen δ. n is the number of CuO_2 layers per 'copper oxide block' (see figure 1.3)

Chemical Formula	Name	Optimal T_c [K]	References
$La_{2-x}Re_xCuO_{4+\delta}$	La-214 / LSCO	40	[23]
$YBa_2Cu_3O_{7-\delta}$	Y-123 / YBCO	93	[24]
$Bi_2Sr_2Ca_{n-1}Cu_nO_{2n+4}$	Bi-22(n-1)n	120	[25]
$Ti_2Ba_2Ca_{n-1}Cu_nO_{2n+4}$	Ti-22(n-1)n	127	[26–29]
$HgBa_2Ca_{n-1}Cu_nO_{2n+2}$	Hg-12(n-1)n	133	[30, 31]

through Ginzburg-Landau Theory. Finally, 'conventional superconductors' are those that can be microscopically described with BCS theory, while 'unconventional superconductors' cannot. While cuprates are relatively simple crystals, most of them have a variety of names and abbreviations attached to them. Table 1.1 lists the most important ones along with their critical temperatures.

The discovery of LBCO

Roughly 30 years after BSC theory was nailed down, in 1986, Bednorz and Müller discovered a new type of superconductor while trying to manipulate the electronic properties of the antiferromagnetic insulator La_2CuO_4. By effectively removing a small number of electrons from the system by substitution of dopant species, they achieved a record T_c of 30 K. Shortly after, in 1987, the sister-compound $YBa_2Cu_3O_{7-\delta}$ was discovered, shattering previous records and finally achieving a critical temperature $T_c = 93$ K that could be reached using liquid nitrogen [24].

While the increased critical temperatures are remarkable on their own, it quickly became apparent that we were dealing with a completely new type of superconductivity which cannot be explained with BCS theory. The normal state ($T > T_c$) of cuprate superconductors is as, if not more, complex when compared to the superconducting state and the BCS assumption of being metallic in the normal state is generally not fulfilled. In addition, the BCS relationship between isotopic mass critical temperature ($T_c \propto m_{ion}^{-0.5}$) is not fulfilled when performing O^{16}/O^{18} isotopic substitution [32].

Similar to semiconductors, the properties of the cuprates are dramatically changed with the introduction of dopant species. In general, we call the addition of electrons *electron doping* and the removal of electrons *hole doping*. In the original paper, La_2CuO_4 was hole-doped by exchanging La^{3+} with Ba^{2+}. We define the amount of hole-doping (n_h) as the fraction of holes added per CuO_2 layer. The amount of electron doping (n_e) is defined similarly. In general, the undoped compounds $n_h = 0$ are anti-ferromagnetic insulators and you need a small amount of doping to make the materials superconducting. It it also possible to dope too much (typically $n_h > 0.25$) and the materials become non-superconducting metals.

The fact that we need finite amounts of doping in order to make cuprates superconducting, makes them inherently inhomogeneous materials. This inhomogeneity may or may not be important for cuprate superconductivity, but there is no denying that it exists. In fact, recent STM studies on underdoped $Bi_2Sr_2CaCu_2O_{8+\delta}$ ($n_h = 0.06$, $T_c = 10$ K) have shown significant spatial inhomogeneities due to random distributions of defects [33].

Structure

Cuprate superconductors are characterized by a layered structure where CuO_2 layers are separated by so-called charge reservoirs (or spacer layers). In general, the conventional Bravais lattice is either tetragonal or orthorhombic with the CuO_2 layers in the a-b plane. A few examples of cuprate crystal structures is shown in figure 1.3. The different structures are generally characterized by the number n of subsequent CuO_2 layers. Interestingly, there appears to be a maximum T_c for compounds with $n = 3$. It has been proposed that this maximum at $n = 3$ is due to a balance between Josephson tunneling between adjacent layers (tends to increase T_c and the charge imbalance between outer and inner layers (tends to decrease T_c) [34].

Doping is performed either by substitution or addition of dopant species as indicated by table 1.1. Doping thus necessarily changes the lattice either due to a difference in ionic radii of a

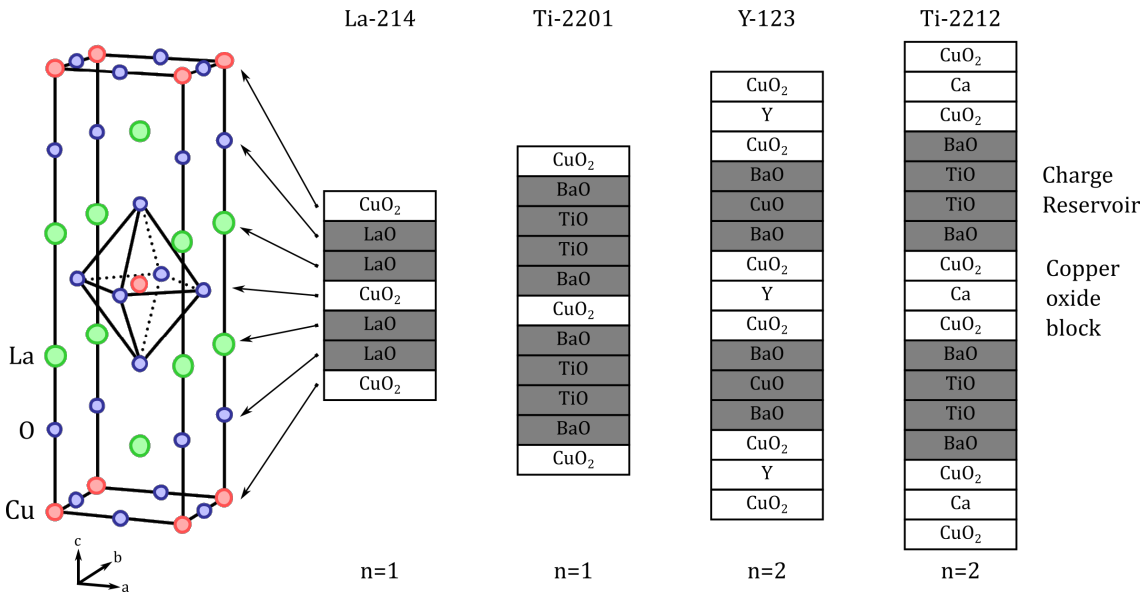

Figure 1.3: A selection of cuprates and a schematic of their layered structure. **Left**: The structure of La_2CuO_4 (La-214) in the tetragonal coordinate system. Modified from [35]. **Right**: The layered structure of various cuprates with $n = 1$ and $n = 2$. For the naming scheme and chemical formulae, see table 1.1

substitutional dopant or a strain in the lattice because of an interstitial species. In the case of substitutional doping of La_2CuO_4, the structural and electronic properties vary wildly (as we shall see in section 1.3) depending on the dopant species (Ba, Sr).

Different members of the cuprate family have their own structural peculiarities. In single-layer LSCO, many structural properties are linked to the CuO_6 octahedra which are not present in structures with $n \geq 2$ and in YBCO, Cu-O chains form along the crystallographic b-axis. Despite these specific structural properties of the various cuprates, they are all equipped with square CuO_2 planes and have remarkably similar phase diagrams.

Phase diagram

A general phase diagram for the cuprates is shown in figure 1.4 illustrating the many macroscopic and microscopic phases in the cuprates as a function of temperature and doping. First, figure 1.4 (left) shows a asymmetry between hole and electron-doping. Since cuprates are superconducting for a wider range of doping on the hole-doped side, most research focuses on this side of the phase diagram. Second, as shown in figure 1.4 (right), cuprates are only superconducting for a narrow range of hole doping typically between $n_h = 0.05$ and $n_h = 0.25$ with a maximum around $n_h = 0.15$. This region is known as the 'superconducting dome'.

I emphasize here the very different states of matter at the boundaries of the superconducting dome at $T = 0$: Over-doped cuprates are typically metals while underdoped cuprates are magnetic insulators. In some sense, superconductivity is optimized in a region between localized (magnet) and itinerant (metal) behavior – a region also containing poorly understood normal state ($T > T_c$) behavior such as the Pseudogap and strange metal phase.

The Pseudogap is a curious phenomena first observed in NMR measurements of YBCO [38] and later on in the c-axis resistivity [39] and specific heat [40]. The name comes from the fact that, by now, it is generally associated with the opening of a gap in the electronic density of states (see below). The difficulty in finding a microscopic origin of the phase transition at the Pseudogap temperature T^* has attracted as much attention as the superconducting transition itself. Many researchers believe that the key to understanding the superconducting transition is directly related to the Pseudogap. One idea is that of 'pre-formed pairs', where Cooper pairs start forming at T^*, but the macroscopic superconducting state fails to settle between T^* and T_c due to incoherent fluctuations in the phase of the pairing field [41, 42].

The strange metal phase is possibly the least understood part of the cuprate phase diagram [37]. A 'strange' metal is essentially a phase of matter where the theory of 'normal' metals (Fermi liquids) breaks down and is a phenomenon seen in a number of correlated electron systems, not just the cuprates. A significant indicator of this behavior is a linear temperature-dependence of

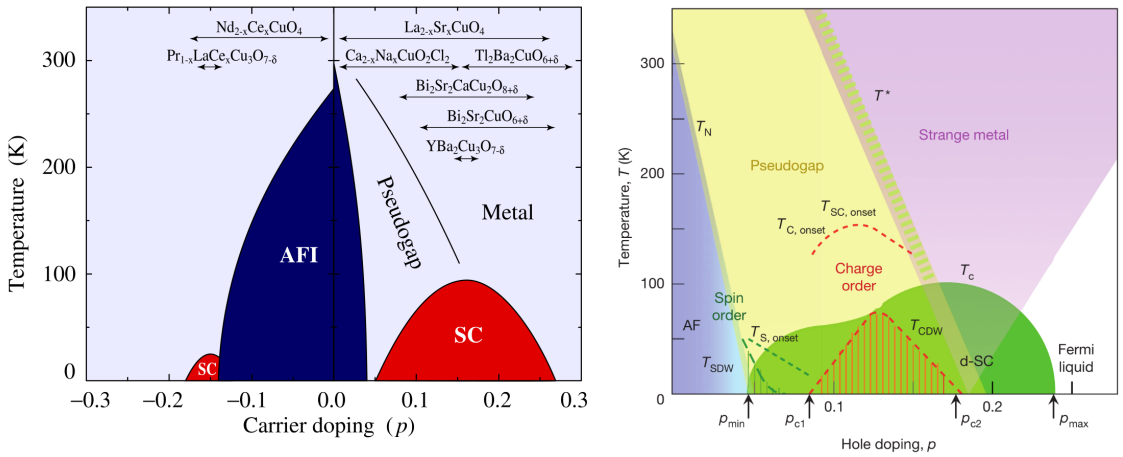

Figure 1.4: **Left:** Generalized phase cuprate phase diagram for selected electron- and hole-doped materials, emphasizing the asymmetry between the two sides of the phase diagram. From [36]. **Right:** Generalized phase diagram for the hole-doped side annotated with microscopic ordering phenomena. From [37].

resistivity (see e.g. [43] for a cuprate example), where a normal Fermi liquid varies as T^2 at low temperatures. A recent study even suggests that this linear-in-T resistivity in the cuprates is a generic property related to a universal scattering rate [44].

By outlining the phase diagram in this way, I intend to illustrate both the difficulty of solving the cuprate problem and the many experimental methods and theoretical tools necessary to investigate the various features of this complex phase diagram. Until now, apart from crystallographic information, we have mainly considered *macroscopic* behavior through bulk measurements such as resistivity, specific heat, optical band gap or magnetic susceptibility. We now turn to a brief overview of *microscopic* behaviour, starting with momentum-resolved measurements of the Fermi surface.

Fermi Surface

Angle-Resolved Photoemission Spectroscopy (ARPES) is a method in X-ray spectroscopy that directly probes the electronic band structure of materials. This method has been extremely important in strongly correlated electron systems in general and has a rich history with the cuprates (see the extensive review by Damascelli et al. [45], which also serves as a good introduction to the experimental method). Although a few ARPES experiments were carried out, (see chapter 9) this thesis primarily concerns itself with neutron scattering as an experimental technique. Thus the technical details of ARPES will not be reviewed here but can be found in literature ([46] is a great introduction).

ARPES experiments are extremely surface sensitive experiments with a typical penetration depth of a few lattice spacings, and thus requires samples that cleave naturally at the interface one wants to probe. While cuprates have a layered structure, the materials themselves are also quite brittle, so the in-situ cleaving procedure can be challenging. However, since superconductivity is generally associated with a gap at the Fermi level due to Cooper pair formation, this technique is extremely valuable for our understanding of unconventional superconductivity.

Figure 1.5A and figure 1.5B shows our 'reference' Fermi surface as calculated from Density Functional Theory (more on this in chapter 2 and 3), representing the overdoped part of the phase diagram. Here we see that the conduction band is made up of electrons from the $d_{x^2-y^2}$ orbital that cross the Fermi level halfway towards the anti-ferromagnetic wave vector (π, π). This crossing defines the so-called 'Fermi arcs' shown in figure 1.5B. As we move towards the optimally underdoped or optimally doped part of the phase diagram, the Fermi arcs are broken up as shown in figure 1.5C, revealing both the superconducting gap Δ_0 and the Pseudogap Δ^*. These gaps have been identified and distinguished in experiments on Bi2212 as shown in figure 1.6. These discontinuities at the Fermi surface are also direct experimental evidence that we are dealing with a system that cannot be explained by conventional theories.

The structure of this superconducting gap (Δ_0) reveals certain symmetries of which, in turn, reveals the 'pairing symmetry' of the Cooper pairs (see [50] for a review) which is related to their total spin and orbital angular momentum. These symmetries are what gives rise to the naming

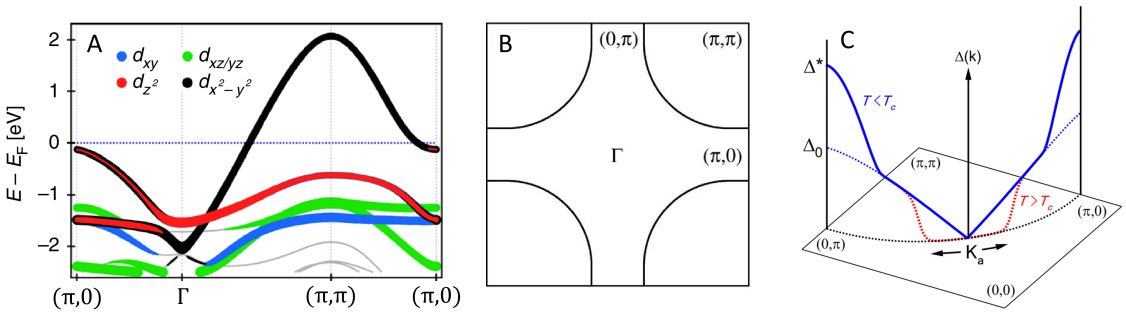

Figure 1.5: Fermi surface of the cuprates with respect to the cupper oxide planes. **A**: Band structure of overdoped $La_{2-x}Sr_xCuO_4$, showing the Cu d orbitals along high-symmetry lines. calculated with Density Functional Theory. Modified from ref. [47]. **B:** The same band structure, this time represented in two dimensions, with the lines showing where the $d_{x^2-y^2}$ band crosses the Fermi surface. [45]. **C**: The gap structure of underdoped $La_{2-x}Sr_xCuO_4$, showing how the 'arcs' in **B** are broken [48].

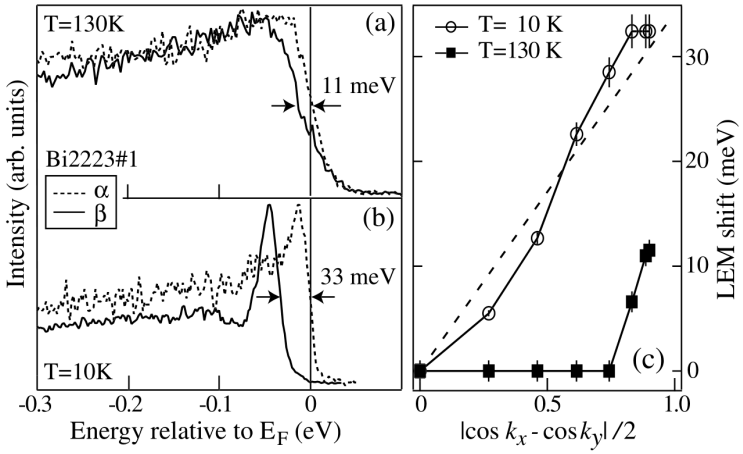

Figure 1.6: Experimental evidence of both the d-wave gap at $T = 10\,\mathrm{K}$ (below T_c and the Pseudogap at $T = 130\,\mathrm{K}$ (just above T_c) in the trilayer ($n = 3$) cuprate Bi2223. The data is taken along the fermi arcs (figure 1.5B) and clearly show the momentum dependence of the two distinct gaps. Figure from ref. [49].

scheme taken from electron orbitals, where s-wave superconductors have an isotropic gap and d-wave superconductors have a gap with momentum dependence $\Delta^* = |\cos k_x - \cos k_y|/2$, where (k_x, k_y) are wave vectors along the Fermi arcs (see Δ_0 in figure 1.5C). Other symmetries have also been found, such as p-wave in Sr_2RuO_4 [51] and f-wave in UPt_3 [52].

While these observations of the electronic band structure and Fermi surface thus tells us a lot about the nature of the superconducting pairing, it does not directly give us a *mechanism* for the pairing similar to how BCS theory and the isotope effect gave us Cooper pairs due to phonons. While theoreticians have been working tirelessly to construct models that can explain all these behaviours, no consensus have been reached at this point. For this reason, some experimentalists are looking at microscopic correlations in order to uncover what the atoms and electrons are 'doing' at the various phase transitions summarized in figure 1.4.

Microscopic correlations

When any type of phase transition happens in a material it, by definition, must be caused by a microscopic phenomenon. Any satisfactory theory in condensed matter physics should be able to explain macroscopic behavior starting from the constituent parts and experiment that can probe microscopic behavior are often essential. Sometimes, as with the isotope effect in conventional superconductors, we can infer the microscopic behavior in indirect ways, but often it is necessary to probe the atomic length scales directly. The microscopic probe used in this thesis is neutron scattering, which is used to infer structure and dynamics through a scattering process between a beam of neutrons and a sample. Technical details of the method will be covered in chapter 2, but

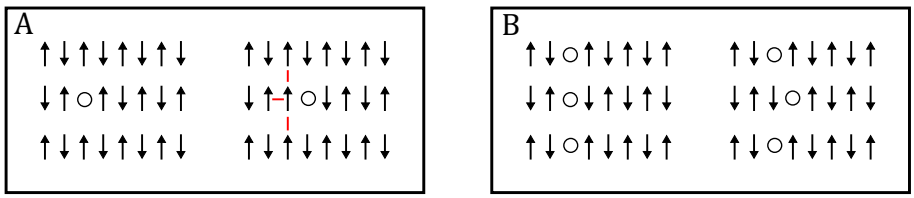

Figure 1.7: An illustration of how holes can get 'stuck' in an antiferromagnetic background. **A**: A single hole is placed in on an antiferromagnetic lattice and tries to propagate to the right. As it moves, ferromagnet links are created which is energetically unfavorable. **B**: One way to overcome this problem is if the holes align next to each other, allowing for a 1-dimensional 'stripe', where the electrons can propagate, despite the strong Coulomb repulsion. In addition, if (as shown) the spins are anti-aligned across the stripe, transverse fluctuations can occur without creating these ferromagnetic links.

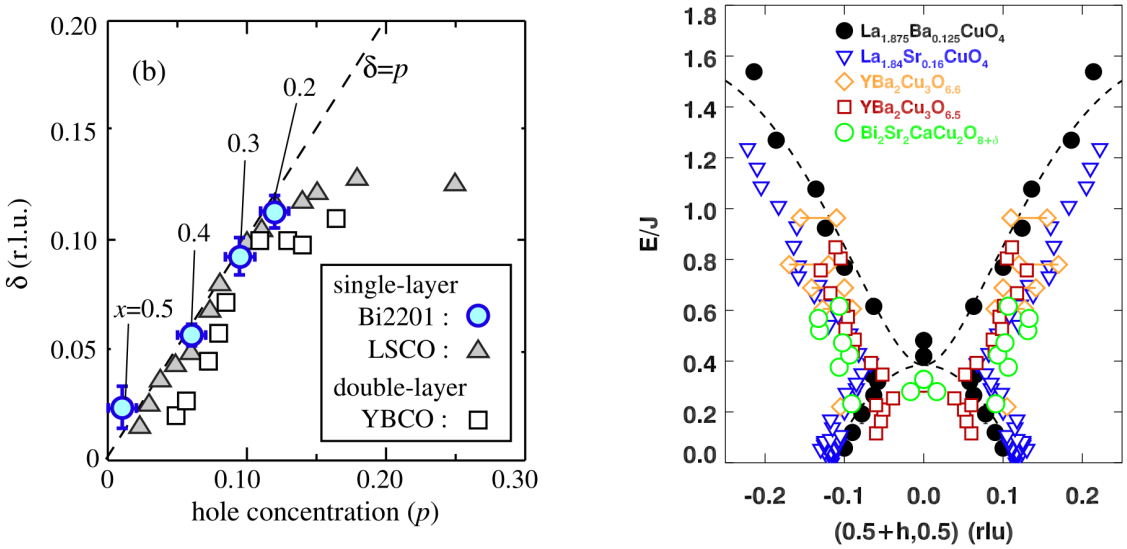

Figure 1.8: **Left**: The so-called 'Yamada plot' [54] of magnetic incommensurability δ as a function of hole doping p in three different cuprates. x is the nominal Sr doping of Bi2201 which has been translated into hole doping. From ref. [55]. **Right:** The dispersion of these incommensurate structures, scaled by magnetic exchange. This hourglass dispersion is a ubiquitous, but not unique [56, 57], feature of the cuprates.

for now we briefly state some of the important results.

As mentioned earlier, the undoped cuprates are anti-ferromagnetic insulators. While an odd number of electrons in the system usually results in metallic behaviour, the localized shape of the d orbitals results in static magnetism due to an exchange interaction J and the physics are reasonably well-described within linear spin wave theory [53].

As one moves to finite values of hole doping, this antiferromagnetic order is interrupted and some electrons can start to propagate through the material. A common analogy is that of magnetic interactions causing a traffic jam of electrons that is then relieved as one moves from left to right in the phase diagram (figure 1.4). A real-space visualization of this analogy is shown in figure 1.7. It turns out that this gradual destruction of magnetic order happens in a peculiar way where the antiferromagnetic ordering becomes incommensurate with respect to the crystal lattice, with an 'incommensurability' δ that is linear in doping as shown in figure 1.8A.

Figure 1.8A also reveals a saturation of this incommensurability at $n_{\mathrm{h}} \approx \frac{1}{8}$, suggesting that period-8 magnetic order is somehow important for cuprate superconductivity. On the other hand, the phase diagram reveals that T_{c} is supressed at exactly this doping in a number of compounds, with optimal T_{c} requiring a few percent more doped holes per CuO_2 plane at $n_{\mathrm{h}} \approx 0.16$. It thus appears as if these observations are universal for the cuprates but at the same time detrimental for superconductivity. This '$\frac{1}{8}$ conundrum' has given rise to the concept of competing orders [58–61], where superconductivity emerges near a plethora of near-degenerate electronic phases where some of them are detrimental to superconductivity.

The excitations of this magnetic order also reveals a ubiquity as shown in figure 1.8B. It

turns out that the magnetic fluctuations from this incommensurate order has a highly unusual 'hourglass'-shape, where the 'neck' of the hourglass is scaled by the strength of the magnetic exchange in the parent compound. Additionally, when static magnetic order disappears the fluctuations persist and become gapped. While this picture is appealing, some experimental results deserve to be mentioned in this context. First, it was recently suggested that the magnetic order and fluctuations are distinct phenomena due to a mismatch in wave vector [62]. Second, Kofu et al. found evidence of gapped excitations *and* static order in samples close to $n_{\mathrm{h}} = \frac{1}{8}$. Third, an hourglass excitation spectrum was observed in cobalt-oxides with no stripe order or superconductivity [56, 57].

These observations, together with the d-wave structure of the Fermi surface, intuitively points to a picture where the behaviour of the $d_{x^2-y^2}$ band alone is the key to understanding cuprate superconductivity. One popular approach is one where pairing happens not due to an external attractive potential, but through spin fluctuations of the electrons themselves [64]. While these models are not without their problems (Anderson has argued that the idea of a bosonic glue might not even be appropriate [65]), they reproduce parts of the phase diagram quite well [66].

1.3 La214

I will now depart from general observations in the cuprates and focus on a particular class of cuprates based on the parent compound La_2CuO_4 (see figure 1.3). Sometimes known as 'La214' or with specific acronyms depending on the dopant species, these materials are single-layer cuprates with a relatively simple crystal structure and a maximum critical temperature $T_{\mathrm{c}} \approx 40\,\mathrm{K}$.

Crystal Structure

La214 generally exist with four different structural symmetries, ordered here from highest to lowest symmetry:

- High-Temperature Tetragonal (HTT). Spacegroup 139 (I4/mmm)
- Low-Temperature Orthorhombic (LTO). Spacegroup 64 (Bmab)
- Low-Temperature Tetragonal (LTT). Spacegroup 138 ($P4_2/ncm$)
- Low-Temperature Less Orthorhombic (LTLO). Spacegroup 56 (Pccn)

which can all be described with reference to the structure shown in figure 1.9. Comparing with figure 1.3, we see that this structure is enlarged and rotated by 45°. The smaller structure is known as the tetragonal coordinate system, and the larger is the orthorhombic coordinate system since they represent the conventional cell of the HTT and LTO phase, respectively. Unless otherwise specified, we will generally use the orthorhombic coordinate system in this thesis.

The difference between the structural phases can be identified with respect to the tilting pattern of the CuO_6 octahedra. We define the rotation Q_1 as a rotation along a (around b) and Q_2 as a rotation along b (around a) with respect to figure 1.9. The tilts Q_1, Q_2 along with the orthorhombic strain $\eta = \frac{b-a}{b+a}$ can fully describe the structural phase transitions [67].

Since this thesis is focussed on specific structural aspects and phonon dynamics, this 'relatively' simple crystal structure is a particularly strong point for us. Since we want to model the full 3-dimensional structure using computationally heavy simulation methods, it is advantageous to consider the simplest system possible. In addition, since the lanthanum cuprates were the first so-called 'high-temperature superconductors' to be discovered, there is a massive amount of literature on which to build our ideas from.

Twinning

The structural transition from HTT to LTT is associated with a process where the a and b directions become inequivalent due to the orthorhombic strain. This strain is caused by a mismatch of the Cu-O and La-O bond lengths due to their different thermal expansions. As the crystal is cooled through this HTT-LTO structural phase transition, the inequivalent directions of a and b are formed in domains separated by grain boundaries.

The result of this phenomenon is the formation of so-called 'twin domains', where both possible choices of the new a and b directions happen in different parts of the crystal. The unfortunate result of twinning is that our measurements will see both twin domains simultaneously, making us

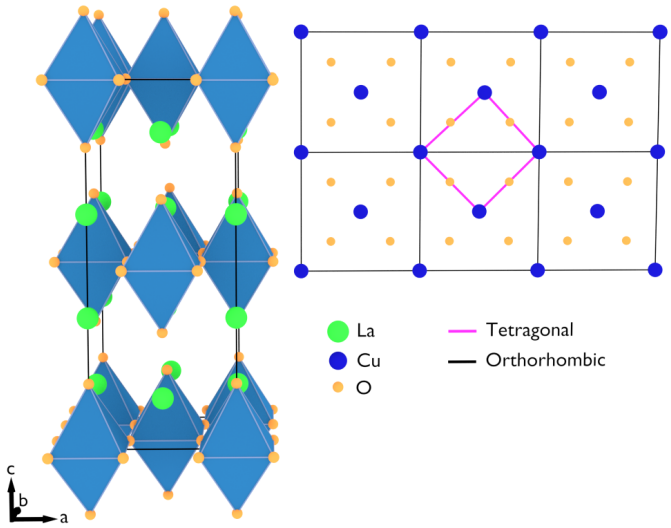

Figure 1.9: Crystal structure of La_2CuO_4. The Cu atoms are not shown in the structural schematic, where the octahedral coordination is emphasized. The inset shows 6 basal CuO_2 planes, where the difference between the tetragonal and orthorhombic coordinate systems is emphasized.

Table 1.2: Atomic species which can be substituted into La_2CuO_4. La, Nd, Pr will not change the doping. Ba, Sr will hole dope the system and Ce can be used for electron-doping. For Ce, the data is from ref. [69], all other species from ref. [70]. When doping with oxygen, the procedure is not substitutional, but rather the addition of an atomic species. Since the oxidation state of oxygen is 2-, we expect the addition of two holes.

Dopant	Oxidation State	Ionic Radius [Å]
La	3+	1.216
Nd	3+	1.163
Pr	3+	1.179
Ba	2+	1.47
Sr	2+	1.31
Ce	3.84+	0.998

unable to tell the difference between the a and b directions. In terms of scattering, it means that any measurement will be a superposition of (hkl) and (khl). These effects will become important in chapters 5 and 6. Further details about this phenomenon in $La_{2-x}Sr_xCuO_4$ can be found in ref. [68].

Stripe Order

La_2CuO_4 can be doped by substitution of La with various atomic species where some of them results in hole doping (e.g. Ba, Sr), while others have been used to modify the structure without changing the effective hole doping (e.g. Nd, Eu). Table 1.2 shows the ionic radius and oxidation state (which determines hole doping) of the species that can be used to dope variants of La_2CuO_4.

It turns out that La214 cuprates have particularly pronounced physics with regards to behaviour at $n_h = \frac{1}{8}$. In $La_{2-x}Ba_xCuO_4$, superconductivity is almost completely supressed at $n_h = \frac{1}{8}$, while in $La_{2-x}Sr_xCuO_4$ we only see a small plateau. In fact, by performing a combination of substitutions it is possible to create materials such as $La_{1.48}Nd_{0.4}Sr_{0.12}CuO_4$ where superconductivity is completely supressed while being at an otherwise 'optimal' doping level. A common thread for $La_{2-x}Ba_xCuO_4$ and $La_{1.48}Nd_{0.4}Sr_{0.12}CuO_4$ is that this suppression of T_c happens simultaneously with the tetragonal (LTT) phase. I note here that a tetragonal phase in itself does not inherently prohibit superconductivity since $La_{2-x}Sr_xCuO_4$ is tetragonal, but with HTT symmetry, at low temperatures for $n_h \geq 0.2125$ [71]. We thus appear to be in a situation where crystal symmetry has a non-trivial relationship with superconductivity. For a thorough discussion of this particular topic, see the review by Hücker [35].

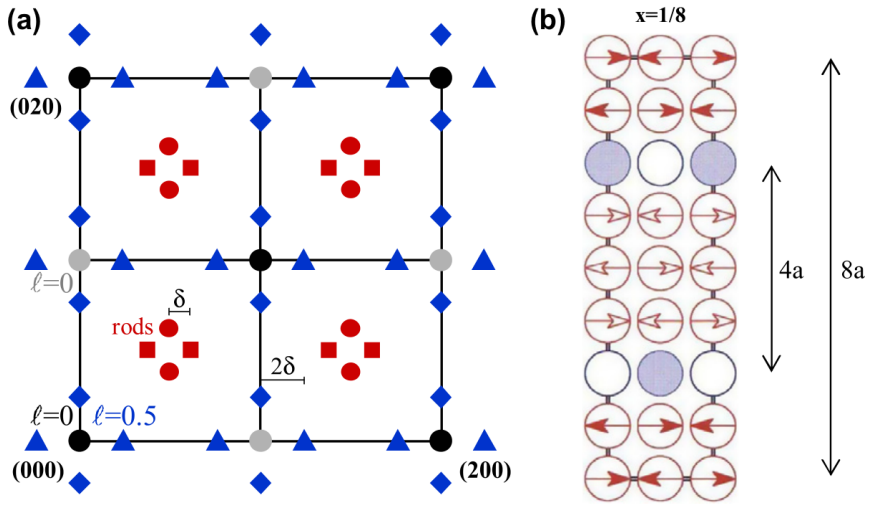

Figure 1.10: The stripe model in real **(b)** and reciprocal **(a)** space. Antiferromagnetic regions are separated by lines of charge due to hole doping, creating a period-8 magnetic and period-4 charge structure which can be observed by neutron scattering at the shown positions. From ref. [35].

It can thus be argued that La214 cuprates are the appropriate materials in which to examine the significance of the $n_\mathrm{h} = \frac{1}{8}$ phase and a lot of attention was given to these phenomena in the early 1990s, culminating in the discovery of so-called 'stripe order' in non-superconducting LNSCO [72]. The stripe model is one where the magnetic period-8 order appears simultaneously with a period-4 charge order. These observations led to the stripe model as shown in figure 1.10, where the magnetic order is separated by one-dimensional 'stripes' of charge.

This model is appealing because it suggests that superconducting electrons are locally segregated from the localized magnetic electrons. It also seems like a reasonable way to relieve the frustration in the traffic jam analogy (figure 1.7). When discussing stripes, a distinction between spin stripes and charge stripes is typically made. While evidence mostly points to a picture where charge and spin stripes are simultaneous, charge stripes are much harder to detect and only seem to be associated with the $n_\mathrm{h} = \frac{1}{8}$ phase [73–75] where spin stripe order is seen in a large part of the phase diagram $0.02 < n_\mathrm{h} < 0.13$ [76].

The excitations associated with the spin stripes exhibit the universal hourglass dispersion as we saw in figure 1.8 [77] and the relationship between stripe order and the associated excitations have been extensively studied as summarized by figure 1.11. In short, the ordering temperature of spin stripe order increases with doping up to $n_\mathrm{h} \approx \frac{1}{8}$ where the excitations become gapped. In the optimally doped region of the phase diagram, the size of the gap E_g is roughly of the order $k_\mathrm{B}T_\mathrm{c}$, suggesting a direct connection between the magnetic excitation spectrum and superconductivity.

1.4 LSCO+O

Finally, we turn to the material studied in this thesis, $La_{2-x}Sr_xCuO_{4+\delta}$ (LSCO+O). In addition to the substitutional doping outlined above, La_2CuO_4 can be doped with additional oxygen using electrochemical methods [78], yielding $La_2CuO_{4+\delta}$ (LCO+O). These materials are sometimes called over-stoichiometric or super-oxygenated and the additional oxygen can be combined with Sr-doping yielding the 'co-doped' samples LSCO+O. Due to the electrochemical method of introducing the additional oxygen, it can be difficult to control the amount of nominal doping, and we are often forced to use relatively imprecise or destructive methods such as titration (see e.g. MSc thesis by Mariam Ahmad [79]) or Thermogravimetric Analysis (TGA) [80] in order to determine the doping n_h.

With that in mind, a comparison of LSCO and LCO+O is sketched in figure 1.12. A peculiar feature of doping with oxygen is the fact that only certain superconducting phases seem to emerge ($T_\mathrm{c} \approx 15, 30, 40\,\mathrm{K}$) and the amount of each phase can be tuned with oxygen content [81], pressure [82] or thermal treatment [83]. The white parts of the LCO+O phase diagram is the 'miscibility gap', where phases co-exist. I emphasize here that LSCO+O has a slightly better T_c when compared to LSCO.

Since the electrochemical doping procedure essentially pushes oxygen atoms into the lattice, we

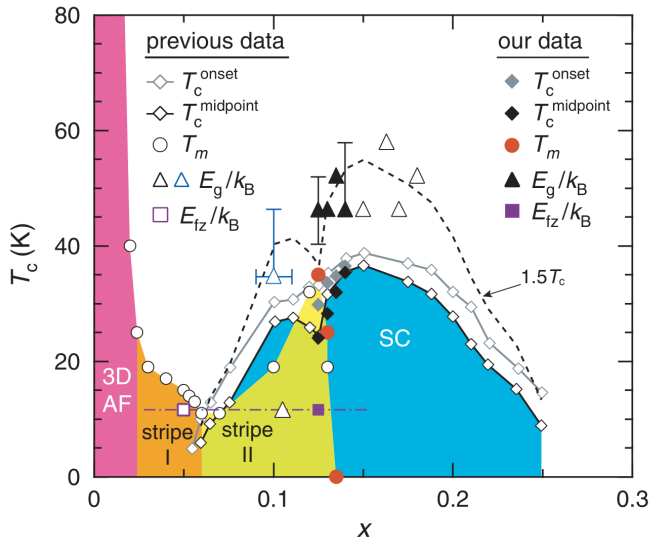

Figure 1.11: Phase diagram of LSCO with respect to T_c and stripe order. Stripe I and II is static, magnetic stripe order and are distinguished by a 45° rotation in propagation direction. Triangles indicate the gap size of the magnetic excitations in units of k_B. From ref. [63].

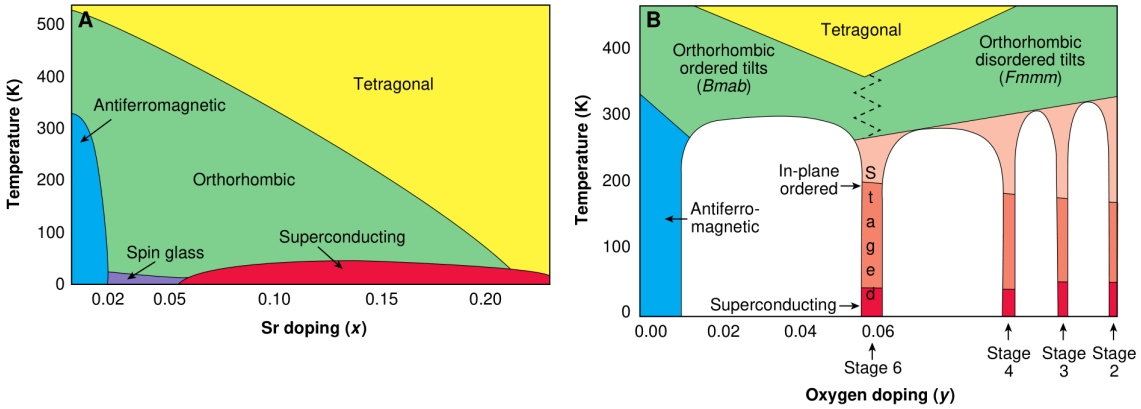

Figure 1.12: Schematic phase diagram of La_2CuO_4 using different dopant species. When doping with Sr, we get the familiar phase diagram (see e.g. figure 1.4 and figure 1.11). When doping with oxygen, on the other hand, we get discrete phases separated by regions where these phases mix. This 'miscibility gap' is shown in white. From ref. [84].

know that the oxygen is equipped with some level of mobility within the lattice and this mobility is likely the reason for this 'discretization' of T_c. Another way of thinking about this is in terms of an 'annealed disorder' [84], where the oxygen can achieve an optimal inhomogeneity [85]. This is in contrast to the 'quenched disorder' [84] of LSCO where the positions of Sr ions are fixed during the solid state synthesis at elevated temperatures ($T \approx 1000\,°C$).

This annealed disorder results in a number of structural phenomena. First, a structural correlation along the c-axis known as staging [86], shown in figure 1.13, is likely the result of the lattice trying to accommodate the interstitial oxygens. There is little reason to believe that staging has anything to do with superconductivity since it appears in a very similar way in the isostructural non-superconducting nickelate $La_2NiO_4 + \delta$ [87] and no direct relation between the staging details and T_c was found in LSCO+O [88].

A more complex three dimensional ordering has been observed both by neutrons [88, 89] and by x-ray micro-diffraction [83, 85]. Since thermal treatments that modify the superconducting phases simultaneously removes some of these structural features [85], it has been suggested that these superstructures might be related to superconductivity through the 'superstripes' idea [90].

A peculiar feature of LSCO+O, is the fact that the superconducting and magnetic phases of LSCO+O are distinct and separate. Magnetic susceptibility and muon-spin-rotation (μSR) measurements have revealed a linear relationship between the volumes of the two phases, suggesting that they are separated in real space [91, 92]. In the context of the LSCO phase diagram, it is

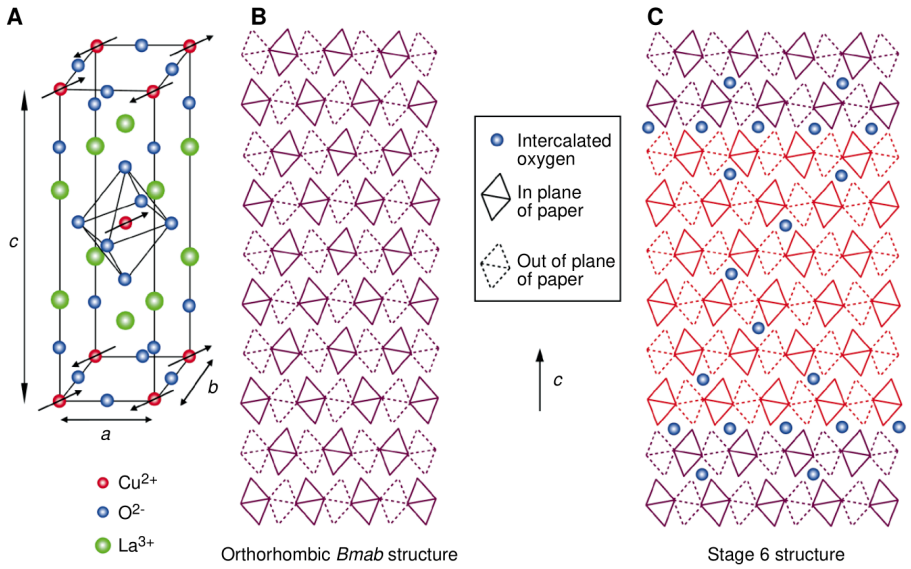

Figure 1.13: Illustration of staging in LCO+O. **A:** Crystal structure of La_2CuO_4, highlighting the octahedra centred at the copper atom. **B:** Displacement pattern of these octahedra as viewed from the side. **C:** Staging pattern due to intercalated oxygen. By creating anti-phase boundaries the structure accommodates the oxygen atoms in an energetically favourable way. The number of CuO_2 planes between the anti-phase boundaries determines the staging number (in this case stage-6). From ref. [84].

believed that these two phases is one with exactly $n_h = \frac{1}{8}$ (magnetic) and one with $n_h \approx 0.16$ (optimally superconducting). Whether this phase separation is unique to LSCO+O is hard to say – one could imagine a scenario where the annealed doping of LSCO+O allows these phases to 'grow' in contrast to LSCO with only quenched doping from Sr [92].

Finally, LSCO+O (with one exception, see chapter 8) is equipped with static stripe order despite having a T_c reminiscent of optimally doped LSCO. In addition, the transition temperature of this static order T_N coincides with T_c [92], suggesting a unique and direct connection between the two electronic phases in this compound.

LSCO+O is thus structurally and electronically distinct from LSCO, while still exhibiting the universal features of the cuprates in a consistent way. This system is important in the larger context because, as we learned in this chapter, 1) the cuprates are fundamentally inhomogeneous systems and 2) the fact that crystal structure clearly interacts with the superconducting state and/or stripe order. Since LSCO+O is unique on these two counts, an investigation of this system can help us understand those unsolved issues.

1.5 Thesis objectives

The objective of this thesis is to investigate phonon dynamics of the LSCO+O system through neutron scattering measurements and molecular simulations. The idea is to consider here the full three dimensional lattice of the cuprates by trying to understand how the surrounding lattice interacts with the CuO_2 planes (which are usually studied). The strategy is to primarily focus on the dynamical aspects of the lattice by measuring and simulating phonons in the system. While phonon-mediated superconductivity in the manner of conventional BCS theory is unlikely in the cuprates, a better understanding of the lattice dynamical effects in the cuprates, and possibly indirect effects on superconductivity could be useful to the community as a whole.

In this context I will mention a few experimental result that emphasizes this motivation. Recently, a longitudinal study of several different cuprates suggested that the Cu-O distance to the apical oxygen (the oxygen atoms directly above and below the copper atoms) has an effect on the in-plane exchange interaction [93]. A different study on thin films showed a similar effect on the in-plane Cu-O distances [94]. Finally, a measurement of atomic pair distribution functions as a function of doping in LSCO has shown that the *distribution* of in-plane Cu-O distances is broadest at optimal doping, suggesting that a phase separation picture might be relevant for LSCO [95].

Just as with stripes picture, the excitations are just as relevant as the static order. In the same way, a study of phonons might reveal subtleties that we have not been able to discern from a purely

structural viewpoint. The goal of this thesis is thus to carefully evaluate the phonon spectrum of LCO, LSCO, LCO+O and LSCO+O in theory and practice. This is done with various techniques in neutron scattering and simulations with density functional theory (DFT). In a more concrete way, this thesis tries to answer the following research questions:

1. Can a relationship between specific dopant type (quenched/annealed) and the phonon spectrum be established?
2. Is it possible to establish a relationship between superconductivity and the phonon spectrum?
3. To what extend can DFT-based simulation methods be used to explain observed changes in the phonon spectrum?

Outline

In chapter 2, the experimental and simulation methods used in this thesis are outlined. Subsequent chapters then deals with specific research projects pertaining to aspects of the research questions outlined above. In chapter 3, phonon calculations on La_2CuO_4 is performed in various structural and electronic phases in order to obtain a 'baseline' for subsequent simulations. Chapter 4 uses these results to perform molecular dynamics of structures with added dopants. The experimental part of this thesis starts in chapter 5, where we look at structural correlations and compare these to observables from molecular dynamics. In chapter 6 investigates low energy phonon dynamics in order to 1) validate our simulations, 2) look at structural instabilities and 3) investigate dynamics related to the observed superstructures seen in chapter 5. In chapter 7 I look at phonon density of states measurements of powders with different dopants in order to directly answer question 2. from above. In chapter 8 I look at an anomaly detected in a specific high-energy phonon mode, possibly connected to stripes. In chapter 9 I report results from an electronic band structure measurement on an oxygen-doped sample. Finally, in chapter chapter 10, the thesis is briefly summarized and discussed.

Chapter 2

Methods

In this chapter, I give an overview of primarily neutron scattering and density functional theory. Since these two methods are central to the experimental and theoretical work performed in this thesis, the objective here is to give the background necessary to understand the remaining chapters. In addition, I attempt to contextualize the reason for using these methods in the study of cuprate superconductors.

2.1 Neutron Scattering

In this section, we give some of the key equations and concepts related to neutron scattering. Basic concepts will not be dealt with in detail, since excellent literature already exists and does a much better job than I would be capable of. See e.g. [96–98] for general theory and [99] for triple-axis spectroscopy. Rather, I will attempt to take a more practical approach with three primary goals:

1. Understand what types of problems can be solved with neutron scattering.
2. Understand the relationship between correlation functions and neutron scattering.
3. Emphasize the equations relevant for our experiments.

General Theory

In neutron scattering, the idea is to illuminate a sample with a beam of neutrons and then record the scattered neutrons. In order to have enough neutrons for our experiments, they are usually produced through nuclear fission in a reactor or by bombarding a target with high energy protons in a so-called spallation source.

The neutron is a neutral, spin-$\frac{1}{2}$ particle with a mass $m_\mathrm{n} = 1.675 \times 10^{-27}\,\mathrm{kg}$ and a magnetic moment $\mu_\mathrm{n} = -1.913\,\mu_\mathrm{B}$. Just like any quantum object, the neutron exhibits particle-wave duality and as it propagates through a medium we can conveniently characterize it by a wavevector $\boldsymbol{k}$ that has a magnitude $k = \frac{2\pi}{\lambda}$, where λ is the wavelength, and points in the direction of propagation. Given the wavevector $\boldsymbol{k}$, along with the fact that typical neutrons for experiments can be treated as non-relativistic particle, we can compute the neutron energy $E = \frac{\hbar^2 k^2}{2m_\mathrm{n}}$ and its equivalent temperature through $E = k_\mathrm{B}T$. In neutron scattering we often categorize experimental methods based on the temperature of the incident neutrons, as summarized in table 2.1.

In general, scattering experiments have optimal conditions when the wavelength of the probe is similar to the studied length scale. Similarly, when studying excitations, it is preferable that the energy of the probe is similar to that of the excitations. This is exactly why neutron scattering is so useful for condensed matter since typical wavelengths matches interatomic distances ($\approx 10^{-10}\,\mathrm{m}$)

Table 2.1: Approximate values of of energies, temperatures and wavelength for the three classifications of reactor sources. From [97].

Source	Energy [meV]	Temperature [K]	Wavelength [Å]
cold	0.1-10	1-120	30-3
thermal	5-100	60-1000	4-1
hot	100-500	1000-6000	1-0.4

and typical energies matches elemental excitations of matter ($\approx 10\,\text{meV}$). In addition, since the neutron has a magnetic moment it can be used to study magnetic structure and excitations.

In order to describe the scattering experiment, we first need to understand how the neutron interacts with the atomic species in our sample. The process is a neutron-nucleus scattering process, where the potential of the nucleus is approximated by the Fermi pseudopotential

$$V(\boldsymbol{r}) = \frac{2\pi\hbar}{m_\text{n}} b\delta(\boldsymbol{r})\,, \tag{2.1}$$

where b is called the *nuclear scattering length* and depends on the specific nuclear species involved in the scattering process. The δ-function in the pseudopotential is an expression of the fact that we are using the *Born approximation*, which is essentially a statement that the nucleus can be thought of as a point-scatterer compared to the neutron. Since the wavelength of a typical thermal neutrons ($\approx 10^{-10}\,\text{m}$) is orders of magnitude larger than the range of nuclear forces ($\approx 10^{-15}\,\text{m}$), this is a reasonable assumption. For a single, free nuclei, the scattering will be isotropic and the total scattering is $\sigma_\text{tot} = 4\pi b^2$.

The general geometry of a scattering experiment is outlined in figure 2.1. An incident beam with wave vector k_i is scattered from the origin to a final wave vector k_f at an azimuthal angle Θ and a polar angle Φ into a solid angle Ω distance r away from the origin. From this geometry we define the differential scattering cross-section as

$$\frac{\mathrm{d}\sigma}{\mathrm{d}\Omega} = \frac{\text{flux of neutrons into } \mathrm{d}\Omega}{\text{incident flux of neutrons}}$$

Since we can only measure the neutron flux, $\mathrm{d}\sigma/\mathrm{d}\Omega$ is our experimental observable, given that we have neutron detectors before and after the sample. Since the neutron flux tells us nothing about the wave vectors or energy, additional constraints are necessary to get information about the scattering process from the experiment. In *elastic scattering*, we assume that no energy is exchanged in the scattering process so that $|\boldsymbol{k}_\text{f}| = |\boldsymbol{k}_\text{i}|$. By fixing one of them (typically $\boldsymbol{k}_\text{i}$), the other is completely described by the geometry of figure 2.1 and we can measure $\mathrm{d}\sigma/\mathrm{d}\Omega$ as a function of $\boldsymbol{k}_\text{f}$ since the location of our detector, and thus Φ and Θ is known. In *inelastic scattering*, we need to fix the lengths, and thus the energy, of both $\boldsymbol{k}_\text{i}$ and $\boldsymbol{k}_\text{f}$. This defines the *partial differential cross-section*:

$$\frac{\mathrm{d}^2\sigma}{\mathrm{d}\Omega\mathrm{d}E_\text{f}} = \frac{\text{flux of neutrons into } \mathrm{d}\Omega \text{ with energy between } E_\text{f} \text{ and } E_\text{f} + \mathrm{d}E_\text{f}}{\text{incident neutron flux with energy } E_\text{i}}\,,$$

where E_i is the energy of the incident neutron and E_f is the energy of the final neutron. With the observables now defined, we can start to discuss how to actually extract useful information about the atomic/microscopic details of a sample from a neutron scattering experiment. Knowing $\boldsymbol{k}_\text{i}$ and $\boldsymbol{k}_\text{f}$, the coordinate system can be redefined with respect to our sample through the scattering vector $\boldsymbol{Q} = \boldsymbol{k}_\text{i} - \boldsymbol{k}_\text{f}$. In addition, we define the *energy transfer* as the amount of energy gained (or lost, for negative values) by the neutron in the scattering process $\hbar\omega = E_\text{f} - E_\text{i}$.

The objective of neutron scattering theory (or really, any scattering theory), is then to find a sample-dependent function $S(\boldsymbol{Q},\omega)$ that can be related to the observable (partial) scattering cross-section. In fact, as we shall see in the next section, it turns out that this *scattering function* $S(\boldsymbol{Q},\omega)$ not only exists, but have an intimate relationship with microscopic correlation functions which can be derived from first principles.

This, somewhat abstract, introduction essentially covers most of what we need to know with regards to the neutron scattering process and coordinate systems. The rest of this section is then dedicated to 1) understanding what the scattering function $S(\boldsymbol{Q},\omega)$ actually represents and 2) outline some of practicalities involved in the neutron scattered methods used in this thesis.

Correlation Functions

After setting up the coordinate system, we are now left with the much more complicated task of constructing models that can help us interpret the partial differential cross-section. As I previously suggested, information about our samples comes from the pattern of $\mathrm{d}^2\sigma/\mathrm{d}\Omega\mathrm{d}E_\text{f}$ as a function of $\boldsymbol{Q}$ and ω, or equivalently: The angles Φ, Θ and neutron energies E_i, E_f. Intuitively, the reason we have any pattern at all is due to interference of the scattered waves. Since the scattering from a single nucleus is isotropic, any pattern in $S(\boldsymbol{Q},\omega)$ comes from the specific composition of, or correlations between, atomic species in our sample.

It turns out that this can be conveniently described through the mathematics of correlation functions, introduced by Van Hove in 1954 [100]. We start with the *time-dependent pair-correlation*

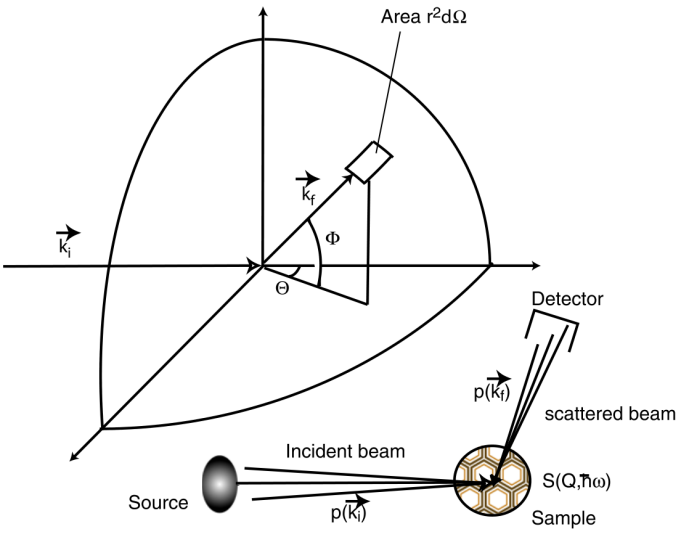

Figure 2.1: Geometry of a scattering experiment. An incident beam of neutrons characterized by the wave vector $\boldsymbol{k}_\mathrm{i}$ impinges on a sample at the origin. The neutron beam is scattered in the direction of $\boldsymbol{k}_\mathrm{f}$, defined by the two angles Φ and Θ. The neutrons are detected at a solid angle $\mathrm{d}\Omega$ at a distance r. From [98]

function for a system of identical particles $G(\boldsymbol{r}, t)$, which describes the probability of finding a pair of particles separated by the spatial vector $\boldsymbol{r}$ at time t. Similarly, the *self time-dependent pair-correlation function* $G_\mathrm{s}(\boldsymbol{r}, t)$ describes the probability of finding the same particle at a distance $\boldsymbol{r}$ at a time t. These concepts can be defined mathematically defined through position operators:

$$G(\boldsymbol{r}, t) = \frac{1}{N} \sum_{i \neq j} \int \langle \delta(\boldsymbol{r}' - \boldsymbol{R}_j(0)) \delta(\boldsymbol{r}' + \boldsymbol{r} - \boldsymbol{R}_i(t)) \rangle \, \mathrm{d}\boldsymbol{r}'$$
$$G_\mathrm{s}(\boldsymbol{r}, t) = \frac{1}{N} \sum_{i} \int \langle \delta(\boldsymbol{r}' - \boldsymbol{R}_i(0)) \delta(\boldsymbol{r}' + \boldsymbol{r} - \boldsymbol{R}_i(t)) \rangle \, \mathrm{d}\boldsymbol{r}' \,,$$

where i, j are particle indices and $\boldsymbol{R}_i(t)$ is the position operator for particle i at time t. Finally the following functions can be obtained through Fourier transforms in time and space:

$$I(\boldsymbol{Q}, t) = \int G(\boldsymbol{r}, t) \exp(i\boldsymbol{Q} \cdot \boldsymbol{r}) \mathrm{d}\boldsymbol{r}$$
$$I_\mathrm{s}(\boldsymbol{Q}, t) = \int G_\mathrm{s}(\boldsymbol{r}, t) \exp(i\boldsymbol{Q} \cdot \boldsymbol{r}) \mathrm{d}\boldsymbol{r}$$
$$S(\boldsymbol{Q}, \omega) = \frac{1}{2\pi\hbar} \int I(\boldsymbol{Q}, t) \exp(-i\omega t) \mathrm{d}t$$
$$S_\mathrm{i}(\boldsymbol{Q}, t) = \frac{1}{2\pi\hbar} \int I_\mathrm{s}(\boldsymbol{Q}, t) \exp(-i\omega t) \mathrm{d}t \,,$$

where $I(\boldsymbol{Q}, t)$ is known as the *intermediate function*, $I_\mathrm{s}(\boldsymbol{Q}, t)$ the *self intermediate function*, $S(\boldsymbol{Q}, \omega)$ the *scattering function* and $S_\mathrm{i}(\boldsymbol{Q}, t)$ the *incoherent scattering function*. The connection to the partial differential cross-section can now be stated succinctly as

$$\frac{\mathrm{d}^2\sigma}{\mathrm{d}\Omega \mathrm{d}E_\mathrm{f}} = \left(\frac{\mathrm{d}^2\sigma}{\mathrm{d}\Omega \mathrm{d}E_\mathrm{f}} \right)_\mathrm{coh} + \left(\frac{\mathrm{d}^2\sigma}{\mathrm{d}\Omega \mathrm{d}E_\mathrm{f}} \right)_\mathrm{inc} \tag{2.2}$$

with

$$\left(\frac{\mathrm{d}^2\sigma}{\mathrm{d}\Omega \mathrm{d}E_\mathrm{f}} \right)_\mathrm{coh} = \frac{\sigma_\mathrm{coh}}{4\pi} \frac{k_\mathrm{f}}{k_\mathrm{i}} N S(\boldsymbol{Q}, \omega)$$
$$\left(\frac{\mathrm{d}^2\sigma}{\mathrm{d}\Omega \mathrm{d}E_\mathrm{f}} \right)_\mathrm{inc} = \frac{\sigma_\mathrm{inc}}{4\pi} \frac{k_\mathrm{f}}{k_\mathrm{i}} N S_\mathrm{i}(\boldsymbol{Q}, \omega)$$

where

$$\sigma_{\text{coh}} = 4\pi\bar{b}^2$$
$$\sigma_{\text{inc}} = 4\pi\left(\overline{b^2} - \bar{b}^2\right)$$

In the above equations, N is the number of particles in the scattering system, b is the nuclear scattering length as defined in equation (2.1) and the bars denote ensemble averages. The *coherent cross-section* σ_{coh} is thus related to the average scattering length, while the *incoherent cross-section* σ_{inc} is related to the distribution of scattering lengths. These cross-sections are determined experimentally and are tabulated for most elements [101].

In a neutron scattering experiment we thus see a superposition of pair-correlations through coherent scattering and self-correlations through incoherent scattering. As an example involving dynamics, phonons (correlated motion) are generally seen as coherent scattering while Brownian motion (random motion) would show up as incoherent scattering.

It thus turns out that there is a direct relationship between the measured partial differential cross-section in neutron scattering and microscopic correlation functions. In fact, many microscopic theories can be translated directly into a theoretical $S(\boldsymbol{Q}, \omega)$ and compared 1-to-1 with experiment. One illustrative example, used in this thesis, is that of a molecular dynamics simulation where we record the atomic positions as a function of time. From this trajectory it is trivial to compute a classical version of $G(\boldsymbol{r}, t)$ and thus obtain predictions for neutron scattering experiments.

Even more generally, given a Hamiltonian (quantum or classical) and assuming a weak (linear) perturbation, it is possible to invoke linear response theory (see e.g. [102, chapter 3]). Importantly, linear response theory provides a link between the spontaneous fluctuations of a system and the response to an external perturbation. The object of interest in this context becomes the dynamic susceptibility $\chi(\boldsymbol{Q}, \omega)$, which can be thought of as

$$\chi(\boldsymbol{Q}, \omega) = \chi'(\boldsymbol{Q}, \omega) + \chi''(\boldsymbol{Q}, \omega) = \frac{\text{'response'}}{\text{'force'}},$$

where the real part $\chi'(\boldsymbol{Q}, \omega)$ describes a response in phase with the perturbation (reactive), while the imaginary part $\chi''(\boldsymbol{Q}, \omega)$ describes an anti-phase response (dissipative). The real and imaginary parts are linked through the Kramers-Kronig relation

$$\chi''(\boldsymbol{Q}, \omega) = -\frac{1}{\pi}\mathcal{P}\int_{-\infty}^{\infty} \frac{\chi'(\boldsymbol{Q}, \omega')}{\omega' - \omega} \mathrm{d}\omega',$$

where $\mathcal{P}$ is the Cauchy principal value. Finally, the scattering function is related to the imaginary part of the dynamic susceptibility through the fluctuation-dissipation theorem:

$$S(\boldsymbol{Q}, \omega) = \frac{1}{1 - e^{\frac{\hbar\omega}{k_{\text{B}}T}}} \chi''(\boldsymbol{Q}, \omega). \tag{2.3}$$

Since the real and imaginary parts of the susceptibility are uniquely connected through the Kramers-Kronig relation, neutron scattering experiments can directly probe predictions of linear response theory. A particularly illustrative example in the context of this thesis is that of a damped harmonic oscillator (DHO). Consider the classical system shown in figure 2.2, with the equations of motion:

$$m\langle\ddot{x}(t)\rangle + mw_0^2\langle x(t)\rangle = -m\gamma\langle\dot{x}(t)\rangle.$$

Assuming an impulsive perturbation (a δ-function displacement) and going through the mathematics of linear response theory (see [96] for details), we arrive at the dynamic susceptibility

$$\chi[\omega] = \frac{1}{m}\frac{1}{\omega_0^2 - \omega^2 + i\gamma\omega} = \frac{1}{m}\frac{\omega_0^2 - \omega^2}{(\omega_0^2 - \omega^2)^2 + \gamma^2\omega^2} - \frac{i}{m}\frac{\gamma\omega}{(\omega_0^2 - \omega^2)^2 + \gamma^2\omega^2}. \tag{2.4}$$

From the last term we thus see that damped harmonic motion can be observed as a Lorentzian as a function of energy in a neutron scattering experiment, where the position ω_0 denotes the fundamental frequency and the width γ is the damping constant. In fact, this expression is typically used as a fitting function when measuring phonons [103]. While rudimentary, the purpose of this example is to emphasize the intimate relationship between observables in neutron scattering and microscopic theories.

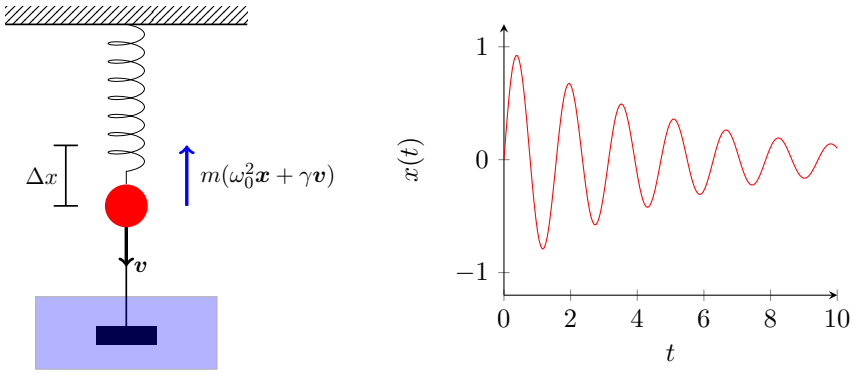

Figure 2.2: Mechanical version of the damped harmonic oscillator. **Left:** A mass on a spring moving with velocity $\boldsymbol{v}$ under the influence of a restoring spring force (blue arrow) with force constant ω_0^2 and a frictional force γ which is linear in velocity. **Right:** Position of the spring as a function of time after applying a an impulsive perturbation, analogous to quickly pulling the mass and letting go.

Resolution

When performing actual neutron scattering measurements, the incident and final wave vectors are not completely defined by a single vector, but rather by some finite distribution. In fact, since neutrons are relatively sparse, it is not uncommon to relax this distribution in order to increase the signal. This finite distribution of wave vectors will broaden the signal in both $\boldsymbol{Q}$ and ω. Since the optics of the instrument is responsible for this broadening, we call the effect *instrumental resolution*.

To make matters more complex, the resolution is not a constant object, but rather varies as a function of both $\boldsymbol{Q}$ and ω. It is therefore important to understand the instrumental resolution for any particular measurement to make sure that, for example, a broad feature is due to the sample and not the instrument. In many cases, the resolution can be measured with respect to a standard and subtracted in the same way for every experiment. In some cases, such as the triple-axis spectrometer, the experimental condition vary wildly between experiments and it might be beneficial to calculate the resolution beforehand.

The resolution is quantified by the *resolution function* $R(\boldsymbol{Q}, \omega)$. which can be represented by a 4 dimensional ellipsoid if we assume that the distribution of neutrons follow a normal distribution as they propagate through the instrument. The 4 major axes of this ellipsoid then represents the Gaussian width σ in each direction. By projecting this ellipsoid onto the scattering plane, one can gain an intuitive understanding of how the resolution affects the experiment.

I will not go into further detail at this point, but rather refer to [99, Chapter 4] for a much more in-depth discussion of this topic in the context of triple-axis spectroscopy. Finally, the best way to understand how resolution affects measurements is to play around with software that can simulate and visualize the resolution ellipsoid in various conditions [104, 105].

2.2 Specific Scattering Methods

Departing from the abstract concepts of the preceding section, I will now outline specific neutron scattering techniques used in the experimental part of this thesis. Despite the significant power generated in a neutron reactor, the number of neutrons expelled from the source is typically small with respect to neutron experiments, especially when compared to X-ray synchrotron radiation. In addition, the neutrons have a wide distribution of wavelengths and propagate in all directions. Neutron facilities and instruments thus take advantage of various optical elements in order to define the neutron beam.

Transporting the neutrons to the instruments is done with neutron guides, which are rectangular tubes where the insides are coated with mirrors that can cause total reflection of neutrons at sufficiently small angles ($0.1° to 1°$). When neutrons reach the instrument, we have so-called a *white beam* with a wide distribution of wavelengths, but most experiments needs a well-defined $\boldsymbol{k}_\mathrm{i}$. Details about neutron instrumentation quickly becomes complex, so we stop the detailed discussion here since it would divert from the purposes of this thesis.

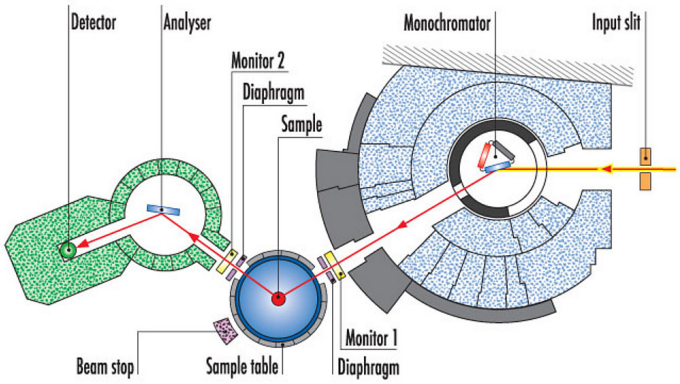

Figure 2.3: Layout of the IN8 instrument at ILL [106]. Neutrons from the thermal source hits one of the 3 optional monochromators (PG002, Cu200, Si111) and continues towards the sample where it is scattered towards the analyser that selects the final energy.

Triple-Axis Spectroscopy

In some way, the triple-axis spectrometer (TAS) is the easiest neutron scattering instrument to understand because it has a one-to-one correspondence with the geometry from figure 2.1. Figure 2.3 shows the view from above of the TAS instrument IN8 at ILL. The triple-axis (or triple-angle) name comes from the fact that all the angles defined by the beam path can be adjusted by moving the motors of the instrument. These angles then completely define $\boldsymbol{k}_\mathrm{i}$, $\boldsymbol{k}_\mathrm{f}$ and we essentially have a two dimensional version of figure 2.1, known as the *scattering plane*.

Because the instrument is essentially two-dimensional, single crystal samples must be aligned with a desired crystal plane in the scattering plane. With the sample in place, we can now completely explore $S(\boldsymbol{Q},\omega)$ with the restriction that $\boldsymbol{Q}$ is restricted to the scattering plane. The sample is placed on a rotating sample stick that, together with the scattering angle, allows us to access the two dimensions of $\boldsymbol{Q}$. The energy transfer $\hbar\omega$ is controlled by monochromator and analyser.

As one might have noticed, figure 2.3 features just a single detector. While other options exists (see chapter 6), this is typical for TAS instruments. As a consequence, measurements are performed along pre-defined paths in $(\boldsymbol{Q},\omega)$ space step-by-step. The main purpose of TAS instruments is then generally to look at specific features in $S(\boldsymbol{Q},\omega)$ with high counting statistics and tight resolution. Since inelastic scattering is orders of magnitude weaker than elastic scattering, spectroscopic measurements are usually the primary focus for TAS instruments.

In this thesis, most TAS measurements are of specific phonon branches. The 1-phonon cross-section gives an expression for the differential coherent cross section of phonons, indexed by the phonon band ν [97].

$$S(\boldsymbol{Q},\nu,\omega) = \frac{k_\mathrm{f}}{k_\mathrm{i}}\frac{N}{\hbar}\sum_{\boldsymbol{q}}|F(\boldsymbol{Q},\boldsymbol{q},\nu)|^2(n_{\boldsymbol{q}\nu}+1)\delta(\omega-\omega_{\boldsymbol{q}\nu})\delta(\boldsymbol{Q}-\boldsymbol{q}-\boldsymbol{G}) \tag{2.5}$$

with

$$F(\boldsymbol{Q},\boldsymbol{q},\nu) = \sum_j \sqrt{\frac{\hbar}{2m_j\omega_{\boldsymbol{q}\nu}}}\bar{b}_j \exp\left(-\frac{1}{2}\langle|\boldsymbol{Q}\cdot\boldsymbol{u}(j0)|^2\rangle\right)\exp[-i(\boldsymbol{Q}-\boldsymbol{q})\cdot\boldsymbol{r}(j0)]\boldsymbol{Q}\cdot\boldsymbol{e}_j(\boldsymbol{q},\nu)$$

where $\boldsymbol{Q}$ and ω are the wave vector and energy of our measurement. ν is a phonon band and $\boldsymbol{q}$ is the phonon wave vector. $\omega_{\boldsymbol{q}\nu}$ is the energy of phonon band ν at wave vector $\boldsymbol{q}$ and $n_{\boldsymbol{q}\nu}$ is the Bose factor at this energy. Atomic species are designated with index j, their mass is m_j and their coherent neutron cross-section is $\bar{b}_j$. $\boldsymbol{u}(j0)$ and $\boldsymbol{r}(j0)$ is the displacement and position of atom j in unit cell 0, respectively. Finally, G is any reciprocal lattice vector and $\boldsymbol{e}_j(\boldsymbol{q},\nu)$ is the phonon eigenvector of atom j, band ν and wave vector $\boldsymbol{q}$.

While this expression rests on some microscopic details that we might not have knowledge of, close inspection of equation (2.5) allows us to extract information from an experiment without

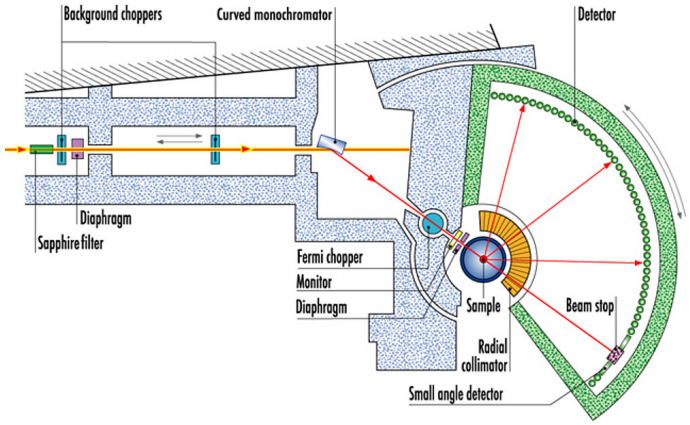

Figure 2.4: Layout of the IN4 instrument at ILL [107]. Neutrons are chopped into discrete packets before hitting the monochomator and continuing towards the sample position. A Fermi chopper is used to make very short neutron pulses, such that their (Q, ω) can be determined from the time-of-flight from the Fermi chopper to the detector,

any prior knowledge of the system. The δ-functions makes sure that we only see scattering at the phonon dispersion. In addition, the $\boldsymbol{Q} \cdot \boldsymbol{e}_j(\boldsymbol{q}, \nu)$ term tells us that scattering is strongest when the eigenvector of the phonon mode is parallel to $\boldsymbol{Q}$ (and vanishes when perpendicular). This allows us to distinguish longitudinal and transverse phonons, since they vibrate parallel and perpendicular to $\boldsymbol{Q}$, respectively. For an example of this, see figure 6.5 in chapter 6.

As it turns out, it *is* possible to obtain prior knowledge about the phonon spectrum through microscopic simulations. These simulations give us direct access to eigenvectors and we can make a detailed analysis of equation (2.5). More information about this type of calculation is given in section 2.4.

One caveat with equation (2.5) is the fact that phonons can be broadened, on top of broadening due to resolution, such that the delta function in energy is replaced with a Lorentzian as we saw in equation (2.4) and (2.3). This is known as *lifetime broadening* and the Lorentzian width can be interpreted as the reciprocal lifetime of the measured phonon.

Time-of-Flight Spectroscopy

In Time-of-Flight (ToF) spectroscopy, we take advantage of the fact that thermal neutrons move at speeds that we can accurately determine experimentally (10 meV neutrons has a speed of roughly $1400\,\mathrm{m\,s^{-1}}$). Figure 2.4 shows a schematic of the IN4c spectrometer at ILL. Neutrons from the reactor are chopped up into discrete packets using two rotating discs (background choppers) and then monochromatized using a crystal monochromator. Before impinging on the sample, the neutrons pass through a 'Fermi chopper' which produces very short neutron pulses (10 µs to 50 µs). Neutrons are then detected radially in one of the many detectors. By recording the time-of-flight from the Fermi chopper to a specific detector, we can determine the energy transfer through the velocity as determined from the flight time and $\boldsymbol{Q}$ from the angle to the detector where the neutron was measured.

Time-of-Flight spectrometers thus perform many simultaneous measurements, but can in some sense be used to probe many of the same things as TAS instruments. The better choice depends, of course, on the sample and phenomena that you are using it to probe. In the case of this thesis, we used the IN4 spectrometer to measure the phonon density-of-states of powdered samples. Since the powder is rotationally averaged, the result of a measurement is a $(Q, \hbar\omega)$ map where Q is defined as the length of $\boldsymbol{Q}$. An example of such a dataset is shown in figure 7.2 in chapter 7. By integrating the full map onto the energy axis we obtain the experimental phonon density-of-states.

While equation 2.5 is still valid since most of our scattering is 1-phonon processes at low temperature, we use the confusingly named *incoherent approximation*. The physical reasoning is that the rotational averaging due to the powder cancels out correlations between distinct atoms.

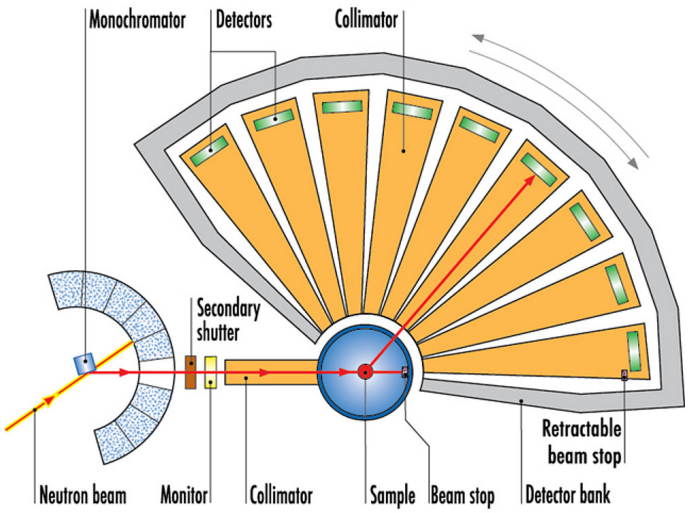

Figure 2.5: Schematic layout of the D4 instrument at ILL [109]. The neutron beam from the hot source hits the monochromator and directed towards the sample position. The scattered neutrons are collected at the nine detectors each containing 64 cells. The detector bank can be moved during the experiment in order to cover the full Q-range.

Mathematically, it is due to factor

$$\left(\sum_j \boldsymbol{Q}\cdot\boldsymbol{e}_j(\boldsymbol{q},\nu)\right)^2$$

which in the incoherent approximation is replaced by [108]

$$\sum_j Q^2\left(\boldsymbol{e}_j(\boldsymbol{q},\nu)\right)^2$$

essentially eliminating the cross terms. With this approximation, the 1-phonon incoherent cross-section becomes:

$$S^{(1)}_{\text{inc}}(Q,E)=\exp\left(-2\bar{W}(Q)\right)\frac{Q^2}{E}\langle n+\frac{1}{2}\pm\frac{1}{2}\rangle\left[\sum_k\frac{\sigma_k^{\text{scatt}}}{2m_k}g_k(E)\right]$$

where $g_k(E)$ represents the phonon density of states. With this, much simpler, expression we can transform our (Q,E) dataset into the phonon density of states, only supplying the mean-squared displacement and atomic composition. Similar to the phonon bands, the phonon density of states can also be directly obtained from simulations methods. ToF spectroscopy on powders thus allows us to investigate properties of the overall phonon spectra, in contrast to the distinct phonon bands as measured by TAS spectroscopy.

Real-space diffraction

The last method I will cover here is a diffraction instrument focussed on obtaining real space structures. In terms of the correlation functions defined in section 2.1, we are interested in the time-averaged value of $G(\boldsymbol{r},t)$ which can be found as the Fourier transform of $S(\boldsymbol{Q},\omega=0)$. In order to perform this Fourier transform, it is desired to measure at a wide range of $\boldsymbol{Q}$ in order to avoid artefacts related to the Fourier transformation pocedure itself.

Figure 2.5 shows the D4 diffractometer at ILL. Since diffraction assumes elastic scattering, the instrument is equipped with a monochromator before the sample, but no energy analysis of the scattered neutrons is performed. Rather, the neutrons are directly measured at the radial detectors. In order to optimize the $\boldsymbol{Q}$-range of the instrument, we want to minimize the wavelength (Bragg's law), so D4 is placed at a hot source so that we can get a large number of high-energy neutrons. For our particular experiment the monochromator selected neutrons with a wavelength $\lambda=0.35\,\text{Å}$, corresponding to an energy of $E=668\,\text{meV}$.

The object of interest in this case is the total pair distribution function $G(r)$, which tells you the probability of finding two atoms separated by a distance r, weighted by the product of

their coherent neutron scattering lengths $\bar{b}$. As we shall see in section 2.6, these distributions can be found from a molecular dynamics simulation. In order to compare with experiment we then consider

$$G(r) = \frac{1}{\bar{b}^2} \sum_{\alpha=1,\beta\geq\alpha} c_\alpha c_\beta \bar{b}_\alpha \bar{b}_\beta (g_{\alpha\beta}(r) - 1)\,,$$

where $g_{\alpha\beta}(r)$ is the *partial radial distribution function* which describes the probability of finding a particle with label β at a distance r away from a particle with label α. $c_i = \frac{N_i}{N}$ is the number concentration, $\bar{b}_i$ is the coherent neutron cross section of species i, and

$$\bar{b}^2 = \left(\sum_\alpha \bar{b}_\alpha c_\alpha \right)^2 .$$

In the research community working with pair distribution functions (PDF) there is a large number of conventions regarding how to normalize and represent pair-correlation functions in theory and experiment (see review by Keen [110]). The $G(r)$ presented here is typically called the *Total Pair-Distribution Function*. Details about the definitions of $g_{\alpha\beta}(r)$ and $G(r)$ and how to obtain them from molecular dynamics trajectories can be found in section 2.5

2.3 Density Functional Theory

We now turn to the computational framework used in this thesis, Density Functional Theory (DFT). Similar to the section on neutron scattering, this is a vast subject that is impossible to fully explore on a few pages, but I will once again try to outline the key concepts, advantages and disadvantages. For more comprehensive material, I recommend the books by Giustino [111] (introduction to the subject) and Martin [112, 113] (comprehensive reviews). The review paper by Hoffmann [114] discusses what kinds of problems DFT can solve and is recommended for anyone curious about DFT.

DFT is a computational method in quantum chemistry, where the objective is to compute the many-body Schrödinger equation for molecules and solids:

$$\left[-\sum_i \frac{\nabla_i^2}{2} - \sum_i \sum_I \frac{Z_I}{|\boldsymbol{r}_i - \boldsymbol{R}_I|} + \frac{1}{2} \sum_{i\neq j} \frac{1}{|\boldsymbol{r}_i - \boldsymbol{r}_j|} \right] \Psi = E\Psi\,, \tag{2.6}$$

where $\boldsymbol{r}_i$ is the position of electron i and $\boldsymbol{R}_I$, Z_I is the position, charge of nucleus I. As one might have noticed, the kinetic energy of nuclei and nuclei-nuclei interactions have been omitted. This is known as the *clamped nuclei approximation*, which assumes immobile nuclei. This results in a vanishing kinetic energy and a constant Coulomb repulsion which can be subtracted from the energy on the right-hand-side of equation (2.6):

$$E = E_{\text{total}} - \frac{1}{2} \sum_{I\neq J} \frac{Z_I Z_J}{|\boldsymbol{R}_I - \boldsymbol{R}_J|}$$

These equations are written in the so-called Hartree units (see [111, chapter 2.3]), such that energies are in units of Hartree energies ($1\,E_\text{h} = 27.2114\,\text{eV}$), distances are in units of the Bohr radius a_0 and masses are in units of electron masses m_e. Since the nuclear coordinates are considered fixed, the many-body wavefunction Ψ in equation (2.6) is a function of electron positions

$$\Psi(\boldsymbol{r}_1, \boldsymbol{r}_2, \ldots, \boldsymbol{r}_n)$$

While this object seems innocent at first glance, the many-body Schrödinger equation quickly becomes a completely unmanageable object. Imagine that we want to calculate this object for a small molecule such as Benzene (C_6H_6) containing 12 nuclei and 42 electrons. This wavefunction exists in $42 \cdot 3 - 3 = 123$ dimensional cartesian space! If we want to store this object on a computer with a modest precision of 10 grid points per coordinate, it would require 10^{156} complex numbers or $64 \cdot 10^{156}$ bits (assuming single-precision floating points numbers of 32 bits). Lloyd estimated the total number of bits available for computation in the observable universe to be 10^{90} [115]. Even with the entire universe at our disposal this object is completely unmanageable. In order to arrive at a reasonably manageable theory, we assume that electrons are independent such that the many-body wavefunction can be written as a product of single-electron wavefunctions:

$$\Psi(\boldsymbol{r}_1, \boldsymbol{r}_2, \ldots, \boldsymbol{r}_n) \longrightarrow \phi_1(\boldsymbol{r}_1)\phi_2(\boldsymbol{r}_2)\ldots\phi_N(\boldsymbol{r}_N) \tag{2.7}$$

Where each of the wavefunctions ϕ_i are found as solutions to the single-electron Schrödinger equation

$$\left[-\frac{\nabla^2}{2} - \sum_I \frac{Z_I}{|\boldsymbol{r} - \boldsymbol{R}_I|}\right] \phi_i = \epsilon_i \phi_i \,.$$

Using these definitions, the many-body Schrödinger equation becomes

$$\sum_i \left[-\frac{\nabla^2}{2} - \sum_I \frac{Z_I}{|\boldsymbol{r}_i - \boldsymbol{R}_I|}\right] \Psi = E\Psi \,, \tag{2.8}$$

where $E = \epsilon_1 + \epsilon_2 + \ldots \epsilon_N$, with the single-electron energies being ordered from smallest to largest. This corresponds to the situation usually taught in condensed matter physics where the lowest energy configuration is found by filling up electronic orbitals starting from the lowest eigenvalue [6]. Inspection of equation 2.8 reveals that the independent electron approximation, as the name implies, has completely ignored the Coulomb repulsion between electrons. To rectify this fact, we make a *mean-field approximation*, such that each electron feels an electrostatic 'Hartree potential':

$$\nabla^2 V_H(\boldsymbol{r}) = -4\pi n(\boldsymbol{r})$$

where the electron density is defined as the sum of single-electron densities:

$$n(\boldsymbol{r}) = \sum_i |\phi_i(\boldsymbol{r})|^2 \,. \tag{2.9}$$

Starting with the many-body Schrödinger equation we have thus arrived at an approximate version that can be approached from a computational point of view. However, at this stage we have ignored exchange (equation (2.7) is not anti-symmetric with regards to a change of variables) and correlation (the mean field approximation used for the Hartree potential). As we shall see, DFT gives us a way to correct for both of these effects in a surprisingly accurate manner.

The Kohn-Sham equations

The main idea behind DFT is expressed through the 'Hohenberg-Kohn theorem', which is the simple but powerful statement that the total energy of a many-electron system is a functional of the electron density. In addition, the 'Hohenberg–Kohn Variational Principle' tells us that the ground state density is the functional that minimizes the total energy. To quote the original paper [116]:

> This paper deals with the ground state of an interacting electron gas in an external potential $v(\boldsymbol{r})$. It is proved that there exists a universal functional of the density, $F[n(\boldsymbol{r})]$, independent of $v(\boldsymbol{r})$, such that the expression $E = \int v(\boldsymbol{r}) n(\boldsymbol{r}) \mathrm{d}\boldsymbol{r} + F[n(\boldsymbol{r})]$ has as its minimum value the correct ground-state energy associated with $v(\boldsymbol{r})$.

The theorem states the existence of the functional $F[n(\boldsymbol{r})]$, but leaves us with no recipe on how to construct this functional. The 'game' in DFT thus consists of constructing functionals and test the computational results against experimental observations. Since the universal functional has not been found, hundreds of functionals [117] have been created with specific purposes in mind. With that being said, very good 'universal' functionals exist and most people stick to a small subset of this 'functional zoo'. Returning the objective at hand, the idea of Kohn and Sham [118] was to split the contributions to the functional $F[n(\boldsymbol{r})]$ into terms of kinetic and coulomb energy and an additional term with 'everything else':

$$E = \int V_{\mathrm{n}}(\boldsymbol{r}) n(\boldsymbol{r}) \mathrm{d}\boldsymbol{r} + F[n(\boldsymbol{r})] \tag{2.10}$$

$$F[n(\boldsymbol{r})] = \sum_i \int \phi_i^*(\boldsymbol{r}) \frac{\nabla^2}{2} \phi_i(\boldsymbol{r}) \mathrm{d}\boldsymbol{r} + \frac{1}{2} \iint \frac{n(\boldsymbol{r}) n(\boldsymbol{r}')}{|\boldsymbol{r} - \boldsymbol{r}'|} \mathrm{d}\boldsymbol{r} \mathrm{d}\boldsymbol{r}' + E_{\mathrm{XC}}[n(\boldsymbol{r})] \,. \tag{2.11}$$

This expression thus lets us evaluate the total energy of our approximate many-body Schrödinger equation given a set of one-electron orbitals ϕ_i, the electronic density $n(\boldsymbol{r})$ and the *exchange correlation functional* $E_{\mathrm{XC}}[n(\boldsymbol{r})]$. These are evaluated using the Kohn-Sham equations [118]:

$$\left[-\frac{1}{2}\nabla^2 + V_{\mathrm{tot}}(\boldsymbol{r})\right] \phi_i(\boldsymbol{r}) = \epsilon_i \phi_i(\boldsymbol{r}) \,, \tag{2.12}$$

where

$$V_{\text{tot}} = V_{\text{n}}(\boldsymbol{r}) + V_{\text{H}}(\boldsymbol{r}) + V_{\text{XC}}(\boldsymbol{r}) \tag{2.13}$$

$$V_{\text{n}}(\boldsymbol{r}) = -\sum_I \frac{Z_I}{|\boldsymbol{r} - \boldsymbol{R}_I|} \tag{2.14}$$

$$\nabla^2 V_{\text{H}}(\boldsymbol{r}) = -4\pi n(\boldsymbol{r}) \tag{2.15}$$

$$V_{\text{XC}} = \frac{\delta E_{\text{XC}}[n]}{\delta n}(\boldsymbol{r})\,. \tag{2.16}$$

Where the last equation defines the *exchange correlation potential*. Methods to actually solve equation 2.12 numerically are outside the scope of this thesis and can be found in literature [112, part IV]. In general, this depends on the representation of our one-electron orbitals ϕ, also known as the *basis set*. In this thesis, we make use of a basis set which is expanded in plane waves. Plane wave DFT is particularly popular for computing crystalline materials, since we are guaranteed that ϕ are cell-periodic (Bloch functions). The main disadvantage is that you need a large number of plane waves to have a reasonable representation of electronic orbitals.

What we have done so far is to reduce the electronic structure problem into one that is completely described by the electronic density. In addition, the contributions to the equations have been split up into well-understood terms (kinetic energy, nuclear-electron potential, mean-field Hartree potential) and the unknown exchange-correlation functional E_{XC}. When the phrase 'choice of functional' comes up in the context of DFT, one actually means the choice of exchange-correlation functional since everything else is fixed in the Kohn-Sham equations.

Exchange-Correlation Functional

With the large number of XC functionals in existence, it may seem a bit daunting to make a reasonable choice. In fact, if we need to build new functionals for every peculiarity, is there even any merit to this method? It turns out that the simplest possible model for interacting electrons, the homogeneous electron gas (HEG), gives a surprisingly good representation of real systems where the distribution of electrons is inhomogenous. In fact, the original paper on the Hohenberg-Kohn theorem was titled 'Inhomogeneous Electron Gas' [116].

The most basic functional to express the exchange-correlation functional is the so-called Local-Density Approximation (LDA) [119, 120], where parameters of the HEG was found using quantum monte carlo methods. For this reason, this functional is entirely non-empirical and built from simple principles, both desirable qualities in any theory. While successful in these respects, it quite significantly overestimates atomization energies [121].

The 'local' in local-density approximation refers to the fact that E_{XC} depends only on the local density. To improve on this, functionals based on the Generalized Gradient Approximation (GGA) also takes into account the gradient of the local density. Of these, especially the Perdew-Burke-Ernzerhof (PBE) functional has gained popularity due to its relatively simple derivation that retains the important features of the LDA while incorporating non-locality and having a better agreement with experiment.

It seems reasonable that adding more non-local components to the E_{XC} will approve accuracy. Perdew and Schmidt suggested that the road to a universal potential should be constructed with respect to the so-called Jacob's Ladder [121] as shown in figure figure 2.6, where the lowest rung is the LDA and the second-lowest is the GGA. Successive improvements should be done in a way that keeps the principles of the previous rungs intact, but include orbital contributions. In the context of this thesis, we stick to the second rung of Jacob's ladder.

The Self-Consistent Field (SCF) Cycle

In order to actually perform a DFT calculation, we need to evaluate the Kohn-Sham equations. The solution to (2.12) depends on the density and gives the one-electron orbitals ϕ_i, but at the same time the density is defined with respect to the orbitals, equation (2.9). For this reason, the Kohn-Sham equations are solved with the Self-Consistent Field method, where we keep performing the calculations of equation (2.12) until the density of successive iterations agree within some pre-defined accuracy. This procedure is outlined schematically in figure 2.7.

The initial guess of the electron density is typically generated as a superposition of atomic charge densities, but can also be supplied to the program from a previous run, significantly speeding up calculations on continuation jobs. Once again, there are many subtleties regarding the actual

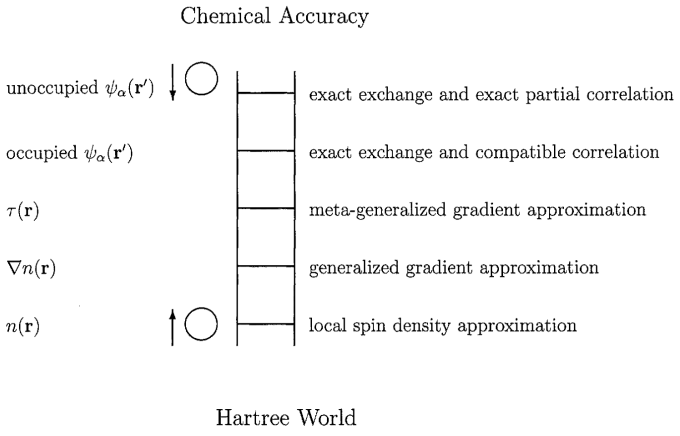

Figure 2.6: Jacob's Ladder of exchange-correlation potentials. At the lowest rung we only consider the local density. At the second rung, we include the gradient of the density. At the third, we include the kinetic energy density for the occupied orbitals $\tau(\boldsymbol{r})$, in the so-called meta-GGA functionals [122]. At the fourth rung we find Hybrid functionals which includes exact exchange and at the fifth we include both exact exchange and orbital contribtions. The original paper [121] 'only guarantees safety on the two lowest rungs'. From [121]

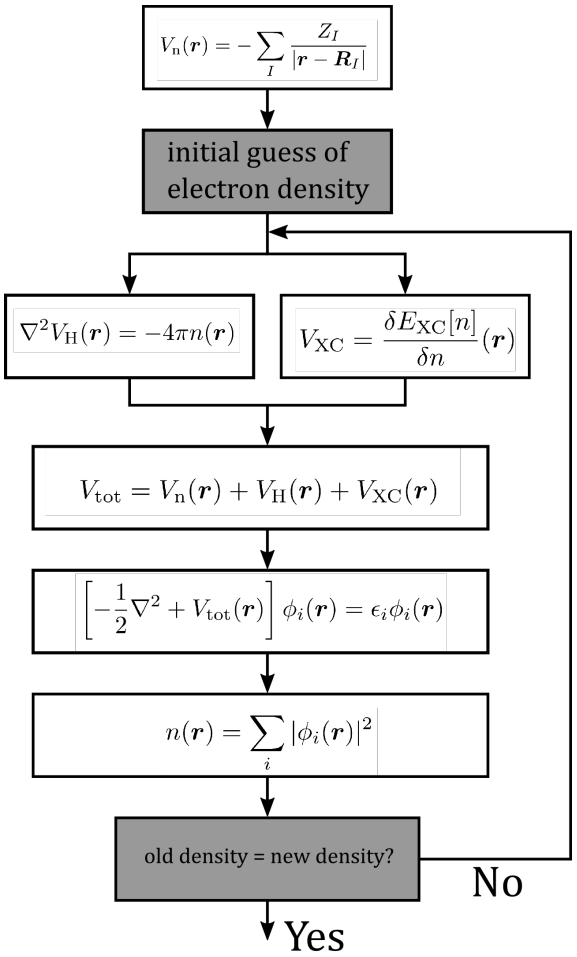

Figure 2.7: The self-consistent field (SCF) cycle used in most DFT calculations. V_{n} is a fixed quantity due to the clamped nuclei approximation and will not change during the SCF cycle. The Hartree V_{H} and exchange-correlation V_{XC} potentials are updated throughout the run due to a change in density and finally the orbitals and electronic density is computed. This is performed until the successive iterations agree on the density. Adapted from ref. [111].

computation of the different steps in figure 2.7 which are outside the scope of this thesis. We will see some of these concepts in the context of the actual calculations in chapter 3.

DFT+U

Despite the success of DFT for many materials, it generally struggles with the so-called strongly-correlated electron systems. One prominent example of this problem is exactly the materials studied in this thesis – the cuprates. While DFT is able to include magnetism through inequivalent spin-up and spin-down densities, LDA and GGA functionals generally fail to describe the anti-ferromagnetic ground state of La_2CuO_4. The strong correlations of the d-orbitals cannot be described at the orbital-independent LDA and GGA level of theory.

DFT+U is an attempt to approximately treat strong correlations of specific orbitals by introducing a non-local screened Coulomb potential. This screened Coulomb interaction U is only added to a sub-system consisting of the 'correlated orbitals', while the remaining orbitals are treated as normal. This results in occupied states of the correlated orbitals to be shifted by $-U/2$ while the unoccupied states are shifted by $+U/2$, essentially creating a gap with the size of U [123]. However, as we shall see in chapter 3, the actual band gap is usually smaller since the interaction is only added to the d orbitals of Cu.

While DFT+U helps us with an accurate description of Mott insulators, it departs slightly from the spirit of ab-initio simulations since we are forced to input external parameters. A different choice could be to move up a rung on Jacob's Ladder (figure 2.6), but this comes at a significant computational cost and exact exchange ignores the screened nature of U [123].

The Hellman-Feynman Theorem and Molecular Forces

Until now, we have only been concerned with calculating the free energy E through computations through the electronic density n and the electronic orbitals ϕ_i. Since we are interested in dynamics, we need some tools to manipulate the atomic positions, despite the fact that we are in the clamped nuclei approximation. The Hellman-Feynman theorem [124]

$$\frac{\partial E}{\partial x} = \int \phi(\boldsymbol{r})^* \frac{\partial \hat{H}}{\partial x} \phi(\boldsymbol{r}) \mathrm{d}\boldsymbol{r}$$

turns out to be extrordinarily helpful in this regards. Intuitively, the theorem states that any derivative of the total energy can be obtained by evaluating a matrix element constructed from the derivative of the hamiltonian $\hat{H}$. Since the atomic forces are simply derivatives of E with respect to atomic postions $\boldsymbol{R}_I$, this derivative can be performed directly on the first term of equation (2.10), since the second term is a function of electronic coordinates only. This results in the remarkable fact that we can calculate the forces on every atom in our system from a single groundstate energy, significantly reducing the computational effort.

For our purposes, the obtained forces are then treated classically with Newton's equations of motion. This will then be used to find equilibrium structures, phonon frequencies and to generate molecular dynamics trajectories. Since phonons are of particular interest to the scope of this thesis, the next section outlines how to obtain phonon frequencies from DFT and in chapter 3 I will show the result of such computations on La_2CuO_4 in various structural and electronic phases.

2.4 Phonon Calculations

In most textbooks (e.g. Kittel [6]), phonon calculations are exemplified by simple models in one dimension consisting of only one or two inequivalent atoms. While these models are useful for providing basic results of lattice dynamical models, the extension to realistic models requires some level of abstraction in order to be useful. In particular, it is essential to cast the problem in terms of linear algebra. In this section, I will start from the (somewhat abstract) formalism used in practice and work backwards towards a physical understanding. While software such as PHONON [125] and Phonopy [126] can be used without prior knowledge of the formalism, it is always useful to have some insights about our frequently used 'black boxes'. In order to calculate the phonon spectrum for a given system in the harmonic approximation, we require the following objects:

1. Primitive unit cell and fractional atomic coordinates

2. Symmetry operations

3. The mass of each atomic species
4. The force constants

Items 1-3 are familiar to most condensed matter physicists and can usually be found in various databases. The force constants, on the other hand, contains information about interatomic forces and is not directly obtainable from experiment. For this reason, phonon calculations requires some modelling either through semi-empirical or ab-initio methods. In the following I will attempt to explain what the force constants represents and how we use them to get phonon band structures.

Theory

We start completely generally in one dimension with an arbitrary number of unit cells containing an arbitrary number of atomic species at equilibrium. Displacements from equilibrium positions are denoted $u(jl)$, where l is the unit cell index and $j \in \{1, \dots, n\}$ is the atomic index. If we consider the displacements u to be small, the total energy of our system can be expressed as a Taylor series

$$E^{\text{tot}} = E_0 + \sum_l \sum_j \left.\frac{\partial E}{\partial u(jl)}\right|_{r_{lj}} + \frac{1}{2} \sum_{l,l'} \sum_{j,j'} u(jl) \left.\frac{\partial^2 E}{\partial u(jl) \partial u(j'l')}\right|_{r_{lj}, r_{l'j'}} u(j'l') + \dots ,$$

where r_{lj} is the equilibrium position of atom j in unit cell l. The main approximation in phonon calculations is the so-called *harmonic approximation* which ignores terms with power greater than 2 in the series. Higher-order contributions are denoted *anharmonic* terms and can become important at higher temperatures (phase transitions, thermal conductivity, thermal expansion). The fact that our system is in equilibrium can be stated succinctly as

$$\frac{\partial E}{\partial u(jl)} = 0 \,,$$

for all values of j and l. Physically these assumptions together correspond to atoms being at rest in a parabolic (harmonic) potential. Since we are interested in dynamics, it is convenient to consider the *harmonic energy* E of the system

$$E = E^{\text{tot}} - E_0 = \frac{1}{2} \sum_{l,l'} \sum_{j,j'} u(jl) \left.\frac{\partial^2 E}{\partial u(jl) \partial u(j'l')}\right|_{r_{lj}, r_{l'j'}} u(j'l') \tag{2.17}$$

If we set $j = j'$ and $l = l'$, we see that the harmonic energy of a single atom has the familiar form of a harmonic oscillator $E = \frac{1}{2} K u^2$, where K is the spring constant. We define

$$\left.\frac{\partial^2 E}{\partial u(jl) \partial u(j'l')}\right|_{r_{lj}, r_{l'j'}} = \mathbf{\Phi}\begin{pmatrix} jj' \\ ll' \end{pmatrix} = -\mathbf{\Theta}\begin{pmatrix} jj' \\ ll' \end{pmatrix} + \delta_{j,j'} \delta_{l,l'} \sum_{j'',l''} \mathbf{\Theta}\begin{pmatrix} jj'' \\ ll'' \end{pmatrix}$$

where $\mathbf{\Phi}$ is the so-called the *force constant* with respect to total energy and $\mathbf{\Theta}$ is the force constant with respect to bond energy. We can now write the harmonic energy as

$$\begin{aligned}
E &= \frac{1}{2} \sum_{l,l'} \sum_{j,j'} u(jl) \mathbf{\Phi}\begin{pmatrix} jj' \\ ll' \end{pmatrix} u(j'l') \qquad (2.18) \\
&= \frac{1}{2} \sum_{l,l'} \sum_{j,j'} u(jl) \left(-\mathbf{\Theta}\begin{pmatrix} jj' \\ ll' \end{pmatrix} + \delta_{j,j'} \delta_{l,l'} \sum_{j'',l''} \mathbf{\Theta}\begin{pmatrix} jj'' \\ ll'' \end{pmatrix} \right) u(j'l') \\
&= \frac{1}{2} \sum_{l,l'} \sum_{j,j'} \left(-\mathbf{\Theta}\begin{pmatrix} jj' \\ ll' \end{pmatrix} u(jl) u(j', l') + \mathbf{\Theta}\begin{pmatrix} jj' \\ ll' \end{pmatrix} u(jl)^2 \right) \\
&= \frac{1}{2} \sum_{l,l'} \sum_{j,j'} \left(-\mathbf{\Theta}\begin{pmatrix} jj' \\ ll' \end{pmatrix} u(jl) u(j', l') + \frac{1}{2} \mathbf{\Theta}\begin{pmatrix} jj' \\ ll' \end{pmatrix} \left(u(jl)^2 + u(j', l')^2 \right) \right) \\
&= \frac{1}{4} \sum_{l,l'} \sum_{j,j'} \mathbf{\Theta}\begin{pmatrix} jj' \\ ll' \end{pmatrix} \left[-2u(jl) u(j', l') + u(jl)^2 + u(j', l')^2 \right] \\
&= \frac{1}{4} \sum_{l,l'} \sum_{j,j'} \mathbf{\Theta}\begin{pmatrix} jj' \\ ll' \end{pmatrix} \left[u(jl) - u(j', l') \right]^2
\end{aligned}$$

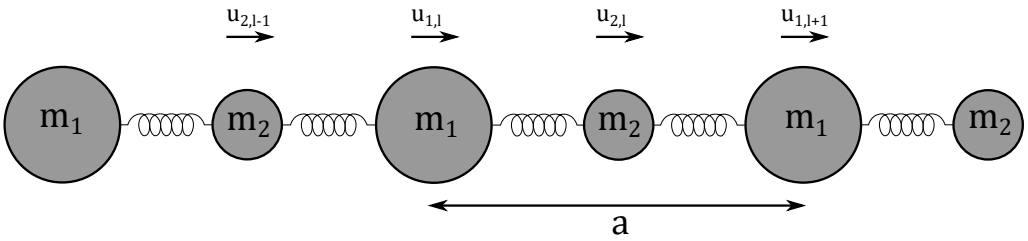

Figure 2.8: Diatomic chain. Two atomic species with masses m_1 and m_2 are connected by springs. The system is periodic with a unit 'cell' of length a. Displacements are denoted $u_{j,l}$, where j is an atomic index, and l is a unit cell index.

and it becomes evident that the harmonic energy can be described with respect to atoms or bonds in mathematically equivalent ways. Since the bond-centered description does not include individual atomic displacements, it is necessary to add a self-term to $\mathbf{\Theta}$. As a visual aid to these index-heavy equations, Figure 2.8 illustrates the one-dimensional diatomic chain, which is often used in introductory texts. If we consider only nearest-neighbour interactions and identical springs, the bond-centered harmonic energy can be written

$$\begin{aligned} E &= \frac{1}{4}\mathbf{\Theta}\sum_l 2\left[u(1,l)-u(2,l)\right]^2 + \frac{1}{4}\mathbf{\Theta}\sum_n 2\left[u(2,l)-u(1,l+1)\right]^2 \\ &= \frac{1}{2}\mathbf{\Theta}\sum_l \left[u(1,l)-u(2,l)\right]^2 + \frac{1}{2}\mathbf{\Theta}\sum_n \left[u(2,l)-u(1,l+1)\right]^2 \end{aligned}$$

where the factor of 2 comes from double-counting. The purpose of this example is to show that the (somewhat abstract) harmonic energy in equation (2.17) is equivalent to our intuitive understanding of coupled harmonic oscillators. With this in mind, we can return to the matter at hand and write the equation of motion for an atom j in cell l through Newtons second law $F = ma$:

$$m_j\ddot{u}(jl,t) = -\frac{\partial E}{\partial u(jl)} = -\sum_{l'}\sum_{j'}\mathbf{\Phi}\begin{pmatrix} jj' \\ ll' \end{pmatrix} u(j'l',t)\,,$$

where m_j is the atomic mass of atom j. Solutions to this equation is given as a sum of travelling harmonic waves with wave vectors q and band indices $\nu \in \{1,\ldots,n\}$

$$u(jl,t) = \sum_{q,\nu}\tilde{u}(j,q,\nu)\exp(iqr(jl))\exp(-i\omega(q,\nu)t)$$

where $\omega(q,\nu)$ is the frequency, $r(jl)$ is the position of atom j in cell l, $\omega(q,\nu)$ is the frequency and the complex number $\tilde{u}$ is called the *displacement vector*. If we insert these solutions into the equations of motion and just consider one band at one wave vector we obtain

$$\begin{aligned} m_j\omega(q,\nu)^2\tilde{u}(j,q,\nu)\exp(iqr(jl)) &= -\sum_{l'}\sum_{j'}\mathbf{\Phi}\begin{pmatrix} jj' \\ ll' \end{pmatrix}\tilde{u}(j',q,\nu)\exp(iqr(j'l')) \\ m_j\omega(q,\nu)^2\tilde{u}(j,q,\nu) &= -\sum_{l'}\sum_{j'}\mathbf{\Phi}\begin{pmatrix} jj' \\ ll' \end{pmatrix}\tilde{u}(j',q,\nu)\exp(iq[r(j'l')-r(jl)]) \\ m_j\omega(q,\nu)^2\tilde{u}(j,q,\nu) &= -\sum_{l'}\sum_{j'}\mathbf{\Phi}\begin{pmatrix} jj' \\ 0l' \end{pmatrix}\tilde{u}(j',q,\nu)\exp(iq[r(j'l')-r(j0)])\,, \end{aligned} \tag{2.19}$$

where the last equality is simply a change of origin in order to follow the convention of most software. The full account of phonon frequencies ω and displacements $\tilde{u}$ can be found as solutions to equation (2.19). At a given q and ν, the equations are indexed by j and we will have n equations with n unknowns with respect to $\tilde{u}(j,q,\nu)$, where n is the number of atoms in the unit cell. In fact, equation (2.19) can be written as an eigenvalue equation:

$$\boldsymbol{D}(q)\cdot\boldsymbol{e}(q,\nu) = \omega(q,\nu)^2\cdot\boldsymbol{e}(q,\nu)\,, \tag{2.20}$$

where

$$\boldsymbol{e}(q,\nu) = \begin{pmatrix} \sqrt{m_1}\tilde{u}(1,q,\nu) \\ \sqrt{m_2}\tilde{u}(2,q,\nu) \\ \vdots \\ \sqrt{m_n}\tilde{u}(n,q,\nu) \end{pmatrix}$$

and the elements of $\boldsymbol{D}(q)$ are given

$$D(jj') = \frac{1}{\sqrt{m_j m_{j'}}} \sum_{l'} \boldsymbol{\Phi}\begin{pmatrix} jj' \\ 0l' \end{pmatrix} \exp(iq[r(j'l') - r(j0)])\,. \tag{2.21}$$

$\boldsymbol{D}(q)$ is known as the dynamical matrix and can be constructed solely from force constants. Furthermore, equation (2.21) reveals that the dynamical matrix is Hermitian so the eigenvalues $\omega(q,\nu)^2$ are real and the eigenvectors $\boldsymbol{e}(q,\nu)$ are orthonormal. In addition, the eigenvalues and eigenvectors are trivially obtained numerically (e.g. `numpy.linalg.eigh` in the Python numpy library). In order to get the full dispersion, this diagonalization is performed for each of the n bands ν at the desired wave vectors in the first Brillouin Zone (FBZ).

The extension to 3 dimensions is done by treating the Cartesian components separately and considering $\boldsymbol{q}$ and $\boldsymbol{r}$ as vectors. The eigenvector then becomes a column vector of $3n$ components

$$\boldsymbol{e}(\boldsymbol{q},\nu) = \begin{pmatrix} \sqrt{m_1}\tilde{u}_x(1,\boldsymbol{q},\nu) \\ \sqrt{m_1}\tilde{u}_y(1,\boldsymbol{q},\nu) \\ \sqrt{m_1}\tilde{u}_z(1,\boldsymbol{q},\nu) \\ \sqrt{m_2}\tilde{u}_x(2,\boldsymbol{q},\nu) \\ \vdots \\ \sqrt{m_n}\tilde{u}_z(n,\boldsymbol{q},\nu) \end{pmatrix},$$

the number of bands increase to $3n$ and we get a $3n \times 3n$ dynamical matrix, where each component (2.21) is a 3×3 block of the form

$$\boldsymbol{D}(jj') = \begin{pmatrix} D(jj')_{xx} & D(jj')_{xy} & D(jj')_{xz} \\ D(jj')_{yx} & D(jj')_{yy} & D(jj')_{yz} \\ D(jj')_{zx} & D(jj')_{zy} & D(jj')_{zz} \end{pmatrix}$$

where

$$D(jj')_{\alpha\beta} = \frac{1}{\sqrt{m_j m_{j'}}} \sum_{l'} \boldsymbol{\Phi}\begin{pmatrix} jj' \\ 0l' \end{pmatrix}_{\alpha\beta} \exp(i\boldsymbol{q}[\boldsymbol{r}(j'l') - \boldsymbol{r}(j0)]) \tag{2.22}$$

While the path was somewhat involved, it is useful to take a step back and consider the consequences of our outlined formalism. Everything we need to know about our phonon system can be obtained from the dynamical matrix that, in turn, is constructed from force constants through equation (2.22). Finally, all of these objects can be constructed in computationally trivial way from force constants.

Practical considerations

At this point, it is useful to consider how we construct elements of the dynamical matrix in practice. Inspection of equation (2.22) contains a sum over all unit cells l' and thus approaches an infinite sum. On the other hand, it is reasonable to assume that the dominant force constants $\boldsymbol{\Phi}$ are short range. The compromise is to use a finite supercell such that the second derivatives involved in calculating force constants outside this cell are minimized. While the reasonable size of such a supercell obviously depends on the system and model, quantum contributions to the force constants generally vanish within a distance of roughly 10 Å to 15 Å. If the force constants can be obtained analytically from a semi-empirical potential, calculation is computationally simple and we can use large supercells. However, since force constants are usually obtained from DFT, we are limited by computational resources and are usually restricted to supercells with a maximal interatomic distance of roughly 5 Å (e.g. a cubic system with $a = 10$ Å).

Since the number of force constants needed is at least equal to the size of the dynamical matrix, the number of calculations to perform is at least $3n \times 3n$. Even for a fairly small system such as LCO in the I4/mmm space group (HTT, $n = 7$) the number of elements in the dynamical matrix is

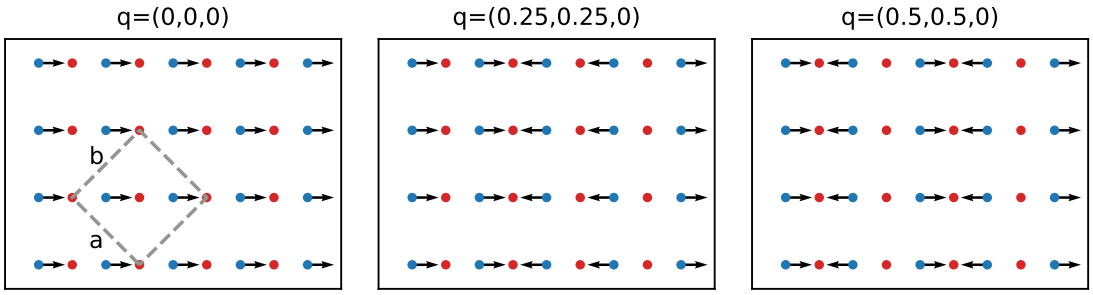

Figure 2.9: Cu-O bond stretching mode in La_2CuO_4 at three different values of $\boldsymbol{q}$ referring to the orthorhombic coordinate system (Bmab) as shown by the grey outline in the leftmost figure. Blue markers are oxygen and red markers are copper. The phase is set to $\phi = \frac{3}{4}\pi$ in equation 2.23 in order to get displacement vectors of equal length.

$(3{\cdot}7)^2 = 441$. In the finite displacement method, each force constant is the result of a self-consistent DFT calculation, so the computational effort appears prohibitively expensive at first glance. For this reason we use a numerical fitting of symmetry inequivalent force constants (see section 2.4). In the case of LCO in the I4/mmm space group the number of necessary displacements is reduced to only 7 (6 if we ignore magnetism), making the problem much more manageable.

Phonon eigenvectors

The phonon dispersion is contained within the eigenvalues $\omega(\boldsymbol{q}, \nu)^2$. We can plot the bands ν along high-symmetry lines in the FBZ by carefully choosing the values of $\boldsymbol{q}$ where the dynamical matrix is diagonalized. Similarly, we can sample the dispersion in a dense $\boldsymbol{q}$-mesh in order to evaluate the phonon density of states. In addition, many thermodynamic properties can be calculated by only considering the eigenvalues.

The eigenvectors $\boldsymbol{e}(\boldsymbol{q}, \nu)$ are more subtle in nature. Each component of $\boldsymbol{e}(\boldsymbol{q}, \nu)$ is a complex number that describes the wave amplitude and phase of one atomic species j in one cartesian direction α. In addition, the eigenvector is normalized and thus only describes relative atomic motion. In order to visualize the collective displacement due to a phonon mode ν at $\boldsymbol{q}$ we can displace all atoms j in unit cells l by

$$\Delta_{jl} = \frac{A}{\sqrt{m_j}} \mathrm{Re}\left[\exp(i\phi)\boldsymbol{e}_j(\boldsymbol{q}, \nu) \exp(i\, 2\pi\, \boldsymbol{q} \cdot \boldsymbol{r}(jl)\right] \tag{2.23}$$

where $\boldsymbol{e}_j(\boldsymbol{q}, \nu)$ is the j'th component of $\boldsymbol{e}(\boldsymbol{q}, \nu)$ and A is an arbitrary amplitude. The phase ϕ describes periodic motion of atoms. An animation can be produced by varying ϕ between 0 and 2π.

In `Phonopy` the eigenvectors are always given with respect to the primitive unit cell and the 3 Cartesian components are along the basis vectors of this primitive unit cell. If we want, for example, to visualize the bond-stretching mode in the HTT phase of LCO at $q = (\frac{1}{4}, \frac{1}{4}, 0)$ in orthorhombic notation, we look at atoms in primitive unit cells with origin (0,0,0), (1,0,1), (2,0,2) and (3,0,3) using the eigenvectors at $q = (0.125, -0.125, 0.125)$. For this specific mode, the movement of oxygen along the Cu-O bond dominates. Figure 2.9 shows this phonon mode at the zone center, halfway through the zone and at the zone boundary.

Imaginary modes

In contrast to real-world phonons, there is no guarantee that the energies obtained from equation (2.20) are positive. Negative energies in a calculated phonon dispersion are called imaginary modes and corresponds to a situation where the system gains energy by a displacement corresponding to the eigenvector of the imaginary mode. In other words, we are not at equilibrium with respect to that particular phonon mode. While this is at odds with one of our assumptions, imaginary modes can reveal that a chosen symmetry might be unstable. In the case of La_2CuO_4, our calculations correctly predict unstable modes in the high-temperature tetragonal phase. The information gathered from imaginary modes is of course limited by the fact that DFT calculations are performed at $T = 0\,\mathrm{K}$.

Obtaining Force Constants from DFT

Force constants from DFT are found in a surprisingly simple way. In the previous sections we defined the force constant with respect to total energy as

$$\mathbf{\Phi}\begin{pmatrix} jj' \\ ll' \end{pmatrix}_{\alpha\beta} = \frac{\partial^2 E}{\partial u_\alpha(jl)\partial u_\beta(j'l')} = -\frac{\partial F_\beta(j'l')}{\partial u_\alpha(jl)}$$

where $F_\beta(j'l')$ is the force on atom $(j'l')$ in the direction β. Notice that everything is now labelled by a Cartesian direction and these directions are treated individually. In practice the Cartesian directions correspond to the unit cell vectors, but to reduce confusion we use the labels (x, y, z). We can approximate the derivative by performing a finite displacement $\Delta u_\alpha(jl)$ and simply taking the numerical derivative

$$\mathbf{\Phi}\begin{pmatrix} jj' \\ ll' \end{pmatrix}_{\alpha\beta} \approx -\frac{F_\beta(j'l'; \Delta u_\alpha(jl)) - F_\beta(j'l')}{\Delta u_\alpha(jl)} \tag{2.24}$$

where $F_\beta(j'l'; \Delta u_\alpha(jl))$ is the force on atom $(j'l')$ in the direction β after performing the displacement $\Delta u_\alpha(jl)$. At equilibrium we assume $F_\beta(j'l') = 0$ and we only need to calculate the forces due to a finite displacement. In ab-initio methods, there is no reason to assume a particular shape of the potential energy landscape and we can only expect the harmonic approximation to be valid for small finite displacements. For this reason, displacements have to be chosen large enough so that we are not subject to numerical noise and small enough to avoid anharmonic contributions. In `Phonopy` the default value is 0.01 Å, while `PHONON` uses 0.03 Å.

As mentioned in section 2.4, we need a large number of force constants to construct the dynamical matrix, even when dealing with small systems. For this reason, a numerical fitting of forces and displacements, known as the Parlinski-Li-Kawazoe method [125], is used to find force constants. We notice that equation (2.24) can be written as a matrix equation for one pair of atoms (jl) and $(j'l')$:

$$\boldsymbol{F}(j'l') = -\boldsymbol{U}(jl)\boldsymbol{P}(jl; j'l')\,,$$

where

$$\boldsymbol{F}(j'l') = (F_x \quad F_y \quad F_z)\,,$$

$$\boldsymbol{U}(jl) = (\Delta u_x(jl) \quad \Delta u_y(jl) \quad \Delta u_z(jl))$$

and

$$\boldsymbol{P}(jl; j'l') = \begin{pmatrix} \Phi_{xx} & \Phi_{xy} & \Phi_{xz} \\ \Phi_{yx} & \Phi_{yy} & \Phi_{yz} \\ \Phi_{zx} & \Phi_{zy} & \Phi_{zz} \end{pmatrix}$$

If we perform m finite displacements, we get m simultaneous equations for each pair of atoms:

$$\begin{pmatrix} \boldsymbol{F}_1(j'l') \\ \boldsymbol{F}_2(j'l') \\ \vdots \\ \boldsymbol{F}_m(j'l') \end{pmatrix} = -\begin{pmatrix} \boldsymbol{U}_1(jl) \\ \boldsymbol{U}_2(jl) \\ \vdots \\ \boldsymbol{U}_m(jl) \end{pmatrix} \boldsymbol{P}(jl; j'l')\,.$$

which can be solved by a Moore-Penrose pseudo-inverse matrix (in Numpy: `numpy.linalg.pinv`) given a sufficient number of displacements. Since $\boldsymbol{U}$ only depends on (jl), we can build up the full force constant matrix by iterating this procedure over $(j'l')$. The minimum number of displacements is equal to the number of non-equivalent atoms in the crystal primitive unit cell multiplied by a number of independent x,y,z coordinates in the site symmetry of a given atom [125]. For this reason, software such as `Phonopy` and `PHONON` determines the primitive unit cell, the supercell expansion matrix and all the symmetry operations before generating displacements.

2.5 Molecular Dynamics

The objective of a molecular dynamics simulations is to generate a *trajectory* of atomic positions as a function of time. This method has a rich history in materials science since it can be use to study ensembles explictely. The general idea is to build a real space model containing particles and their interactions and then integrate the Newtons equations of motion for this many-body system. By analyzing the resulting trajectory, one can obtain information about thermodynamic, structural and (of course) dynamical properties.

In the context of this thesis, the forces for our simulation is obtained through a DFT calculation, so that every configuarion of atomic postions requires a self-consistent calculation. For this reason, the forces are obtained ab-initio and we only have to worry about integrating the equations of motion. This can be done very efficiently using the Verlet algorithm [127]:

$$\boldsymbol{r}_i(t+\Delta t) = -\boldsymbol{r}_i(t-\Delta t) + 2\boldsymbol{r}_i(t) + \boldsymbol{a}_i(t)\Delta t^2 + \mathcal{O}(\Delta t^4)$$

where $\boldsymbol{r}_i$ is the position of atom i, $\boldsymbol{a}_i$ is the acceleration, Δt is the time step. This equation can easily be obtained by summing the Taylor expansions of $\boldsymbol{r}_i(t+\Delta t)$ and $\boldsymbol{r}_i(t-\Delta t)$. The time step is a crucial choice for any MD simulation. On one hand, it is important to have a small enough time step such that the dynamics are accurately described. On the other hand, if the total simulation time is too short, we might not probe a large enough part of phase space to make the ensemble averages represenatative. In other words, short simulation times might trap you in a local minimum of phase space.

MD simulations are, unlike DFT ground state calculations, generally performed at finite temperatures. Generally this temperature is initialized by giving every atom an initial velocity taken from the Boltzman distributon at the initial temperature. During the simulation, the temperature can be controlled in different ways, depending on the thermodynamic ensemble one wishes to simulate. While energy should be conserved, the Verlet algorithm might cause the total energy to drift, especially if the system is out of equilibrium. For this reason, it is usually desirable to have a thermostat that controls the temperature. For the simulations performed in this thesis, we use the Nosé-Hover thermostat [128]. I will not repeat the details here, but the general idea of MD thermostats is to scale the velocities such that the temperature is kept constant.

After having performed a MD simulation, we want to be able to compare with experiment. The trajectories can be analyzed in a variety of ways, but there are a few basic observables that are easy to compute in the case of crystalline materials: The phonon density of states and the pair-distribution function. In the following, I outline how these observables are obtained in practice.

VACF and gDOS

It turns out [129] that the phonon density of states can be found from the power spectrum of the mass-weighted velocity autocorrelation function (VACF). The VACF is, as the name implies, an expression of the correlation between velocites at different times. In liquids, the VACF will rapidly decay to zero and in solids the VACF will fluctuate due to coherent vibrations around equilibrium positions. The VACF for a single atomic species α is defined as

$$C_\alpha(t) = \frac{1}{3}\langle \boldsymbol{v}_\alpha(t_0)\cdot\boldsymbol{v}_\alpha(t)\rangle$$

By invoking ergodicity, the ensemble average can be replaced with a time average with respect to t_0.

$$C_\alpha(t) = \frac{1}{3}\frac{1}{T-t}\sum_{t_0=0}^{T-t}\boldsymbol{v}_\alpha(t_0)\cdot\boldsymbol{v}_\alpha(t_0+t) = \frac{1}{3}\frac{1}{T-t}\sum_{t_0=0}^{T-t}\sum_{\beta=x,y,z} v_{\alpha\beta}(t_0)v_{\alpha\beta}(t_0+t)$$

where T is the total simulation time and $v_{\alpha\beta}$ is the velocity of atom α in direction β. The total VACF is defined as

$$C(t) = \sum_\alpha m_\alpha C_\alpha(t)$$

where m_α is a weight depending on the atomic species and the terms of the sum are the *partial* VACFs. To get the mass-weighted VACF m_α is equal to the atomic weight of species α divided

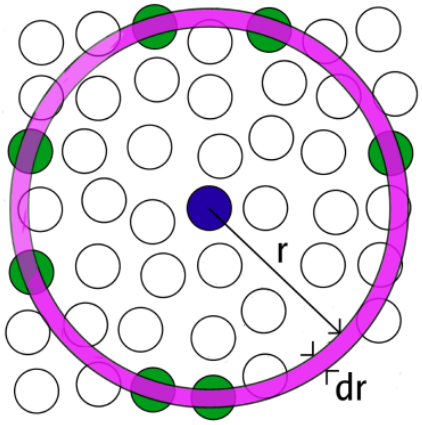

Figure 2.10: Visualization of the radial distribution function. Centered on an atom α (blue), we count the number of atoms β (green) that can be found in a spherical shell at a distance r with a with dr. As shown in the text, this can be used to construct the radial distribution function $g(r)$. Figure from [130].

by the average weight of atomic species. The density of states is obtained as the power spectrum of the mass-weighted velocity autocorrelation function:

$$\mathrm{DOS}(\omega) = \sum_\alpha \sigma_\alpha \frac{1}{2\pi} \int_{-\infty}^{+\infty} \mathrm{d}t \exp[-i\omega t] m_\alpha C_\alpha(t) \,,$$

where the terms of the sum, once again, determines the *partial* density of states for atomic species α. To get the neutron-weighted DOS, we set σ_α equal to the coherent neutron cross-section of species α. In practice both the VACF and DOS is found numerically by FFT methods. The neutron-weighted phonon DOS obtained from simulations in this thesis are all evaluated using the tools created in appendix A.

Radial distribution function

The radial distribution function is defined as

$$g(r) = \frac{\rho(r)}{\rho} \,,$$

where $\rho(r)$ is the particle number density at a distance r from an arbitrary atomic origin and $\rho = \frac{N}{V}$ is the number density of the unit cell. A visual representation of this quantity is shown in figure 2.10. Formally this can be found from atomic positions

$$g(r) = \frac{1}{N\rho} \left\langle \sum_i^N \sum_{i \neq j} \delta(r - r_{ij}) \right\rangle$$

where i and j are particle indices and r_{ij} is the distance between particle i and j. N is the total number of particles and the brackets denote an ensemble average. Due to the delta function, this expression is not particularly useful when analysing MD trajectories of discrete particle positions. To overcome this, we define $n(r, \mathrm{d}r)$ as a function that counts the number of particles at a distance r within a spherical shell of thickness dr.

$$g(r) = \frac{2\,\langle n(r, \mathrm{d}r)\rangle}{N\rho V_\mathrm{s}(r, \mathrm{d}r)} \,, \tag{2.25}$$

where $V_\mathrm{s}(r, \mathrm{d}r) \approx 4\pi r^2 \mathrm{d}r$ is the thickness of the spherical shell. Due to the ergodic hypothesis, the ensemble average is replaced with a time average, so that

$$\langle n(r, \mathrm{d}r)\rangle = \frac{1}{M} \sum_{k=1}^{M} n_k(r, \mathrm{d}r)$$

where M is the number of time steps. In practice n_k is evaluated by creating a list of all particle-particle distances in the frame k and generating a histogram with bin size $\mathrm{d}r$. The factor of two in equation (2.25) comes from the fact that n_k only counts each pair once.

The $g(r)$ we just defined treats all particle pairs on an equal footing. In order to compare simulations with neutron scattering data it is necessary to weigh distinct particle pairs by the product of their neutron cross sections. First, we define the partial radial distribution function $g_{\alpha\beta}(r)$ as the probability of finding a particle with label β at a distance r away from a particle with label α plus the probability of finding a particle with label α at a distance r away from a particle with label β.

$$\begin{aligned} g_{\alpha\beta}(r) &= \frac{\langle n_{\alpha\beta}(r,\mathrm{d}r)\rangle}{N_\alpha \rho_\beta V_\mathrm{s}(r,\mathrm{d}r)} + \frac{\langle n_{\alpha\beta}(r,\mathrm{d}r)\rangle}{N_\beta \rho_\alpha V_\mathrm{s}(r,\mathrm{d}r)} \\ &= \frac{2V}{N_\alpha N_\beta} \frac{\langle n_{\alpha\beta}(r,\mathrm{d}r)\rangle}{V_\mathrm{s}(r,\mathrm{d}r)}\,, \end{aligned}$$

where N_i is the number and ρ_i is the density of particle species i. The reason to define it in 'both directions' is that $n_{\alpha\beta}$ is symmetric to exchange of particles. From the partial pair distribution functions, $G(r)$ can be trivially computed and optionally weighted by neutron cross sections, as we saw in section 2.1:

$$G(r) = \frac{1}{\bar{b}^2} \sum_{\alpha=1,\beta\geq\alpha} c_\alpha c_\beta \bar{b}_\alpha \bar{b}_\beta (g_{\alpha\beta}(r) - 1)\,,$$

Atomic distance histograms

If our MD simulations fulfils the ergodic hypothesis, it is useful to look at various distributions that can be extracted from the simulation. While a lot of this information is contained in the radial distribution function, the system studied in this thesis is not isotropic. In fact, the 2-dimensional nature of the cuprates appears to be essential for the electronic properties. By generating histograms for certain atoms, we can ask a few pertinent questions such as:

- What is the distribution of Cu-$\mathrm{O_{eq}}$ distance?
- What is the distribution of Cu-$\mathrm{O_{ap}}$ distance?
- What is the distribution of octahedral tilts (Q_1, Q_2)?
- What is the nature of $\mathrm{O_{int}}$ diffusion?

All of these questions are well-defined in the context of molecular dynamics trajectories, but it can be tedious for large systems to label all the relevant atoms. To overcome this, we generate pairs of atomic species based on certain conditions. For example, if we want to find pairs of Cu and $\mathrm{O_{eq}}$, we loop over all Cu-O pairs and only list the pairs where the distance vector is less than $\boldsymbol{r} = (2.1, 2.1, 1)$ Å. After building the pair-lists it is trivial to generate histograms of certain distances.

Similarly, we can build the $\mathrm{CuO_6}$ octahedra by applying the same idea to both equatorial and apical oxygen atoms. We can identify the 6 corners of the octahedron simply by checking the signs of the 6 distance vectors (e.g. the 'top' apical oxygen will have a positive z component). Q_1 and Q_2 can then be computed and we can generate histograms of the octahedral tilts.

Finally, we can also use these pairs to generate symmetry operations in a fairly simple way. Since we know that the octahedra have alternating tilt patterns, we can check the tilt pattern at frame 1 and generate a list of the 4 different combinations of Q_1 and Q_2 ((+,+),(+,-),(-,+),(-,-)). Applying these symmetry operations to our calculations then lets us obtain a histogram of the symmetry-adapted octahedral tilts.

2.6 Comparing Simulation and Experiment

Finally, we conclude this chapter by giving examples of how to compare the simulation methods with neutron scattering experiments. As we saw in section 2.1, this thesis features 3 types of neutron measurements.

1. Direct measurements of phonon bands with TAS spectroscopy

2. Phonon density of states on powders with time-of-flight methods.

3. PDF measurements of powders

All of these can be compared directly with simulations in various ways, but there are some subtleties on how to perform this comparison correctly. In this section we thus treat them one at a time.

Phonon bands with TAS

The master equation for phonon scattering can be found in [97] and directly relates the measured differential cross-section to the phonon band structure as we saw in section 2.2, equation (2.5) (repeated here for clarity)

$$S(\boldsymbol{Q},\nu,\omega) = \frac{k_\mathrm{f}}{k_\mathrm{i}}\frac{N}{\hbar}\sum_{\boldsymbol{q}}|F(\boldsymbol{Q},\boldsymbol{q},\nu)|^2(n_{\boldsymbol{q}\nu}+1)\delta(\omega-\omega_{\boldsymbol{q}\nu})\delta(\boldsymbol{Q}-\boldsymbol{q}-\boldsymbol{G}) \tag{2.26}$$

$$F(\boldsymbol{Q},\boldsymbol{q},\nu) = \sum_j \sqrt{\frac{\hbar}{2m_j\omega_{\boldsymbol{q}\nu}}}\bar{b}_j \exp\left(-\frac{1}{2}\langle|\boldsymbol{Q}\cdot\boldsymbol{u}(j0)|^2\rangle\right)\exp[-i(\boldsymbol{Q}-\boldsymbol{q})\cdot\boldsymbol{r}(j0)]\boldsymbol{Q}\cdot\boldsymbol{e}_j(\boldsymbol{q},\nu) \tag{2.27}$$

Note that the equations have been rewritten slightly when compared to Squires [97] (similar to what is presented on the Phonopy website [131]), such that $S(\boldsymbol{Q},\nu,\omega)$ is defined separately for each phonon band. In addition, the sum in the phonon structure factor runs over atomic indices in unit cell 0, consistent with the definitions made earlier in this chapter.

By close inspection of equation (2.26) and (2.27), we realise that the information obtained by the calculation of phonon band structures provides us with all the information necessary to construct $S(\boldsymbol{Q},\nu,\omega)$. Since normalization on an absolute scale is usually not possible when performing a TAS experiment, the neutron-weighted band structures are shown with $Nk_\mathrm{f}/k_\mathrm{i} = 1$.

The δ-functions in equation (2.5) tells us that a neutron measurement will only have intensity if we measure at values of $\boldsymbol{Q}$ and ω that correspond to a point of the dispersion of band ν. We thus reduce our calculations to sampling $S(\boldsymbol{Q},\nu,\omega)$ at $(\boldsymbol{q},\omega_{\boldsymbol{q}\nu})$. The only computationally heavy part then becomes the Debye-Waller factor

$$W = \frac{1}{2}\langle|\boldsymbol{Q}\cdot\boldsymbol{u}(j0)|^2\rangle$$

which has to be sampled at some finite grid in unit cell 0 in order to get a reasonable estimate of the ensemble average. In many cases we compare measurements to a phonon dispersion in the first BZ where W varies only slightly, so if we want to sample a large number of $\boldsymbol{Q}$-points it can be advantageous to simply omit the Debye-Waller factor. As of this writing, this is not possible in Phonopy directly, so we have to live with someone heavy computations for now.

With these equations in mind, we can now plot the neutron-weighted phonon bands and compare them with TAS-measurements. We can represent the neutron weighted bands either by colouring the band-structure lines according to intensity or by giving the dispersion curves a finite Gaussian width to replicate a finite instrument resolution and/or linewidth broadening. Figure 2.11 shows examples of the two kinds of representations. By adding obtained neutron data to these plots, we can then directly compare theory and experiment. We note here that a comparison with MD simulations is not possible since these simulations give no information about the discrete phonon bands.

Phonon Density of States

The phonon density of states (DOS) is a simple projection of the phonon bands onto the energy axis. While this obviously reduces the amount of information due to the reduction of dimensionality, the phonon DOS is a useful object for a couple of reasons:

1. Often only powders are available for experiments and resolving bands can be difficult due to the rotational averaging.

2. Many neutron scattering instruments are specifically designed for DOS measurements.

3. DOS can be obtained from molecular dynamics as well as band structure calculations.

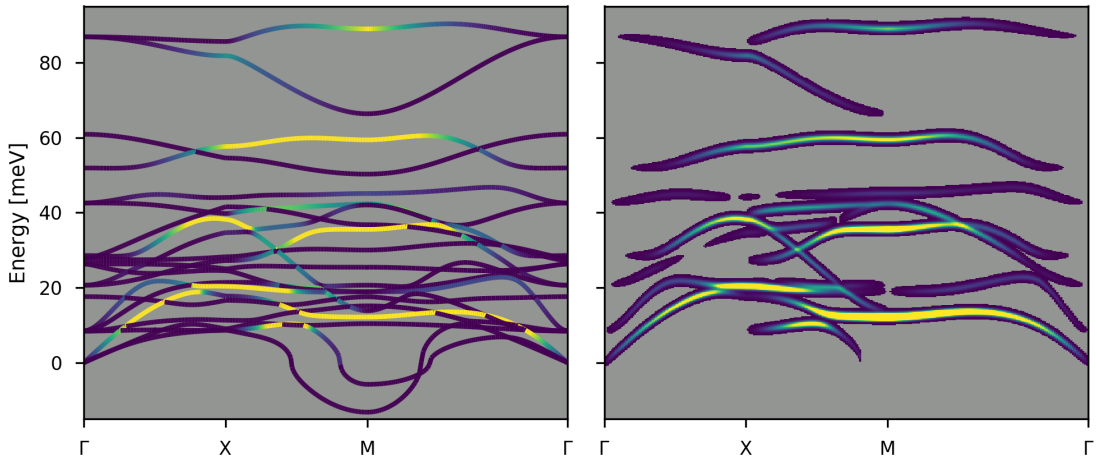

Figure 2.11: Neutron weighted phonon band structure of La_2CuO_4 in the high-temperature tetragonal phase. On the **left**, the bands are shown as a line plot where the lines are colored according to neutron intensity. On the **right** the same simulation is shown, but the bands are given a Gaussian width along the energy axis of $\sigma = 0.5\,\text{meV}$, giving a better idea of what the measured neutron spectrum would look like. Additionally, this plot is produced with a minimum threshold of neutron intensities in order to remove bands with very little intensity (the calculation will allways return a finite intensity).

The last point is particularly important in the case where we are working with defect structures such as oxygen interstitials. Here, the (local) symmetry is usually severely broken (often to P1 symmetry) and a phonon calculation would be prohibitively expensive. As shown in section 2.5, the phonon DOS can be obtained, in the harmonic approximation, rather simply from a MD trajectory.

To obtain the DOS from a band-structure calculation, we perform an integration over a commensurate grid in the 1st BZ and project the result onto the energy axis for each atomic species j in the following way:

$$g^j(\omega) = \sum_{\hat{\boldsymbol{n}}=\{x,y,z\}} \frac{1}{N} \sum_{\boldsymbol{q},\nu} \delta(\omega - \omega_{\boldsymbol{q}\nu}) \left|\hat{\boldsymbol{n}} \cdot \boldsymbol{e}_j(\boldsymbol{q},\nu)\right|^2$$
$$g(\omega) = \sum_j g^j(\omega)$$

where $\hat{n}$ is the unit vector in the three cartesian directions. Comparing this equation with equation (2.5) we notice that we only need to weigh by mass and the neutron cross-section in order to go from the true density of states $g(\omega)$ to the neutron $S(\omega)$. If we performed a TAS experiment on a single crystal with perfect resolution at every relevant $(\boldsymbol{q}, \omega_{\boldsymbol{q}\nu})$ point, these definitions would be correct and we could perform the integration on our massive 4-dimensional dataset. However, due to the nature of typical DOS measurements, we need to invoke the so-called *incoherent approximation* and use the incoherent 1-phonon partial differential cross-section when treating the data. In practice this means using the total neutron cross sections (σ_{tot}) with the incoherent 1-phonon $S(\boldsymbol{q}, \omega)$ as shown in section 2.2.

Pair-density function measurements

When performing neutron PDF measurements, it is possible to extract the normalized total neutron PDF (construction of partials require several measurements, see ref. [132]). As such, we should be able to compare directly with the PDF as extracted from molecular dynamics as shown in section 2.5. PDF from phonon band structure calculations are in principle possible since we can extract thermal displacements, but it is currently not a feature in Phonopy, so this analysis has not been performed here.

Chapter 3

Phonon Calculations

In this chapter, results from ab-initio simulations are presented independent of experimental data. It turns out that a careful investigation of various phases of La_2CuO_4 presents us with valuable clues regarding the average and local structure. While DFT is unable to capture the strongly correlated nature of the cuprates, it turns out to be a reasonable description with regards to intermolecular forces. The subsequent strategy is to carefully validate our simulations and establish a 'one-electron baseline' for the studied systems. Experimental deviations from this baseline can then be analysed for clues possibly pertaining to superconductivity or other phenomena not captured at the DFT level of theory.

One example of such a deviation is shown in Chapter 8, where we can detect potentially interesting physics by following how a certain phonon mode diverges from our otherwise robust simulation results. In this chapter we perform DFT simulations based on the La_2CuO_4 parent compound across three structural and two electronic phases, all of which have been observed experimentally in the lanthanum-based cuprates. We then calculate phonons within the 'Frozen-Phonon' approach and obtain the neutron-weighted phonon band structure. Since the computational requirements of phonon calculations are heavily influenced by symmetries, we do not consider defects such as interstitials in this chapter as this would make the computational effort unmanageable. To understand the dynamics due to dopant species, molecular dynamics simulations based on the results of this chapter are presented in Chapter 4.

3.1 Computational Details

The theory and principles behind Density Functional Theory (DFT) is presented in chapter 2, section 2.3. DFT simulations in this thesis are performed using the Vienna Ab-Initio Simulation Package (VASP) [133–136] using Projector Augmented-Wave Pseudopotentials (PAW) [137, 138] to describe the atomic wavefunctions. While ab-initio loosely translates to 'from the beginning', There are several choices to be made with regards to computational parameters. First, we need to define the pseudo-potentials that describes the valence electrons of each atomic species in our system. For L(S)CO(+O), the relevant pseudo-potentials are listed in Table 3.1 along with their electronic configuration. For both La and O we used the recommended potentials, while for Cu we used a more accurate version where all 6 3p electrons are included (`_pv` is short for 'p in valence'). The reason for this is simply because it was difficult to have the simulations converge with the standard potential – not because we necessarily believe that the Cu 3p states are important for the chemistry of our system. To run a simulation in VASP, or in any DFT software, the following information (files) is required:

- Crystal lattice and atomic coordinates (`POSCAR`)
- Pseudopotential configuration (`POTCAR`)
- k-point mesh (`KPOINTS`)
- Computational parameters (`INCAR`)

The choice of crystal lattice and atomic positions are typically taken from experiment, but it is important to realize that the simulation might not 'agree' completely. This is especially important if we want to calculate phonons through the evaluation of forces due to displacements away from equilibrium positions. The pseudopotential configuration is usually taken from a database since the generation of consistent, transferable potentials is a difficult, time-consuming task. In fact,

the main selling point of VASP is their high-quality pseudopotentials. The k-point mesh defines the number of k-points where the wavefunctions and density is evaluated and has a huge impact on computational effort (going from e.g. a $2 \times 2 \times 2$ grid to a $4 \times 4 \times 4$ takes 8 times as many evaluations). Luckily, the amount of k-points needed for an accurate calculation usually converges rapidly and we often check this convergence explicitly. Since the density of the k-point mesh depends on the system size, it is common to state the k-point density which is defined as the number of k-points per reciprocal atom (or simply #k-points $\times$ #atoms).

Finally, there is a large number of computational parameters that can be tweaked depending on the desired type of calculation. The VASP `INCAR` file has more than 300 optional tags [139], but usually only a few needs to be tweaked depending on the desired type of simulation. For the simulations performed in this thesis the following keywords are important:

- `ENCUT`: The plane-wave cut-off and thus the size of the basis set. Usually the default performs well, but for accurate forces, this needs to be increased. In the manual they recommend 1.3 times the default cut-off, but there are cases where even this is insufficient [140].
- `EDIFF`: The threshold for the the self-consistent cycle to terminate. For accurate forces this needs to be increased.
- `PREC`: A tag that defines the 'precision' by setting new defaults for certain parameters. I generally increase this to 'Accurate' for all simulations. 'Normal' is the default.
- `LREAL`: A PAW pseudopotential specific tag which determines if an evaluation of a certain projection operator is performed in real or reciprocal space. This operation is faster in real space, but at the cost of accuracy. For phonons we want to perform the operation in reciprocal space.
- `GGA`: Sets the exchange-correlation functional (see section 2.3). Usually the default (PBE) is a good starting point, but experimentation is encouraged!
- `ISPIN` and `MAGMOM`: Turns on a spin-polarized calculation.
- `IBRION` and `ISIF`: How and when to update the ionic positions. This can be used to perform molecular dynamics and structural optimizations in different ways.
- `ISMEAR` and `SIGMA`: A tag that controls 'fermi surface smearing', which is important for metallic systems where we need to evaluate a discontinuous function at the fermi level due to partial occupancies. This can be done in several ways, and it is usually good practice to test the convergence and performance of these methods.
- `LDAU`: Switches on LDA+U (see section 2.3) which can alleviate the intrinsic problem of DFT when dealing with localized d- and f-orbitals. This is needed in our simulations if we want to describe the anti-ferromagnetic structure of La_2CuO_4.
- `ISYM`: Controls how VASP deals with space group symmetry.

The take-home message here is that phonon calculations generally needs increased precision with respect to the recommended default values. When one is mainly concerned with the electronic band structure the dominant energies are typically on the order of eV, where typical phonon energies are on the order of meV, 3 orders of magnitude smaller. In addition, forces are evaluated as derivatives of the total energy (per the Hellmann-Feynmann Theorem, see section 2.4) so numerical noise is amplified. For molecular dynamics this precision is less crucial since the many time steps will average out this numerical noise.

	Z	Core (# electrons)	Valence (# electrons)
`La`	57	$1s^2 2s^2 2p^6 3s^2 3p^6 3d^{10} 4s^2 4p^6 4d^{10}$ (46)	$5s^2 5p^6 5d^1 6s^2$ (11)
`Sr_sv`	38	$1s^2 2s^2 2p^6 3s^2 3p^6 3d^{10}$ (28)	$4s^2 4p^6 5s^2$ (10)
`Cu_pv`	29	$1s^2 2s^2 2p^6 3s^2$ (12)	$3p^6 3d^{10} 4s^1$ (17)
`O`	8	$1s^2$ (2)	$2s^2 2p^4$ (6)

Table 3.1: PAW pseudopotential electronic configuration used in VASP calculations. While lanthanum is typically placed in the f-block on periodic tables it's electronic configuration has no f-electrons. This is fortunate since DFT (in)famously struggles with highly localized orbitals.

Functional and Energy Cut-off

As we discussed in Section 2.3, a large number of functionals have been developed for DFT calculations. At the GGA level of theory 24 functionals are available in VASP and choosing one can seem like an daunting task at first glance. It is, however, important to realize that most functionals have been created to treat a specific problem. This is an expression of the fact that, despite our best efforts, no universal functional exists currently. With that in mind, functionals with high transferability do exist and the default PBE functional in VASP has been used to describe a wide variety of systems, emphasized by the 40000+ citations of the original paper [141].

While PBE is technically a semi-empirical functional, the only experimental parameter is derived from the uniform electron gas. The simplicity and transferability of this functional thus makes it an excellent starting point for any DFT calculation. Generally one would start with PBE and then turn to other functionals if calculations fail to line up with empirical data. As we shall see, we run into this exact problem when evaluating forces in our system and we have to change our functional to PBESol (PBE revised for solids) in order to get a reasonable description of low energy phonons.

We run into a similar problem with the plane wave energy-cutoff when evaluating forces. The default energy-cutoff is generally set by the element with the highest recommended cut-off, in our case oxygen at 400 eV. For accurate forces it is recommended to increase this by a factor of 1.3, but for phonon calculations, we see improvements all the way up to an 800 eV cut-off. The lesson here is a cautionary tale – at times, the lack of precision in the calculation might not reveal itself before having performed an expensive phonon calculation.

3.2 Electronic and Structural Phases

With an understanding of the functionality and limitations of DFT, and in particular VASP, we can begin to formulate a strategy to investigate the La_2CuO_4 (LCO) system. From diffraction studies, we know that LCO can exist in (at least) three structural phases depending on doping and temperature (see section 1.3). While the electronic structure of superconducting cuprates cannot be accurately described within DFT, undoped and overdoped La_2CuO_4 can be described as Mott-Insulator and Fermi-Liquid, respectively. Both of these electronic phases can be approximately described with DFT.

In order to say anything about the superconducting cuprates with DFT, we are thus limited to a study of limiting cases in terms of the electronic structure. On the other hand, if we want to study phonons through atomic forces, many-body theories will struggle with realistic system sizes. Quantum Monte Carlo methods are making progress, but accurate forces are still a significant limitation [142]. Since we are working with the knowledge that the exact behaviour of the electrons are poorly described in our theory, our simulations must be carefully evaluated against experiments to ensure that our simulations are capturing the dominating contributions to atomic forces.

Electronic Structure

Since 'electronic structure' is the output of a DFT calculation, one might object to the statement that we want to investigate different electronic structures of La_2CuO_4. Without any additional constrains, DFT at the GGA level of theory generally results in a metallic state [143], where the observed antiferromagnetic (AFM) solution requires a non-local theory [144]. Since non-local theories (beyond GGA) are computationally expensive, they become impractical for our purposes. Some authors have reported an AFM solution using certain GGA functionals [145], but I have not been able to reproduce this result in a consistent way. If a magnetic solution is found, the magnetic moment usually vanishes by small changes to the k-point mesh or energy cut-off, suggesting that the magnetic ground state is a local minimum.

A compromise developed specifically for correlated electron systems is the LDA+U (sometimes called DFT+U or GGA+U) method [123] described in section 2.3. This ad-hoc method treats the strong on-site Coulomb interaction of localized electrons with a Hubbard-like term parametrized through an on-site repulsion U and an exchange parameter J. In the method by Dudarev et al. [146] these are reduced to one parameter $U_{\text{eff}} = U - J$. The LDA+U method was developed specifically to treat Mott-Insulators [123], but has been used to calculate hole doped La_2CuO_4 and La_2NiO_4 [123]. Some recent studies have even looked at stripe ordered phases of $La_{2-x}Sr_xCuO_4$ [147, 148]. In these studies, hole doping is done by removing electrons and adding a neutralizing background, rather than the introduction of actual dopant species. Since LDA+U comes at a much

Table 3.2: Crystal structures found in various lanthanum-based cuprates. All structural phases can be parametrized with respect to LTLO, where Q_1 and Q_2 represent octahedral tilts as described in the text and $\eta = \frac{b-a}{b+a}$ is the orthorhombic strain.

Space Group (#)	Name (shorthand)	Tilts	η
I4/mmm (139)	High-Temperature Tetragonal (HTT)	$Q_1 = Q_2 = 0$	$= 0$
Fmmm (69)		$Q_1 = Q_2 = 0$	$\neq 0$
Bmab (64)	Low-Temperature Orthorhombic (LTO)	$Q_2 \neq 0$, $Q_1 = 0$	$\neq 0$
$P4_2/ncm$ (138)	Low-Temperature Tetragonal (LTT)	$Q_1 = Q_2 \neq 0$	$= 0$
Pccn (56)	Low-Temperature-Less-Orthorhombic (LTLO)	$Q_1 \neq Q_2 \neq 0$	$\neq 0$

lower computational cost compared to e.g. hybrid functionals and since it was developed with the cuprates in mind, it becomes an obvious choice for our purposes.

Crystal Structure

The observed structural phases of lanthanum based cuprates fall into a moderate number of space groups as listed in Table 3.2 and introduced in section 1.3. All of the structural phases can be described with reference to Figure 1.9 where we define Q_1 as a rotation along a (around b) and Q_2 as a rotation along b (around a). In addition, we define the orthorhombic strain as $\eta = \frac{b-a}{b+a}$. In our simulations we have chosen to focus on three structural phases

- HTT: The parent high-symmetry phase observed at high temperatures and/or overdoped samples.
- LTO: The most common structural phase at low temperatures for relevant superconducting samples.
- LTT: A lower symmetry phase than LTO observed in $La_{2-x}Ba_xCuO_4$ and $La_{1.6-x}Nd_{0.4}Sr_xCuO_4$. Appears to supress superconductivity with the notable exception of $La_{1.88}Ba_{0.12}CuO_4$ ($T_c \approx 5\,K$)

3.3 Coordinate systems

Having decided on the phases to investigate, we take a short detour to describe the coordinate systems used in real and reciprocal space. Since we are dealing with several electronic and structural phases, we need a common description to compare between phases. In real space, we use the Q_1, Q_2, η description from above and in reciprocal space we use the HTT Brillouin Zone.

Octahedral Tilts

In order to quantify the octahedral tilts for use in simulations, we use the coordinate system sketched in Figure 3.1. All possible tilts can be described with reference to the lowest symmetry space group (LTLO, Pccn). The octahedra are described with two in-plane oxygens (O_1, O_2) and one apical oxygen O_3 and the Pccn space group is the only one with three inequivalent oxygen atoms. Due to symmetry constrains, a rotation of this octahedron will cause a displacements in the c-direction of the in-plane oxygen and in the a, b direction of the apical oxygen (a reasonable approximation at small angles). Following [67], we define Q_1 as a rotation around the (010) axis and Q_2 as a rotation around the (100) axis in orthorhombic notation. In more intuitive terms, Q_1 'tilts' the octahedron along a, while Q_2 'tilts' along b.

By inspection of Figure 3.1, a Q_1 rotation will displace O_3 in the x-direction and O_1, O_2 in the negative z-direction. A Q_2 rotation will displace O_3 in the y-direction, O_1 in the positive z-direction and O_2 in the negative z-direction. If we want to express Q_1 and Q_2 as angles, the displacements become:

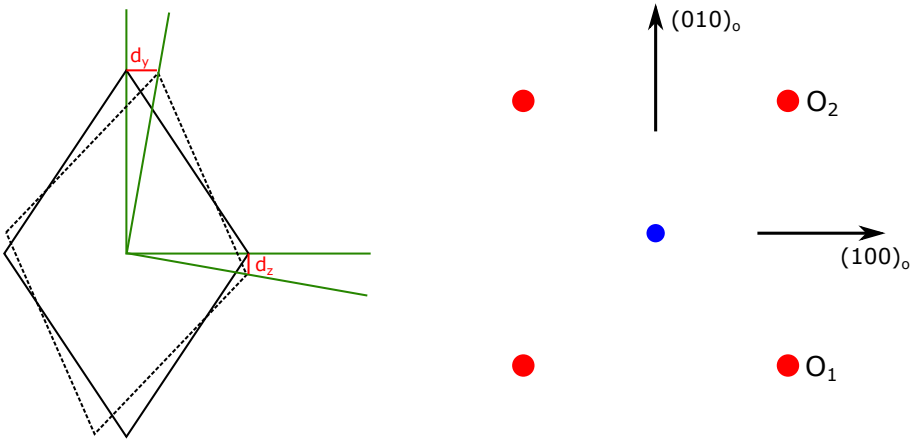

Figure 3.1: **Left:** Geometry of octahedral tilts in the with the c-axis vertical. **Right:** Illustration of the two inequivalent in-plane oxygens. Q_1 is a rotation around the (010) axis while Q_2 is a rotation around the (100) axis.

$$
\begin{aligned}
\mathrm{O}_3^x &= \mathrm{O}_{\mathrm{ap}}^z \sin(Q_1)\frac{c}{a} \\
\mathrm{O}_3^y &= \mathrm{O}_{\mathrm{ap}}^z \sin(Q_2)\frac{c}{b} \\
\mathrm{O}_1^z &= \frac{1}{4c}\left[-a\sin(Q_1) + b\sin(Q_2)\right] \\
\mathrm{O}_2^z &= \frac{1}{4c}\left[-a\sin(Q_1) - b\sin(Q_2)\right] ,
\end{aligned}
$$

where O_j^i is the i-component of oxygen j in fractional coordinates. Since these equations uniquely define displacements in terms of tilt angles, we can also find tilt angles from structural displacements from either the apical oxygen:

$$
\begin{aligned}
Q_1 &= \sin^{-1}\left(\frac{\mathrm{O}_3^x}{\mathrm{O}_{\mathrm{ap}}^z} \times \frac{a}{c}\right) \\
Q_2 &= \sin^{-1}\left(\frac{\mathrm{O}_3^y}{\mathrm{O}_{\mathrm{ap}}^z} \times \frac{b}{c}\right) ,
\end{aligned}
$$

or the equatorial oxygen:

$$
\begin{aligned}
Q_1 &= \sin^{-1}\left(-\frac{2c}{a} \times (\mathrm{O}_1^z + \mathrm{O}_2^z)\right) \\
Q_2 &= \sin^{-1}\left(-\frac{4c}{b} \times \mathrm{O}_2^z - \frac{a}{b} \times \sin(Q_1)\right) .
\end{aligned}
$$

To apply an orthorhombic strain η to a tetragonal structure with an in-plane lattice parameter a', while keeping the volume constant (which is important when comparing DFT simulations due to Pulay Stress, [149]), the following equations can be used to find the a and b lattice parameters:

$$
\begin{aligned}
a &= \frac{a'}{1+\eta} \\
b &= (1+\eta)a' .
\end{aligned}
$$

These equations can then be used to generate desired tilts and extract tilt angles from any given structure. Since every tilt is defined with respect to only 3 oxygen atoms, these equations require at least Pccn symmetry which is preserved for geometry optimizations and phonon calculations. For lower symmetries (in e.g. MD simulations) we define a 'symmetrized average tilt' (see chapter 4). Code to generate these structures and extract rotation angles from any structure can be found in appendix A. This methodology can also be used with any software that can generate crystal

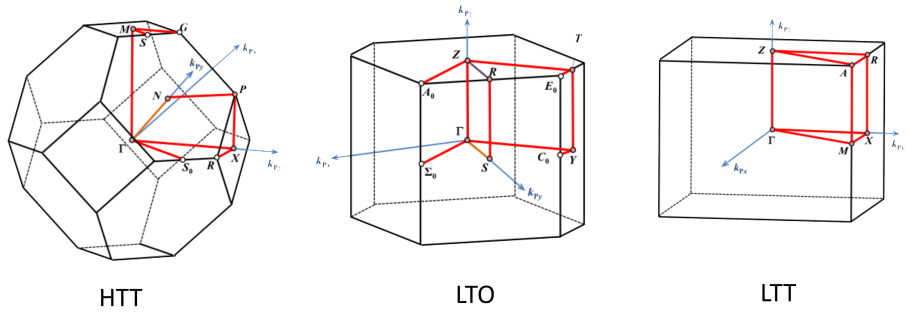

Figure 3.2: Brillouin Zones of the HTT, LTO and LTT phases (see Table 3.2). Modified from [152]

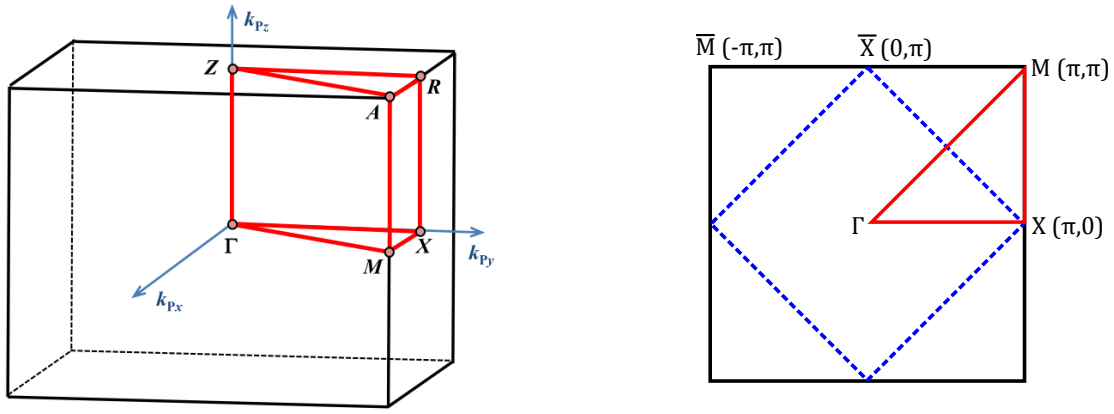

Figure 3.3: **Left:** BZ of a primitive tetragonal cell with high-symmetry lines. **Right:** The in-plane BZ with the same labels and the usual Γ-X-M-Γ path. If the large BZ is the crystallographic HTT phase, then the broken blue lines represent the LTO/LTT/LTLO BZ and we can consider the Γ-X-$\frac{M}{2}$-Γ path, since M becomes Γ for this (smaller) BZ. In literature the labels are often confused, while (π, π) and $(\pi, 0)$ are universally agreed upon. In any band structure diagrams presented here, the labels in this figure is used.

structures from space group symmetry and fractional coordinates (e.g. ASE [150] and VESTA [151]). The same result can, of course, also be obtained by considering each of the space groups individually and then figuring out how to generate tilts and transform the lattice to a common coordinate system. If one is only interested in atomic coordinates, starting from Pccn is convenient. This way, atomic indices are also identical for all structures.

Reciprocal Space: Band Structures

Band structures are described with respect to the reciprocal lattice. Due to the enlargement of the real-space crystal structure as we move through HTT → LTO → LTT, the Brillouin Zone (BZ) shrinks by the same amount. Similar to how it is useful to describe our real-space lattice with respect to the Pccn coordinate system, it is useful to describe reciprocal space with respect to a common coordinate system when comparing results. As we can see in Figure 3.2, the BZs of HTT, LTO and LTT have vastly different shapes, so it is difficult to superimpose results.

For this reason, we chose a *primitive* tetragonal BZ to describe the HTT phase (note that this shape is different from the *actual* HTT BZ in figure 3.2) and then construct the smaller LTO and LTT BZZs with respect to this construction. The idea is sketched in Figure 3.3. This construction also helps emphasize the 2-dimensional nature of the cuprates. In all following simulations, the band labels in Figure 3.3 will be used, keeping in mind that the nature of high-symmetry points can change depending on the considered structural phase. One example is that the M point, which is the zone boundary of HTT, becomes the zone centre of LTO and would thus usually be denoted Γ.

While this construction is useful for our intuitive understanding of the different phases, phonon calculations require k-vectors with respect to the primitive unit cell. For this reason, we need the transformation matrices from our constructed coordinate system to the primitive HTT and LTO

unit cells (the LTT transformation is the identity matrix). This conversion can be done with the following matrices.

$$\mathrm{PA_{HTT}} = \begin{pmatrix} 0 & 0 & \frac{1}{2} \\ \frac{1}{2} & \bar{\frac{1}{2}} & 0 \\ \frac{1}{2} & \frac{1}{2} & \bar{\frac{1}{2}} \end{pmatrix} \qquad \mathrm{PA_{LTO}} = \begin{pmatrix} \frac{1}{2} & \frac{1}{2} & 0 \\ 0 & 0 & 1 \\ \frac{1}{2} & \bar{\frac{1}{2}} & 0 \end{pmatrix}$$

these matrices can be used to generate k-points starting from the more 'intuitive' notation outlined in Figure 3.3. For example, the X-point ($(\frac{1}{2}\frac{1}{2}0)$ with respect to our coordinate system) in the HTT phase becomes $(\frac{1}{2}\frac{1}{2}0) \cdot \mathrm{PA_{HTT}} = (\frac{1}{4}\bar{\frac{1}{4}}\frac{1}{4})$.

3.4 Strategy

To find a connection between the structural phases, we start with the highest symmetry phase (HTT) using cell parameters and fractional positions approximated from literature [71]. The AFM structure is based on La_2CuO_4 that has been modified in a way such that $\eta = 0$ and $Q_1 = Q_2 = 0$. The metallic structure is based on $La_{1.775}Sr_{0.225}CuO_4$, which is tetragonal (HTT) at 10 K.

The structure is then optimized and we calculate the electronic and phonon band structures. We then break the symmetry by applying a small rigid tilt $Q_2 = 5°$ along with small orthorhombic strain $\eta = 0.005$, resulting in the LTO phase which we then optimize and finally perform the same set of calculations. A HTT-LTT transformation is performed in a similar fashion with $Q_1 = Q_2 = 5°$ and $\eta = 0$. This procedure is then performed in parallel for the anti-ferromagnetic solution using LDA+U and the metallic solution. The resulting band structures, density-of-states and total energies are then analysed and validated against experimental data.

All calculations in this chapter is performed on La_2CuO_4 in the conventional orthorhombic unit cell, which corresponds to the primitive Pccn lattice that we use to generate the structures. This cell contains four formula units and is large enough to accommodate anti-ferromagnetism. Since VASP can handle symmetry through the `ISYM` keyword, we don't need an input cell corresponding to the primitive cell of the considered structural phase. Before starting any 'production' DFT calculation, it is advantageous to benchmark certain computational parameters in order to get an idea of how well-behaved the SCF convergence is and what energy scales we can expect to probe.

3.5 Benchmarking

When performing DFT calculations in VASP there are a few parameters that have significant impact on the precision of the calculation. Increasing the precision also results in significantly longer computation time, so it is important to find a compromise.

Figure 3.4 shows a benchmark of AFM LCO with respect to the k-point mesh and smearing width σ. Since there are no states at the Fermi level, the smearing width converges rather quickly, and we can safely use a value of $\sigma = 0.1$ eV. The k-point density also converges rather quickly, and we achieve a precision of 0.1 meV using a fairly coarse MP-grid of $8 \times 8 \times 4$ (7168 k-points per reciprocal atom). In AFM LCO we also checked the effect on electronic structure due to the on-site repulsion U. The result is shown in Table 3.3 and the values of $U = 8$ eV, $J = 0.8$ eV are chosen based on the proximity to experimental evidence [153, 154] and previous theoretical studies of the La_2CuO_4 system, where the values of U and J where found self-consistently [147, 155].

Table 3.3: LDA+U Benchmarking of the parameters U and J calculated with `LDAUTYPE=4` in the HTT phase of La_2CuO_4. Experimentally the Cu moment is $(0.48 \pm 0.15)\,\mu_B$ [153] and the optical gap is ≈ 2 eV [154]. As a reasonable compromise we chose $U = 8$ eV and $J = 0.8$ eV, a set of values also used in a previous study of the same system [147].

U [eV]	J [eV]	Moment [μ_B]	Optical gap [eV]
4.0	0.4	0.330	0.348
6.0	0.6	0.481	1.016
8.0	0.8	0.588	1.686
10.0	1.0	0.676	1.877
12.0	1.2	0.755	2.042

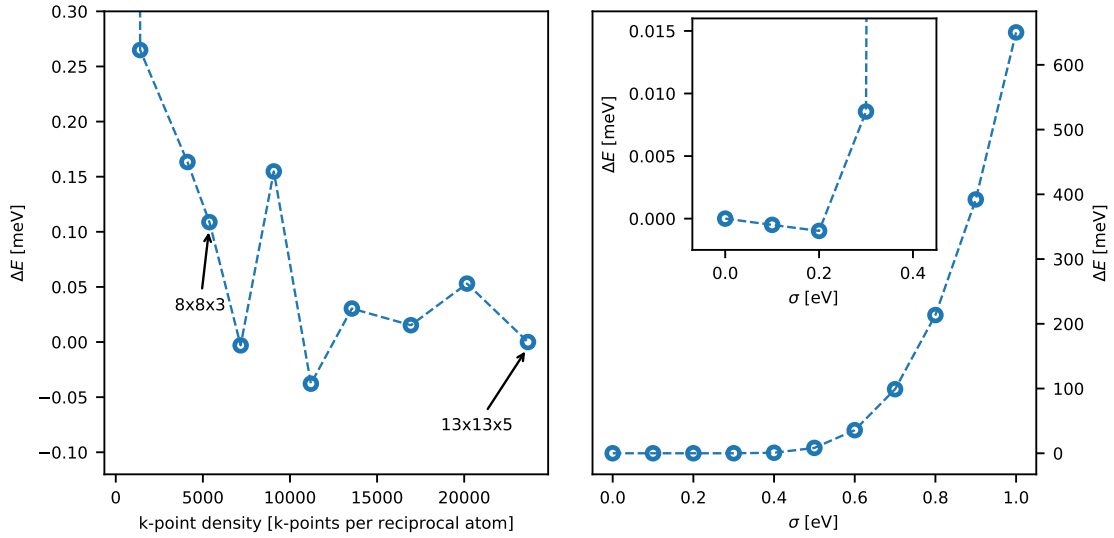

Figure 3.4: Simulation Benchmarks: GGA+U with $U = 8\,\text{eV}$ and $J = 0.8\,\text{eV}$. **Left:** Energy as a function of k-point density with $\sigma = 0.1\,\text{eV}$. ΔE is total energy (with entropy) with respect to the $13 \times 13 \times 5$ mesh. **Right:** $\Delta E = E_0 - E$ as a function of Gaussian smearing σ, E is the total energy and E_0 is the energy where $\sigma = 0$ calculated with the tetrahedron method (`ISMEAR=-5` in VASP). The inset is a zoom of the 4 lowest points.

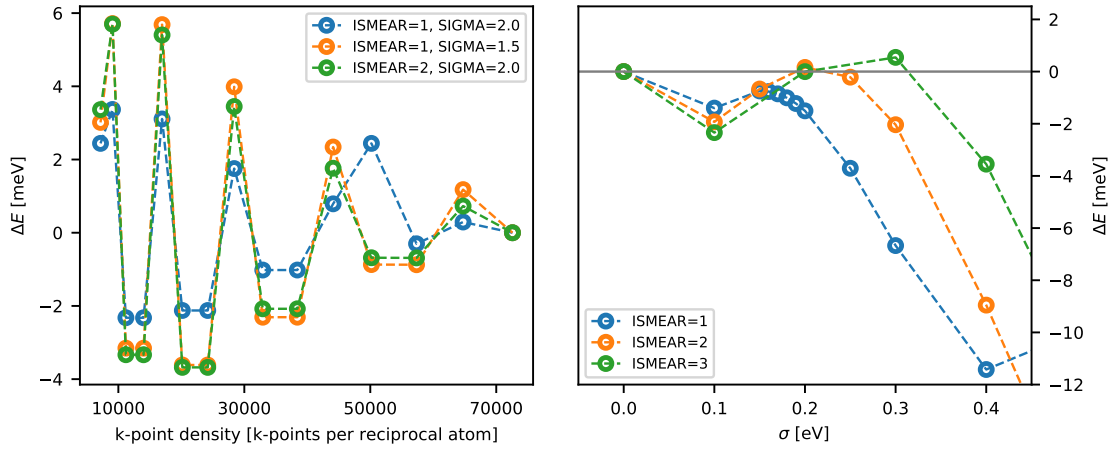

Figure 3.5: Simulation Benchmarks: Paramagnet/Metal. Note the significant variation in energy compared to the insulating case (see figure 3.4), even with much higher k-point density. **Left:** Energy as a function of k-point density for three combinations values of σ and smearing type. ΔE is total energy (with entropy) with respect to the $18 \times 18 \times 8$ mesh. **Right:** ΔE as a function of σ with the Methfessel-Paxton method (orders 1, 2, 3) while using a $16 \times 16 \times 8$ k-point mesh (57344 k-points per reciprocal atom). $\sigma = 0$ corresponds to the tetrahedron method (`ISMEAR=-5`). Below $\sigma = 0.4\,\text{eV}$ the entropy term is 0.5 meV per atom or lower, so forces should be well-behaved.

Due to partial occupancies, metallic systems are generally more sensitive to k-point density and smearing width/method. For this reason, we performed a more comprehensive set of benchmarks as shown in Figure 3.5. While the numerical fluctuations are within a few meV, the precision on total energy is decreased by a few orders of magnitude. Based on these results, we evaluate the metallic simulations at twice the k-point density with a mesh of $16 \times 16 \times 8$ (57344 k-points per reciprocal atom).

Electronic Structure

While we are generally interested in lattice dynamics, a DFT calculation is leveraging the electronic structure in any simulation. It is thus worthwhile to check if the electronic structure, at least approximately, represents reality in the benchmarking phase of our simulations. In the cuprates,

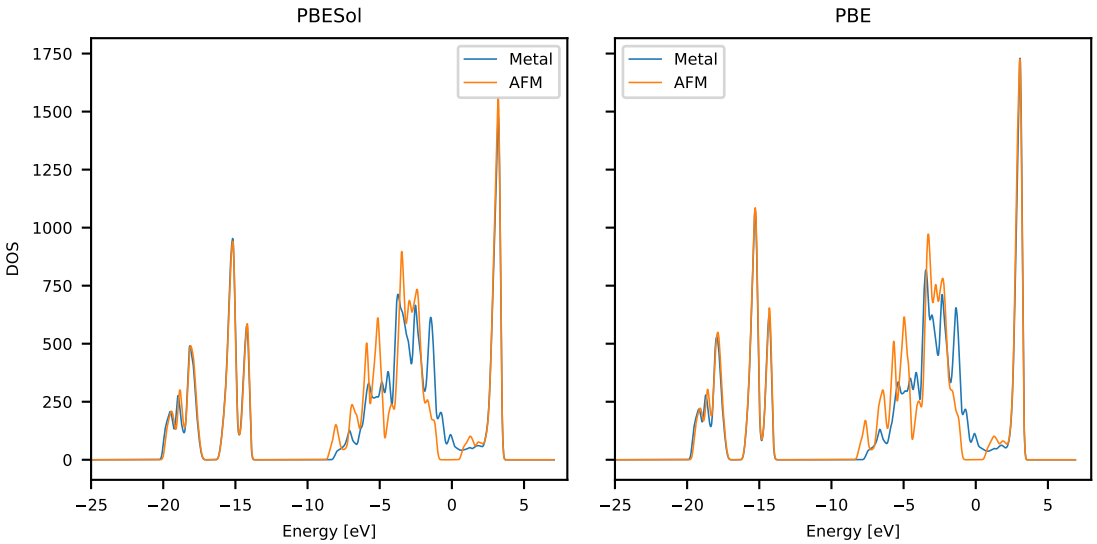

Figure 3.6: Electronic density of states for HTT phase with two different functionals in a metallic (paramagnetic) and AFM (GGA+U) states. The two functionals appear to describe the system identically. The AFM state is shifted by −1 eV for comparative purposes (which is why the Fermi level is in the middle of the gap).

it is well known that DFT is unable to explain the peculiarities in the superconducting phase. However, we can get fairly close in the limit of zero doping (AFM Mott Insulator) and over-doping (fermi liquid). Figure 3.6 compares the electronic density of states of the Mott Insulator and fermi liquid for our chosen functionals. We clearly see how the DFT+U opens a gap by pushing states below the Fermi level. We also notice that, in terms of DOS, the functionals behave qualitatively similar.

To further illustrate this point, Figure 3.7 and 3.8 shows the electronic band structures coloured by atomic projections in the AFM and metallic state, respectively. We now notice that DFT+U is pushing the Cu states down by about 8 eV, as expected from the on-site repulsion U. Comparing our band structures to literature we have, as expected, a qualitative agreement in both the AFM [144] and metallic [47, 156] cases. The question of LDA+U being an appropriate model for the undoped AFM system is still not settled [45].

3.6 Geometry optimization

Having settled on a set of appropriate computational parameters, we can proceed with the original goal of optimizing the geometry of the various structural phases. Optimizing geometry in VASP can be performed with 3 different algorithms controlled by the `IBRION` tag:

1. RM-DIIS
2. Conjugate Gradient (CG)
3. Damped molecular dynamics

All algorithms requires to set the `POTIM` tag which controls the step-size. Usually the default value of 0.5 is reasonable. Damped molecular dynamics requires a damping factor in addition, set by the `SMASS` tag. For this reason RM-DIIS and CG require less user intervention and are good first choices. While RM-DIIS is usually a good choice for systems close to equilibrium, it struggles with rigid unit modes such as octahedral tilts in perovskites. Since these tilts are at the centre of our investigation, we use CG in all geometry optimizations.

The optimization routine is constrained by the point group symmetry as determined by VASP. The `ISIF` tag controls how the positions, cell shape and cell volume is updated during the optimization. It might seem obvious to simply optimize everything, but for complex problems convergence can be problematic. In addition, changing the cell volume affects the plane-wave basis set. Intuitively, this can be understood through thinking of the plane waves as standing waves in our finite

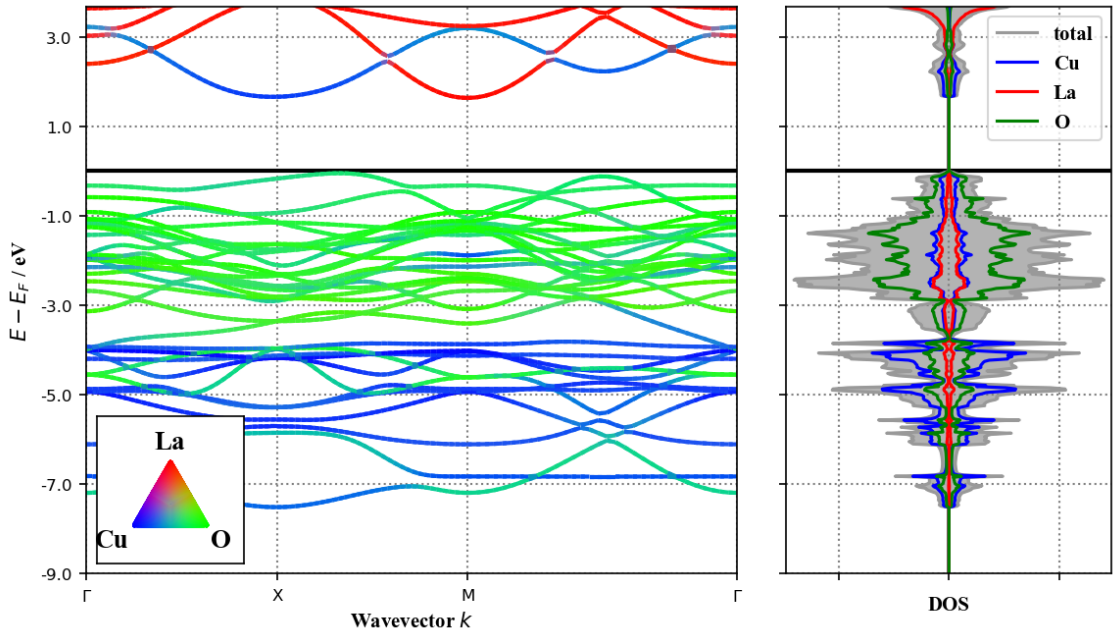

Figure 3.7: GGA+U: AFM Electronic Band Structure of the Bmab LTO structure along the Γ-X-M-Γ path (HTT high symmetry lines). The upper and lower Hubbard bands are clearly visible and are separated by 8 eV as expected.

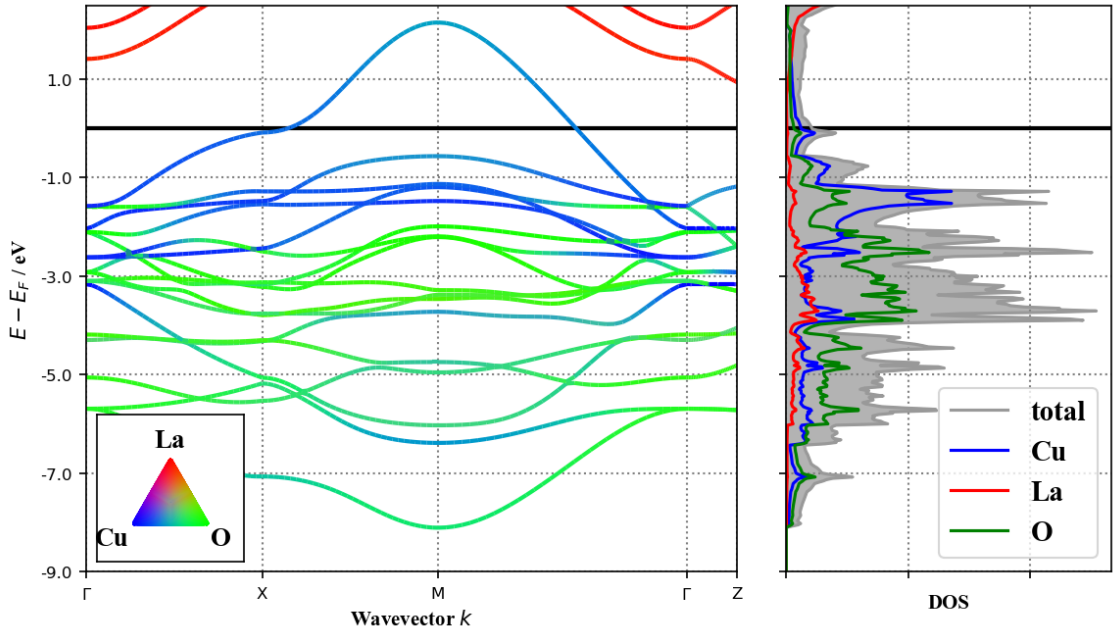

Figure 3.8: Metallic Electronic Band Structure of the I4/mmm HTT structure. Path is through the high-symmetry points as defined in Figure 3.3 with respect to the conventional unit cell. The Γ-Z path is shown to illustrate the 2-dimensional nature of the electronic structure (The dispersion is relatively flat).

box. Changing the size of the box necessarily changes the plane waves. This is also true when considering changes to the cell shape, but in a less significant way. These effects are known as 'Pulay stress' [149] and are important to keep in mind when performing geometry optimizations. The effect of this can be avoided by changing the size of the basis set through the energy cut-off or by avoiding volume relaxations all together. In practice, there are two primary strategies for getting accurate geometry optimizations in VASP. The first is a step-wise optimization of parameters in the scheme

$$\text{Coordinates} \rightarrow \text{Coordinates/Shape} \rightarrow \text{Coordinates/Shape/Volume},$$

where we are susceptible to significant Pulay stress only in the last step. The second is perform successive coordinate+shape optimizations at a set of fixed volumes and fit the resulting volume-energy curve to an equation-of-state (EOS). This avoids the most significant contribution to Pulay stress by never performing a volume optimization explicitly. While this method is more computationally expensive, it is more accurate and provides us with additional information about volume-dependent behaviour such as the bulk modulus, tilt patterns and orthorhombic strain. In practice we use the exponential EOS formulated by Vinet et al. [157]:

$$E(V) = E_0 + \frac{2B_0V_0}{(B_0'-1)^2} \times \left\{2 - \left[5 + 3\left(\frac{V}{V_0}\right)^{\frac{1}{3}}(B_0'-1) - 3B_0'\right] \exp\left[-\frac{3}{2}(B_0'-1)\left[\left(\frac{V}{V_0}\right)^{\frac{1}{3}} - 1\right]\right]\right\}$$

where V_0 is the equilibrium volume, B_0 is the bulk modulus and

$$B_0' = \left(\frac{\partial B_0}{\partial P}\right)_T,$$

where P is pressure and T is temperature. There exists several alternative energy-volume EOS formulations in literature [158–160] designed for different conditions and materials. By testing several of these formulations on the same data, we get practically indistinguishable results, so the choice of the Vinet formula is somewhat arbitrary. In practice, roughly 10 volumes ranging from $\pm 5\%$ of the equilibrium are chosen, adding more volumes to fill out the graph if necessary. While performing the fits, we extract information about the volume-dependent tilt angles and cell ratios.

Since forces are more susceptible to the energy cut-off, test were performed at the recommended cut-off, 1.3 times the cut-off and 2 times the cut-off. While the latter seems extreme at first glance, our phonon calculations show that we iron out certain artefacts of low-energy modes by using a large cut-off. A similar effect was seen in simulations of $CsSnI_3$ [140], a perovskite with distorted octahedra. As we shall see, the forces related to tilting octahedra is quite subtle in DFT.

Geometry of AFM LCO

We performed equation-of-state fits to AFM La_2CuO_4 in all three structural phases. Figure 3.9 shows the Energy-Volume fits, Figure 3.10 shows the volume dependence of the cell ratios and Figure 3.11 shows how the angles in the LTO and LTT phases change as a function of volume. Contrary to experiment, the LTO phase is energetically unfavourable and the favoured phase is LTT. In the tetragonal phases, the optimal c/a ratio is reduced as a function of volume while the LTO phase has a maximum at optimal volume. The orthorhombicity in the LTO phase increases as a function of volume and tilts in the LTO and LTT phases increase wit increasing volume. Figure 3.11 additionally reveals that the Q_1 and Q_2 are not completely rigid, consistent with experiment [71]. Intuitively, it is 'easier' to move the apical oxygen due to the interlayer region being less dense. The observations on LTO are consistent with structural studies of LSCO under pressure [161], where both the orthorhombic strain and tilt angle are decreased with increasing pressure.

Geometry of metallic LCO

The same geometry optimization was performed in the metallic state of La_2CuO_4. EOS fits are shown in Figure 3.12, cell ratios are shown in Figure 3.13 and the LTO/LTT angles are shown in Figure 3.14. Qualitatively, we notice very similar behaviour to AFM LCO with regards to cell ratios and tilt angles, but for these calculations LTT and LTO are the preferred phases with very similar total energies. This is inconsistent with, the electronically well-described, over-doped

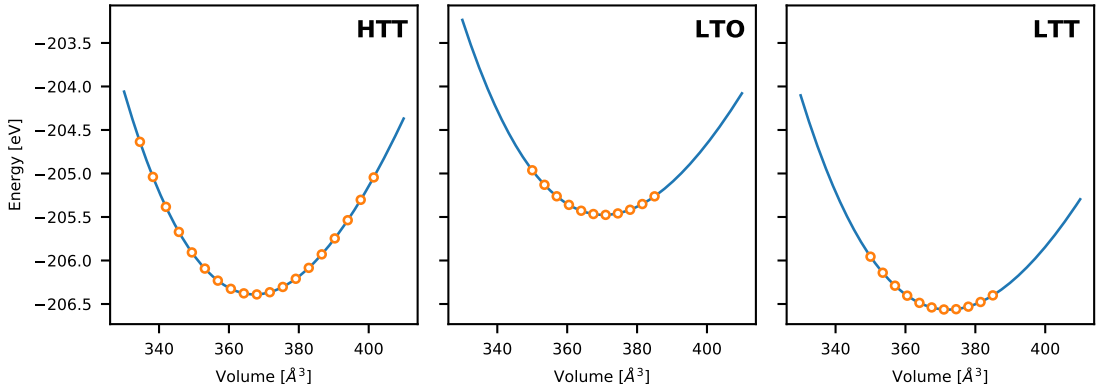

Figure 3.9: Equation-of-state fits (AFM). Optimal volume of simulated structures are found by performing optimization of fractional coordinates and cell shape at a series of fixed volumes. The resulting Energy/Volume curve is then fit to a Vinet exponential equation of state [157]. This is done for the HTT, LTO and LTT phases with the PBESol functional.

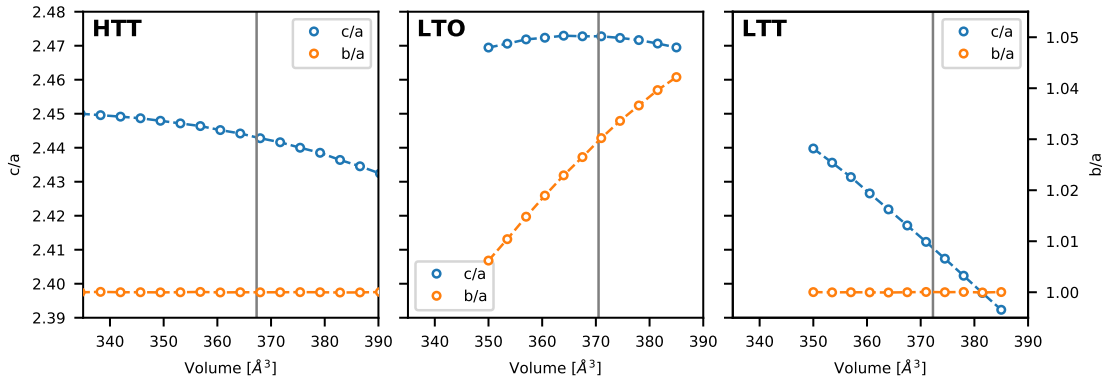

Figure 3.10: Cell Ratios (AFM). During the equation-of-states fits from Figure 3.9, the cell shape is modified, changing the b/a ratio (orthorhombicity) and c/a ratio (larger values correspond to a cell that is elongated along c). Due to symmetry $b/a = 1$ for the HTT and LTT phases. Vertical line is the optimal volume from the fit.

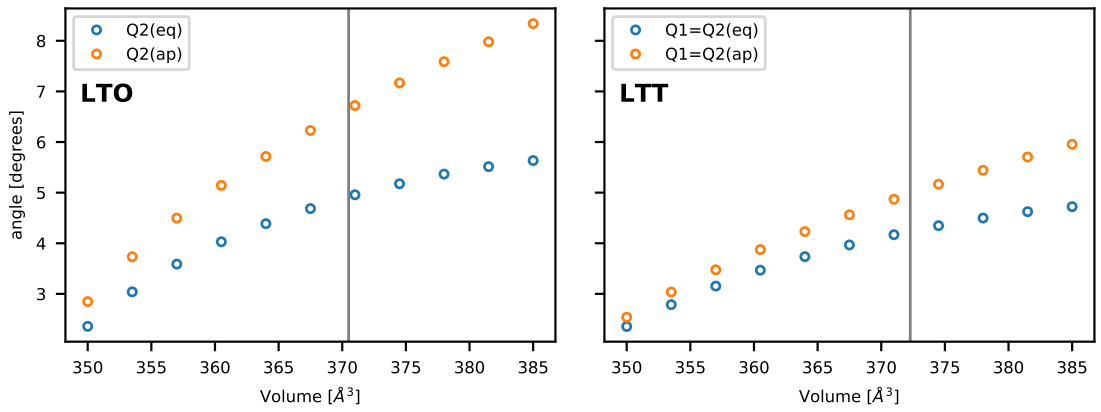

Figure 3.11: LTO/LTT Angles (AFM) During equation-of-state fits, we record the tilt angles for the LTO and LTT phase. Here, they are plotted as a function of Volume. Note that for LTO $Q_1 = 0$ and for LTT $Q_1 = Q_2$. However, the rotation angle is measured differently from the equatorial (eq) and apical (ap) oxygen. The difference in values can be thought of as 'non-rigidity' of the rotation.

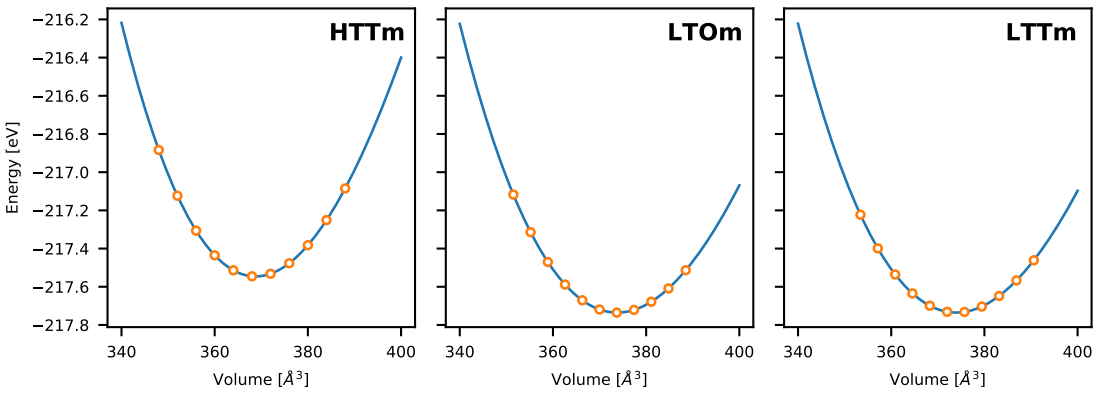

Figure 3.12: Equation-of-state fits (Metal). Optimal volume of simulated metallic structures are found by performing optimization of fractional coordinates and cell shape at a series of fixed volumes. The resulting Energy/Volume curve is then fit to a Vinet exponential equation of state [157]. This is done for the HTT, LTO and LTT phases with the PBESol functional.

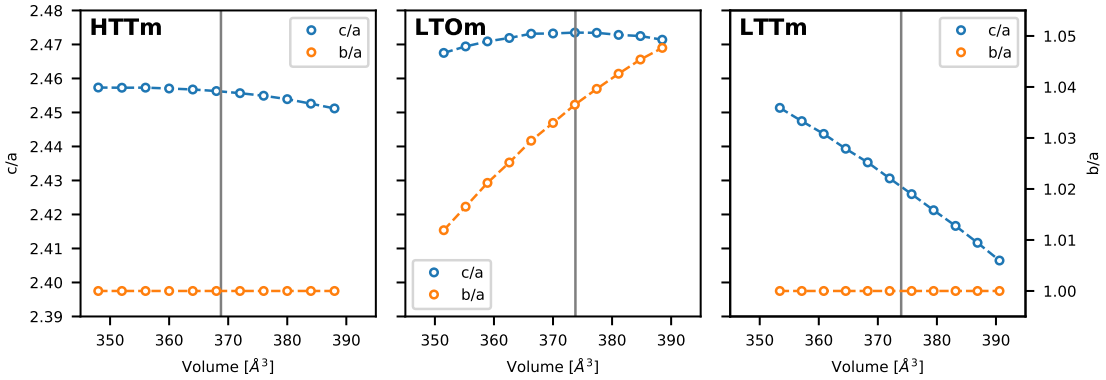

Figure 3.13: Cell ratios (Metal). During the equation-of-states fits from Figure 3.12, the cell shape is modified, changing the b/a ratio (orthorhombicity) and c/a ratio (larger values correspond to a cell that is elongated along c). Due to symmetry $b/a = 1$ for the HTT and LTT phases. Vertical line is the optimal volume from the fit.

phase where the structure is actually HTT at low temperatures [71]. Since the difference is roughly 0.2 eV = 200 meV and our uncertainty in energy is around 2 meV (see Figure 3.5), it is hard to imagine a scenario where the discrepancy is due to numerical noise, especially since the calculations were performed with a very dense k-point mesh of $16 \times 16 \times 8$. It is, however, worth noting that the evaluation of forces is quite different between metallic and insulating solutions in plane wave DFT.

Summary of geometry optimization

A summary of all the geometry optimizations are shown in Table 3.4. Additional data from simulations with a different functional have been added to this table. We notice that the PBE functional finds a volume closer to experimental value, but phonon calculations show a more consistent behaviour of the PBESol functional.

3.7 Phonons

Phonons are calculated using the Phonopy software using the finite displacement (also known as the direct method or the frozen phonon method). Details on the methodology is given in section 2.4. Phonon calculations were performed on both metallic and AFM LCO in the HTT, LTO and LTT structural phases. We use the same computational parameters as in the preceding sections, but expand to a $2 \times 2 \times 1$ supercell in order to compute phonon energies at finite values of $\boldsymbol{q}$. Since the cell is expanded, we reduce the k-point mesh to $4 \times 4 \times 4$ for both the metallic and magnetic

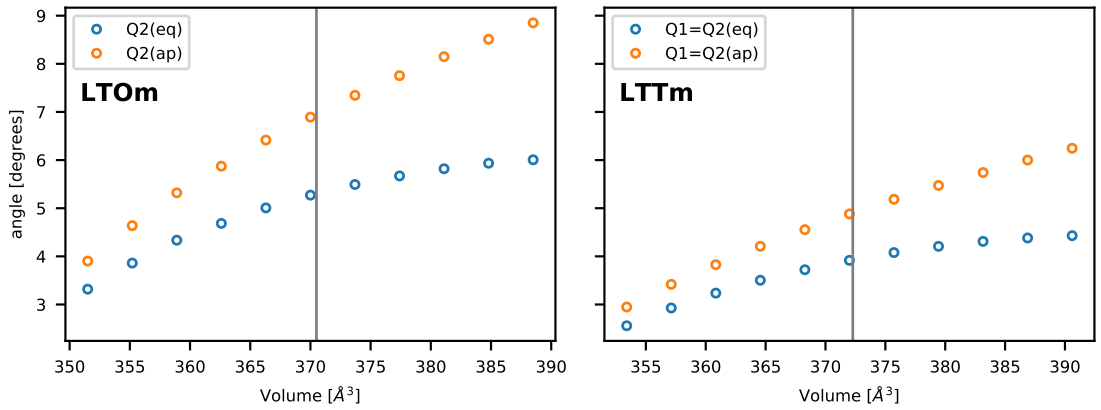

Figure 3.14: LTO/LTT angles (Metal). During equation-of-state fits, we record the tilt angles for the LTO and LTT phase. Here, they are plotted as a function of Volume. Note that for LTO $Q_1 = 0$ and for LTT $Q_1 = Q_2$. However, the rotation angle is measured differently from the equatorial (eq) and apical (ap) oxygen. The difference in values can be thought of as 'non-rigidity' of the rotation.

Table 3.4: Resulting structure due to EOS fits to various structural phases and functionals. The two values given for Q_1/Q_2 are angles calculated from equatorial and apical oxygens, respectively. Interestingly, in terms of energy LTT < HTT < LTO, while the phonons are 'more unstable' for HTT than LTO (See Figures 3.16, 3.17, 3.18). For the metallic cases, we note the optimal geometry is similar to the magnetic case. While the energy is lower, it is not meaningful to compare total energies between GGA+U and GGA.

structure	phase	encut	XC	E0	V0	c/a	η	Q_1	Q_2
HTT	afm	520	PBE	-194.352	383.410	2.431	0.000	0.000	0.000
HTT	afm	800	PBE	-194.494	383.297	2.430	0.000	0.000	0.000
HTT	afm	800	PBESol	-206.390	367.310	2.443	0.000	0.000	0.000
LTO	afm	800	PBESol	-205.476	370.500	2.437	1.465	0.000	5.786
LTT	afm	800	PBESol	-206.565	372.282	2.410	0.000	4.612	4.612
HTT	metal	800	PBESol	-217.546	368.774	2.456	0.000	0.000	0.000
LTO	metal	800	PBESol	-217.735	373.793	2.430	1.795	0.000	6.421
LTT	metal	800	PBESol	-217.735	373.948	2.428	0.000	4.528	4.528

solutions. While it would be preferable to perform the metallic simulation at a higher k-point density, memory requirements became a problem when performing computations on a supercell with P1 symmetry. While we can rely on most of the computational parameters chosen/obtained in the preceding sections, we check the effect of functional choice and energy cut-off (`ENCUT`) on phonon bands since these are more susceptible to instabilities in forces. In Figure 3.15, we show the phonon band structure in the AFM phase with `ENCUT=520` and `ENCUT=800`. While the effect of increasing the plane wave cut-off is small, we see immediately that it fixes some instabilities at Γ. While we do expect instabilities at the M point in the HTT phase, the results could be improved.

For this reason, we keep the 800 eV cut-off and perform the same phonon calculation using the PBESol [162] functional. This functional has been successful for phonon calculations in other perovskite systems with tilt disorder [140], so it is a likely candidate for improvement.

Band structures

Figure 3.16 shows phonon band structures in the HTT phase using both AFM and metallic electronic structures. We immediately notice improvements on two fronts. First, the low-energy modes are 'more stable' and the low-energy optic modes have been moved up. In addition the unstable modes are localized around M where we expect a structural phase transition. Second, the high-energy bond-stretching mode (Γ-X) has increased in energy and is much closer to experimental values. In addition, we reproduce the softening of this mode at X due to doping.

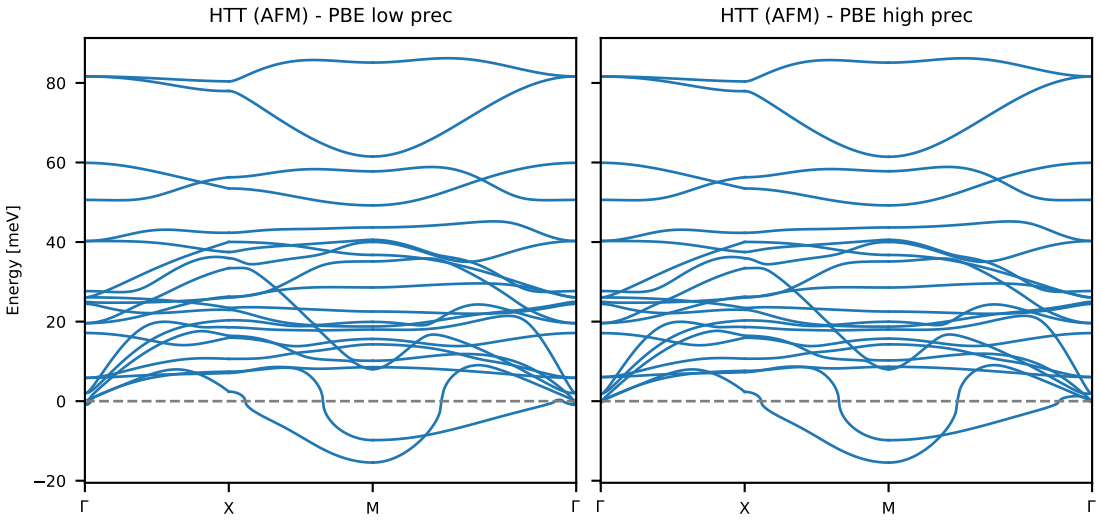

Figure 3.15: Phonon band structure of LCO in the HTT phase using the PBE functional with a 520 eV (low prec) and 800 eV (high prec) plane wave cut-off. Both simulations are performed using a magnetic electronic structure within the DFT+U formalism.

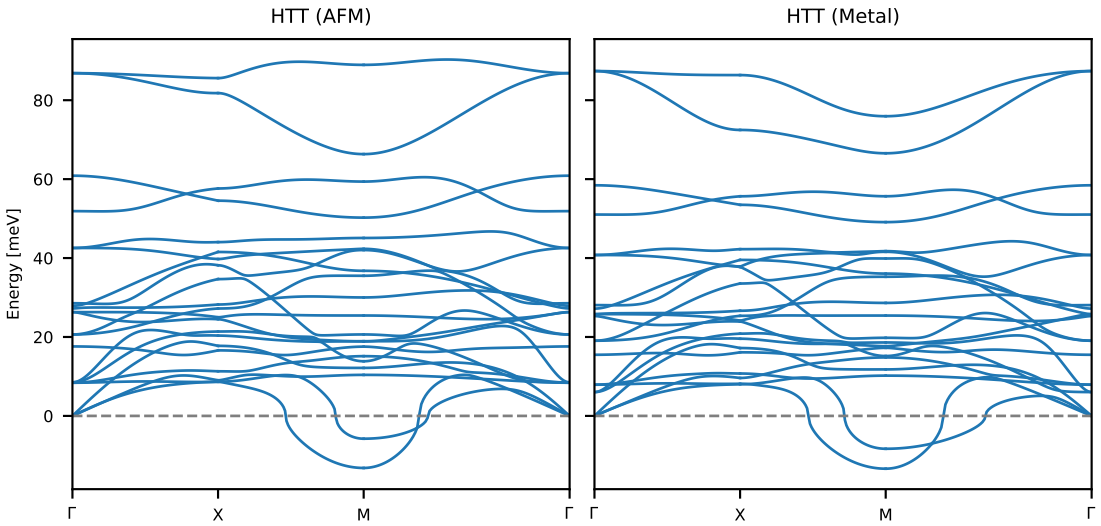

Figure 3.16: Phonon band structure of LCO in the HTT phase using the PBESol functional and an 800 eV plane-wave cut-off. The high-symmetry lines are with respect to the primitive tetragonal BZ (See Figure 3.3)

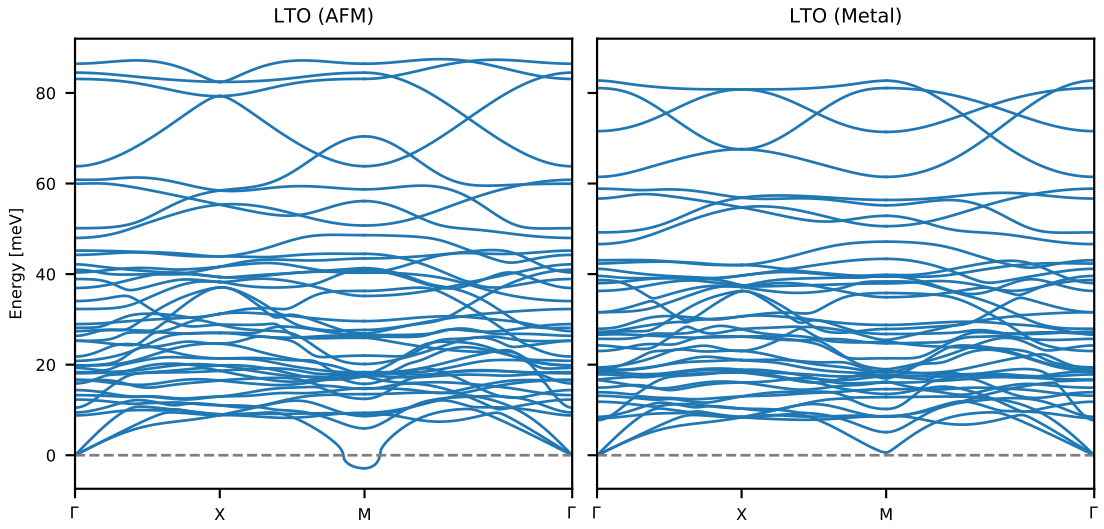

Figure 3.17: Phonon band structure of LCO in the LTO phase using the PBESol functional and an 800 eV plane-wave cut-off. The high-symmetry lines are with respect to the primitive tetragonal BZ (See Figure 3.3)

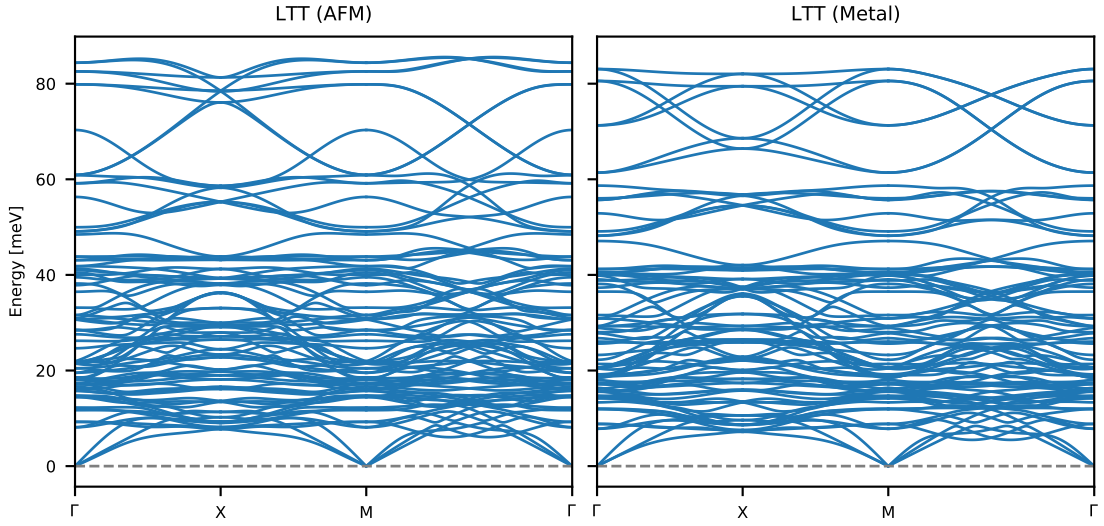

Figure 3.18: Phonon band structure of LCO in the LTT phase using the PBESol functional and an 800 eV plane-wave cut-off. The high-symmetry lines are with respect to the primitive tetragonal BZ (See Figure 3.3)

While there, in principle, are a huge number of functionals one could try, phonon calculations are quite expensive and the PBESol results are reasonable in the context of lattice dynamics. We thus stick to the PBESol functional in simulations moving forward. To check the stability of structural phases in LCO, we perform phonon calculation in the LTO and LTT phases, shown in Figure 3.17 and 3.18. Qualitatively, we see similar features to HTT (apart from the obvious increase of bands). The most significant result is that the LTO and LTT phases clearly stabilizes at the M-point, suggesting that our simulations reproduce the observed structural phase transitions. The stability of LTT is particularly interesting in this case, since this phase is believed to suppress superconductivity. In particular when combined with the fact that LTO and LTT are very close in energy when looking at the metallic simulations.

Density of states

As discussed in section 2.6, the the calculation of phonon bands makes it trivial to compute the (partial) phonon DOS by evaluating the bands on a grid and integrating onto the energy axis. By evaluating the partial DOS and weighing each partial by scattering cross section (σ^{total}) and ionic

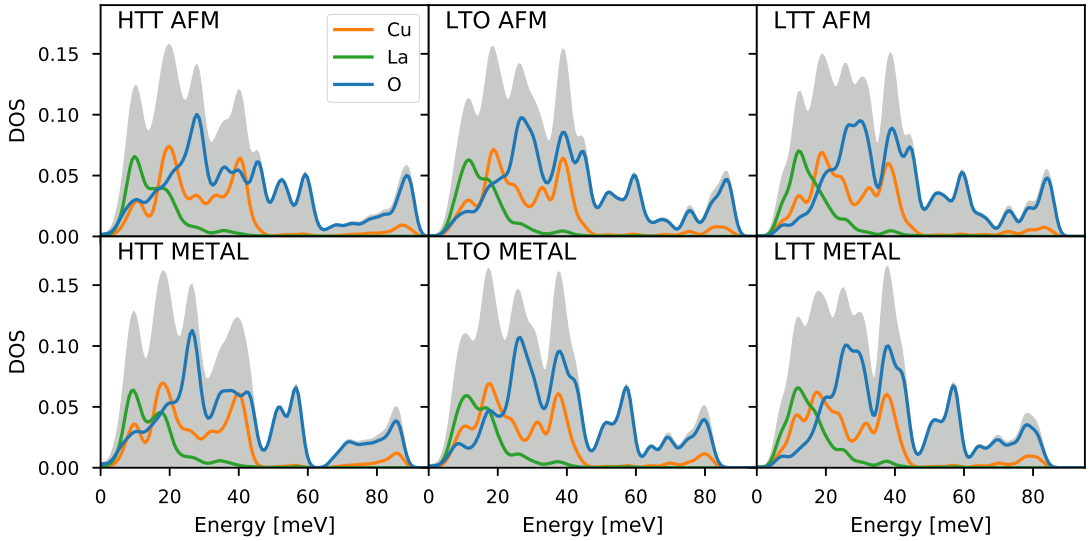

Figure 3.19: Neutron-weighted phonon density of states in the various structural and electronic phases of LCO. Both the partial and total density of states is shown in the plot.

mass, we obtain the generalized phonon DOS as seen by a time-of-flight neutron spectrometer in the incoherent approximation.

Figure 3.19 shows the neutron weighted partial and total density of states due to the 6 different phonon calculations we performed. The density of states was evaluated on a $48 \times 48 \times 48$ grid, integrated using the tetrahedron method and an applied Gaussian smearing of $\sigma = 1\,\text{meV}$ (2.35 meV FWHM). To get comparable values of $g(\omega)$, the plots are normalized to the BZ volume ($4V^{\text{BZ}}_{\text{HTT}} = 2V^{\text{BZ}}_{\text{LTO}} = V^{\text{BZ}}_{\text{LTT}}$).

Qualitatively, the main difference between the structural phases is a modification of the peak at $\approx 30\,\text{meV}$ as you go to progressively lower symmetries. A quick inspection of the eigenvectors of the HTT calculation reveals 4 modes in this energy-range (inspection performed at Γ):

1. 26.3 meV: An in-plane oxygen mode where the oxygens move along c and the two diagonals of the octahedra is out of phase.

2. 27.2 meV: An apical oxygen mode where apical of the same 'plane' move together with the direction alternating between each plane

3. 27.9 meV: A mode where every oxygen-atom moves in-phase along c, keeping the rest of the lattice still.

4. 28.6 meV: A lanthanum mode where the atoms move out of phase along c.

The metallic simulations mainly have the effect of generally pushing phonon energies down and a 'smoothing' of high-energy modes. Extrapolating from the HTT phase, this is directly linked to the softening of the Cu-O bond-stretching mode at the zone boundary, as will be discussed in chapter 8. In addition, the two peaks at 50 meV and 60 meV have weight shifted towards the latter. The mode at 50 meV is a bond-stretching mode of the apical oxygen, while the mode at 60 meV involves vibration of all oxygen-atoms along the c axis, with in-plane and apical oxygen atoms being relatively out of phase.

3.8 Validation of simulations

Since LSCO is such an extensively studied system, there is data available in the literature to compare our band structures. By inspection of the band structure plots in the previous section, it seems like a difficult task to actually separate the bands in a neutron scattering experiment. Luckily, there are a few modes that can be distinguished. Figure 3.20 compares our HTT band phonons band structures along Γ-X with experimental data from a range of LSCO samples. The highlighted modes is the Cu-O half-breathing mode ($\approx 80\,\text{meV}$) and the apical oxygen stretching mode ($\approx 60\,\text{meV}$). We will discuss this mode in detail in Chapter 8

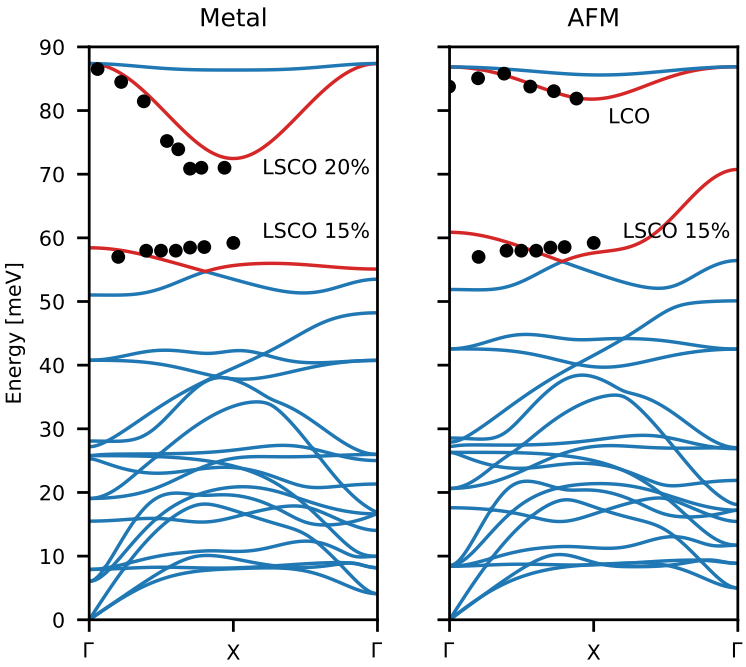

Figure 3.20: Comparison of phonon band structures in the HTT structural phase along the Γ-X path with data from literature. Data for LSCO 15% taken from ref. [163], data for LSCO 20% and 0% taken from ref. [164]. Modes associated with data are highlighted in red.

Further validation of our simulations are performed in the experimental Chapters 6 and 7 where we look at low-energy phonon modes and density-of-states measurements, respectively. In addition, some of the ideas developed here will be used in the investigation of simulations with O/Sr defects using ab-initio MD in the following chapter.

3.9 Summary

I summary, we performed ab-initio phonon calculations of La_2CuO_4 in 3 structural and two electronic phases, using the PBESol functional and an increased plane wave energy cut-off in order to correctly stabilize low-energy phonons. We discover imaginary modes at the M point of the HTT, consistent with the observation of the HTT-LTO structural phase transition due to octahedral tilts. The relationship between the LTO and LTT phases are less consistent and we get different results for the metallic and AFM solutions. For the AFM case, LTT is the stable phase (and LTO is 'less stable' compared to HTT), never seen in experiments on the undoped compound. In fact, the orthorhombic strain and octahedral tilt are both largest at zero doping [71]. For the metallic case, LTO and LTT are nearly degenerate (indistinguishable energies within our numerical precision), while experiments tells us that HTT is the stable phase at overdoing, at least for $La_{2-x}Sr_xCuO_4$.

Despite our results being inconsistent with regards to total energies and observed structural phases, we proceed our investigations based on the computational parameters decided on throughout this chapter. There are two reasons for this. First, we have a remarkable agreement with phonons at both high (chapter 8 and Figure 3.20) and low (Chapter 6) energies. Second, we *know* that a one-electron theory such as DFT is unable to explain the correlated nature of the cuprates at optimal doping, so we settle on the best description possible in the edge cases and try to extrapolate from that. The electronic structure of the cuprates at intermediate doping is essentially an unsolved problem outside the scope of this thesis.

Chapter 4

Molecular Dynamics

Using the lessons learned in the previous chapter and after a reasonably successful validation of simulations (see section 3.8), we can use the computational parameters at a lower precision and perform Molecular Dynamics simulations in VASP. The purpose of this chapter is to discuss the computational details, outline the chosen defect structures and finally present how defects (interstitial or otherwise) modifies the structure and dynamics of the parent compound. While molecular dynamics simulations are unable to provide information about the phonon band structure directly, it is possible to extract the phonon DOS and other relevant dynamical information as outlined in section 2.5. In order to distinguish the simulations, we use a similar notation as in the previous chapter, but with the option to add dopants: [HTT/LTO/LTT][m]+[Sr/O_i], where omitting the [m] refers to the AFM electronic structure. For example, LTOm+Sr refers to a calculation starting from orthorhombic (Bmab) symmetry, in the metallic phase, with added Sr dopant.

4.1 Computational Details

Since Molecular Dynamics simulations require a large number of SCF cycles, it is necessary to drastically reduce the precision of our simulation. In general, the most drastic approximation comes from only running the simulation at one k-point (Γ). Other parameters are benchmarked by small test runs of a couple hundred steps and then evaluating the computational resources/time available. In our case we end up with the following additional reductions in precision:

- Planewave cut-off at the default: 400 eV (`ENCUT=400`)
- Threshold for the SCF to stop reduced to 10^{-5} eV (`EDIFF=1E-5`)
- A faster algorithm for electronic minimization (`ALGO=F`)
- Projection operators calculated in real space (`LREAL=A`)

We keep the `PREC` tag set to 'Accurate', since changing to 'Normal' resulted in convergence issues. In addition, we need to specify the temperature and type of ensemble (see section 2.5). For all simulations, we run at $T = 300$ K (`TEBEG=300`) within the canonical (NVT) ensemble using the algorithm of Nosé with a Nosé-mass such that the temperature fluctuates with a frequency of roughly 38 THz (`SMASS=1`). In order to get reasonable statistics we run with a time step $\Delta t = 2$ fs (`POTIM=2`) for a total of 21000 (`NSW=21000`) steps, corresponding to a simulation time of 42 ps. For the analysis, we discard the first 2 ps in order to let the system equilibrate.

For the initial structures where defects have been added, we perform a geometry optimization of the supercell in order to find a structural minimum from which to start the MD simulation. Due to the reduced symmetry (compared to the phonon calculations in chapter 3) this is a fairly expensive computation, so we perform the optimization with the same parameters as the MD simulation, except that we increase the k-point mesh to $4 \times 4 \times 4$ and the SCF threshold to 10^{-6} eV. Similar to the phonon calculations, we use the conjugate gradient algorithm for this minimization.

4.2 Octahedral tilts

In order to obtain octahedral tilts from MD simulations where symmetry is turned off, we are forced to define the octahedral tilts for each octahedra in the supercell. In fact, by writing which octahedra each oxygen atom (excluding interstitials) in our simulation belongs to, we can extract

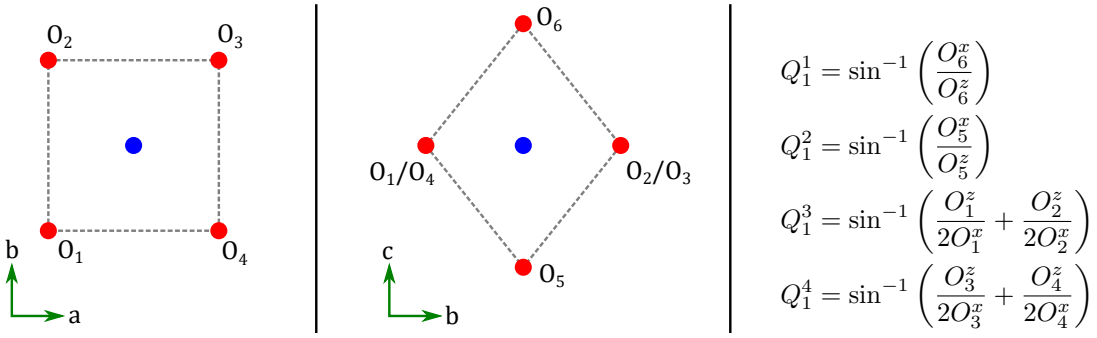

$$Q_1^1 = \sin^{-1}\left(\frac{O_6^x}{O_6^z}\right)$$
$$Q_1^2 = \sin^{-1}\left(\frac{O_5^x}{O_5^z}\right)$$
$$Q_1^3 = \sin^{-1}\left(\frac{O_1^z}{2O_1^x} + \frac{O_2^z}{2O_2^x}\right)$$
$$Q_1^4 = \sin^{-1}\left(\frac{O_3^z}{2O_3^x} + \frac{O_4^z}{2O_4^x}\right)$$

Figure 4.1: Finding octahedral tilts from arbitrary oxygen positions. Q_2 angles can be found in an analogous way by replacing x with y and 'pairing up' O_1 with O_4 and O_2 with O_3.

the (Q_1, Q_2) tilt as seen from that oxygen. Since the tilts alternate, each tilt belongs to one of four symmetries with respect to (Q_1, Q_2): (+,+), (+,-), (-,+), (-,-). In practice, we analyse the initial $t = 0$ structure with the following steps for each Cu atom in the supercell:

1. Record the position of the Cu atom
2. Find apical oxygens by searching for (Cu, O) pairs with a distance less than $r = (1, 1, 2.7)$ Å
3. Find equatorial oxygens by searching for (Cu, O) pairs with a distance less than $r = (2.1, 2.1, 1)$ Å
4. Determine the Q_1, Q_2 tilt as seen from each of the 6 oxygen atoms in the list.
5. Apply the symmetry operations.
6. Save the 4 (Q_1, Q_2) value pairs.

Step 4 is performed by first converting fractional coordinates to real-space coordinates and then finding angles as outlined in Figure 4.1. The symmetry operations in step 5 is a matrix with 8 columns corresponding to the 8 tilt values and a number of rows equal to the number of octahedra – 16 in the case of our $2 \times 2 \times 1$ supercell. Each element of the matrix is either +1 or -1, where -1 will reverse the tilt direction and +1 will keep it as-is. The matrix can be generated by examining the output of the starting structure (which has the correct space group symmetry) and then constructing the matrix such that all (Q_1, Q_2) tilts agree. While the same result can be archived by manually assigning the different atoms of our manageable supercell, this methodology allows the code to eventually be expanded to other systems, since we can set up arbitrary local coordinate systems.

After having performed this analysis, we can apply the same operations to every time step and obtain statistics about the time-evolution of the octahedral tilts in our system. This is similar to the Positional Recurrence Maps (PRM) methodology [165] that has been used to extract information about the apical oxygen dynamics in $Nd_2NiO_{4+\delta}$ [166].

4.3 Structures with dopant ions

Since the introduction of dopant ions breaks the crystal symmetry, we cannot perform phonon calculations using the direct method without making an excessive amount of high-precision calculations. Our typical $2 \times 2 \times 1$ supercell containing 112 ions with P1 symmetry would require $112 \times 3 = 336$ displacements just to describe phonon frequencies and eigenvectors at Γ. The worst case phonon calculation (LTT with magnetism) in the preceding chapter required just 21 displacements. For this reason, we are essentially forced to use molecular dynamics. In the following, the model for placing the initial dopants is outlined for Sr- and O-doped systems separately.

LCO+O

We start by considering the $La_2CuO_{4+\delta}$ System, which is simply LCO with added oxygen atoms at interstitial sites. It is generally accepted that the oxygen enters in the middle of the rock-salt layer, the least dense area of the crystal structure. Figure 4.2 shows possible interstitial positions for the LTO (Bmab) and LTT ($P4_2/ncm$) phase, taken from a model proposed for the $La_2NiO_{4+\delta}$ system

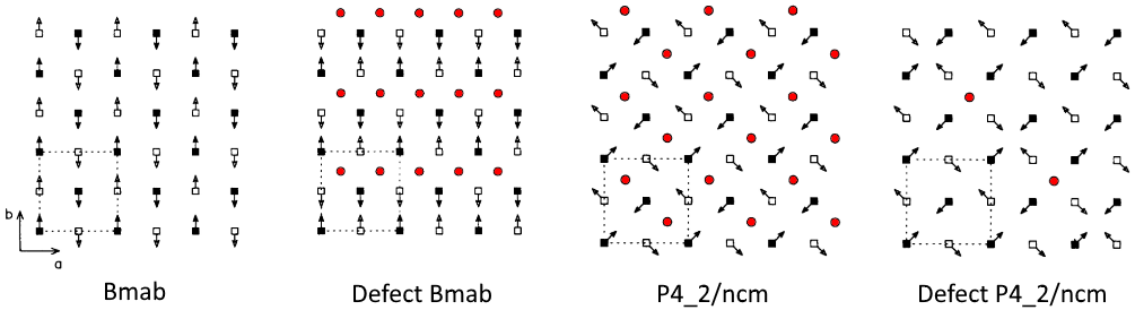

Figure 4.2: Illustration of interstitial oxygen in-plane (a-b) location with respect to the apical oxygen displacements in the rock-salt layer. Open squares represent apical oxygens 'hanging down' while closed squares represent apical oxygens 'sticking up'. Interstitial oxygen are red circles and are shown on every possible interstitial site for clarity. Adapted from ref. [87].

[87]. Simulations in the defect phases are denoted by subscript 'defect'. We ignore the HTT phase for molecular dynamics since the symmetry is broken and the preliminary geometry optimization would tend to tilt the octahedra similar to the LTT phase. To represent a reasonable doping level, we consider the addition of a single interstitial. It is generally accepted that the oxidation state is, at least approximately, O^{2-}, such that each dopant adds two holes. In our $2 \times 2 \times 1$ supercell with 16 formula units, this corresponds to a doping of $n_h = \frac{2}{16} = 0.125$.

To see how the symmetry is broken, Table 4.1 shows the resulting space groups when inserting an interstitial into various starting symmetries. As expected, the symmetry is lowered substantially, especially if the z-component of the interstitial is different from $\frac{1}{4}$. While the symmetry isn't reduced to P1, it is difficult to imagine that any of the space groups in Table 4.1 could be used solve the observed superstructures in LCO+O (see section 1.4). Diffraction studies point to the interstitial being placed at either $(\frac{1}{4}\frac{1}{4}z)$ with z close to $\frac{1}{4}$ or on a general (xyz) position [167]. When modelling this position in diffraction studies, it is possible to keep the parent symmetry by assigning an occupation factor to the interstitial and thus keeping the symmetry of the parent phase. Since we are not afforded that luxury when building structures for molecular dynamics, defects will naturally break the symmetry of our parent phase. Table 4.1 should thus not be seen as proposed models, but rather as an illustration of our inability to model partial occupancies in a small real-space box.

LSCO

In the $La_{2-x}Sr_xCuO_4$ system, our current best guess is that the distribution of the doped Sr species is completely random and homogeneous. Since randomness is difficult to implement in a (relatively) small system with periodic boundary conditions, we initially place them at a distance of about half the box side in order to represent homogeneous doping. Replacing La^{3+} with Sr^{2+} adds one hole, so we add two dopants in order to be at $n_h = 0.125$ doping.

4.4 Geometry Optimization

We performed high-precision geometry optimizations of ionic positions only on these LCO+O defect structures starting from the various relevant symmetries. The starting structures were the optimized structures from chapter 3 with an interstitial inserted according to Table 4.1. The defect structures were created by reversing certain tilts according to Figure 4.2. For the geometry optimization we kept the volume fixed at the value obtained from the parent structures without tilt defects, substitutions or interstitials. Performing an equation-of-state geometry optimization for all structures as in section 3.6 is computationally expensive for the defect supercells, but Figure 4.3 shows a EOS fit of the LTT structure with a limited number of points, revealing that the Volume does not change significantly due to the interstitial.

Table 4.2 shows the resulting total energies and (Q_1, Q_2) tilts for a variety of starting structures including oxygen interstitials. A few trends emerge from this investigation. First, the defect structures in Figure 4.2 has the effect of reducing the *average* tilt of the structure, if we keep the symmetry operations from the non-defective phase. In the case of LTO the average tilts completely cancel out, while in the case of LTT they are cut in half. In addition, both the average and local tilts move towards the tilt pattern of the non-defective phase during optimization. In general,

Table 4.1: Space group symmetry due to the introduction of an interstitial oxygen in various structures all described in a $2 \times 2 \times 1$ supercell of the Bmab (conventional) coordinate system. HTT, LTO and LTT are the usual phases as described in literature [35]. The structures labelled defect is (1) in the LTO case: A stacking fault where the middle layer has its tilts reversed and (2) in the LTT case: A line along [110] with reversed tilts. Both are described in [87] and are designed in order to 'make room' for the interstitial oxygen (see Figure 4.2).

Phase	Space Group	O_i^x	O_i^y	O_i^z
HTT	I4/mmm (139)			
HTT + O_i	P-42m (111)	0.125	0.125	0.25
HTT + O_i	Cmm2 (35)	0.125	0.125	0.24
LTO	Bmab (64)			
LTO + O_i	P2 (3)	0.125	0.125	0.25
LTO + O_i	P2 (3)	0.125	0.125	0.24
LTO_{defect}	Pmna (53)			
LTO_{defect} + O_i	P2 (3)	0.875	0.375	0.25
LTO_{defect} + O_i	P2 (3)	0.875	0.375	0.24
LTT	$P4_2/ncm$ (138)			
LTT + O_i	P-4 (81)	0.375	0.125	0.25
LTT + O_i	P2 (3)	0.375	0.125	0.24
LTT_{defect}	Pmma (51)			
LTT_{defect} + O_i	Cmm2 (35)	0.875	0.375	0.25
LTT_{defect} + O_i	Cmm2 (35)	0.875	0.375	0.24

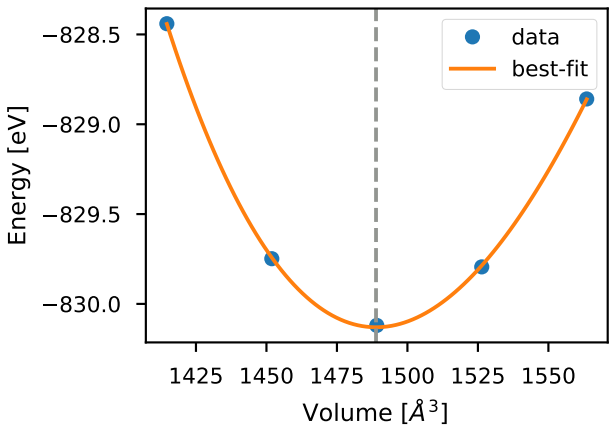

Figure 4.3: Equation-of-state fit to $La_2CuO_{4.0625}$ starting from the LTT phase with one added interstitial oxygen in our supercell. The broken vertical line is the minimum of the fit, showing that our starting volume was reasonable. Each minimization was performed without symmetry while relaxing both ionic positions and the cell shape. The orthorhombic strain due to the cell shape change was below $\eta = 0.0004$ for all volumes, suggesting that the tetragonal crystal shape is a stable minimum.

our simulations find that it costs more energy to reverse the tilts compared to the addition of the interstitial. This is inconsistent with the observation of staging (see section 1.4) and is likely related to the limited size of our simulation. Since a well-defined energy minimum is important for the initial configuration of the MD simulations, we stick with the parent, undistorted phases when investigating LCO+O. Finally, we notice that the tilts tend towards an 'LTT-like' tilt-pattern in the optimization of metallic LTO, while keeping a significant orthorhombic strain.

Table 4.3 shows the same optimizations performed on Sr-doped La_2CuO_4. The results here are as we expect from the small difference between the ionic radius of La^{3+} and Sr^{2+} (see table 1.2). We seem to be in a well-defined minimum and the average tilt is only modified slightly. While geometry optimizations are only able to locate a local minimum, the results in Tables 4.2 and 4.3 point toward the expected conclusion that interstitial oxygen has a more significant effect on the octahedral tilt patterns compared to Sr doping. The nature of these effects cannot be obtained from geometry optimizations alone, and we turn to molecular dynamics for the detailed analysis of structure and dynamics.

4.5 Benchmarking

Similar to our phonon calculations in the previous chapter, molecular dynamics simulations are typically benchmarked in various ways. Depending on the type of ensemble and thermostat, either the temperature or total energy is expected to be conserved. It is, however, possible for numerical noise to cause these quantities to drift. In our case the Nosé thermostat controls temperature through velocities, so it can be useful to plot the temperature as a function of simulation time to see if the fluctuations are reasonable. The temperature can be calculated from the MD trajectory by first computing the velocities through the Verlet algorithm (see section 2.5) and then evaluating

$$T = \frac{1}{3k_{\mathrm{B}}(N_{\mathrm{ions}} - 1)} \sum_j M_j |\boldsymbol{v}_j|^2 \,,$$

where N_{ions} is the number of atoms, M_j is the mass of atom n and $\boldsymbol{v}_j$ is the velocity of atom j. We divide by $(N_{\mathrm{ions}} - 1)$ rather than N_{ions}, since temperature is defined with respect to degrees of freedom and we can arbitrarily redefine our coordinate system with respect to a particular

Table 4.2: Oxygen interstitial phases, geometry optimization. Geometry optimization performed on ionic positions only. E_0 corresponds to the energy after inserting the interstitial oxygen, but before geometry optimization. E_1 is the total energy after optimization. The octahedral tilts (Q_1, Q_2) are similarly defined before and after the optimization.

	E_0 [eV]	E_1 [eV]	$(Q_1, Q_2)_0$	$(Q_1, Q_2)_1$
HTT + O_i	-827.27669	-829.76250	(0.00, 0.00)	(1.00, 1.00)
LTO + O_i	-828.29890	-830.39658	(0.00, 5.79)	(1.21, 5.92)
LTO_{defect} + O_i	-823.09516	-830.03588	(0.00, 0.00)	(2.12, 4.48)
LTT + O_i	-828.04663	-830.08248	(4.61, 4.61)	(3.77, 3.72)
LTT_{defect} + O_i	-826.03173	-829.94243	(2.31, 2.31)	(2.80, 2.70)
LTOm + O_i	-872.73074	-876.56079	(0.00, 6.42)	(3.76, 3.90)
LTTm + O_i	-872.35546	-876.56195	(4.53, 4.53)	(3.85, 3.85)

Table 4.3: Sr doped phases, geometry optimization. E_0 corresponds to the energy after replacing La with Sr, but before geometry optimization. E_1 is the total energy after optimization. Geometry optimization performed on ionic positions only. The octahedral tilts are similarly defined before and after the optimization.

	E_0 [eV]	E_1 [eV]	$(Q_1, Q_2)_0$	$(Q_1, Q_2)_1$
LTO + Sr	-858.73485	-859.48650	(0.00, 5.79)	(0.00, 5.38)
LTOm + Sr	-858.57712	-859.39905	(0.00, 6.42)	(0.00, 5.69)
LTT + Sr	-858.68994	-859.49712	(4.61, 4.61)	(3.87, 3.97)
LTTm + Sr	-858.57810	-859.40170	(4.53, 4.53)	(3.98, 4.08)

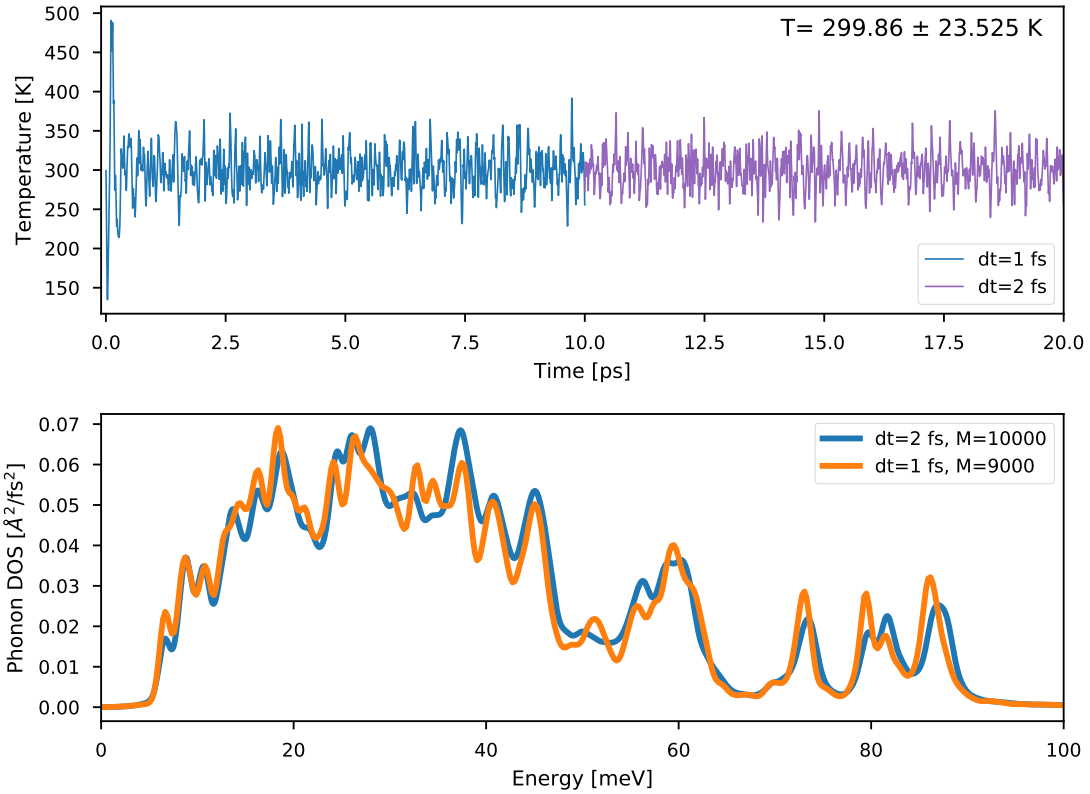

Figure 4.4: Benchmark of molecular dynamics, using LCO in the LTO phase with no dopant ions or defects. **Top:** Temperature fluctuations for a simulation stitched together with the first 10 ps using a 1 fs time step and the last part of the simulation using a 2 fs time step. **Bottom:** Density of States weighted by neutron-cross sections and broadened by a Gaussian with $\sigma = 0.5$ meV (1.18 meV FWHM) evaluated at the same two parts of the simulation.

atom. When considering the instantaneous temperature in this way, we expect the mean-squared temperature fluctuations to be [168]

$$\langle (\Delta T^2) \rangle = \frac{2T_0^2}{3N_{\text{ions}}} .$$

Four our simulation with $N_{\text{ions}} = 112$ at $T_0 = 300$ K we thus expect temperatures fluctuations of ± 23.15 K. Figure 4.4 is a summary of benchmarks performed on the LCO in the LTO phase with no dopant ions or defects. Simulations were performed with two different time steps and the difference in temperature fluctuations and the resulting phonon DOS was recorded. In terms of temperature fluctuations, there is little effect of going from 1 to 2 fs time steps, but there are slight modifications to the DOS, especially in the region around 30 meV. While this may be seen as problematic, it is important to realize that we are probing a relatively small number of steps, and it is unlikely that our simulation is completely ergodic. In other words, we may be probing a different area of phase space in the two simulations. It is unlikely that the time step resolution itself is causing the effects on DOS, since an energy of 30 meV = 7.3 THz is probed by simulation times of roughly 137 fs. While higher precision is always desirable, we stick with a time step of 2 fs in order to be able to probe dynamics for longer time scales in more systems. Now, almost by definition, different time steps do probe different dynamics. I emphasize that any comparison between MD simulations is done at the same time step.

4.6 DOS and PDF

Molecular dynamics simulations have been performed with 7 starting configurations based on geometry optimizations in Table 4.2 and 4.3 as well as references without dopant ions. Since the full matrix of combinations now includes 3 structural phases, 2 dopant ions, 2 electronic phases and 2 'defect' phases, the total number of desired simulations is 20. In order to limit the scope and

focus computational resources, we chose to focus on the LTO phase and end up with the following list of simulations:

1. LTT: LTT in AFM phase.
2. LTO: LTO in AFM phase.
3. LTO+Sr: LTO in AFM phase with added Sr dopants.
4. LTO+O: LTO in AFM phase with added O dopant.
5. LTOm: LTO in metallic phase.
6. LTOm+Sr: LTO in metallic phase with added Sr dopants.
7. LTOm+O: LTO in metallic phase with added O dopant

Our primary observables when comparing to experiment is the phonon density of states and pair-density-function. We start by considering the DOS of all simulations, calculated with the method described in section 2.5 and the scripts developed in appendix A. Figure 4.5 shows the neutron-weighted phonon DOS for all 7 simulations. While the overall shape of the phonon DOS is mostly unchanged, there are some subtleties that we might consider for further analysis. For the magnetic simulations, we see a similar modification of modes at $\approx 30\,\text{meV}$ when comparing the LTO and LTT phases. Interestingly, the sharp dip in DOS at 30 meV is seen in LTO+O as well. In fact, the LTT and LTO+O phases appear to share more qualitative features with each other compared to the parent LTO phase. This is consistent with the initial geometry optimization of LCO+O in table 4.2 moving towards a LTT-like tilt pattern. LTO+Sr, on the other hand, mostly seem to broaden features rather than directly modify then.

For the metallic simulations, we see similar trends but in a much more smeared out fashion, possibly due to reduced accuracy of these simulations due to the fermi surface smearing (see figure 3.5 in section 3.5). Similar to the observations in chapter 3, the main modification of the phonon DOS compared to the magnetic simulations is related to the high energy modes.

In order to compare more directly these observations, Figure 4.6 shows a direct comparison of DOS and PDF of our LTO, LTO+O and LTT simulations. This comparison clearly shows that the LTT and LTO+O share common features especially around 30 meV (various c-axis modes, see section 3.7 and 60 meV (apical oxygen bond-stretching mode). The PDF in the same figure show only very subtle deviations, most notably around 5.2 Å where, once again, the LTT simulation shares features with LTO+O.

4.7 Microscopic analysis

In addition to observables for comparison with experiment, the purpose of molecular dynamics simulations is to relate microscopic phenomena to these observables. For this reason, we will try to extract relevant information from the simulation trajectory in order to understand what is causing the changes in the phonon DOS and PDF. In the cuprates, there is much experimental evidence of the fact that Cu-O distances and distributions are important for superconductivity [93–95]. Inspired by these results, Figure 4.7 show the distribution of Cu-$O_{\text{equatorial}}$ and Cu-O_{apical} distances for selected simulations. In general, they follow a normal distribution showing that the harmonic approximation works well for our system, with the notable exception of the apical oxygen distance in LTO+O.

Table 4.4 summarizes these distances for all of the performed simulations. As expected from the almost identical PDF across simulations, the mean Cu-$O_{\text{equatorial}}$ distances does not seem to have any discernible trends, but there is a slight widening of the distributions in the systems containing dopants. In some sense this is expected since we have created different local environments by the introduction of impurity dopants. The same trend can be seen in the Cu-O_{apical} distanced, but here we additionally have an shortening of the mean distance due to the introduction of oxygen (notice also that this shortening is identical to the LTT distance in magnetic case). For Sr-doping there is an elongation in the magnetic simulation but a shortening in the metallic simulation. It is, however, important to note that these differences are extremely subtle and may just be due to numerical peculiarities.

Using the definitions of octahedral tilts described in section 4.2, Figure 4.8 shows a histogram of (Q_1, Q_2) tilts from all of our performed MD simulations on a logarithmic scale. Similar to observations from DOS and PDF, the tilt patterns of LTO+O are LTT-like, while the Sr-doped

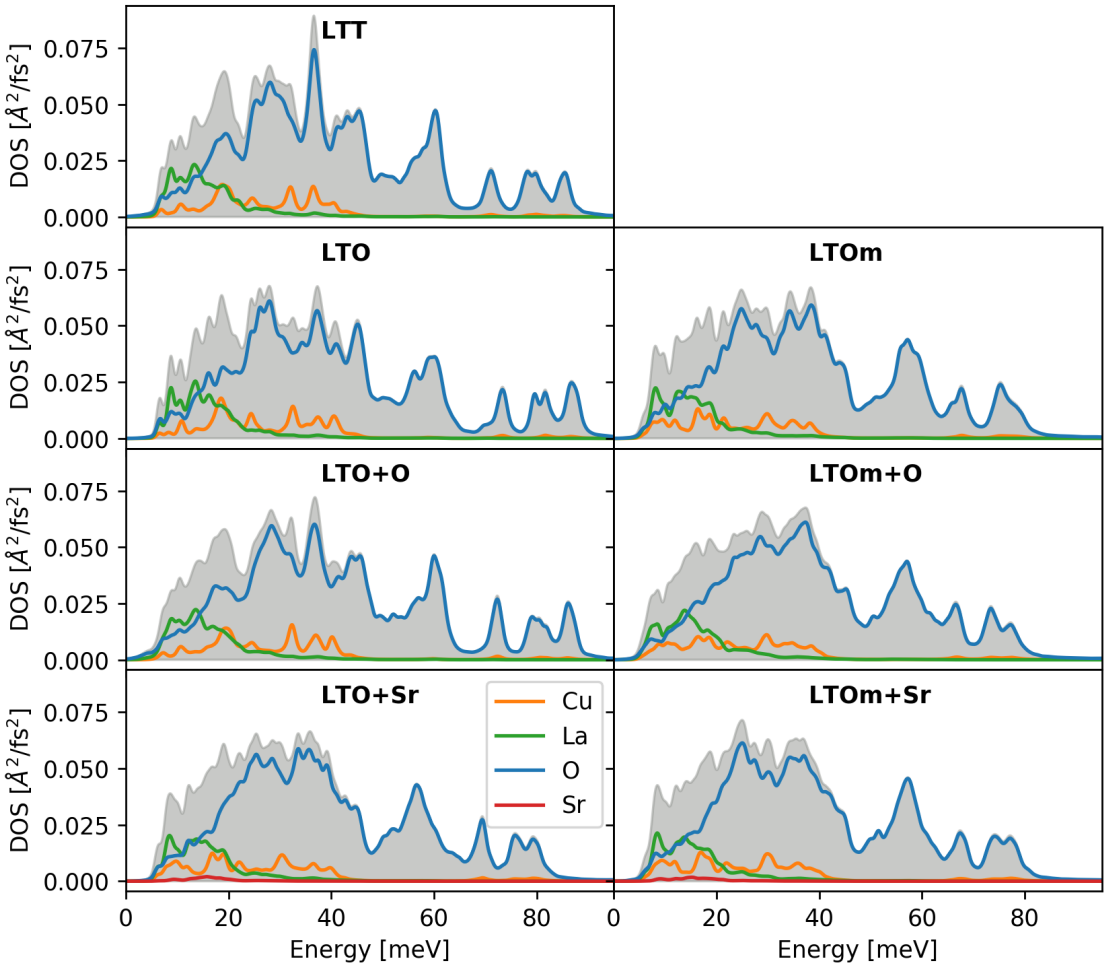

Figure 4.5: Neutron-weighed density-of-states for all molecular dynamics simulations performed in this chapter. The filled grey area is the total DOS and the lines are the partial atomic DOS. The initial conditions for the MD simulation is annotated on each plot according to the notation outlined in the beginning of this chapter. The density-of-states was obtained through the power spectrum of the velocity autocorrelation function (see section 2.5). The power spectrum was smoothed by a Gaussian kernel with width $\sigma = 0.5\,\text{meV}$ (1.18 meV FWHM).

Table 4.4: Cu-O Distances distance statistics for all MD simulations performed in this chapter. Columns 2 and 3 show the mean distance and standard deviation for the Cu-O equatorial distance. Column 3 is the R^2 value of a linear regression assuming a normal distribution. Columns 4-6 show the same values for the Cu-O apical distance.

name	$\langle O_{eq} \rangle$ [Å]	σ (O_{eq}) [Å]	R^2 (O_{eq})	$\langle O_{ap} \rangle$ [Å]	σ (O_{ap}) [Å]	R^2 (O_{ap})
LTO	1.898	0.0455	0.9972	2.421	0.113	0.9989
LTO+O	1.902	0.0464	0.9972	2.406	0.127	0.9608
LTO+Sr	1.898	0.0507	0.9947	2.438	0.146	0.9995
LTOm	1.909	0.0514	0.9951	2.462	0.140	0.9997
LTOm+O	1.908	0.0532	0.9934	2.440	0.156	0.9992
LTOm+Sr	1.905	0.0523	0.9947	2.451	0.151	0.9992
LTT	1.907	0.0461	0.9971	2.406	0.109	0.9992

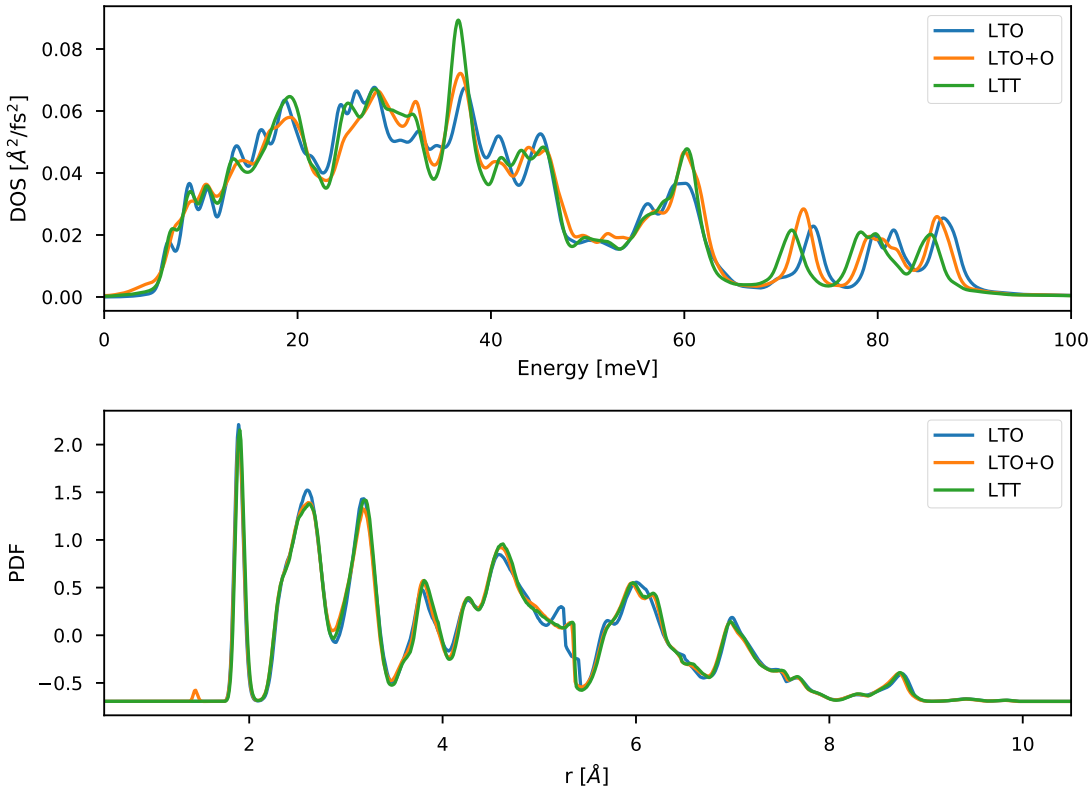

Figure 4.6: **Top**: Total DOS for selected MD simulations. In general, differences are subtle, but we see some surprising similarities between the LTO+O and LTT simulation, indicating LTT-like behavior due to the interstitial (see text). **Bottom**: PDF of the same simulations, showing almost identical spectra for the 3 simulations. At roughly 5.2 Å there is a small modification where, once again, LTO+O and LTT simulations show similarities.

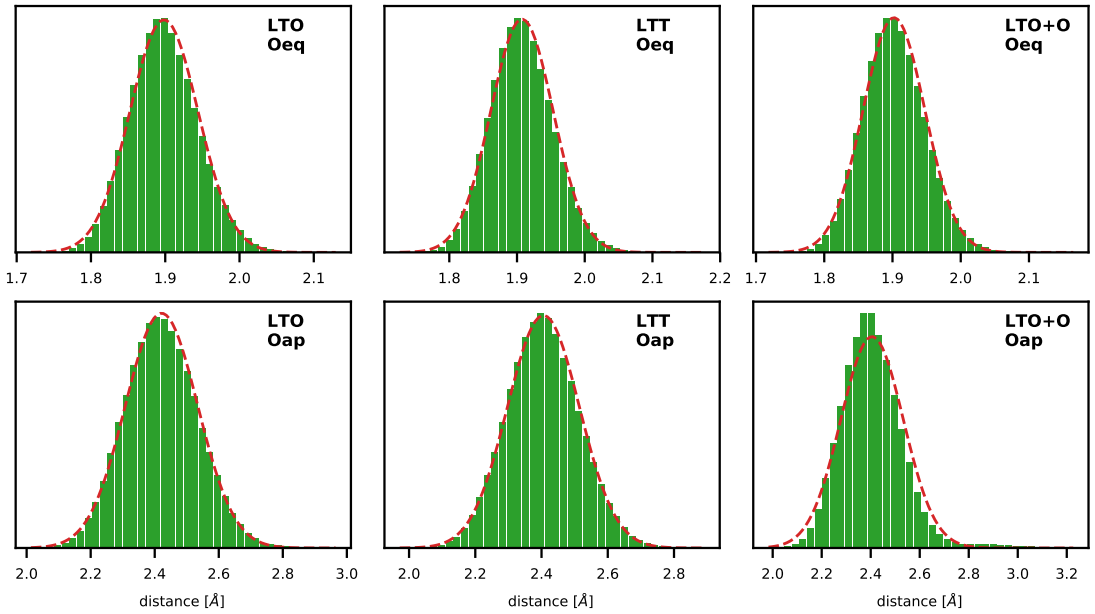

Figure 4.7: Distance histograms of Cu-O distances with respect to the equatorial oxygen (Oeq) and apical oxygen (Oap) in the three simulations we compared in Figure 4.6. The data was generated by recording all appropriate distances at every time step of the simulation. The y-axis is normalized to unity and the broken line is a Gaussian function with expected value and variance calculated from the data. The histograms are normalized to unity.

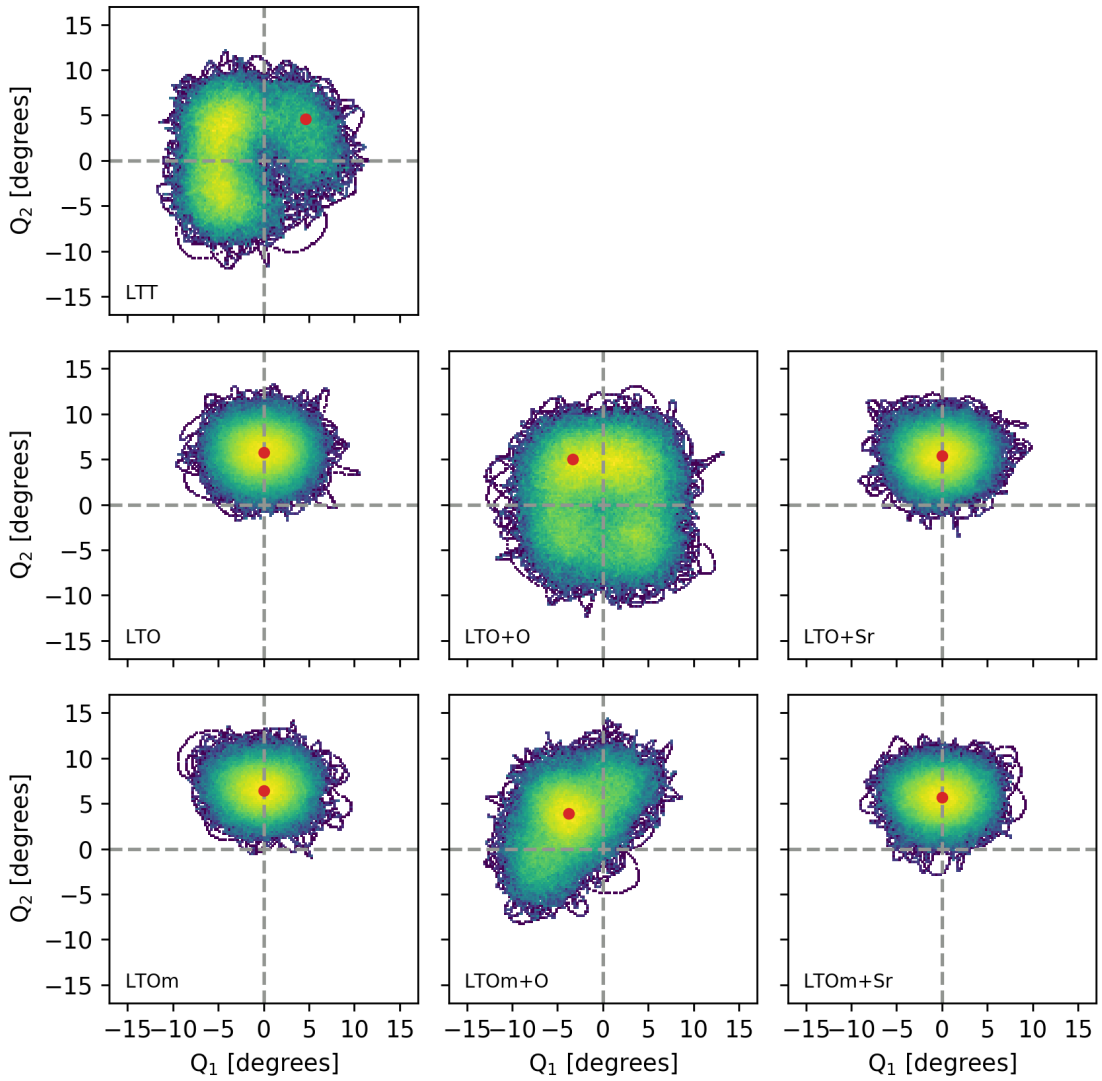

Figure 4.8: Tilt histograms of all performed molecular dynamics simulations. Plots are generated by obtaining the tilt as seen from apical oxygens and pairs of equatorial oxygens (as described in section 4.2) for each time step and then plotting a 2D histogram of the resulting data on a logarithmic scale. The red circle denotes the starting tilt. As discussed in the text, we distinguish between LTT-like tilts sitting on the diagonals of this figure and LTO-like tilts sitting along the main axes. The same symmetry operations are applied at each time step, such that transitions between symmetrically equivalent configurations is visible in this plot.

and parent compounds have tilts distributed around $(Q_1, Q_2) = (0, 5)$ which is the equilibrium LTO structure. We also notice that the LTT-like simulations (LTT, LTO+O, LTOm+O) are able to transition between the symmetrically equivalent tilt patterns, while the LTO-like simulations are 'stuck' in the initial configuration. This is an indication that LTT-like tilts have distinct dynamics compared to LTO-like tilts.

Finally, figures 4.9 investigates the dynamics of the placed interstitial in LTO+O by following the in-plane location of the interstitial by plotting a histogram of its location as well as a line depicting its time evolution at equally spaced points in time. Additionally, we plot the c-axis evolution with a 1d histogram. For contrast, Figure 4.10 shows the same plots for a 'normal' apical oxygen. Finally, Figure 4.11 shows the distribution of the apical oxygen near the interstitial, revealing a very similar distribution. These figures together show that the interstitial forms a 'binary system' with the closest apical giving rise to a very localized effect. At $T = 300\,\mathrm{K}$ we thus see no indication of diffusion. In some sense this is not surprising since diffusion is likely slow and not accessible within our relatively short 40 ps simulation times. In fact, the estimated 'annealing time' for $La_2CuO_{4+\delta}$ has been estimated to be one week at room temperature [89] (1 week divided

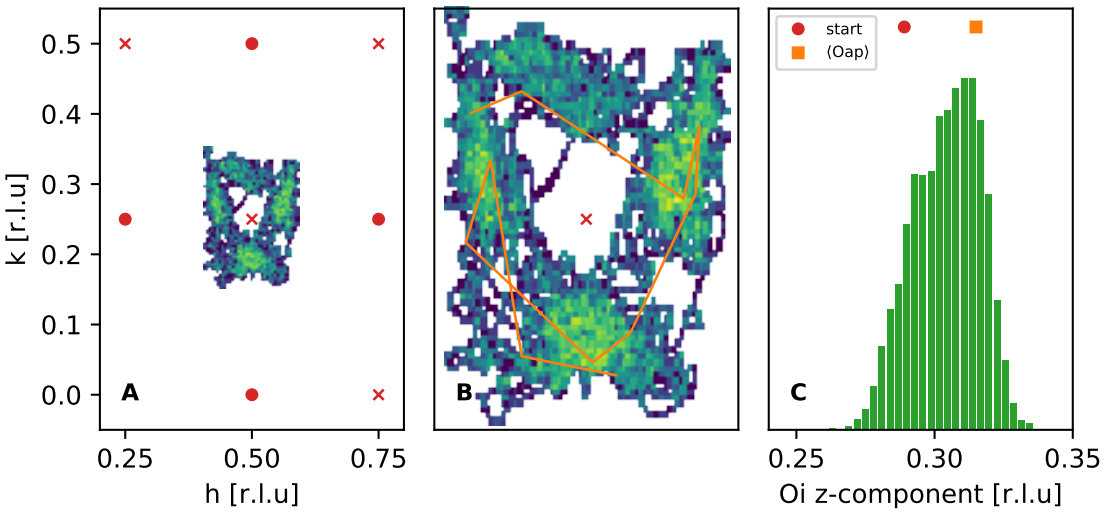

Figure 4.9: Distribution of the interstitial oxygen in LTO+O. **(A)**: In-plane distribution of the interstitial. Circles denote apical oxygens 'sticking up', while crosses denote apical oxygen 'hanging down' (similar to Figure 4.2). **(B)**: Zoomed-in version of **(A)** with the line marking the time-evolution of the interstitial sampled at isochronal points. **C**: c-coordinate distribution of the interstitial with the initial and average position marked in red and orange, respectively.

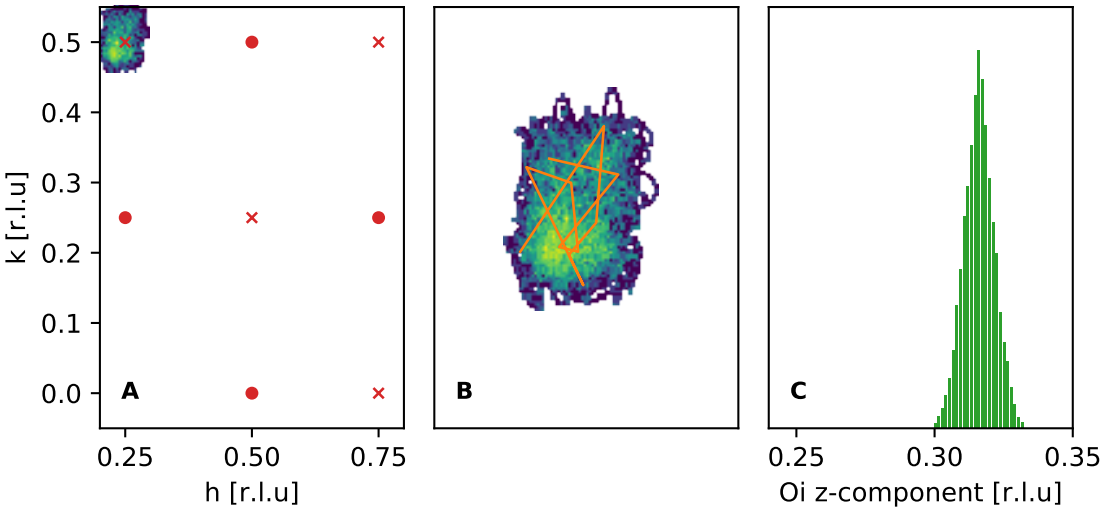

Figure 4.10: Distribution of a normal apical oxygen in LTO+O. **(A)**: In-plane distribution of the apical. Circles denote apical oxygens 'sticking up', while crosses denote apical oxygen 'hanging down' (similar to Figure 4.2). **(B)**: Zoomed-in version of **(A)** with the line marking the time-evolution of the interstitial sampled at isochronal points. **C**: c-coordinate distribution of the apical.

by 40 ps is roughly 10^16).

4.8 Summary

The main take-home message from chapter is the fact that interstitials seem to have a very subtle effect on structure but a more significant effect on dynamics. In particular, an observable such as PDF will se barely any difference between our simulations but high-quality DOS measurements should be able to see subtle differences due to dopants.

If we can obtain a reasonable validation of these simulations, the microscopic analysis reveals very clearly that oxygen interstitial phases move towards LTT-like tilt dynamics. Since the average structure of LCO+O at accessible temperatures is LTO, a possible explanation is that this tendency toward LTT-like tilts can result in the observed superstructures (and/or staging) [83, 88] if we had

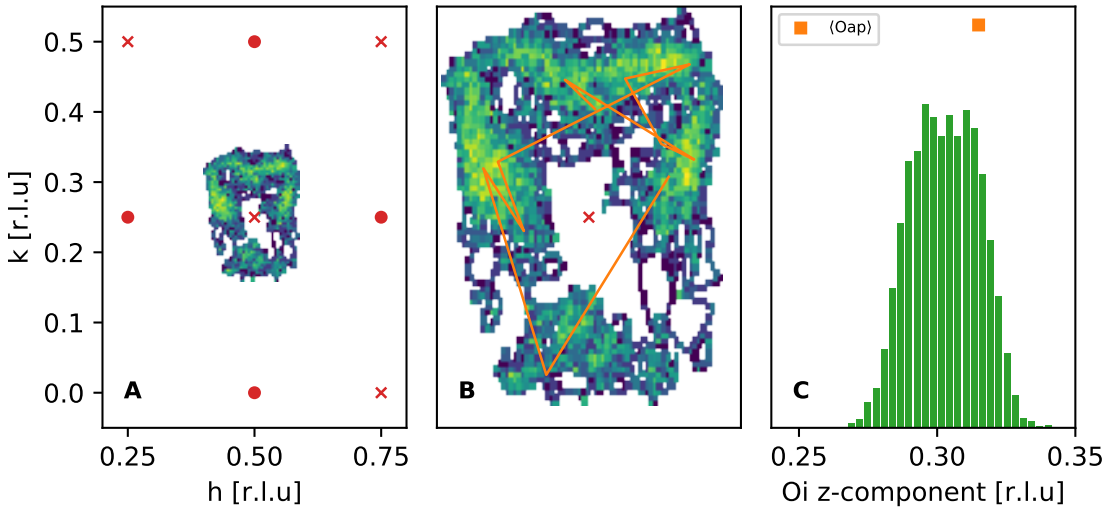

Figure 4.11: Distribution of an apical oxygen in LTO+O near the interstitial. **(A)**: In-plane distribution of the apical. Circles denote apical oxygens 'sticking up', while crosses denote apical oxygen 'hanging down' (similar to Figure 4.2). **(B)**: Zoomed-in version of **(A)** with the line marking the time-evolution of the interstitial sampled at isochronal points. **C**: *c*-coordinate distribution of the apical, with the average position marked in orange.

access to bigger simulation boxes and longer simulation times. It might be valuable to examine this more closely with real-space methods such as reverse monte-carlo (RMC) or by performing classical MD based on the results obtained in this chapter.

Before moving on to experimental comparisons, Figure 4.12 shows a comparison of phonon DOS as calculated from the previous chapter and the one obtained from molecular dynamics here. While there is a definite distinction between the spectra, it is important to realize that they are obtained by very different methods, while being based on the same computational background. In addition, molecular dynamics are not constrained by symmetry.

A direct comparison between molecular dynamics and phonon calculations should thus only be performed with extreme caution. For this reason, we mainly use the phonon calculations to identify the kinds of bands that correspond to certain features in the phonon DOS. When analyzing the role of dopants, simulations will all be done in the context of molecular dynamics (e.g. figure 4.6). In the experimental chapters I will leverage the phonon band structure calculations in context of triple-axis measurements of single crystals. Molecular dynamics simulations, on the other hand, will be used in the context of PDF and inelastic time-of-flight measurements of powdered samples.

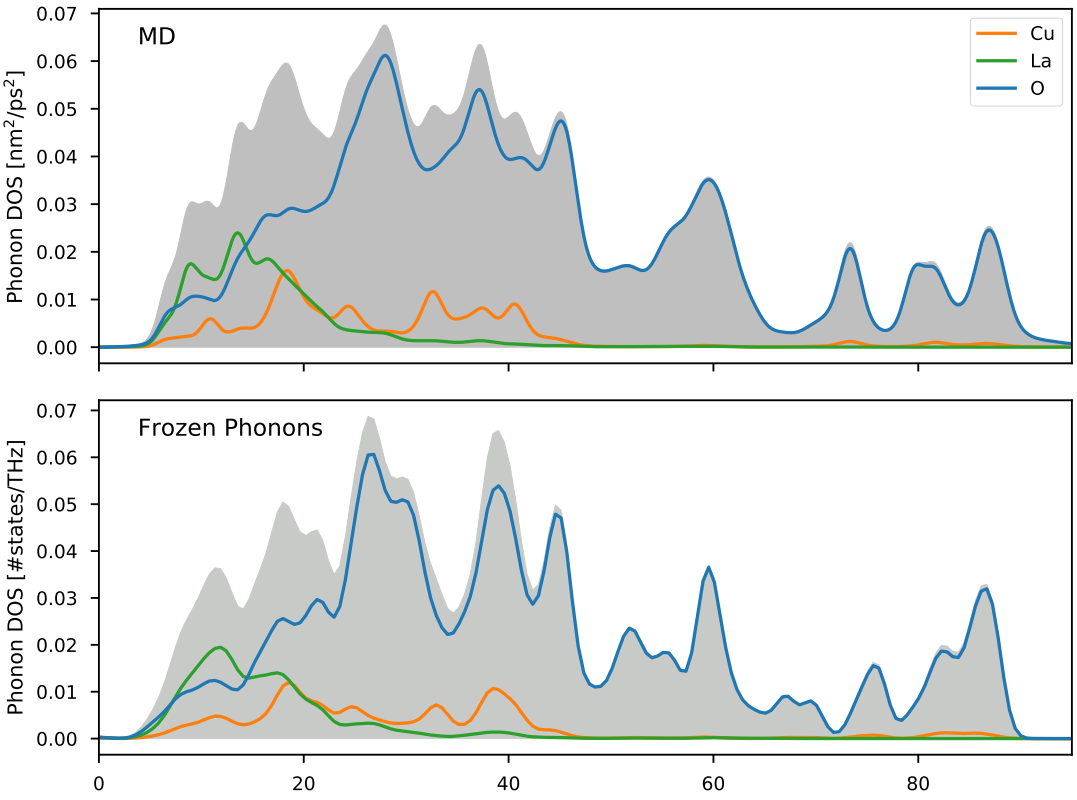

Figure 4.12: Comparison of neutron-weighted phonon density of states obtained from **top:** the velocity autocorrelation function of a molecular dynamics trajectory and **bottom:** by integration of phonon bands calculated using the direct method (see chapter 3). Both simulations are based on the low-temperature orthorhombic (LTO) structural phase.

Chapter 5

Local structure

In this chapter, we look at structural correlations in $La_{2-x}Sr_xCuO_{4+\delta}$ (LSCO+O) containing oxygen interstitials. As discussed in section 1.4, LSCO+O is known to form complex superstructures that shows up in single-crystal diffraction. To recap, 'staging' [84, 88] was discovered early on and appears unrelated to superconductivity. On the other hand, novel superstructures, known as 'Local Lattice Distortions' (LLD) and 'Oxygen Interstitials' (O_i), are suggested to have a connection with superconductivity [169]. In fact, it appears that these two orderings are anti-correlated in real space, forming 'puddles' on µm scale [85].

The data shown in this chapter is a collection of experiments performed on three different instruments: IN8 [106], ThALES and D4 [109] at Institut Laue-Langevin in Grenoble, France. In the first part, we explore some of the superstructures mentioned above in two single crystals of LSCO+O: $La_2CuO_{4+\delta}$ ($T_c = 43\,K$) and $La_{1.94}Sr_{0.06}CuO_{4+\delta}$ ($T_c = 37.5\,K$). In the second part, we perform a diffraction experiment on powders of LSCO+O with the purpose of looking at real space correlation through pair-distribution-function (PDF) analysis.

5.1 Superstructures in single crystals

While superstructures in LSCO+O have been extensively studied in the past, it is always useful to check if your samples comply with previous observations. The measurements shown here were mostly performed as a reference for some of the work shown in chapter 6, but I present it here since it has relevance for structural correlations and can help us with the analysis of the PDF data in the following section. Superstructures in LCO+O are generally observed at $Q_2 = (0, 0.21, 0.29)$ and $Q_3 = (0.09, 0.24, 0.50)$ [170] and should thus mainly be observable in the a-c (or equivalently b-c due to twinning) plane.

When using certain Triple-Axis spectrometers (IN8, IN20, ThALES) at the ILL, we have the option of a secondary spectrometer (everything after the sample) called FlatCone [171] where we can probe a large part of reciprocal space simultaneously. In particular, the FlatCone analyser system is built in such a way that you probe a large part of the scattering plane at a constant energy transfer $\hbar\omega$. In the following we are interested in structural correlations, so we are measuring at $\hbar\omega = 0$. In chapter 6 we will investigate finite energy transfers in detail.

Figure 5.1 shows the result of such a measurement of $La_2CuO_{4+\delta}$ on the thermal TAS IN8, performed in the a-b plane using the orthorhombic coordinate system (see section 1.4). The coverage of our measurement is such that we see the (200), (020) and (220) fundamental Bragg peaks. Some satellite peaks are visible at roughly $Q = (0.2, \pm 0.05, 0)$ as marked on the zoomed-in right-hand-side of the figure. Satellite peaks with zero l-component was previously observed by our group [172], but the nature of these peaks are currently unknown. We can, however, make the simple observation that this peak corresponds to a real-space structural periodicity with a characteristic length scale $d_1 \approx 26\,Å$ in the a-b plane.

Figure 5.2 shows the same type of measurement, but this time of $La_{1.94}Sr_{0.06}CuO_{4+\delta}$ on the cold triple-axis spectrometer ThALES. While similar features are visible, the satellites seen in figure 5.1 are smeared out, suggesting that the tiny amount of Sr in this sample causes a significant amount of disorder which shows up as diffuse satellites.

Finally, in figure 5.3, we show a measurement of $La_2CuO_{4+\delta}$ in the a-c plane also performed on ThALES. This measurement is entirely consistent with superstructures known from literature [170], and we can clearly index the peaks as $Q_2 = (0.19, 0, 0.31)$ (even showing 2nd and 3rd order reflections) and $Q_3 = (0.25, 0, 0.5)$. I note here that, because of twinning, we can not distinguish

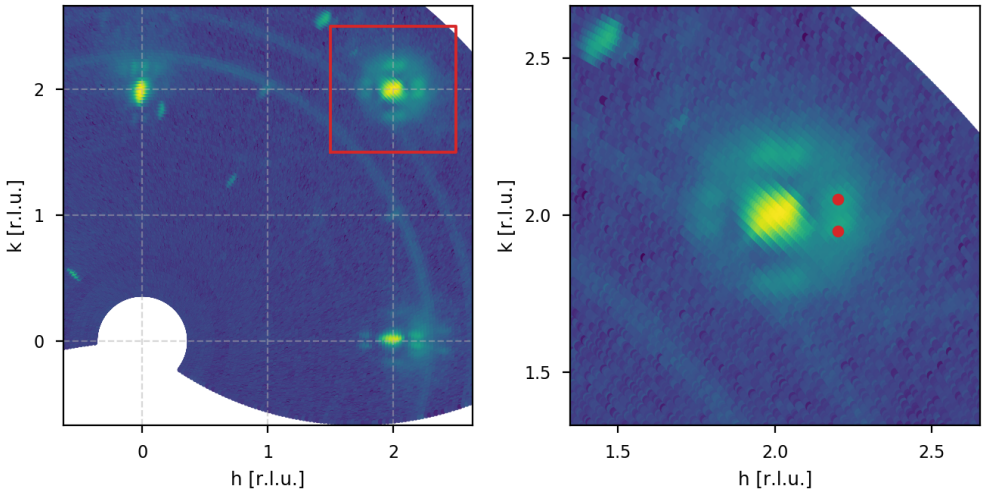

Figure 5.1: Reciprocal space map of single crystal $La_2CuO_{4+\delta}$, measured in the *a*-*b* plane with the unconventional Bmab orthorhombic coordinate system. **Left**: Full map, showing mainly the fundamental Bragg peaks. Circular arcs are powder lines from Al. **Right**: Zoomed-in view of the are marked in red. We notice satellite peaks around (220) at $Q = (0.2, \pm 0.05, 0)$ ($|Q| = 0.241\,\text{Å}^{-1}$).

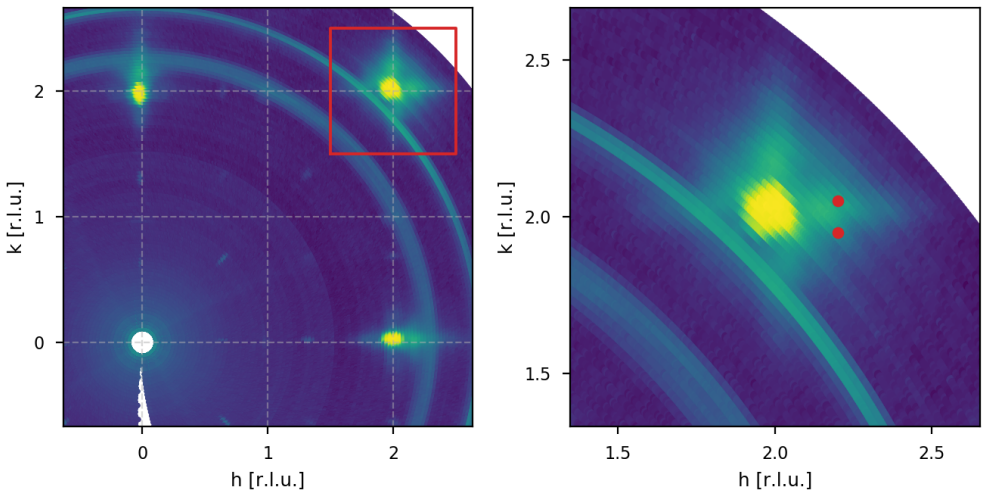

Figure 5.2: Reciprocal space map of single crystal $La_{1.94}Sr_{0.06}CuO_{4+\delta}$, measured in the *a*-*b* plane with the unconventional Bmab orthorhombic coordinate system. **Left**: Full map, showing mainly the fundamental Bragg peaks. Circular arcs are powder lines from Al. **Right**: Zoomed-in view of the are marked in red, showing diffuse scattering. The marks are at identical locations to figure 5.1 as a reference for comparison.

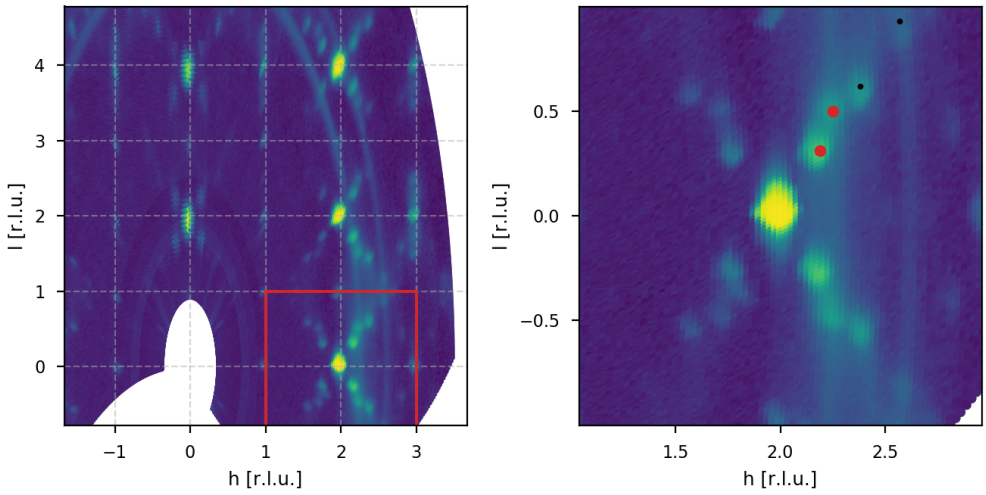

Figure 5.3: Reciprocal space map of single crystal $La_2CuO_{4+\delta}$, measured in the a-c plane with the unconventional Bmab orthorhombic coordinate system. **Left**: Full map, showing mainly the fundamental Bragg peaks. Circular arcs are powder lines from Al. **Right**: Zoomed-in view of the are marked in red. We notice satellite peaks around (002) at $Q_2 = (0.19, 0, 0.31)$ ($|Q_2| = 0.267\,\text{Å}^{-1}$) and $Q_3 = (0.25, 0, 0.5)$ ($|Q_3| = 0.378\,\text{Å}^{-1}$).

between a and b (see section 1.3). The length scales associated with these peaks are $d_2 \approx 24\,\text{Å}$ and $d_3 \approx 17\,\text{Å}$, respectively.

While none of these measurements are new (see [172, Chapter 10]), they help to confirm that the samples we use for spectroscopic measurements in chapters 6, 8, 9 are comparable to observations from literature. While constructing models for these superstructures is outside the scope of this thesis, they help identify some general length scales that might be relevant in a real-space model. Unfortunately, we also immediately notice that these correlations are inaccessible in our DFT MD simulations from chapter 4, where the maximal simulation box is a $2 \times 2 \times 1$ cell such that the only non-zero $\boldsymbol{Q}$ we can represent is $(\frac{1}{2}\frac{1}{2}0)$. These length scales, while rather large, are still accessible by PDF measurements as we shall see below.

5.2 Real-space correlation in powders

We now turn to experiments performed on a series of powdered samples, where we use an instrument well-suited for obtaining *real-space* correlations (see section 2.2, chapter 2) using the pair-distribution function (PDF). There are multiple purposes to this experiment.

First, we want to simply measure oxygen-doped $La_{2-x}Sr_xCuO_{4+\delta}$ with the PDF method. From single-crystal measurements, as we saw above, it is well known that the presence of oxygen interstitials result in intricate long-range ordering phenomena. This ordering is, to my knowledge, usually not detectable in standard powder diffraction experiments with a limited Q-range. As explained in chapter 2, the large Q-range provided by hot neutrons allows for PDF analysis well-suited for determining correlations at 5 Å to 30 Å.

Second, we wanted to see if oxygen ordering we could detect oxygen re-ordering caused by cooling rate. Single crystal measurements have shown that certain structural peaks can be removed by 'quenching', that is, rapid cooling from 300 K to 200 K in single crystal samples of $La_2CuO_{4+\delta}$ [85, 89].

Third, PDF measurements of $La_{2-x}Sr_xCuO_4$ have shown that the *distribution* of Cu-O distances is heavily influenced by doping [95]. In addition, the distribution is widest at optimal T_c as shown in figure 5.4. Since we are using a completely different dopant species, it is interesting to ask this same question for our samples. Finally, we want to compare high and low temperature phases to look for any peculiarities related to superconductivity or other low-temperature phases.

Samples

Three powdered samples were measured:

- **LCO**: La_2CuO_4 (2.7844 g, insulating)

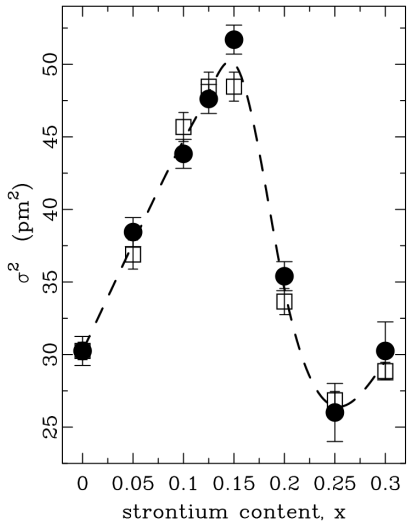

Figure 5.4: Relationship between strontium content x in $La_{2-x}Sr_xCuO_4$ (LSCO) and the width of the Cu-O equatorial bond distribution σ. For reference, LSCO is superconducting from $x = 0.05$ to $x = 0.25$ and reaches the largest T_c at $x = 0.15$. Figure from [95]

- **LCO+O**: $La_2CuO_{4.05}$ (0.7403 g, $T_c \approx 40$ K)
- **LSCO3+O**: $La_{1.97}Sr_{0.03}CuO_{4.05}$ (3.3612 g, $T_c \approx 40$ K)

Measurements were performed at the Disordered materials diffractometer D4 at Institut Laue-Langevin in Grenoble, France. Reduction and transformation of data was performed at the instrument with software specifically built for D4. All steps of the data treatment is saved, but we will mainly use the fully reduced and normalized datasets in both Q- and r-space. When comparing subtle differences between spectra (such as the same sample after different cooling procedures), we might construct a difference curve from the raw data since the background subtractions will cancel out.

Experiment

Table 5.1 contains a list of the measurements performed in the order which they were performed. The quenching was performed by submerging the 300 K sample in liquid nitrogen and then transferring to the 100 K cryostat. Annealing was performed by heating the cryostat to 350 K for about an hour which is known to disorder the oxygen [85]. The reason we performed the quenching before the annealing was due to time constraints. Each acquisition was approximately 2 hours.

In summary we have a total of three samples to compare at 300 K. For the oxygen-doped samples we can additionally look at the low temperature phase as well as the difference between 'quenched' and 'annealed' doping.

Results

We start with the second objective of figuring out if there is any difference due to cooling procedure. Figure 5.5 shows the difference between cooling procedures for the two oxygen-doped samples. In general there are no systematic differences apart from the slight decline of the difference curve for the LCO+O sample. This is likely due to a small amount of hydrogen in the cryostat as a consequence of the quenching procedure. The preliminary conclusion is that there is no difference between quenched and annealed measurements to a high degree of certainty. This is somewhat surprising since it is well known that certain structural peaks can be removed from quenching in single crystals [85]. We cannot conclude if our result is due to the sample being a powder or due to rotational averaging. Since we detect no difference in the spectra, we can use the annealed 15 K data and initial 300 K data for the remaining analysis.

In Figure 5.6 we compare the three samples at 300 K in both real and reciprocal space. While the differences are quite small, the difference curves (green) seem to be larger between parent/oxygenated compounds compared to the two oxygenated compounds. This is consistent with a picture

index	sample	temperature	state
0	LCO	300	initial
1	LCO+O	300	initial
2	LCO+O	100	quenched
3	LCO+O	15	quenched
4	LCO+O	300	quenched
5	LCO+O	350	annealing
6	LCO+O	300	annealed
7	LCO+O	100	annealed
8	LCO+O	15	annealed
9	LCO+O	300	annealed
10	LSCO3+O	300	initial
11	LSCO3+O	100	quenched
12	LSCO3+O	15	quenched
13	LSCO3+O	350	annealing
14	LSCO3+O	15	annealed

Table 5.1: List of measurements performed at D4 in chronological order. 'Quenched' refers to the rapid cooling as described in the text, and annealing refers to keeping the sample at 350 K for roughly 30 minutes.

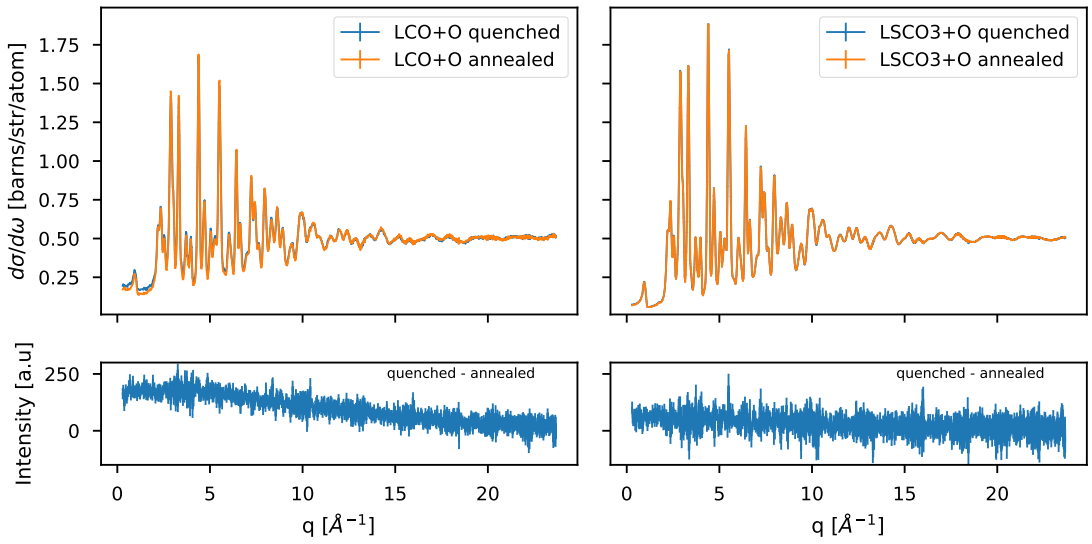

Figure 5.5: Difference between quenched and annealed cooling procedures for LCO+O and LSCO3+O samples. The topmost plots are comparisons of the reduced and corrected $\mathrm{d}\sigma/\mathrm{d}\omega$ in absolute units, while the difference curves are extracted from the raw $\boldsymbol{q}$ data.

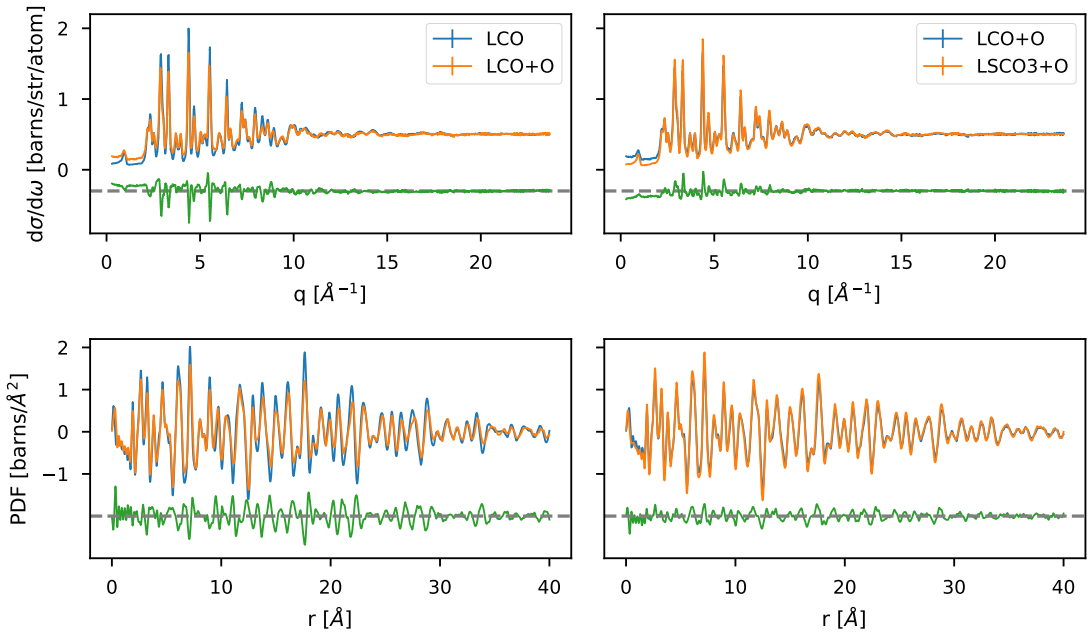

Figure 5.6: Comparison of the three different samples at 300 K in both real and reciprocal space. On the **left** we compare LCO with LCO+O in order to see if there is an effect of oxygen. On the **right** we look at LCO+O versus LSCO3+O to have a similar comparison between two *different* oxygen-doped samples.

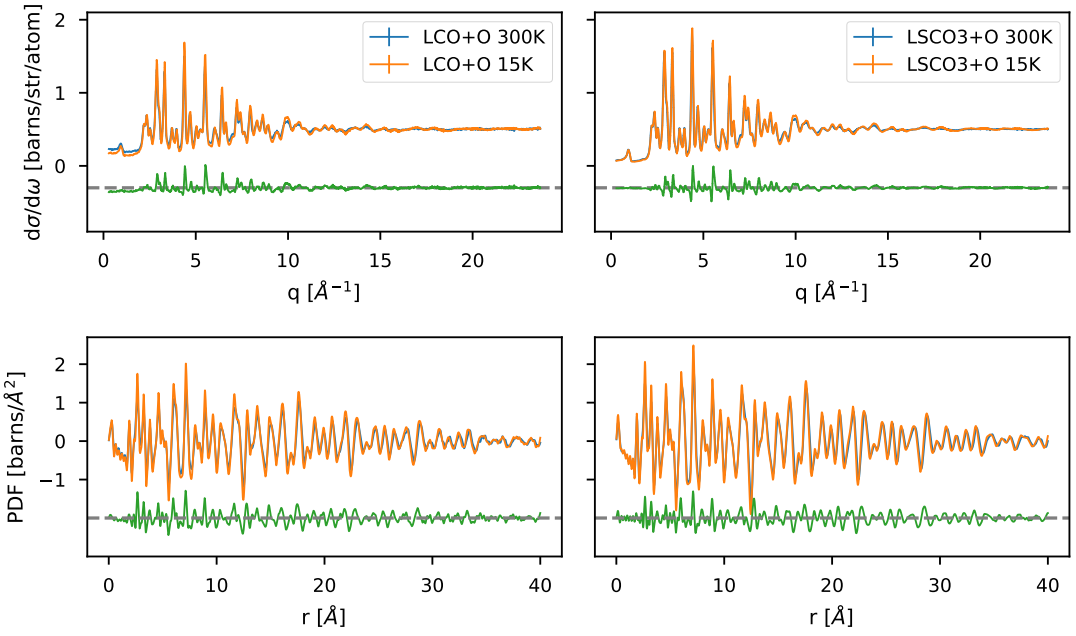

Figure 5.7: Temperature dependence of 300 K and 15 K for LCO+O and LSCO3+O in both real and reciprocal space.

where oxygen distorts the lattice in a meaningful way, while the effect of a small amount of strontium is negligible. Figure 5.7 shows the high- and low-temperature data for the two oxygen-doped samples. At first glance there seems to be nothing out of the ordinary, peaks are shifting slightly due to thermal expansion (this is particularly easy to spot in the real-space data).

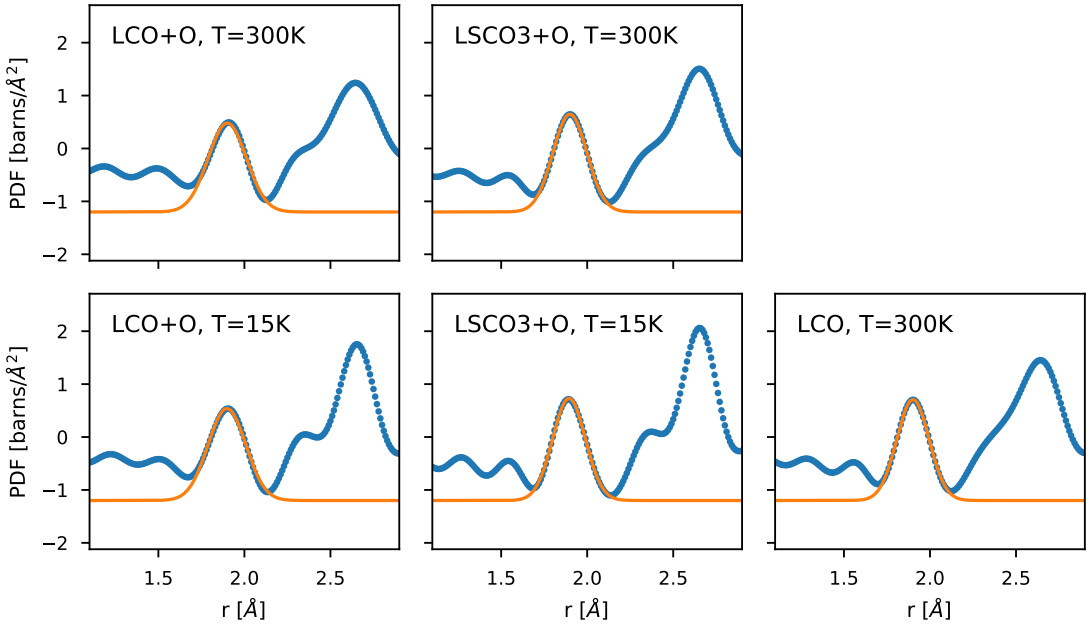

Figure 5.8: Cu-O distance Gaussian fits. For each of the five temperature/sample combinations (figure text), the short range PDF is shown along with a Gaussian fit of the first peak. In order to compare between the fits, the constant background has been fixed to $-1.2\,\mathrm{b\,Å^{-2}}$

Sample	Temperature [K]	Cu-O mean distance	Cu-O sigma
LCO	300	1.9010 ± 0.0003	0.0941 ± 0.0003
LCO+O	300	1.9005 ± 0.0012	0.1112 ± 0.0014
LSCO3+O	300	1.8995 ± 0.0003	0.0989 ± 0.0004
LCO+O	15	1.8983 ± 0.0009	0.1096 ± 0.0010
LSCO3+O	15	1.8944 ± 0.0003	0.0951 ± 0.0004

Table 5.2: Cu-O distances in all samples at all available temperatures as extracted from the fits in figure 5.8.

Analysis

Without performing detailed modelling, we can take a look at the first peak in the real-space data which corresponds to the Cu-O in-plane bond. This bond-length is suspected to be important for superconductivity by controlling the Coulomb interaction (the Hubbard-U) [94]. Previously, as mentioned above, measurements on $La_{2-x}Sr_xCuO_4$ have shown that the width of the Cu-O bond-length distribution is largest at optimal doping $x = 0.15$ and qualitatively tracks the superconducting dome [95]. We fit the first peak of all relevant datasets to a single Gaussian as shown in Figure 5.8 and report the fitting parameters in Table 5.2.

Comparing to $La_{2-x}Sr_xCuO_4$, our samples have roughly the same peak position at $r = 1.9$ Å. At 300 K LCO has a smaller width compared to LCO+O and LSCO3+O. At 15 K the widths are slightly smaller as one would expect from the reduced temperatures. Our measurements are thus consistent with the observations of [95], that the Cu-O bond-length tracks T_c , but with an entirely different dopant species. Interestingly, the sample with a small amount of Sr has a slightly smaller σ, indicating that the addition of Sr restricts the Cu-O bond lengths.

In figure 5.9, we take a closer look at the PDF from the three samples obtained at 300 K. As we mentioned earlier, any differences between the plots are quite subtle, but our initial analysis that there is a 'larger' difference between LCO and LCO+O when compared to the difference between LCO+O and LSCO3+O seems to be correct. Marked in figure 5.9 are regions where there is a qualitative difference between the curves. That is, we don't just see sharpening/broadening, but the shape of the peaks are noticeably different. In addition, I marked the possible correlation lengths identified in the previous section.

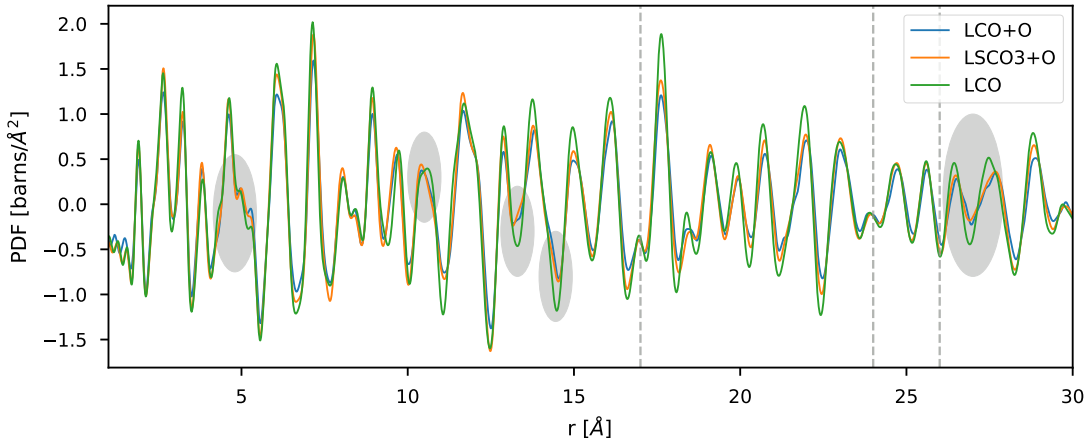

Figure 5.9: PDF at 300 K for the three samples studied here across the accessible range. Differences between stoichiometric and oxygen-doped samples are highlighted with grey circles. Grey vertical lines mark the correlation lengths identified in section 5.1.

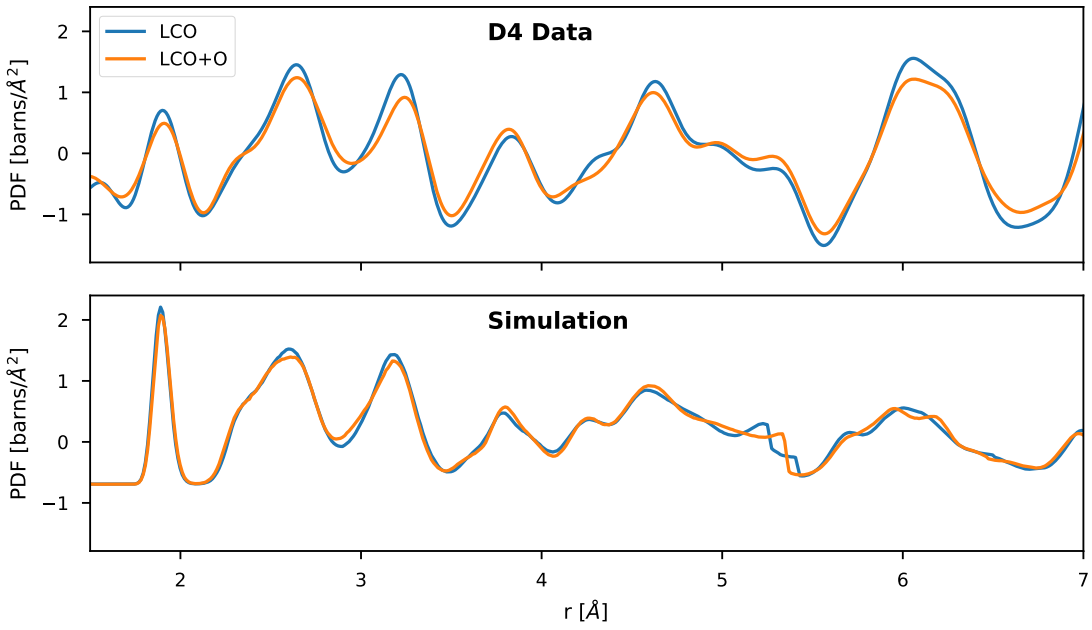

Figure 5.10: Comparison of short-range PDF between experiment and molecular dynamics simulation. **Top:** Data for LCO and LCO+O at 300 K (left side of figure 5.6 shows the full range). **Bottom:** PDF obtained from molecular dynamics trajectory from La_2CuO_4 (LCO) and $La_2CuO_{4.0625}$ (LCO+O), at 300 K (see chapter 4).

Unfortunately, there seems to be no real signature of a change due to interstitial that is related to the superstructures identified earlier. In addition, even though there are differences where we can clearly separate the oxygen-doped samples from La_2CuO_4, the changes that we do see are barely noticeable.

Finally, in figure 5.10 I compare LCO and LCO+O at 300 K with molecular dynamics simulations in the LTO phase also at 300 K on an absolute scale. In general, we seem to have a quite good agreement between experiment and simulation, especially with regards to the short range correlations around 3 Å. Noticeably, the shortest Cu-O bond is significantly sharper in the simulation, so perhaps we are not accurately describing short range forces. At higher r, the simulation PDF naturally dies out due to limited system size.

5.3 Summary

In this chapter, we performed experiments with the intention of gaining a further understanding of the various superstructures present in LSCO+O. Through single-crystal measurements we independently confirmed the existence of the superstructures reported by various groups [170] and additionally observed in-plane satellites only seen by us [172].

We performed high-quality PDF measurements of 3 powdered samples with and without interstitial oxygen, confirming subtle differences due to interstitials. A direct connection to the superstructures observed in single crystals could, however, not be made. If this is a consequence of superstructures not being visible in the rotationally averaged diffraction pattern or if the powders are different with regards to superstructure signatures, is hard to say. Our measurements appears consistent with the observation of Božin et al. [95] and have an increased distribution of in-plane Cu-O distances in superconducting samples, slightly more so in LCO+O compared to LSCO3+O.

Finally, the MD simulations performed in chapter 4 are consistent with the shape of the measured PDF, especially in the 2 Å to 4 Å range. In order to properly describe the differences we see at higher correlation lengths, some real space modelling and/or reverse monte-carlo fitting of the PDF would be required to properly analyse the data. The work performed in this chapter could thus be used as a first step for constructing real-space models of non-stoichiometric oxides.

Chapter 6

Low Energy Lattice Dynamics

In this chapter we investigate the lattice dynamics of $La_{1.94}Sr_{0.06}CuO_{4+\delta}$ as observed by neutron scattering with the intention of comparing with simulations performed in chapter 3. Similar to the elastic reciprocal space maps done with the FlatCone analyser in the previous chapter, we now look at the same maps with finite energy transfers. These are compared to experiment by constructing neutron-weighted band structures and 2D (Q_x, Q_y) maps from simulation data.

We also look at soft phonons related to the LTO-LTT transition in $La_2CuO_{4+\delta}$. These phonons have shown interesting behavior in $La_{2-x}Sr_xCuO_4$, and we are interested in how this picture changes when working with oxygen-doped samples. Finally, we look at the superstructures discussed in the previous chapter and search for possibly related dynamics.

6.1 Acoustic Phonons and Simulation Validation

We start by considering measurements performed on IN8 at ILL, using the FlatCone secondary spectrometer as described in section 5.1. By measuring a large region of $\boldsymbol{Q}$ while changing the energy transfer $\hbar\omega$, we can build up a three-dimensional data-set of low energy phonon dispersions. The sample is a single crystal $La_{1.94}Sr_{0.06}CuO_{4+\delta}$ ($T_c = 37.5\,K$) aligned in the a-b plane. The elastic signal was shown in the previous chapter, figure 5.2. The spectroscopic measurements were performed from 1 meV to 16 meV in steps of 1 meV.

Figure 6.1 shows representative data at 3 meV, 9 meV and 12 meV in the top row. The bottom row shows simulations results of La_2CuO_4 in the Low-Temperature Orthorhombic structural phase (see figure 3.17 for the phonon band structure along high-symmetry lines). As shown in section 2.4, phonon band structure calculations result in a data structure where we can obtain phonon eigenvectors at arbitrary reciprocal wave vectors $\boldsymbol{Q}$. By combining this fact with the coherent one-phonon dynamic structure factor (equation (2.5)), we can evaluate the neutron intensity at any point in reciprocal space due to phonon scattering.

Technically, the output from a phonon calculation gives you the band structure as a list of energies, corresponding to the number of bands, at every value of $\boldsymbol{Q}$. This means that they are δ-functions in 4-dimensional $(\boldsymbol{Q}, \hbar\omega)$ space and we need to give them a finite width in order to produce plots as in figure 6.1. This is done by evaluating the phonons as Gaussian along the energy-axis with a width σ. Details about this implementation and the production of 2-dimensional phonon colorplots are described in appendix A.

Now, as we can see in figure 6.1, there is a nice qualitative correspondence between theory and experiment. I emphasize here that the experimental and simulation data is shown without any scaling in energy. In order to quantify our experimental data, one dimensional spectra have been extracted by interpolation along the annotated directions in figure 6.1 using the `nplot` software [173]. Transverse polarization of phonon modes are annotated by 'T', while longitudinal motions are annotated with 'L'. Due to the polarization factor $\boldsymbol{Q}\cdot\boldsymbol{e}$ (see equation (2.5)), different directions in $\boldsymbol{Q}$ distinguish different polarization components. At the fundamental Bragg peak position (400), the steeper acoustic phonon modes with longitudinal polarization along the [100] direction are visible as inner shell, while the outer acoustic modes along [010] have transverse character (figure 6.1 top middle). At (220) essentially longitudinal acoustic modes (parallel to [110]) and transverse longitudinal modes (parallel to [1-10]) are visible. In addition, we noticed a small amount of spectral weight at 7 meV to 10 meV at the (310) position.

Figures 6.2 and 6.3 shows the peak positions as a function of energy along the transverse and longitudinal directions, respectively along with a naive fit to the shape of a monoatomic phonon dispersion [6]. Details about the peak finding feature and plots of the data is shown in appendix

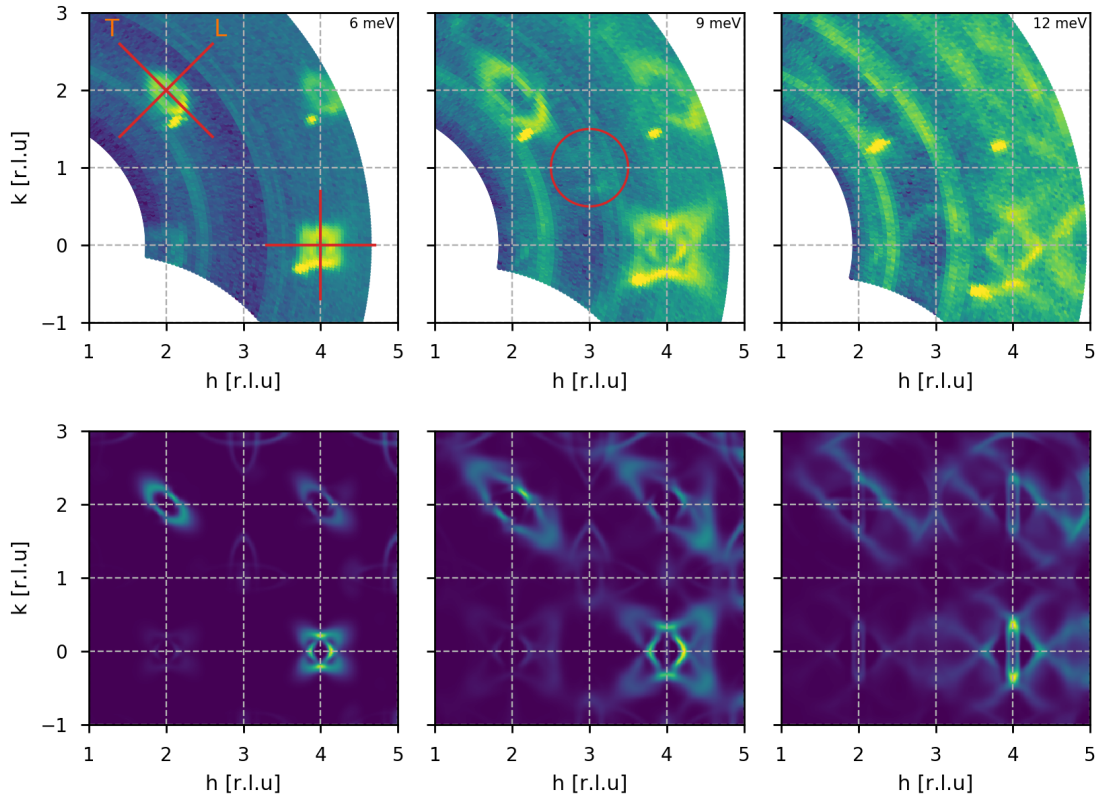

Figure 6.1: FlatCone data of $La_2CuO_{4+\delta}$ in the a-b plane at three energies and simulation data of La_2CuO_4 at the same energies. **Top**: Raw data at 6 meV, 9 meV and 12 meV annotated with cut directions in the leftmost figure. In addition, the middle figure highlights a small amount of spectral weight observed in a narrow range of energies near (310). **Bottom**: Simulation data at energies corresponding to the top row. Details about the simulation data is given in the text.

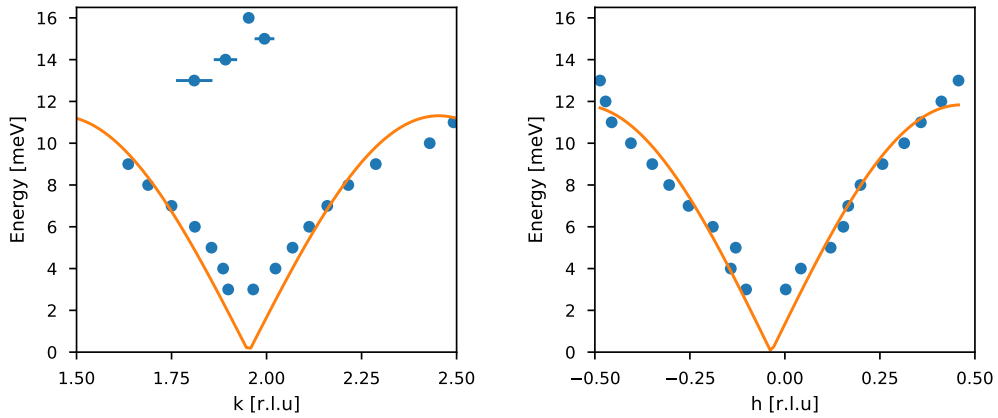

Figure 6.2: transverse flatcone dispersions at 220 (left) and 400 (right). Fit is a simple acoustic phonon dispersion for monoatomic systems: $\omega = \sqrt{4C/M}|\sin(\pi(q-q_0))|$, where M is the mass C is the spring constant and q_0 is an offset to adjust for possible misalignment of the sample. q is in reciprocal lattice units.

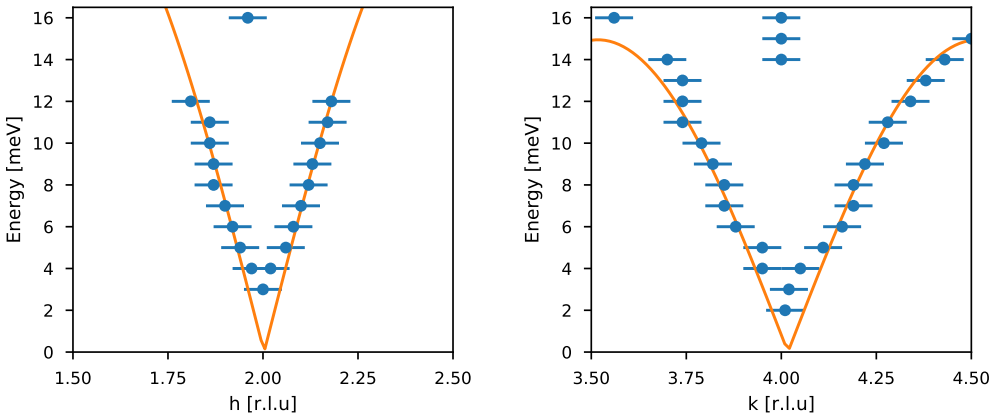

Figure 6.3: Longitudinal flatcone dispersions at 220 (left) and 400 (right). Fit is a simple acoustic phonon dispersion for monoatomic systems: $\omega = \sqrt{4C/M}|\sin(\pi(q-q_0))|$, where M is the mass C is the spring constant and q_0 is an offset to adjust for possible misalignment of the sample. q is in reciprocal lattice units.

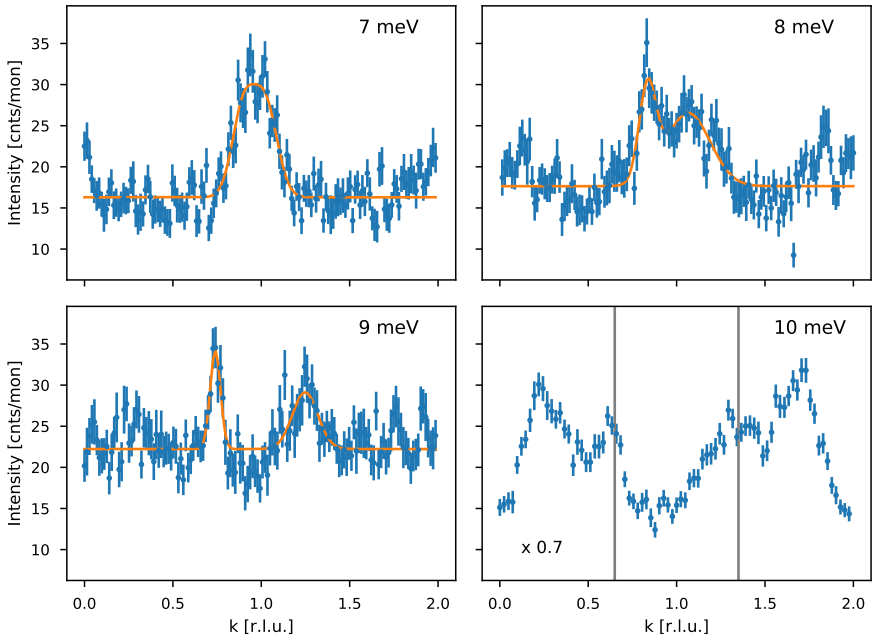

Figure 6.4: 310T flatcone raw data. The dispersion appears quite flat: $\delta_k = \{0.06, 0.12, 0.25, 0.35\}$ for the 4 energies shown, with the last one (10 meV) being a very rough estimate from visual inspection. The direction is (400)-(220).

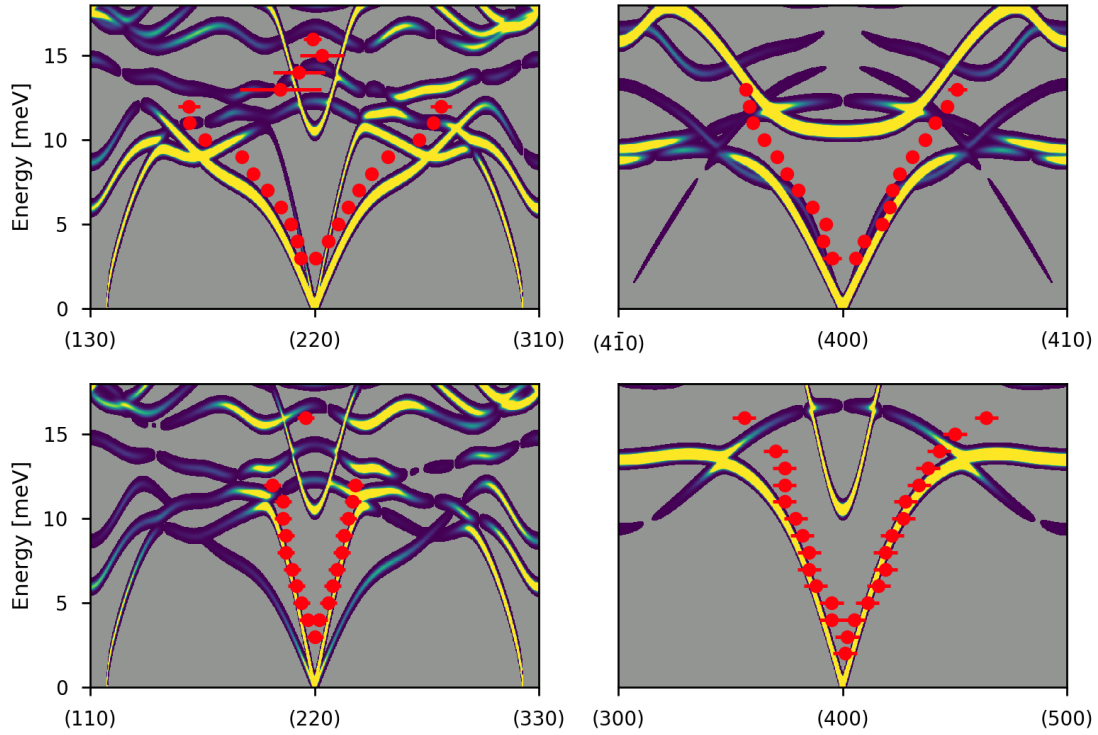

Figure 6.5: Data obtained from FlatCone measurements $La_2CuO_{4+\delta}$ in the a-b plane ar shown in red (figure 6.2 tranverse in top row) and figure 6.3longitudinal in bottom row) superimposed on the neutron-weighted simulation data of La_2CuO_4 in the orthorhombic phase. The simulation data is given a small Gaussian width in order to emphasize what a neutron experiment should look like according to simulations.

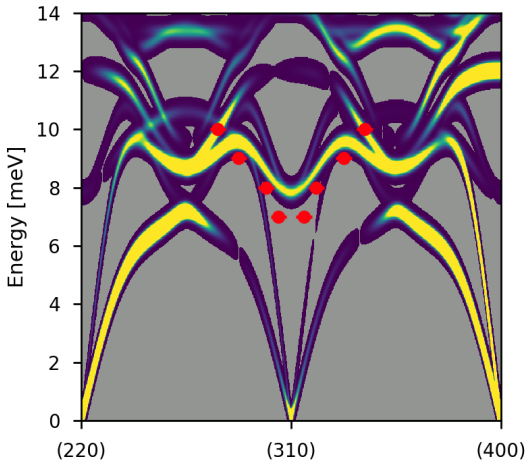

Figure 6.6: FlatCone data of the shallow features observed in the transverse direction near (310) (figure 6.4), superimposed on neutron-weighted simulation data in the same direction.

B. We have the expected results that longitudinal acoustic phonons are steeper since they are essentially bond stretching motions, where transverse phonons resembles a shear motion with a flatter dispersion. Finally, in Figure 6.4 we show the raw data for the four spectra where we see a signature of excitations around (310).

Once again, we can use this extracted dispersion to compare with our simulation data. In figure 6.5, we see the data from figures 6.2 and 6.3 together with a simulated neutron weighted band structure plot along the same directions. Once again, the simulations have been broadened along the energy axis in order to emphasize the neutron cross-section. This also means that there are certain bands not visible in these plots because their intensity vanishes (see figure 2.11 for a visual

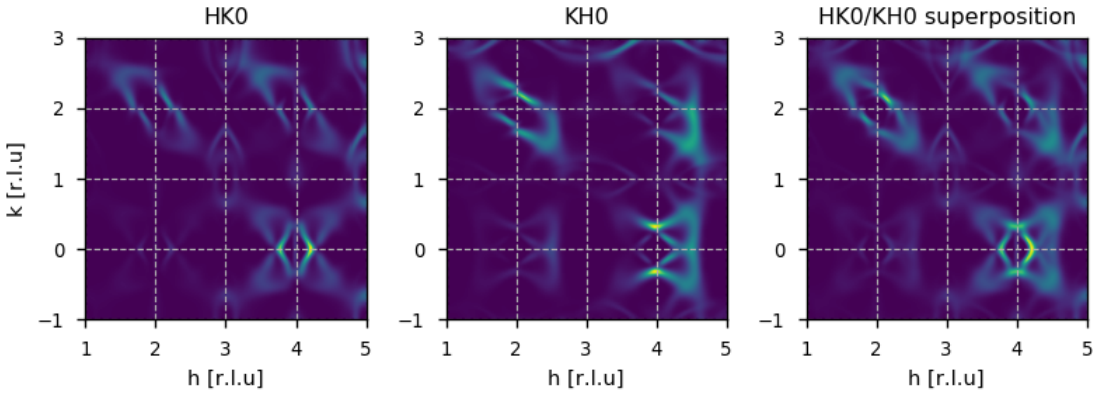

Figure 6.7: Simulation data in the a-b plane of La_2CuO_4 at 9 meV in the low-temperature orthorhombic phase. The first two images show the effect of exchanging the a and b directions when generating the plot and the last shows the superposition of the two.

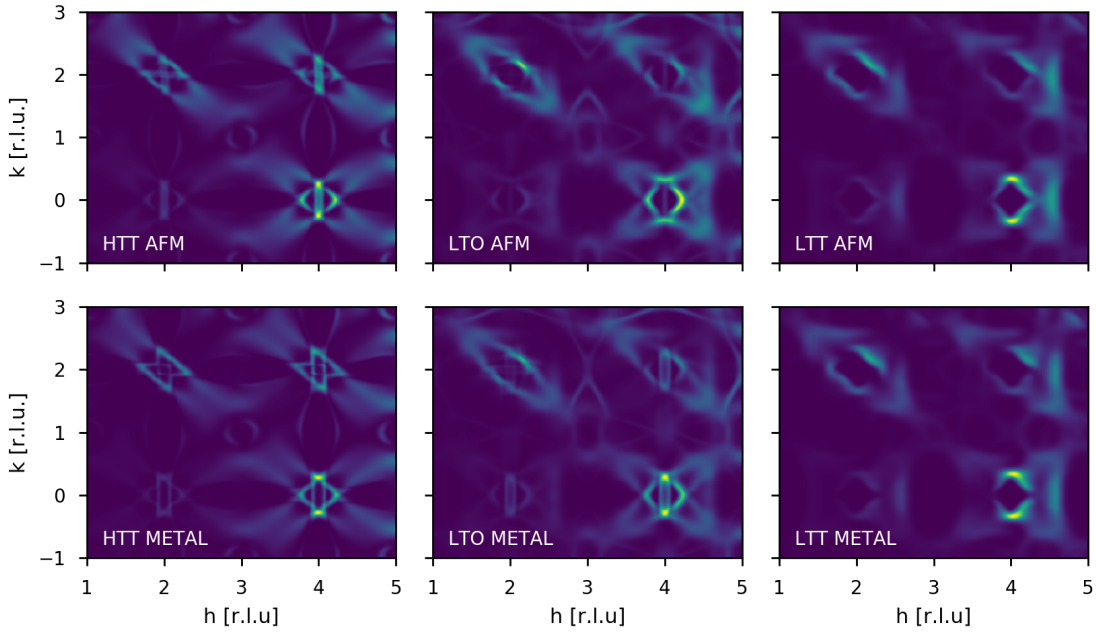

Figure 6.8: Simulation data in the a-b plane at 9 meV from the six different phonon calculations performed in chapter 3.

explanation of this point). As indicated by the two dimensional color plot in figure 6.1, we have excellent agreement between measurement and simulation. I mention here that that it was only possible to fit the steeply dispersive acoustic phonons as shown in appendix B. Since FlatCone measurements are constant energy scans, flat modes are difficult to extract unambiguously. Where fitting was not possible, the peaks were assigned from visual inspection.

As the attentive reader might have noticed, we performed simulations of several different versions of La_2CuO_4 in chapter 3. The comparison shown here is the low-temperature orthorhombic structural phase in the insulating state with static magnetism. This was chosen using through a visual inspection of the different simulations. The remaining five plots are shown in appendix B.

In addition, the bottom row of figure 6.1 was generated taking twinning (see section 1.3) into account. Since a and b directions in the low-temperature orthorhombic phase are close in length, twinning essentially makes the two directions indistinguishable. To show how this affects the dynamics, figure 6.7 gives a visual indication of this superposition at 9 meV. While the HK0/KH0 planes have a similar overall shape, it becomes clear that the superposition has the strongest resemblance to our data.

For the sake of completeness, figure 6.8 shows all six simulations from chapter 3 at 9 meV. Once again, it seems likely that the 'LTO AFM' simulation is the best representation of the

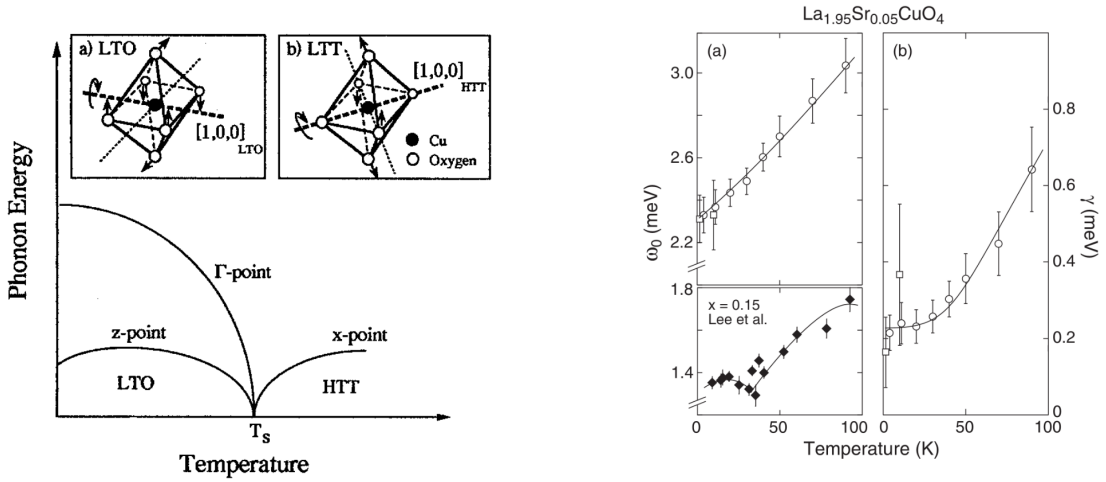

Figure 6.9: Soft phonons in $La_{2-x}Sr_xCuO_4$. **Left:** Schematic of the phonons related to structural phase transitions, with HTT being high-temperature tetragonal, LTO low-temperature orthorhombic and LTT low-temperature tetragonal. Decreasing the temperature across the structural phase transition temperature T_s, the X-point phonon becomes soft and finally splits into Γ and Z-point phonon branches. If the Z-point phonon softens completely, the LTT phase is realized. **Right**: Measurements of the Z-point phonon in $La_{1.95}Sr_{0.05}CuO_4$ and $La_{1.85}Sr_{0.15}CuO_4$, showing a softening of this mode where the phonon energy ω_0 decreases with decreasing temperature. This softening is associated with a sharpening of the linewidth γ.

sample chosen for this experiment, $La_{1.94}Sr_{0.06}CuO_{4+\delta}$.

While they may not be groundbreaking in terms of scientific impact, I believe that these comparisons confidently shows that our simulations can be trusted to some degree with regards to lattice dynamics. In addition, I hope that the tools (appendix A) developed to generate these plots can be helpful for neutron scatterers in the future. To end this section, I direct the reader to a video at `https://youtu.be/LC-qV3CjqBM` which illustrates the dispersive features of the 2D colorplots in this section by moving through the energy axis which may be instructive for the reader to predict what may be observed at constant neutron energy measurements besides the ones explicitly plotted in this thesis.

6.2 Structural instabilities

In this section, we investigate a peculiarity with regards to the low-temperature orthorhombic phase in $La_{2-x}Sr_xCuO_4$. In the mid 2000s, it was discovered that this material is unstable towards a low-temperature tetragonal phase. This shows up as the softening of a phonon at (104) and the temperature-dependence has been measured in optimally doped $La_{1.85}Sr_{0.15}CuO_4$ and insulating $La_{1.95}Sr_{0.05}CuO_4$, summarized in figure 6.9. Back then, it was suggested that the softening abruptly stops at T_c for the optimally doped sample, essentially preventing the tetragonal phase from emerging – or at least stopping the instability in its tracks.

These ideas are consistent with the idea that lanthanum cuprates near $x = \frac{1}{8}$ have their T_c suppressed due to the proximity of this tetragonal phase. This is particularly apparent in $La_{2-x}Ba_xCuO_4$ where the tetragonal phase appears and T_c drops to a few Kelvin [35].

We set out to do a similar experiment on the cold Triple-Axis ThALES at ILL. The sample is a single crystal $La_2CuO_{4+\delta}$ aligned in the a-c plane. Measurements were constant-$\boldsymbol{Q}$ scans, and the temperature dependence is shown in figure 6.10 and the summary of the fits are shown in 6.11.

We immediately notice that our experiment stands out when compared to $La_{2-x}Sr_xCuO_4$. First, the energy dependence resembles that of $La_{1.85}Sr_{0.15}CuO_4$, but shifted up by roughly 1 meV and our linewidth increases with decreasing temperature. In this case, the Sr-doped samples are unusual, since soft phonons is usually accompanied by an increased linewidth. I stress here that we performed these experiments with an extremely tight energy resolution (roughly 0.1 meV, see figure 6.12), so the broadening is definitely unique to this system.

I foresee two scenarios causing this broadening. Either it is the expected broadening that is typically observed with soft phonons or it is caused by a splitting or distribution of modes at this

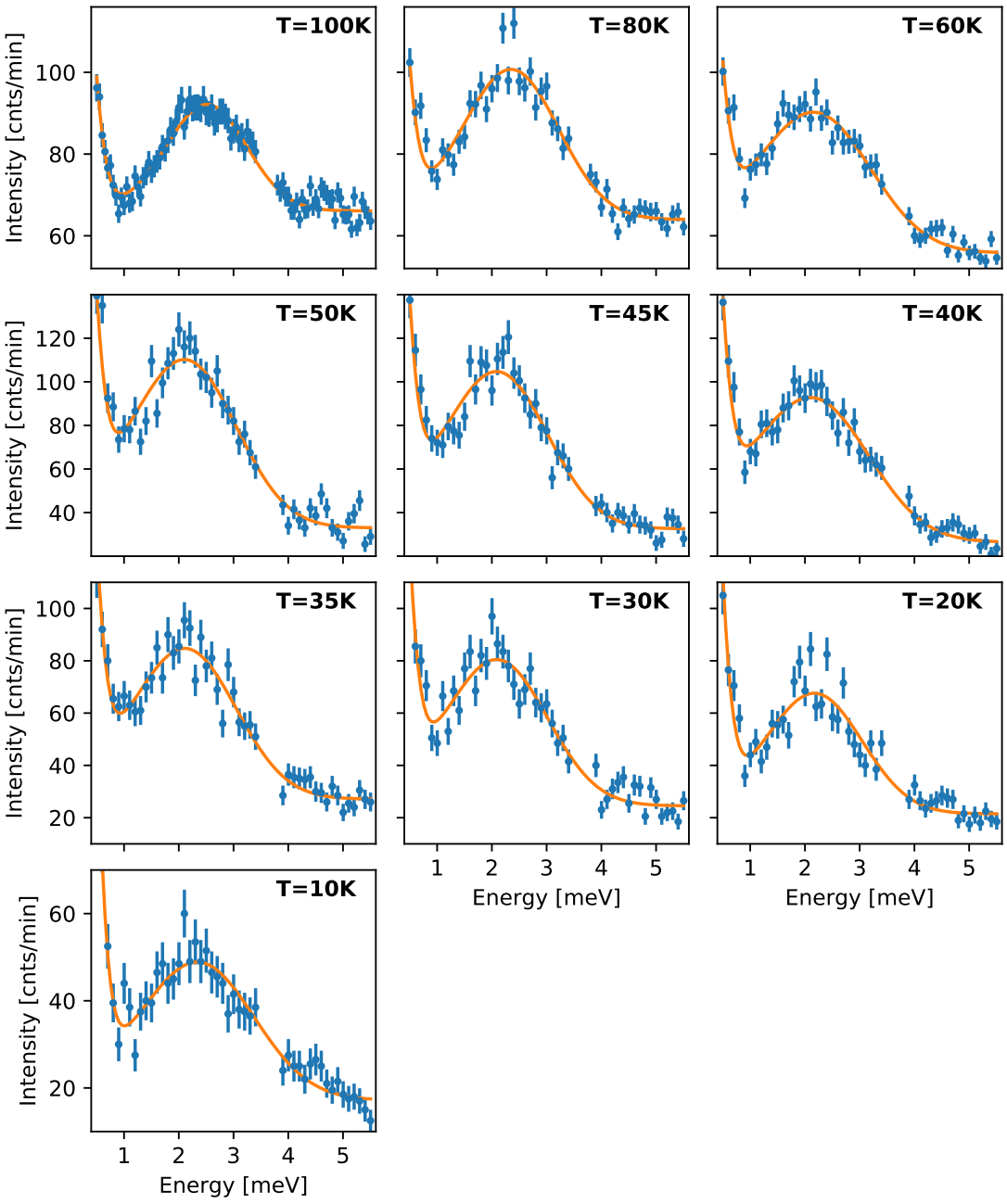

Figure 6.10: Measurements of the Z-point phonon in $La_2CuO_{4+\delta}$. At each temperature an energy scan from 0.5 meV to 5.5 meV is performed, clearly showing the phonon at ≈ 2.5 meV. The strong Bragg tail comes from the fact that we are measuring (104) and (014) simultaneously as a result of twinning. (104) is Z in the orthorhombic phase, while (014) is Γ. The data is fitted to a sum of two Gaussian functions, describing the Bragg tail and phonon plus a constant background. The use of a Gasussian rather than Lorentzian for the phonon is phenological, since it described the data much better.

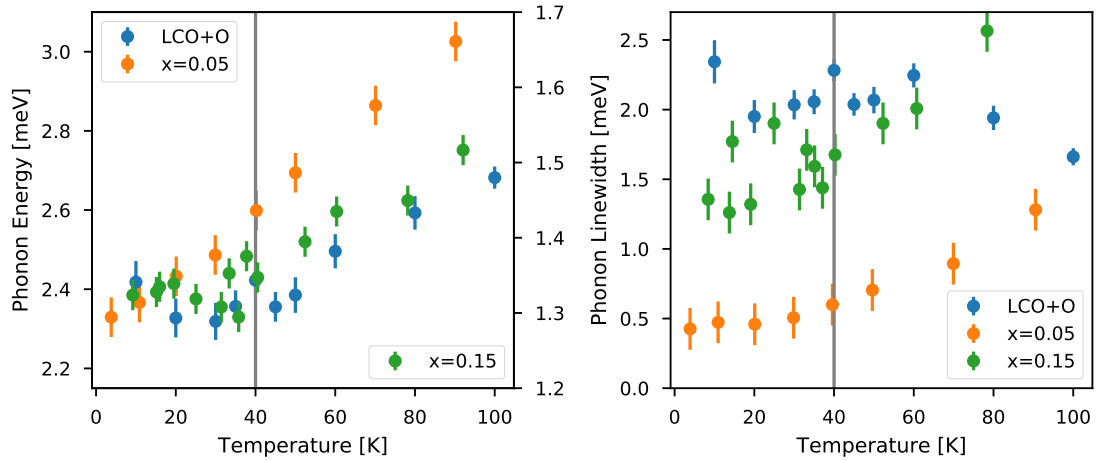

Figure 6.11: Temperature dependence of the Z-point phonon in $La_2CuO_{4+\delta}$ compared to $La_{2-x}Sr_xCuO_4$ with $x = 0.05$ (insulating) [174] and $x = 0.15$ ($T_c = 37\,K$) [175]. **Left**: Phonon energy as a function of temperature. The left energy axis correpsonds to the $x = 0.15$ data. **Right:** Phonon linewidth as a function of temperature, with the width measured as Full-Width Half-Maximum in meV.

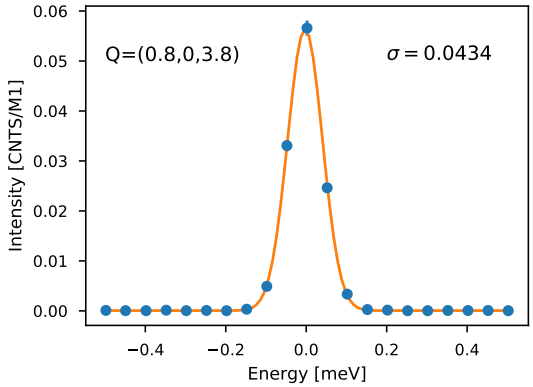

Figure 6.12: Energy resolution of ThALES in the conditions used to measure soft phonons. An energy scan at an arbitrary $\boldsymbol{Q} = (0.8, 0, 3, 8)$ close to the (104) peak we are interested in reveals an energy resolution with a $\sigma = 0.04\,meV$ Gaussian with corresponding to $0.10\,meV$ Full-Width Half-Maximum.

energy. Since we know that the interstitial oxygen in $La_2CuO_{4+\delta}$ is spatially inhomogeneous, it would not be surprising to have spatially separated regions with different 'spring constants' for this phonon modes. In particular, we know that this mode is related to octahedral tilts which are affected by the interstitial near the apex of the CuO_6 octahedra. While not conclusive, this points to abnormal behavior which would be in favor of the second scenario.

6.3 Low energy modes of superstructures

Finally, we take a look at the superstructures observed in chapter 5 and use the Triple-Axis Spectrometer ThALES to look for a dynamic signature of these satellites. It is well known that structural peaks, per Goldstone's theorem, should have acoustic modes emerging from their position.

We start by looking at these dynamics with the FlatCone analyser as shown in figure 6.13. We, once again, clearly see the elastic scattering from the superstructures, but as we move up in energy, we only see the acoustic phonon emerging from the Bragg peak. It should however be noted that since the FlatCone analyser measures at a fixed energy, it can be difficult to detect flat modes.

For this reason, we switched to a single detector and made detailed measurements along the line shown in figure 6.13. The result is shown in figure 6.14, revealing that we do not observe any phonon-like signature, despite very strong satellite reflections (roughly 20000 neutron counts per

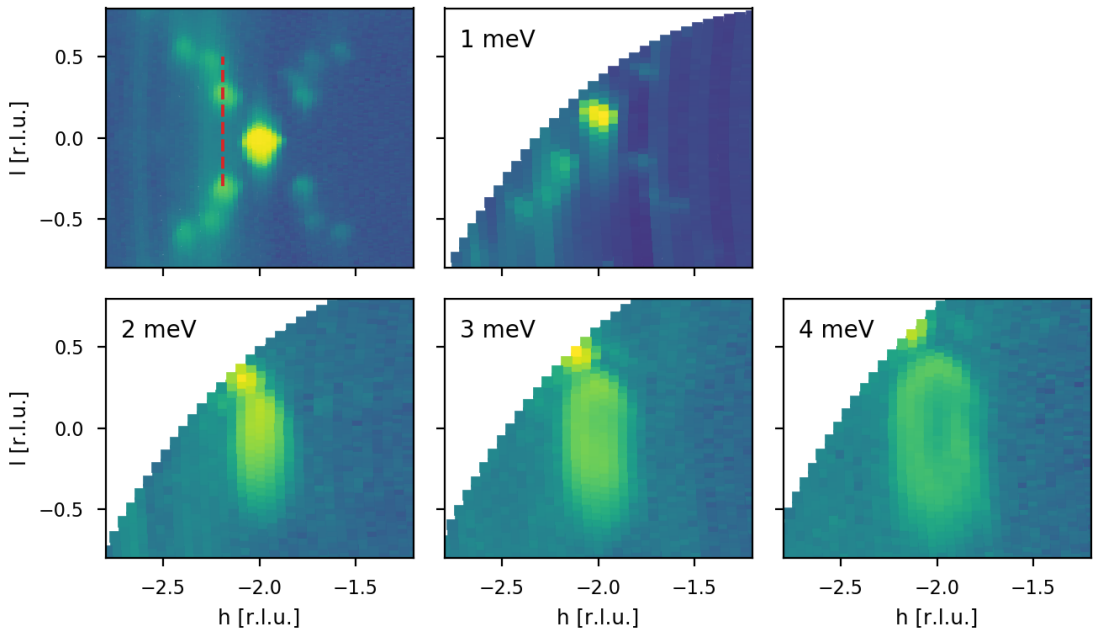

Figure 6.13: FlatCone data of $La_2CuO_{4+\delta}$ in the a-b plane in the elastic condition (top left) and at 1 meV, 2 meV, 3 meV and 4 meV as indicated by the figures. In general, the energy-dependant features show no signature of superstructures, and we only see the acoustic phonon from the (200) Bragg peak.

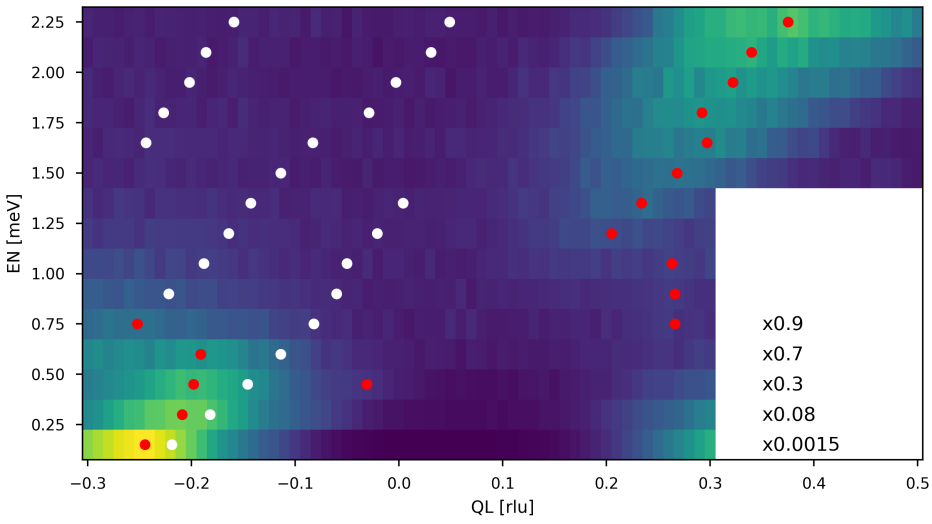

Figure 6.14: Data collected with a single-detector setup, designed to search for fundamental excitations from the satellite peaks as shown in figure 6.13, which also shows the direction where this data was obtained. The red and white markers indicate features visible in the individual scans, see appendix B for details. Due to the linear shape of these features, it seems likely that these are artifacts of the experiment.

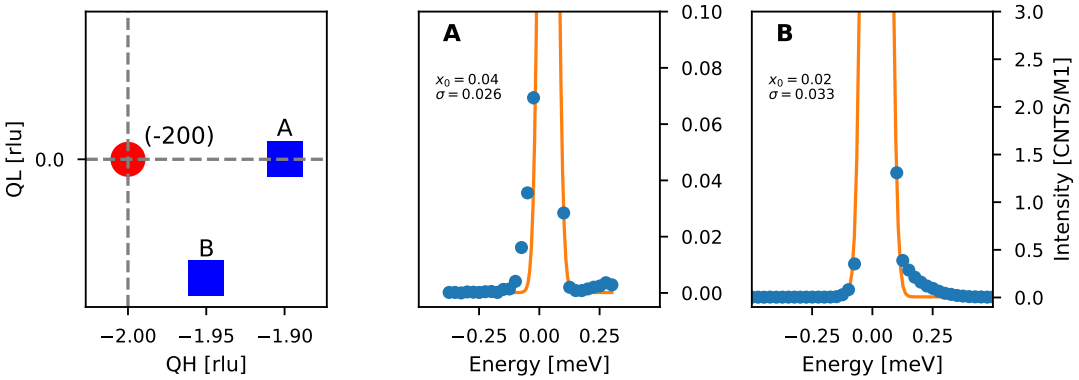

Figure 6.15: Resolution in the experiment where we look for dynamics associated with superstructures. **Left**: Schematic of reciprocal space where we measured the energy-resolution of the instrument. I remark here that the superstructures are seen in the direction of **B**. Subfigures **A** and **B**, shows the raw data with a Gaussian fit at the two locations corresponding to the schematic. Since we are measuring close to the elastic Bragg peak, the increased intensity at **B** suggests that our resolution ellipsoid has points along the (200)-**B** direction.

second). We even confirmed that we were in the best conditions possible with regards to resolution as shown in figure 6.15.

I do not currently have a satisfying explanation for these observations and I would be cautious about insisting that the excitations simply do not exist. Since we have no idea about the polarization fo these modes, I would suggest additional experiments at different $\boldsymbol{Q}$ values. In particular, I note that our measurements were performed around $l = 0$. For the phonos associated with CuO_6 tilt patterns in section 6.2, a finite l-component is necessary in order to get phonon intensity. Since we believe that the superstructures are associated with tilt patterns, we might be in a similar situation.

6.4 Summary

In this chapter, a few experiments concerning low-energy phonons were bundled together in order to help us better understand the dynamic nature of octahedral tilts in oxygen doped La_2CuO_4. We have shown that our simulations are highly reproducible in experiment, suggesting that we can expand our models to include interstitals through molecular dynamics in the next chapter.

We also observed unusual behavior in $La_2CuO_{4+\delta}$ when trying to investigate soft phonons related to a structural instability. The behavior is significantly different from that of $La_{2-x}Sr_xCuO_4$, but we still see a correlation between this phonon and T_c. It was suggested that this behavior could be associated with a distribution of domains, each with different 'tilt dynamics'.

Finally, we found no evidence of dynamics related to the well-known superstructures in $La_2CuO_{4+\delta}$, which is highly unusual if we expect the dynamics to behave like acoustic phonons. We interpret this lack of intensity as either a consequence of the measurement conditions with respect to the mode eigenvectors or as an extremely flat dispersion. Since these superstructures are associated with a long-range modulation, the dynamics are not likely to be very energetic.

Chapter 7

Phonon Density of States

In this chapter, we take a closer look at the phonon Density-of-States (DOS) in a series of insulating and superconducting samples with different dopant species. In the previous chapter, we looked at certain low-energy phonon branches which could be properly separated and measured due to the sparse nature of bands from 0 meV to 10 meV. This was due to the fact that the neutron differential cross-section 'sees' preferentially vibrations parallel to the neutron wave vector due to the $\boldsymbol{Q} \cdot \boldsymbol{e}_j$ factor in equation (2.5). At higher energies, the phonon bands are heavily entangled (in the literal sense) making it difficult to separate different contributions to a measured spectrum where we have a finite resolution.

As a reminder, figure 7.1 shows the neutron-weighted bands in La_2CuO_4 with orthorhombic symmetry. At energies from 10 meV to 40 meV we have a lot of intensity originating from multiple bands. Even if we took the data in all these directions, which would be a very laborious task, comparing experiment and simulation would be much harder compared to the analysis performed in chapter 6. On the right-hand side of figure 7.1 we see the neutron-weighted DOS, which is found by essentially summing up the three dimensional band structure onto the energy axis.

The advantage of using the phonon DOS, is that we can obtain a 'dynamical fingerprint' of a specific sample and consequently compare different samples, temperatures or other parameters of interest. In addition, the phonon DOS can be obtained experimentally by measuring powders with a Time-of-Flight (ToF) spectrometer as we covered in section 2.2, chapter 2.

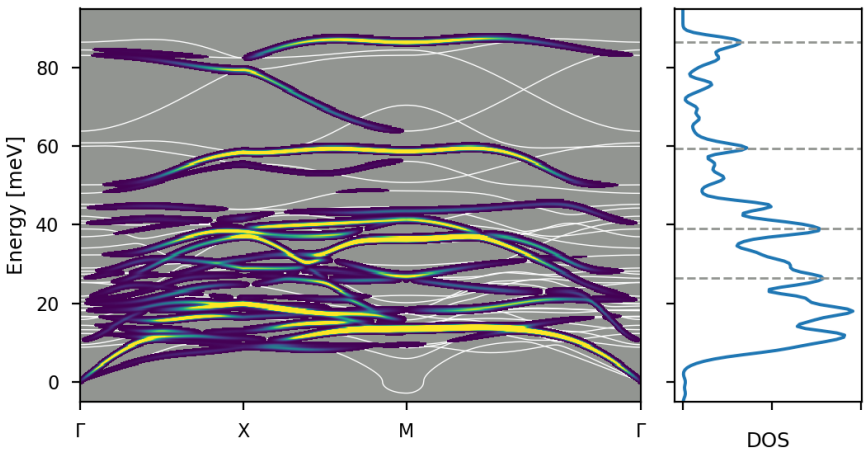

Figure 7.1: Neutron weighted phonon bands and DOS computed for La_2CuO_4 in the orthorhombic (LTO) crystal structure and magnetic, insulating electronic structure. **Left**: Band structure shown with neutron intensity where the energy axis have been given a Gaussian width of 0.3 meV Full-Width Half-Maximum (FWHM). The white lines shows the δ-function dispersion and thus reveal certain bands invisible to neutrons. **Right**: Phonon DOS obtained by integration of the first Brillouin Zone on a $20 \times 20 \times 20$ grid and broadening the spectra with a Gaussian width of 1 meV FWHM. Certain Features that we observe in experiments are marked with grey horizontal lines. See discussion in the text, figure 7.4 and table 7.4.

Table 7.1: Samples used in the experiment, along with a naming scheme used in this chapter, the composition and the superconducting transition temperature as obtained from susceptibility measurements. For additional details about these powdered samples see the MSc thesis by Ahmad [79].

Name	Composition	T_c
LCO	La_2CuO_4	-
LCOO	$La_2CuO_{4.05}$	$\approx 40\,K$
LSCO3	$La_{1.97}Sr_{0.03}CuO_4$	-
LSCOO3	$La_{1.97}Sr_{0.03}CuO_{4+\delta}$	$\approx 40\,K$

Table 7.2: Overview of incident energies and corresponding monochromators used in the experiments on IN4C.

λ [Å]	Monochromator	k [Å^{-1}]	E [meV]	Sapphire Filter
1.6	PG004	3.93	31.95	`IN`
1.1	PG004	5.71	67.61	`IN`
0.85	Cu220	7.39	113.22	`OUT`

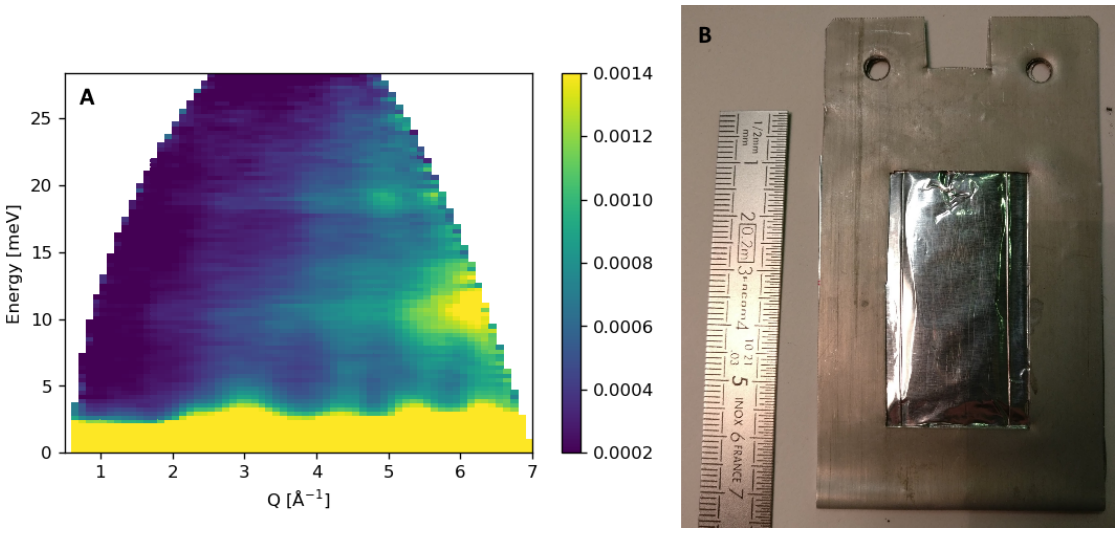

Figure 7.2: **A**: $S(\boldsymbol{Q},\omega)$ map of LSCO3 at 10 K with $\lambda = 1.6$ Å incident wavelength. Data has normalized by the Bose factor. **B:** Sample mounted in cadmium frame.

7.1 Experiment

We performed inelastic neutron time-of-flight experiments on a series of $La_{2-x}Sr_xCuO_{4+\delta}$ powdered samples in order to better understand the relationship between mobile (O) and static (Sr) dopants similar to the objectives outlined for Pair-Distribution Function analysis in chapter 5. The samples used here are listed in table 7.1 and are identical to the ones as used in 5 [79]. The naming scheme of table 7.1 will be used throughout this chapter.

Experiments were performed at the thermal neutron time-of-flight spectrometer IN4c at Institut Laue-Langevin in Grenoble, France. In order to see excitations in the 5 meV to 100 meV range, each sample/temperature was measured at three different incident neutron wavelengths as shown in Table 7.2. Sample was mounted in a cadmium frame as shown in Figure 7.2B. Each of the 4 samples was measured for 3.5-4 hours per temperature/wavelength combination.

The raw time-of-flight data was reduced to $S(\boldsymbol{Q},\omega)$ using the `Mantid` [176] software and the measured background was corrected by subtracting measurements of a sample of polycrystalline vanadium from our data. Due to the isotropic nature of the powder, we only consider the magnitude of $\boldsymbol{Q}$ and the resulting data can be viewed in two dimensions as shown in Figure 7.2A. Obtaining the density-of-states is done in Mantid with the `ComputeIncoherentDOS` [177] algorithm, using the

Table 7.3: Q and E-ranges used in the computation of DOS. For all spectra a mean squared displacement of $\langle u^2 \rangle = 0.015\,\text{Å}^2$ was used.

λ [Å]	Q_{min} [Å^{-1}]	Q_{max} [Å^{-1}]	E_{min} [meV]	E_{max} [meV]	ΔE [meV]
1.6	2.0	7.0	4.0	26.0	0.2
1.1	3.0	10.0	7.0	59.0	0.4
0.85	4.0	12.0	15.0	98.0	1.0

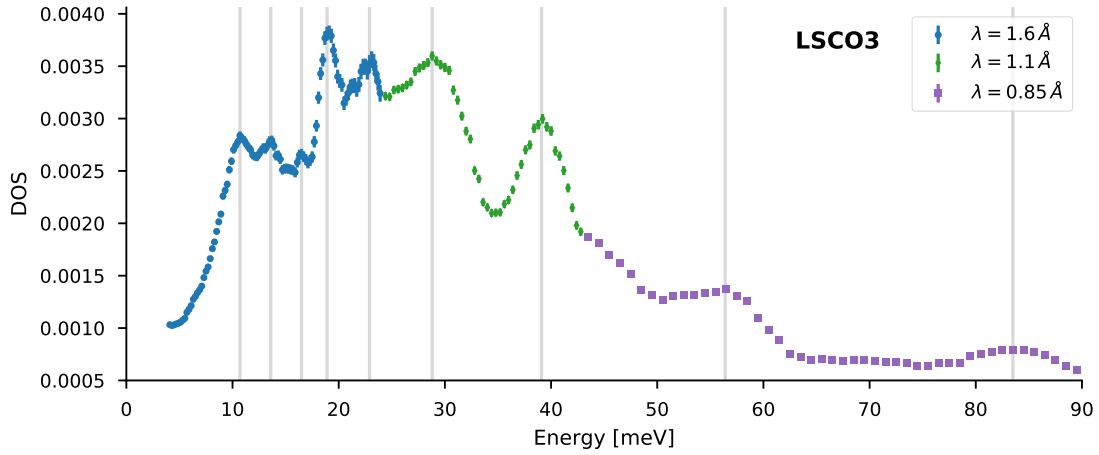

Figure 7.3: Visualization of the data 'stitching' procedure. Our spectra are obtained at low temperatures and we thus only consider neutron energy loss, meaning that the maximal energy of the spectrum is limited by the incoming neutron energy. For this reason, a full spectrum is obtained from three separate measurements and are put together as shown. The energies where data is stitched together is determined by a visual inspection such that we minimize artifacts created by this procedure.

following expression for the one-phonon incoherent scattering function (see section 2.2 for details):

$$S^{(1)}_{\text{inc}}(Q,E) = \exp\left(-2\bar{W}(Q)\right)\frac{Q^2}{E}\langle n+\frac{1}{2}\pm\frac{1}{2}\rangle\left[\sum_k \frac{\sigma_k^{\text{scatt}}}{2m_k}g_k(E)\right],$$

where $\bar{W} = Q^2\langle u^2\rangle/2$ with $\langle u^2\rangle$ being the average mean-squared displacement. n is the Bose factor and E is the energy transfer. Finally, the term in brackets is the neutron-weighted density of states with k running over the different elements in our sample. The calculated DOS is given in milibarns/steredians per formula unit per meV. The mean squared displacement is set to $\langle u^2\rangle = 0.015\,\text{Å}^2$, which is a good compromise between qualitatively describing our data and the actual values of $\langle u^2\rangle$ as obtained from experiments [178] and simulations.

In order to get meaningful results from this procedure, reduction of the raw data is usually required. Generally, one chooses a range of Q and E to sum over along with a binning of E (which is measured through time-of-flight and thus on a continuos scale). Since the measured (Q,E) space is different between incident energies, the integration ranges are chosen for each of the three configurations independently (see Table 7.2). The parameters used for our data reduction are shown in Table 7.3.

7.2 Results

In order to visualize our spectra, we start by stitching the different wavelengths together. Since the energy resolution of the instrument decreases with increasing incoming energy E_i we stitch together data from the different wavelengths, such that the $\lambda = 1.6$ Å data describes low energies up to ≈ 24 meV, $\lambda = 1.1$ Å data describes intermediate energies up to ≈ 43 meV and $\lambda = 0.85$ Å data describes high energy data.

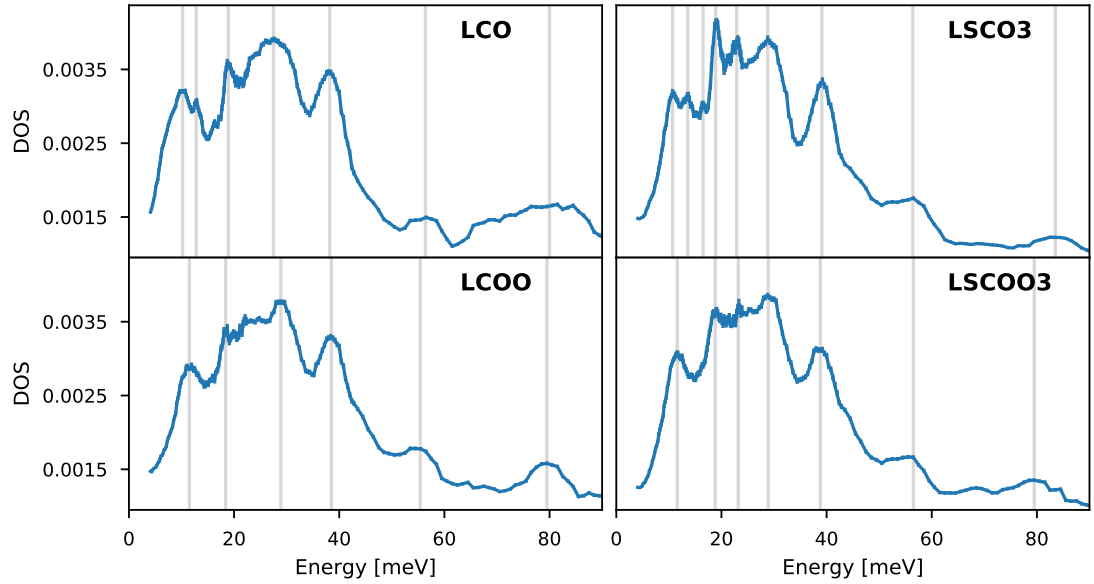

Figure 7.4: DOS of all measured samples (see table 7.1 for naming scheme) at 10 K. Data was reduced with Mantid and stitched together from several measurements as described in the text.

Table 7.4: Peaks in the phonon DOS at 10 K of samples considered in this chapter, obtained through visual inspection of figure 7.4 (grey vertical lines).

Sample	E_1	E_2	E_3	E_4	E_5	E_6	E_7	E_8	E_9
LCO	10.2	12.8	-	18.9	-	27.5	38.2	56.4	80.0
LCOO	11.5	-	-	18.4	-	28.9	38.5	55.4	79.5
LSCO3	10.7	13.6	16.5	18.9	22.9	28.8	39.1	56.4	83.5
LSCOO3	11.6	-	-	18.8	23.2	28.9	38.8	56.5	79.5

Data is stitched together by choosing some cut-off energies such that no features are introduced when we combine the data. The data for $\lambda = 1.1$ Å and $\lambda = 0.85$ Å is then scaled such that we get a continuous spectrum across the full range. For this reason, the absolute values of the DOS is only representative for the $\lambda = 1.6$ Å data. Figure 7.3 shows the result of such a concatenation of data. In addition, vertical lines have been added to show qualitative 'peak' features of the spectrum.

Applying this procedure to all 4 samples, figure 7.4 shows the phonon DOS for all samples at 10 K. Since no noticeable temperature dependance was found, apart from a tendency to smooth out features, spectra at 60 K and 300 K are not shown here, but can be found in appendix C. Vertical lines in the plots mark peaked features in the spectra and are obtained from a visual inspection. These features are mainly a convenient way to quantify certain differences between samples.

Table 7.4 shows these features in a list of peak-energies E_k, indicating that we can generally identify four separate high-energy peaks at $\approx$ 28 meV, 39 meV, 56 meV and 80 meV which are general similar between our samples. Comparison with figure 7.1 shows that these features are qualitatively consistent with the calculated spectrum and that the two highest energy features originate from distinct bands. Features below 30 meV are much more subtle and will have to be analyzed based on changes in the shape of our measured DOS.

Comparing between samples with and without interstitial oxygen, our visual inspection reveals two distinct features. First, we see a subtle modification of the high-energy mode at $\approx$ 80 meV, where it seems that spectral weight is moved to lower energies. This is consistent with softening of the Cu-O bond-stretching mode which we will return to in the next chapter. Second, there is a general smoothing of features below 30 meV when introducing interstitial oxygen into the sample. Intuitively, one would expect a smoother DOS with increased disorder, so this observation is, at least qualitatively, consistent with what we would expect. On the other hand, we also see a slight sharpening of features when comparing Sr-doped LSCO3 with the parent compound LCO,

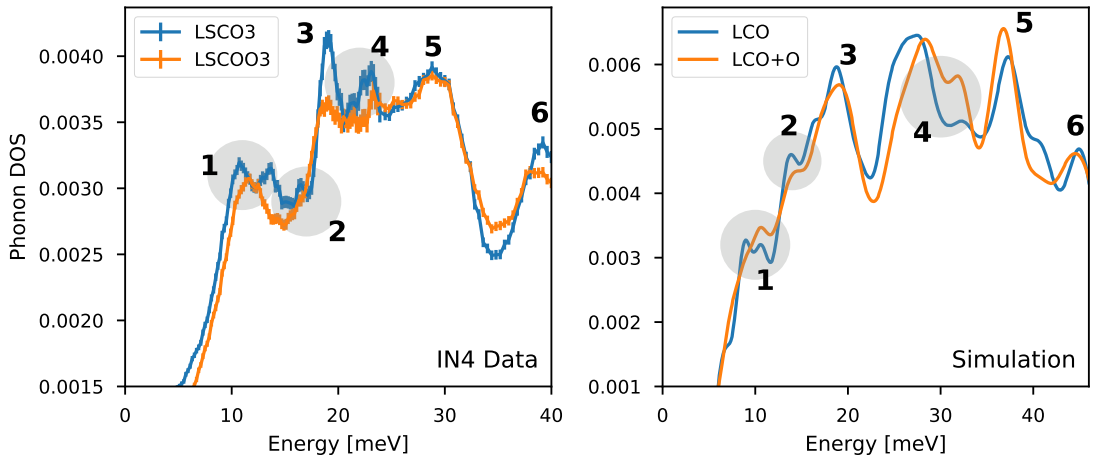

Figure 7.5: **Left:** Phonon DOS data for LSCO3 and LSCOO3 at 10 K. Features are numbered and dissimilarities between the samples are highlighted **Right**: Simulations from LCO AFM and LCO+O AFM (see chapter 4 for details) with the same highlighted features as from the data. The simulation data is smoothed by a width that depends on the energy such that FWHM $= 1.4 + 0.024E$, with E being the energy in meV.

inconsistent with the intuitive notion of disorder-induced smoothing of the spectra. On the other hand, it does seem consistent with the sharper distribution of Cu-O in-plane distances that we observed in the previous chapter (see table 5.2). LCO has a peculiar broad feature at high energies (65 meV to 85 meV), that is unique to that sample and cannot be explained by the logic we used so far.

7.3 Comparison with Simulation

Since the high energy features are either very similar between samples (28 meV, 39 meV and 56 meV) or considered separately in the next chapter (80 meV), the following analysis will be focussed on the low-energy part of the phonon DOS. Since the differences between spectra are quite subtle, we consider the effects of oxygen-doping of LSCO3 first, since we are free of the peculiar features of the LCO sample.

Figure 7.5 shows a comparison of LSCO3 and LSCOO3 in the low-energy regime below 40 meV alongside a comparison of phonon DOS obtained by molecular dynamics for LCO and LCO+O. Since the Sr content is very low in this sample ($x = 0.03$), it is reasonable to assume that it is, at least, approximately similar to LCO with $x = 0$. While we had reasonable success in chapter 6 when comparing band structures directly, the correspondence between spectra are not quite as convincing in this case. We recover general features as shown in the figure, but the spectral weight and absolute energies deviate slightly from the experimental spectrum (notice the different energy-axes between experiment and simulation).

While the agreement is not perfect, we can still assign the features with some confidence as shown in the labeled features in figure 7.5. In both the experiment and simulation we see the double-peak at **(1)** merging, the peak at **(2)** disappearing and a modification of spectral weight to higher energies at **(4)** when adding oxygen to the sample. Features at **(3)**, **(5)** and **(6)** stay roughly the same.

Figure 7.6 shows the same idea, but this time for the effect of Sr-doping. We note here that the simulation has roughly four times the doping ($x = 0.125$) of the experimental sample ($x = 0.03$). The minimal possible doping (one substitution) in our simulation cell would be $x = 0.0625$. It appears as if the addition of strontium has a similar effect to that of oxygen, but with a smaller magnitude – there is an overall smoothing of the spectrum due to the introduction of disorder. Interestingly, we reproduce the 'dip' at ≈ 30 meV in our simulation. One thing that we cannot explain in these measurements, is the very sharp features of LSCO3 when compared to LCO, especially at ≈ 20 meV.

For the sake of completeness, figure 7.7 shows the experimental phonon DOS as a function of the two dopants (oxygen, strontium), where it becomes clear that the modification of spectral weight

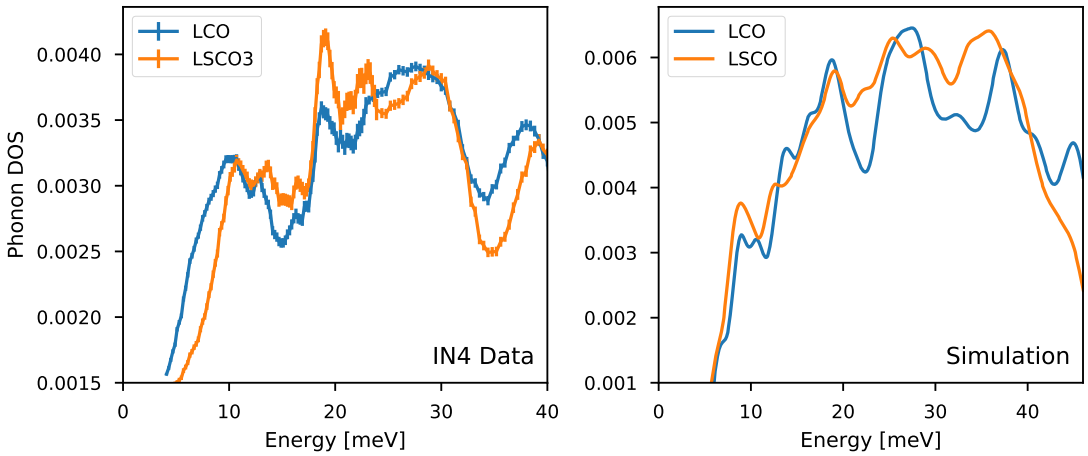

Figure 7.6: **Left:** Phonon DOS data for LCO and LSCO3 at 10 K. **Right**: Simulations from LCO AFM and LCO+Sr AFM (see chapter 4 for details). The simulation data is smoothed by a width that depends on the energy such that FWHM $= 1.4 + 0.024E$, with E being the energy in meV.

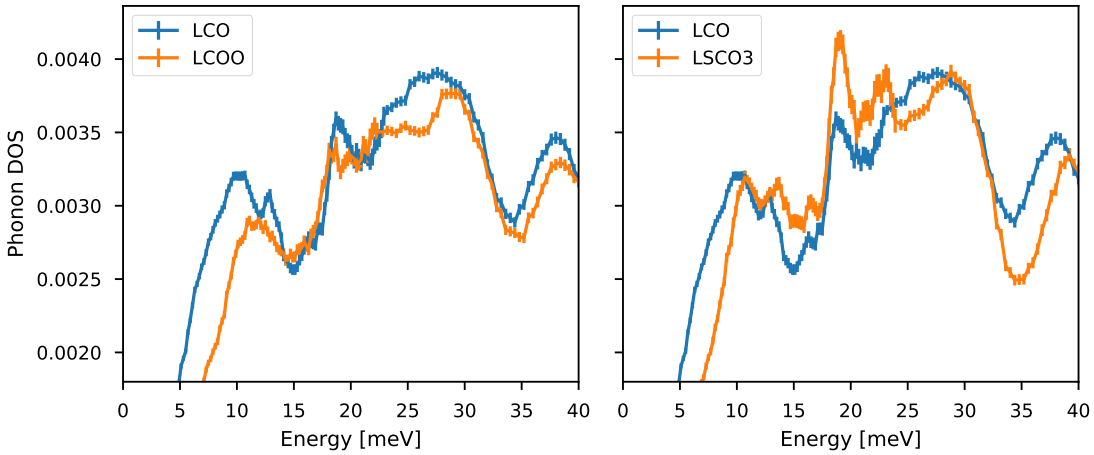

Figure 7.7: Dopant dependence of measured phonon DOS. **Left:** Effect of oxygen through a comparison of LCO and LCOO. Notice in particular the modification at low energies. **Right**: Effect of strontium through a comparison of LCO and LSCO3. While the LSCO3 spectra is much sharper, low energy features are similar in energy when compared to the effect of oxygen.

at low energies ($\approx$ 5 meV to 15 meV) are more dramatic in the case of oxygen. A corresponding comparison of the simulations can be found in figure 4.5, chapter 4.

7.4 Summary

In this chapter we measured several samples of La_2CuO_4 with different dopant species in order to shed light on the effect of specific types of chemical disorder on the phonon density of states. While it is possible to discern certain features in the experimental spectra related to the dopant species, differences are in general quite subtle.

With that in mind, we have been able to identify features at low energies which are qualitatively reproduced by our molecular dynamics simulations. At higher energies we only see a modification of the topmost phonon band which will be discussed in the following chapter.

It thus appears, despite the significantly reduced simulation precision, that our molecular dynamics simulations can be used to identify a microscopic origin of the modified phonon DOS. The analysis of molecular dynamics simulations concluded that the inclusion of interstitial oxygen species resulted in local 'LTT-like tilts' despite the structure being LTO. In fact, it is quite remarkable that the structure of these samples are almost identical in our diffraction experiments (the data

in chapter 5 is from the same samples), but we clearly see a signature of the dopant species in the dynamics.

While our simulations reproduce the general features of the phonon spectrum, there are still a few unexplained phenomena. The addition of oxygen seem relatively well-understood through the comparison with simulations; features around 10 meV and 20 meV are broadened due to the interstitial. The effect of Sr-doping, on the other hand, is difficult to explain as a purely structural phenomena. It appears as if the LSCO3 sample is sharpening features quite substantially, opposite to the effect we see from simulations. From an intuitive, structural perspective, one would also expect disorder to broaden features when compared to the stoichiometric compound. While the LSCO3 sample is insulating, it lies in the underdoped region where the magnetic properties are similar to samples with $x \leq 0.125$ [76].

To summarize, it appears that our simulations can explain features in the phonon dos due to oxygen doping, but *not* due to a small amount of strontium doping. One way to think about this is a scenario where the effect of oxygen dopants is dominated by phenomena which we can explain in a semi-classical way without having to consider the complex electronic structure. Since strontium-doping barely modifies the structure, it is possible that the sharpening of the phonon DOS is mostly due to electronic correlations. This is also somewhat consistent with the fact that structural correlations due to interstitials take over, once again, when comparing LSCO3 and LSCOO3 (figure 7.5).

Chapter 8

Phonon Anomalies

In this chapter we focus on a specific phonon mode which has been extensively studied in the cuprates and is believed to be related to stripe order and, consequently, superconductivity. The idea is that Cu-O bond-stretching phonons interact with stripe order, causing a softening at certain wave vectors. We perform measurements of this phonon anomaly in two distinct samples of oxygen doped LSCO+O in order to establish if the anomaly is related to dopant disorder. In order to establish a connection with stripe order, we also measure the phonon in high magnetic fields known to modify the spectral weight of magnetic stripes. We find that this phonon in LSCO+O has a very similar signature to that of optimally doped LSCO ($x = 0.15$) and that a magnetic field of 10 T has no effect on the phonon spectral weight. Part of the material in this chapter has been submitted to Physical Review Letters. The manuscript is currently available at arXiv:1908.09546v1.

8.1 Motivation

As discussed in the introduction (section 1.3), stripe order and excitations related to stripe order appear to be ubiquitous in cuprate superconductors and in particular in the lanthanum cuprates. However, while the magnetic component of stripes have been extensively studied with neutron scattering, the charge component in this model is much more elusive. Static charge stripes only show up in superconducting samples close to the $x = \frac{1}{8}$ anomaly [72–75, 179] and direct evidence of dynamic charge stripes has only been reported for isostructural, but insulating $La_{2-x}Sr_xNiO_4$ [180].

If we believe that the charge rivers in the stripe model carries the superconducting current, we need additional information about their behavior. For this reason, researchers have been looking for alternative methods of probing charge stripes. Additionally, since static charge order is usually associated with a suppression of superconductivity, one is naturally pushed towards understanding the fluctuations associated with static charge stripes. While the importance of 'fluctuating stripes' were known early on [181], I believe it is fair to say that we still know very little about their behavior. Just this year (2019), evidence of dynamic charge in a large area of the cuprate phase diagram was found using resonant X-ray techniques [182]. It has also recently been suggested that these fluctuating charge stripes are characterized by diffusive dynamics [183] – that is, the dynamics is similar to brownian motion rather than coherent oscillations (e.g. phonons).

8.2 Phonon Anomalies

Since direct, spectroscopic evidence of fluctuating charge stripes in superconducting cuprates is lacking, it may be possible to find an avenue of progress through indirect measurements. Recently, it was discovered that the dispersion of the Cu-O bond-stretching longitudinal-optical (LO) phonon in SC $La_{1.85}Sr_{0.15}CuO_4$ (LSCO15, $T_c = 38\,K$) [184] and $La_{1.80}Sr_{0.20}CuO_4$ ($T_c \approx 35\,K$) [164] displays a strong anomalous softening interpreted as a coupling to a novel charge collective mode [164]. Furthermore, merely a weak signature of the anomaly is visible in the phonon linewidth of $La_{1.93}Sr_{0.07}CuO_4$ ($T_c \approx 15\,K$) and $La_{1.75}Sr_{0.25}CuO_4$ ($T_c \approx 15\,K$), suggesting that the strength of the anomaly tracks the doping-dependence of T_c [164]. Similar phonon anomalies have been observed in $Bi_2Sr_2CaCu_2O_{8+\delta}$ [185], $La_{1.875}Ba_{0.125}CuO_4$ (LBCO) [186], $La_{1.48}Nd_{0.4}Sr_{0.12}CuO_4$ (LNSCO) [184] and $YBa_2Cu_3O_{6.6}$ [187] hinting at a ubiquitous feature of cuprate superconductors.

These phonon anomalies have been extensively reviewed by Reznik [188] and we give just a brief overview in this chapter. In the specific case of the lanthanum cuprates, the phonon mode of interest is related to a stretching of the Cu-O bond in the CuO_2 plane. Intuitively, we can

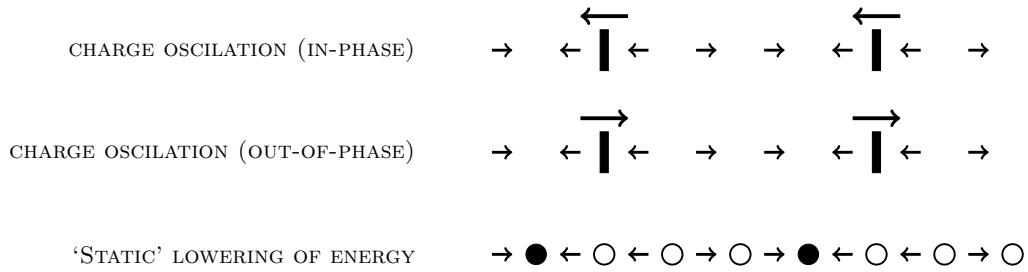

Figure 8.1: Possible scenarios of the phonon anomaly. In the first two scenarios, only the movement of the oxygen atoms are shown and the bars represent charge stripe dynamics with the propagation as shown. In these cases the charge oscillation can be either in-phase (shown top rown) or out-of-phase (shown in middle row) with the phonon [189]. In the last scenario (shown in the bottom row) open circles represent Cu atoms with magnetic ordering and closed circles are charge stripes running perpendicular to the chain. The static charge order then lowers the energy of the phonon [186].

already see why this phonon mode might be interesting to look at since the vibrational frequencies could be modified by charge modulations in the CuO_2 plane. In addition, phonon anomalies have been observed at exactly the charge ordering wave vector $\boldsymbol{Q}_{\rm co} = \left(\frac{1}{4}\frac{1}{4}0\right)$ in the Bmab orthorhombic coordinate system (see section 1.3).

Figure 8.1 shows a sketch of possible scenarios involving a chain of Cu atoms (circles) separated by oxygen atoms with a certain displacement pattern (arrows). In one scenario [189], the charge stripes are fluctuating and the phonon 'resonates' with this fluctuation, essentially lowering its energy. In the second scenario [186], static charge order changes the forces between certain Cu-O pairs, an effect that is also minimized at $\boldsymbol{Q}_{\rm co}$ as shown in the figure. A third possibility is one where the phonon anomaly is found in the perpendicular direction to the one shown in figure 8.1. In this case the phonon would resonate with the modulation 'within' the charge stripe. Since the softening happens close to $\boldsymbol{Q}_{\rm co}$ it seems more likely that one of the first two cases are responsible, but it has technically not been settled.

8.3 Experiment

We measured the phonon dispersion highlighted in figure 3.20 in two oxygenated single crystal samples: $La_2CuO_{4+\delta}$ and $La_{1.94}Sr_{0.06}CuO_{4+\delta}$ at the triple-axis spectrometer IN8 at ILL. Measuring this phonon dispersion turned out to be more difficult than anticipated, and several attempts were spent in order to reach optimal conditions where we could actually observe the phonon dispersion with relative success.

After our initial attempts, we realized that our signal was contaminated by so-called spurious scattering. While not immediately apparent to us, we identified this 'spurion' as accidental Bragg scattering from the analyzer [99]. This means that we are in the unfortunate situations where the analyser is at angle where the sample scatters strongly from a structural Bragg peak. While the 'job' of the analyser is to select a desired final energy, Bragg scattering is so strong that the signal at the detector will be contaminated by incoherent, scattering from the analyser crystals.

Figure 8.2 shows the geometry of this accidental Bragg scattering in reciprocal space. From this sketch we see that the spurious scattering comes from the (8,4,0) reflection. In order to quantify where we would observe this scattering in our measurements, we can make a simulation where we evaluate the strength of the spurion at the desired values of $(\boldsymbol{Q}, \omega)$. This is done by constructing the geometry as in 8.2 (top) and then defining the spurious strength through the distance to (8,4,0). The result of such a simulation is shown in figure 8.2 (bottom), and we clearly see that this signal intersects the expected phonon dispersion.

Two measures were taken to avoid this spurious scattering. First, by using the goniometers installed on IN8 we can effectively rotate the sample around the [110] axis, which has no affect on our measurements in the [hh0] direction, but does move further away from the condition for spurious scattering since (8,4,0) will be out of the scattering plane. Second, we installed a position-sensitive detector (PSD) with the hope that the spurious scattering is spatially separated from the phonon scattering. It turns out that the spurious scattering indeed can be separated from the phonon as shown in Figure 8.3. Unfortunately, this background subtraction procedure is associated with a large increase in error bars as shown in the figure.

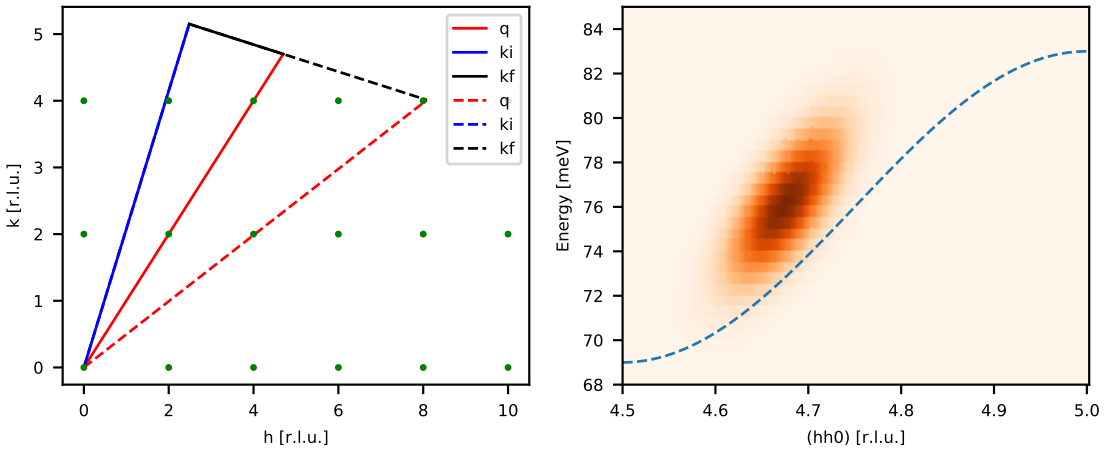

Figure 8.2: **Left**: Scattering triangle responsible for the A-type spurious scattering (broken lines) at $\boldsymbol{Q} = (4.7, 4.7, 0)$. Green points represent Bragg peaks in the (h,k)-plane. The (8,4,0) Bragg refection is responsible for the spurious scattering. **Right**: Simulated effect of the (8,4,0) reflection on a Q-$\hbar\omega$ map assuming a Gaussian spurious signal depending on distances in Q. Broken line represents a 'normal' sinosoidal dispersion in this region as described in the text.

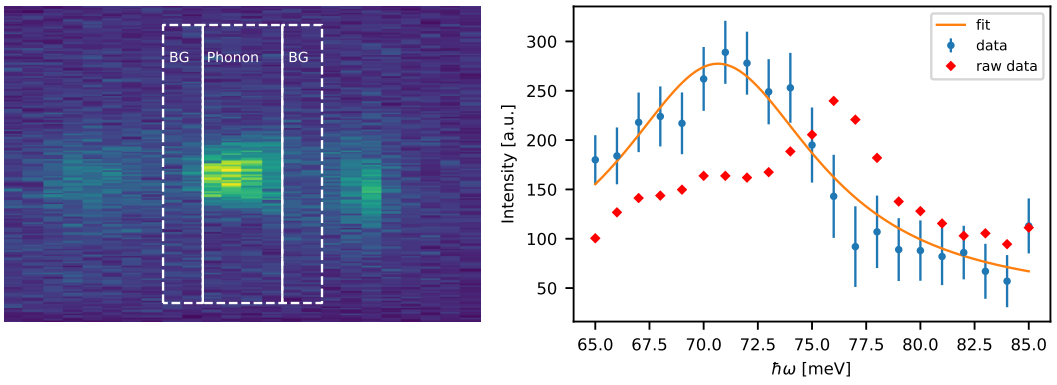

Figure 8.3: Illustration of the data reduction performed using the PSD. **Left**: Summed raw data from an energy scan at $\boldsymbol{Q} = (4.65, 4.65, 0)$. The dashed lines denote the regions of interest (ROI) used in the data reduction. The geometry of the instrument ensures that the desired phonon scattering will occur in the 'Phonon' ROI. **Right**: Corresponding raw (diamonds) and reduced/normalized (circles) data. The raw data is obtained by only considering the 'Phonon' ROI, while the reduced data is obtained by subtracting the intensity from the two 'BG' ROIs. The solid line is a fit to a DHO lineshape as described in the text.

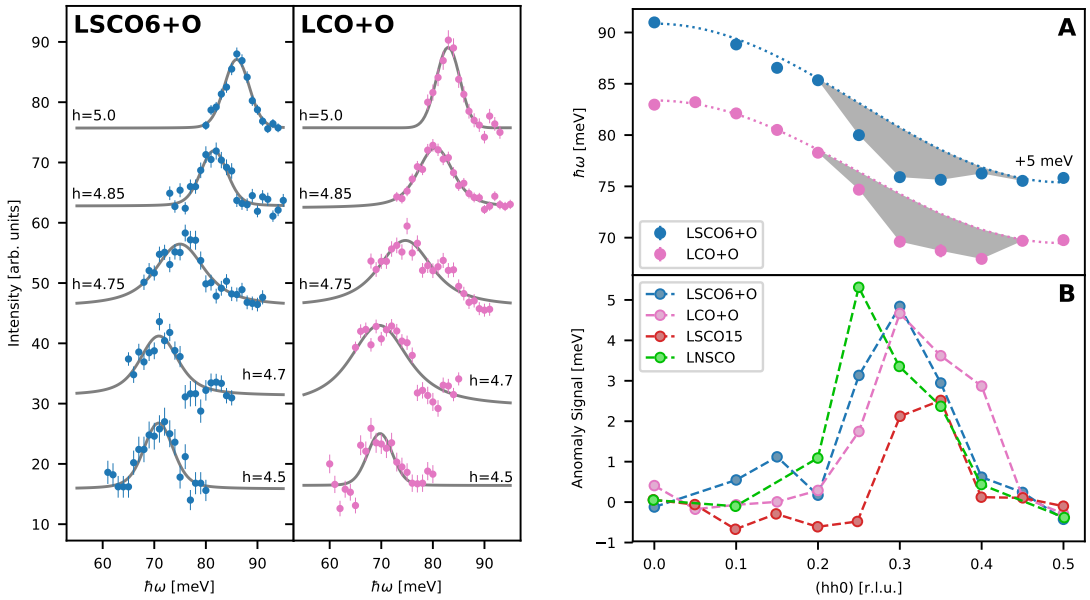

Figure 8.4: **Left:** Reduced data at selected wavevectors of the form $Q = (h, h, 0)$ for both LSCO6+O and LCO+O at $T = 5\,\mathrm{K}$. Data at $\boldsymbol{Q} = (5, 5, 0)$ and $\boldsymbol{Q} = (4.85, 4.85, 0)$ was scaled by a factor of $\frac{1}{2}$ for clarity due to an increase of intensity from the phonon form factor. Data at different h are offset for clarity. Solid lines are fits to a DHO lineshape (see text). **Right: (A)** Dispersion of the LO phonon obtained from the peak positions of individual spectra of both LCO+O and LSCO6+O (offset by 5 meV for clarity). Error bars smaller than the markers are not shown. Dashed line is the normal sinusoidal dispersion as described in the text. All data was obtained at $T = 5\,\mathrm{K}$. **(B)**: Difference between sinusoidal and measured dispersion in $La_2CuO_{4+\delta}$ (LCO+O) $La_{2-x}Sr_xCuO_{4+\delta}$ (LSCO+O), $La_{1.85}Sr_{0.15}CuO_4$ (LSCO15) and $La_{1.48}Nd_{0.4}Sr_{0.12}CuO_4$ (LNSCO). Data for LSCO15 and LNSCO adapted from [184].

Using these procedures, we were able to measure the phonon as shown in figure 8.4 for both $La_2CuO_{4+\delta}$ (LCO+O)and $La_{1.94}Sr_{0.06}CuO_{4+\delta}$ (LSCO6+O). The raw data is fit to a Damped Harmonic Oscillator (DHO) model [103] (see also chapter 2), which has a Lorentzian shape:

$$S(\boldsymbol{q}, \omega) = I_{\mathrm{ph}} \frac{1}{\pi \omega_{\boldsymbol{q}}} \frac{\gamma}{(\omega - \omega_{\boldsymbol{q}})^2 + \gamma^2} + I_{\mathrm{BG}}\,, \tag{8.1}$$

where I_{ph} is the phonon intensity, $\omega_{\boldsymbol{q}}$ the phonon energy at wave vector $\boldsymbol{q}$, γ the phonon linewidth and I_{BG} the background intensity. The extracted dispersion from the data is shown in Fig. 8.4 along with a normal sinusoidal dispersion, $\hbar\omega_q = \alpha \cos(2\pi q) + \beta$, inferred from phonon calculations on LSCO using Density Functional Theory as shown in figure 3.20. We fit the cosine-function to points near the zone center ($\boldsymbol{Q} = (0, 0, 0)$) and edge ($\boldsymbol{Q} = (\frac{1}{2}, \frac{1}{2}, 0)$) to obtain the dashed curves of Fig. 8.4A. To quantify the magnitude of the anomaly, we define the 'anomaly signal' as the difference between the normal dispersion and the measured data (gray shaded area in Fig. 8.4A). Fig. 8.4B shows our anomaly signal for $La_2CuO_{4+\delta}$ and $La_{1.94}Sr_{0.06}CuO_{4+\delta}$ along with previous results from optimally doped $La_{1.85}Sr_{0.15}CuO_4$ and insulating, stripe-ordered $La_{1.48}Nd_{0.4}Sr_{0.12}CuO_4$ [184]. We emphasize the presence of similar anomaly signals on an absolute scale across all studied samples.

8.4 Phonon Anomaly and Magnetic Stripe Order

Since we have now confirmed the presence of a Cu-O bond stretching phonon anomaly in both $La_2CuO_{4+\delta}$ and $La_{1.94}Sr_{0.06}CuO_{4+\delta}$, we wanted to see if this phonon dispersion could be modified by magnetic fields. The background for this idea is the fact that magnetic stripe order in $La_{2-x}Sr_xCuO_4$ has a significant response to magnetic fields in a wide range of doping [60, 63, 190–192]. In general, the application of a magnetic field appears to 'fill in' the gap of the magnetic excitation spectrum for $x \geq \frac{1}{8}$. While this, in general, is consistent with a picture where the gap is directly related to the superconducting gap, there is evidence that the filled states have a different

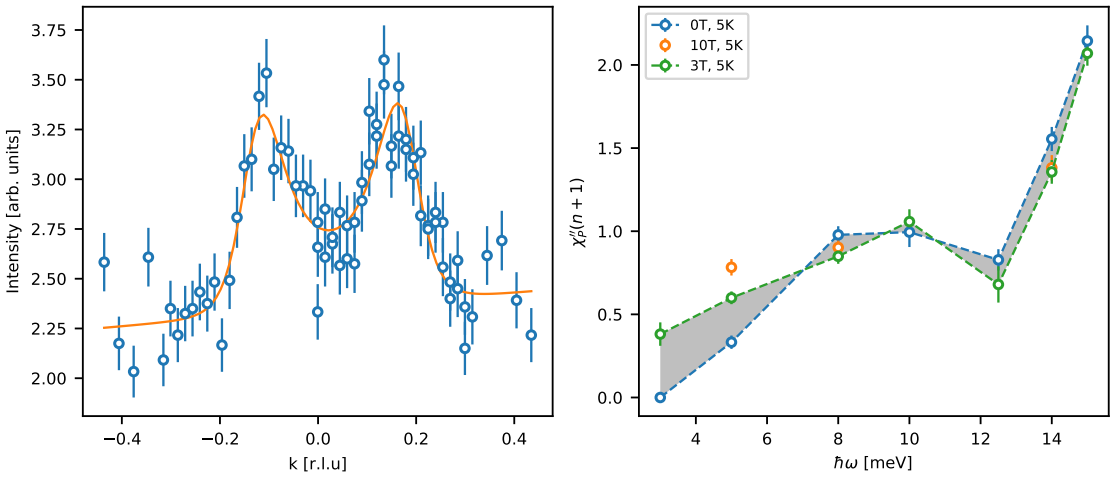

Figure 8.5: Magnetic fluctuations in $La_{1.94}Sr_{0.06}CuO_{4+\delta}$. **Left:** Example spectrum obtained as a constant-energy scan in the k direction with $h = 0.125$. Solid line is a fit to the functional form outlined in ref. [194]. **Right:** Amplitude of the magnetic excitations, as extracted from the fitting procedure, in at a variety of fields and temperatures as a function of energy transfer.

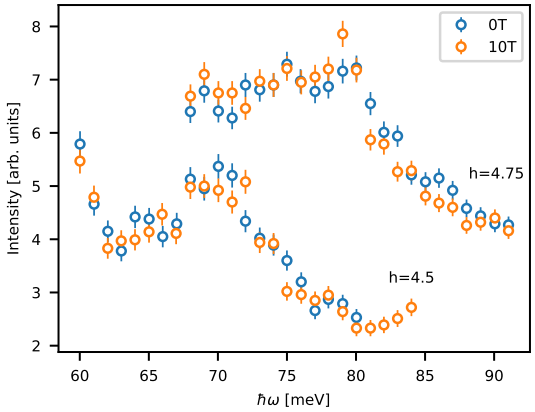

Figure 8.6: Comparison of representative constant-Q $(h,h,0)$ scans of $La_{1.94}Sr_{0.06}CuO_{4+\delta}$ in zero-field and with an applied field of 10 T. All measurements performed at $T = 5$ K

origin [63]. Since one could write books about the spin excitation spectrum in $La_{2-x}Sr_xCuO_4$, I will keep the discussion somewhat limited and refer to the excellent review by Tranquada [193].

Returning to the objective at hand, our idea was to both measure the spin excitation spectrum and anomalous phonons in the same experimental conditions in order to directly probe any correlation (or lack thereof) between the two phenomena. These measurements were only performed for the $La_{1.94}Sr_{0.06}CuO_{4+\delta}$ sample. Figure 8.5A shows the amplitude of the magnetic fluctuations as a function of energy transfer and figure 8.5B shows an example of the neutron scattering data used to extract this amplitude. The figure clearly shows that $La_{1.94}Sr_{0.06}CuO_{4+\delta}$ has gapped excitations which are filled in with the application of a magnetic field (or raising the temperature above T_c). This is in contrast to other oxygen-doped samples (e.g. $La_2CuO_{4+\delta}$ [62]) where the excitations are not gapped.

In figure 8.6 we have measured the phonon at a 'normal' and anomalous wavevector at $T = 5$ K with and without an applied field of 10 T. From this measurement it is thus clear that a field of 10 T has no effect on the bond stretching phonon at anomalous wave vectors.

8.5 Discussion

To begin the discussion of our results, we remark that softening and/or broadening of phonon modes is generally a signature of an incipient structural or electronic instability. Typical examples include structural phase transitions, $\boldsymbol{Q}$-dependence of the electron-phonon matrix element, Fermi

surface nesting and electronic correlations [188]. In order to determine the origin of a given phonon anomaly, it is therefore important to carefully exhaust alternatives before making statements about the connection to novel phases such as dynamic charge stripes [188].

The phonon anomaly appears in vicinity of the wave vector $\boldsymbol{Q}_{\mathrm{co}} = (\frac{1}{4}, \frac{1}{4}, 0)$, consistent with charge stripe ordering as illustrated in Fig. 8.1. Measurements of LNSCO [195], LSCO15 [184] and LBCO [184] have shown a suppression of the anomaly as one moves away from the bond-stretching direction [195], supporting a one-dimensional stripe-like picture. Additionally, the phonon anomaly in LSCO15 and LBCO has almost no temperature dependence apart from a slightly sharper peak shape when heating from 10 K to 300 K [184, 186]. These phenomena rule out anharmonicity and structural inhomogeneity as mechanisms for the phonon anomaly in these systems.

A combination of inelastic X-ray and ARPES measurements on overdoped LSCO ($x = 0.2$ and $x = 0.3$) have shown that the phonon anomaly wavevector is inconsistent with Fermi surface nesting [164, 196], contradicting the idea of a phonon softening due to a Kohn anomaly. A different, possibly $\boldsymbol{Q}$-dependent, electron-phonon coupling could still be responsible for the phonon anomaly. Such an effect would renormalize the electronic quasiparticle dispersion (the so-called 'ARPES kink' [197]) at energies similar to the phonon softening. The ARPES kink has been observed in LSCO $x = 0.2$ and $x = 0.3$, but since of these two dopings only LSCO $x = 0.2$ shows anomalous phonons, the two phenomena appear to not be connected [164].

Thus, all previous studies are unable to explain the phonon anomaly through conventional means and any coupling to stripe order is likely dynamic. One possible scenario is a coupling of the Cu-O bond-stretching phonon with steeply dispersing charge fluctuations. Kaneshita et al. performed calculations based on the Hubbard model of this scenario, predicting anomalous phonon dispersions due to both transverse (meandering) and longitudinal (compression) coherent stripe fluctuations [189] (see Fig. 8.1 for a sketch of the transverse mode). We emphasize that the observed phonon anomaly reported here (see Fig. 8.4) and in LBCO/LSCO [184, 186] is remarkably similar to the calculation by Kaneshita et al. (see Fig. 5 in [189]).

Despite differences in the magnetic excitation spectra as recorded by neutron scattering (including low and zero energy transfers), the three materials LCO+O, LSCO6+O and LSCO15 have remarkably similar in-plane Cu-O bond-stretching dispersions (Fig. 8.4). Furthermore, static charge order at zero field has been observed in a different sample of LCO+O [198] and in LNSCO [179] but so far not in LSCO6+O nor in LSCO15. These observations together indicate that there is no direct connection between static stripes (spin and charge) and the phonon anomaly. In order to further confirm this point, we performed scans of LSCO6+O at selected wave vectors in a $H = 10\,\mathrm{T}$ magnetic field which is known to induce a considerable volume of stripe-like magnetic order in this particular sample [199]. While static charge order has not been observed in LSCO6+O, measurements on LSCO ($x = 0.12$) have shown that static charge and spin stripes respond identically to magnetic fields [73].

Figure 8.6 contains data at two wave vectors with and without an applied magnetic field of 10 T, clearly showing the absence of any detectable field effect on the in-plane Cu-O bond-stretching phonon at $\boldsymbol{Q} = (\frac{1}{4}, \frac{1}{4}, 0)$. These measurements were performed simultaneously with measurements of the low-energy magnetic fluctuations as shown in figure 8.5, confirming a significant increase in the magnetic spectral weight towards lower energies consistent with the appearance of field-induced stripe-order [199]. Thus, the appearance of static magnetic stripe order does not affect the phonon anomaly in LSCO6+O. A similar insensitivity of the phonon anomaly to an applied magnetic field has been observed in underdoped ($T_{\mathrm{c}} = 66\,\mathrm{K}$) $YBa_2CuO_{6.6}$ [200].

8.6 Summary

In this chapter, I showed that the phonon anomaly is a robust feature in optimally doped as well as stripe-ordered cuprates which is independent of the structural details related to the doping process. Since it is equally well-formed in stripe-ordered and optimally doped systems, where the latter show no static magnetic order, the anomaly is surprisingly insensitive to low-energy magnetic characteristics. This is further confirmed by the absence of a magnetic field effect of the charge dynamics in which is known to introduce static magnetic stripe-order in the same LSCO6+O sample.

The phonon anomaly is strongest in the doping region around optimal T_{c} ($0.125 \leq n_{\mathrm{h}} \leq 0.20$) (LSCO15, LNSCO [184], LBCO [186], LSCO6+O, LCO+O), regardless of the presence of static charge order (LNSCO [72], LBCO [201]), suppression of bulk superconductivity (LNSCO [179]) or dopant disorder (LCO+O, LSCO6+O). In addition, the phonon anomaly is unaffected by magnetic

fields (LSCO6+O, $YBa_2CuO_{6.6}$ [200]) and temperature (LBCO, LSCO15) [184]). Thus it appears to be an intrinsic, robust signature of doped cuprates near optimal doping.

If fluctuating stripes are the fundamental degrees of freedom relevant for the cuprates, it is appealing to draw a connection to Pair-Density-Wave superconductors [202]. In this system, the fundamental degrees of freedom are transverse charge fluctuations in an 'electronic liquid crystal' phase without long range order [203]. In this scenario, the phonon anomaly in materials without static stripe order is due to a matching of the phonon wavevector with, otherwise undetectable, short-range transverse stripe correlations. The $x = \frac{1}{8}$ anomaly then corresponds to the special case where stripes exhibit long-range order.

To summarize, we measured the in-plane Cu-O bond-stretching phonon in LSCO6+O and LCO+O and provided evidence for significant anomalous behavior. Since one sample (LCO+O) exhibits charge order [198] while the other (LSCO6+O) does not [199], and since the samples also have different magnetic spectra with distinct field dependencies [62, 199] we conclude that the phonon anomaly has no direct, trivial relationship to either magnetic or charge static order. In addition, the unique structural characteristics of oxygen-doped samples rule out a connection between the specific dopant species and the phonon anomaly. We proceed to conclude that the phonon anomaly is a signature of transverse charge stripe fluctuations, which is a common characteristic of the cuprate family and appears to be a pre-requisite to optimal superconductivity in these systems.

Chapter 9

Electronic Structure

In this brief chapter, we take a look at the Fermi surface as measured by Angle-Resolved Photoemission Spectroscopy (ARPES) on a sample of $La_2CuO_{4+\delta}$. Tha majority of the experimental work was performed with assistance from Johan Chang's group at the Laboratory for Quantum Matter Research (LQMR) in Zürich, Switzerland. I mention in particular Masafumi Horio, who helped me prepare the samples and did all of the data analysis. I was present at the measurements, but success would not have been possible without the expertise of the LQMR group.

While the analysis presented here is *very* preliminary, I include it because it is, to my knowledge, the first ARPES experiment performed on an oxygen doped $La_2CuO_{4+\delta}$ sample. Since these samples are known to phase separate electronically [92], we expect a superposition of a magnetic '$\frac{1}{8}$' phase and an optimally superconducting phase. It is possible that we could see some of this behavior in an ARPES experiment.

The fermi surface evolution of $La_{2-x}Sr_xCuO_4$ is shown in figure 9.1, indicating how the broken Fermi arcs at $\left(\frac{\pi}{2}, \frac{\pi}{2}\right)$ become connected at optimal doping. Since $La_2CuO_{4+\delta}$ is phase separated, we would expect to see signatures of either $x = 0.1$, $x = 0.15$ or both. The naive expectation would be a superposition of the two, removing any signature of the $\frac{1}{8}$ phase. In this context, I also mention the fact that $La_{1.48}Nd_{0.4}Sr_{0.12}CuO_4$ (stripe ordered, insulating) and $La_{1.85}Sr_{0.15}CuO_4$ (optimally doped, $T_c = 37\,K$) have curiously similar Fermi surfaces despite being electronically distinct [205].

9.1 Sample

The sample is a small piece ($\approx 1\,cm^3$) of $La_2CuO_{4+\delta}$, carefully cut with the c-axis vertical. Before cutting the sample, we characterized it with a Laue camera and magnetization measurements as shown in figure 9.2. When performing ARPES experiments, you need an atomically flat surface. Since La_2CuO_4 is a very brittle material, the only way to do this is by gluing on a small pin, knocking it off and hoping that the sample breaks in an atomically sharp way. Luckily, the 2-dimensional nature of the cuprates also translate to their structural integrity, so they are likely to cleave naturally at the CuO_2 interface. Before going to the ARPES experiment, the procedure was tested in the lab as shown in figure 9.3.

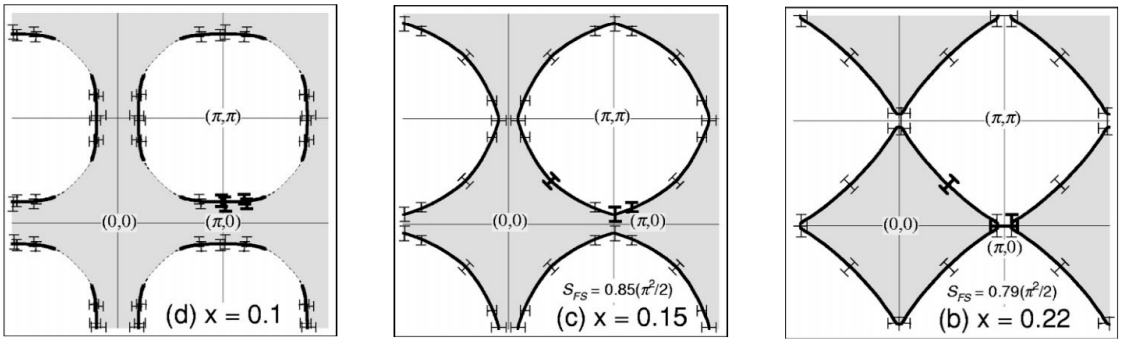

Figure 9.1: Fermi surface evolution of under- ($x = 0.1$), optimally- ($x = 0.15$) and overdoped ($x = 0.22$) $La_{2-x}Sr_xCuO_4$. From ref. [204].

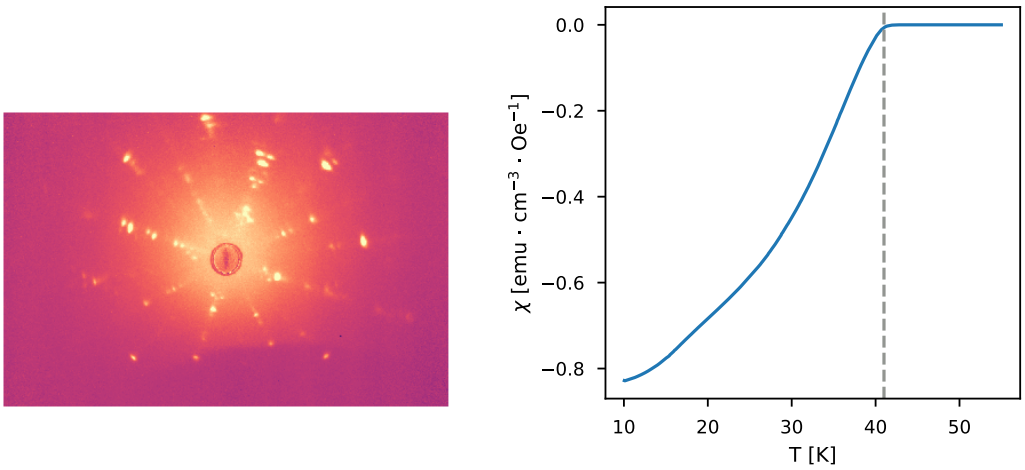

Figure 9.2: **Left:** Laue diffraction pattern of the $La_2CuO_{4+\delta}$ sample, aligned with the c axis vertical. **Right:** Vibrating Sample Magnetometry (VSM) performed on a Quantum Design MPMS. Normalization performed through $\chi = 4\pi \frac{\mu(1-N)}{V H_{\text{app}}}$, where μ is the measured signal, V is the volume, H_{app} is the applied field and N is the demagnetization factor. Vertical line marks the onset superconducting transition temperature $T_c = 41\,\text{K}$

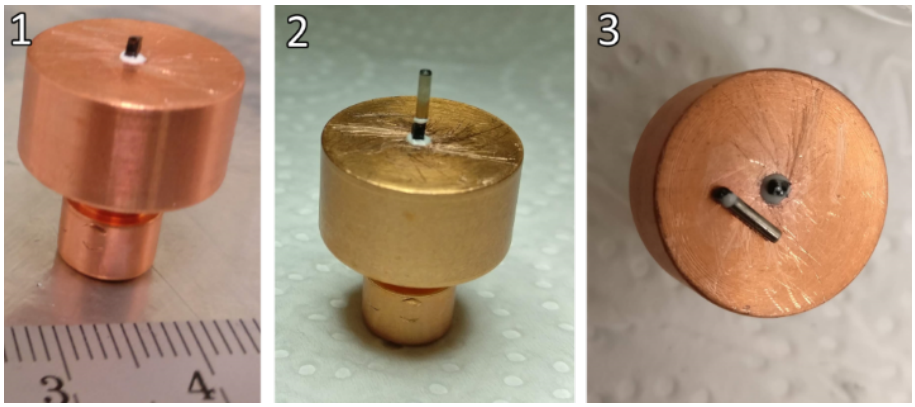

Figure 9.3: Cleaving procedure. **1:** The sample is mounted using Torr Seal Low Pressure Epoxy. **2:** A stainless steel pin ($L = 6\,\text{mm}$, $d = 1\,\text{mm}$) is glued to the top of the sample and subsequently **3:** knocked off with a regular screwdriver.

9.2 Experiment

ARPES experiments were carried out on the $La_2CuO_{4+\delta}$ sample at the Surface/Interface Spectroscopy (SIS) beamline at the Swiss Light Source. The sample was cleaved in situ at $\approx 20\,\text{K}$ under ultra high vacuum ($\leq 5 \times 10^{-11}\,\text{Torr}$) by employing the top-post technique as shown in figure 9.3. Cleaving in vacuum is essentially the same procedure as our ambient test-case, made possible with a screwdriver that we can control from outside the vacuum chamber. Ultraviolet ARPES spectra were recorded using a SCIENTA R4000 electron analyser with horizontal slit setting. All the data were recorded at the cleaving temperature. Figure 9.4 shows the Fermi surface map at $T = 22\,\text{K}$ recorded using circularly polarized 160 eV phonons. Detailed cut along the nodal direction with circularly polarized light is shown in Figure 9.5. A comparison of different photon polarizations along with data from $La_{1.77}Sr_{0.23}CuO_4$ is shown in Figure 9.6.

9.3 Summary

The area of the Fermi surface as shown in Figure 9.4 corresponds to a carrier (hole) doping $n_h = 0.16$ and a hopping parameter $\frac{t'}{t} \approx -0.14$, according to analysis performed by Masafumi Horio from the LMQR group. It turns out that the measured spectra as e.g. the cut shown in Figure 9.5 are very similar to what was observed by the LMQR group in overdoped $La_{1.77}Sr_{0.23}CuO_4$ [156]. There is thus no indication of '$\frac{1}{8}$-physics' which is generally characterized by the formation

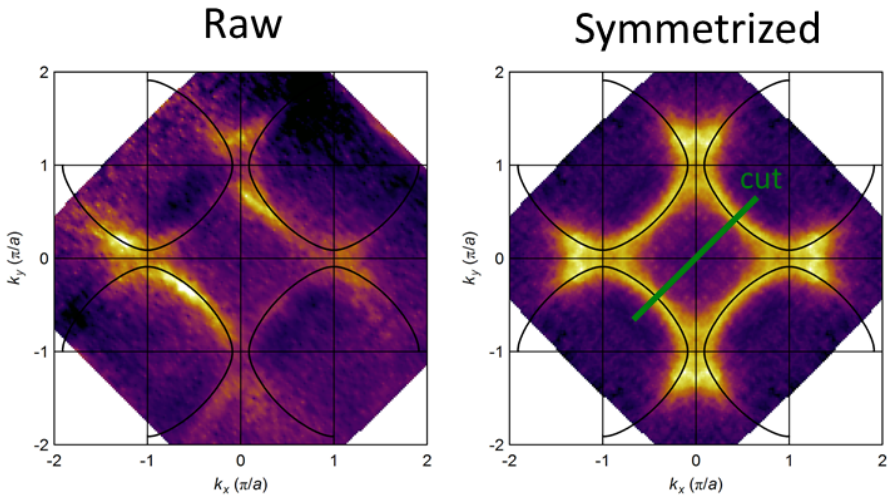

Figure 9.4: Fermi surface of at 22 K represented as raw and symmetrized data. k_x and k_y are in tetragonal (I4/mmm) units. The cut indicates the nodal direction as used in subsequent measurements of the band structure.

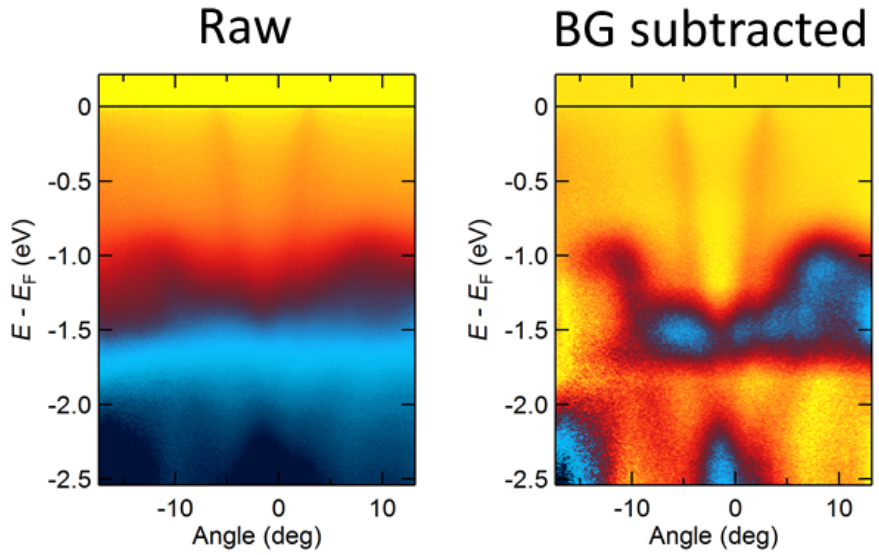

Figure 9.5: Cut along the nodal direction (see Figure 9.4) with 160 eV circularly polarized photons. The subtracted background is defined by the minimum Momentum Distribution Curve (MDC) intensity at each binding energy.

of Fermi arcs. We cannot however rule out that such arcs are not observed due to an unfavorable superposition of photoemission from the 1/8 phase and optimally doped phase in our sample.

By using different polarizations of light (linear horizontal and linear vertical) Figure 9.6 shows that we can separate the $d_{x^2-y^2}$ band from the d_{z^2} band. In the same figure, data from overdoped $La_{1.77}Sr_{0.23}CuO_4$ [156] is shown. The band structure is very similar except that the d_{z^2} band is moved down by about 0.2 eV. This could be due to an elongation of the c-axis, but while oxygen-doped samples are elongated when compared to the parent compound, $La_2CuO_{4+\delta}$ has a similar (or even smaller) c-axis when compared to $La_{1.77}Sr_{0.23}CuO_4$.

Thus there must be another explanation for the decreased energy of the d_z band further away from the Fermi energy. Maybe the coupling along c is weakened by oxygen-doping and this in fact enhancing T_c for oxygen doped samples? There is some evidence that relieving Josephson frustration along c gives 2D superconductivity with $T_c = 40$ K [206].

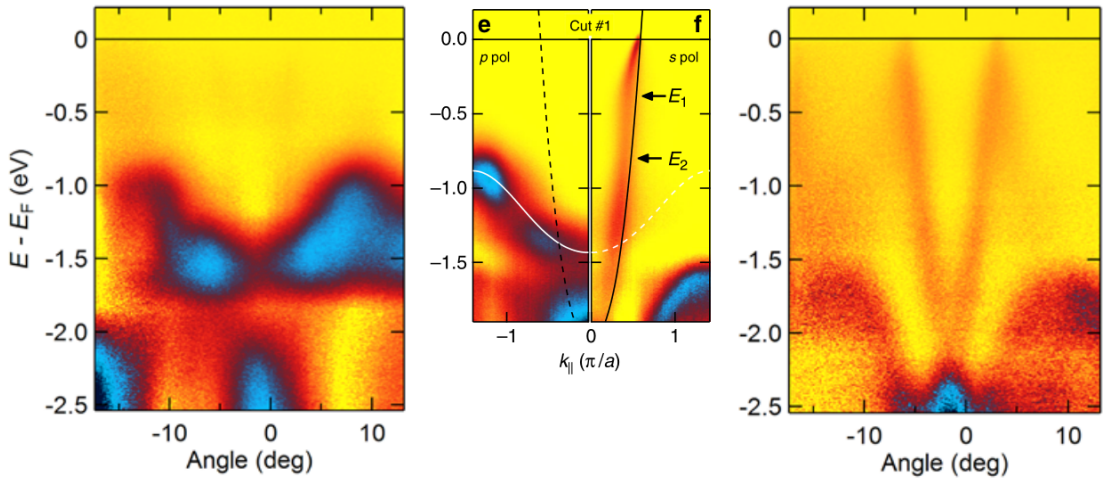

Figure 9.6: Cut along the nodal direction (see Figure 9.4) with 160 eV photons using different polarizations. **Left:** Linear horizontal polarization, showing clearly the d_{z^2} band dispersing from roughly -−1 eV to −1.5 eV. **Right:** Linear vertical polarization, showing the steeply dispersing $d_{x^2-y^2}$ band. **Center**: Comparison with data of $La_{1.77}Sr_{0.23}CuO_4$ from ref. [156], showing similar features to our sample.

Chapter 10

Conclusion

In this chapter, I will attempt to condense the thesis as a whole in order to discuss what was learned through the process of the various experimental and theoretical exercises. In a broad sense, the objective of this thesis is to investigate the effects of chemical disorder through different dopant species in La_2CuO_4 as introduced in chapter 1 with the methods presented in chapter 2. This was primarily done through DFT simulations being compared to a neutron scattering experiment. The challenge with this objective is that we know that the exact electronic structure of the cuprates, at the relevant doping levels, is an unsolved problem in condensed matter. DFT, in particular, has not been very successful in the underdoped part of the phase diagram and many-body methods are usually necessary to explain phenomena such as stripe order and fermi arcs.

Figure 10.1 attempts to visualize this problem by showing how superconductivity is squeezed between localized electrons giving rise to antiferromagnetic order and a fermi liquid with itinerant electrons and a continuous Fermi surface. The solution to this problem was to simply consider the two cases available to us and perform the calculations with this drawback in mind. In some sense, we are trying to figure out how well this level of theory can explain experimental observations. Exactly for this reason, I think a crucial part of this thesis is a careful evaluation of theory with experiment – essentially we need to know 'how wrong' the theory is.

Now, we are certainly not the first to consider La_2CuO_4 within a one-electron theory. Since DFT was well-established when the high-temperature superconductors were discovered, this methodology was applied right away (see review by Pickett [143]). Various levels of theory have applied to La_2CuO_4, including pure Hartree-Fock [207], and semi-local potentials [144]. Correlated phenomena, such as stripes [147] and broken up Fermi arcs [208, 209] have even been calculated within

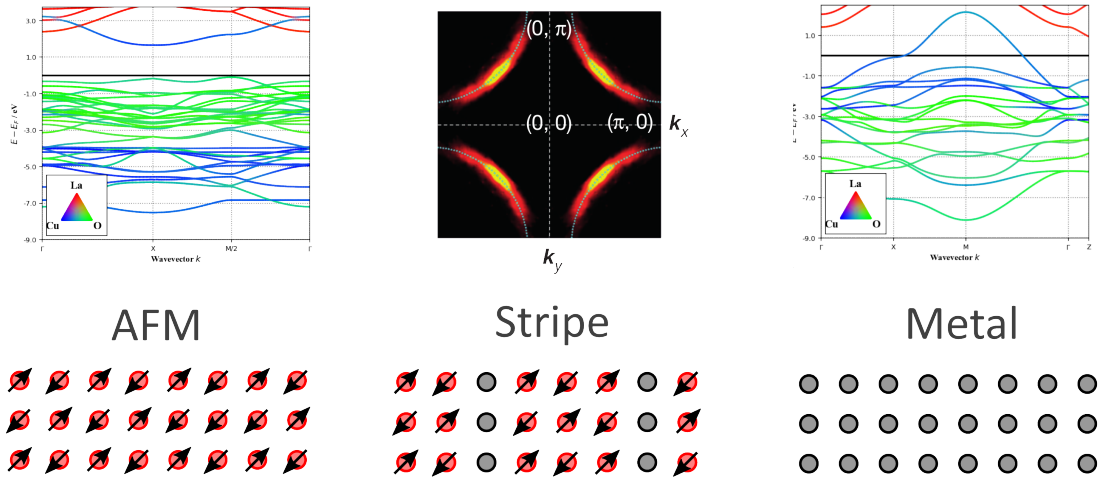

Figure 10.1: Schematic of the electronic structure as a function of hole doping n_h. As one moves from left to right, n_h increases. On the left we have the undoped compound where there is a gap in electronic density of states due to the antiferromagnetic ground state. As doping is increased, the strong antiferromagnetic interactions are disrupted and novel phenomena such as stripe order and broken Fermi arcs emerge [37]. Finally, on the right, the hole doping is sufficient such that the material becomes a normal metal and the strong correlations are destroyed. The electronic band structures are calculated and presented in chapter 3.

DFT, albeit with ad-hoc methods such as DFT+U.

In this thesis, I make no attempt to contribute to this discussion. Rather, I prioritize getting accurate inter-atomic *forces* such that we get the best possible representation of the phonon spectrum. We thus stick to the generally accepted GGA level of theory. As we saw in chapter 3, some experimentation lead us to the PBESol functional and a significantly increased plane-wave cutoff in order to get reasonable acoustic phonons.

Within this framework, it was possible to get a good description of the unstable modes related to the structural phase transitions observed in La_2CuO_4. However, it turns out that the low-temperature tetragonal (LTT) phase is the 'most stable' structural phase both with respect to total energy and unstable phonons. Since this LTT phase is known to be suppressing superconductivity, our calculations are consistent with a picture where superconductivity competes with this structural phase and thus prevents the structural phase transition. In this context, I remark that the isostructural, non-superconducting compound La_2NiO_4 is LTT at low temperatures [87].

While more experimentation with structural phases, functionals and computational parameters is always desireable, I decided to move on with the relatively successful description of phonon dynamics in La_2CuO_4 within DFT. In chapter 4, we use these simulations to approach the actual objective of treating doped La_2CuO_4 as a defect structure with molecular dynamics. Our analysis of the trajectories show that oxygen interstitials tend towards a LTT-like structure, while undoped and strontium-doped compounds stay LTO-like. While our simulation box and total simulation time is somewhat limited, these results is a good indication of *distinct* dynamics associated with interstitials. Importantly, these distinct dynamics are associated with a modification of the phonon density-of-states which can be observed experimentally.

10.1 Oxygen Interstitial Observables

A large part of this thesis has been dedicated to finding signatures of oxygen interstitials. As mentioned in the introduction, these materials appear to optimize the superconducting transition temperature T_c and it is suspected that the mobile, interstitial nature might be important for the elevated T_c. As we also show in chapter 5, the 'annealed doping' [84] associated with interstitial oxygen is mainly observed in diffraction experiments. Remarkably, our high-quality PDF measurement shows almost no signature of oxygen interstitials. The superstructures observed in single-crystal measurements are so strong that this absence must be due to either rotational averaging or because powdered samples simply don't have these superstructures.

However, the dynamics of the *same* powdered samples (measured in chapter 7) does have a signature of oxygen interstitials through a broadening of the phonon DOS in the 10 meV to 25 meV range. We can qualitatively identify this broadening, through our simulations, as a signature of oxygen disorder. In the case of strontium-doping, on the other hand, we see a sharpening of features which cannot be explained through our simulations. It is possible that the electronic structure of the LSCO $x = 0.03$ sample modifies the phonon spectrum in a novel way, but more experiments are required to understand the observations. The fact that we can identify the features in this manner suggests that our model captures some of the dynamics associated with interstitials. This, in extension, is evidence for LTT-like tilts in $La_2CuO_{4+\delta}$ in a sample that is always observed to be structurally LTO.

This intimate relationship to an incipient tetragonal phase is also observed in our measurements of soft phonons in chapter 6. While none of these measurements are conclusive on their own, taken together they point to LTT-like behavior being important in $La_2CuO_{4+\delta}$ (LCO+O). To briefly recap, I have found that LCO+O features

1. LTT-like tilt dynamics.
2. Instability towards LTT which is stabilized at T_c.
3. Phase separation into distinct $n_h = \frac{1}{8}$ and optimally superconducting phases [91, 92].

Allowing myself to speculate wildly, this is consistent with a scenario where $La_2CuO_{4+\delta}$ is able to optimize the relationship between a stripe phase and a superconducting phase by leveraging LTT-like tilts. In this way, the annealed oxygen order, optimally superconducting phase can be 'close' to the static stripe phase without actually being pinned by LTT symmetry. This is consistent with a situation where 'stripe degrees of freedom' are necessary for superconductivity, but where we need to be sufficiently far away from static order. Essentially, one could think of a situation where the mobile dopants in $La_2CuO_{4+\delta}$ self-organize in a way that optimizes the conditions for these

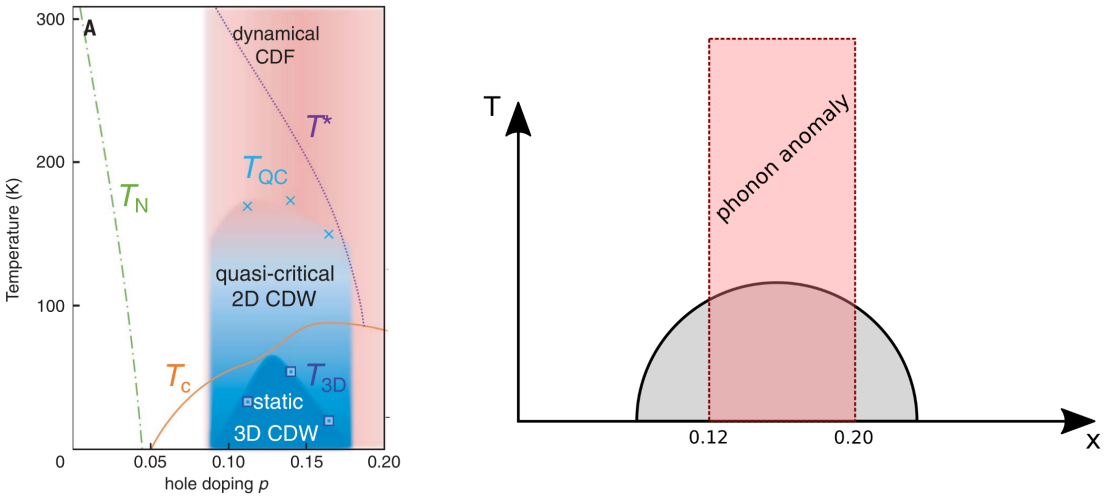

Figure 10.2: **Left:** $YBa_2Cu_3O_{7-\delta}$ and $Nd_{1+x}Ba_{2-x}Cu_3O_{7-\delta}$ phase diagram showing charge fluctuations in a wide doping/temperature range [182]. **Right:** Schematic of where the phonon anomaly appears in a generalized cuprate phase diagram (see dicussion in chapter 8).

competing orders. A similar idea has been put forward by Poccia et al. [210], where it is suggested that grain boundaries help optimize this mechanism.

10.2 Phonons and Stripes

The relationship to stripe order in LCO+O was also investigated through measurements of the phonon anomaly in chapter 8. Contrary to what we saw in the preceding chapters, the phonon anomaly appears to be unrelated to the type of dopant or stripe order. In fact, when reviewing the samples where the phonon anomaly has been observed it appears to be a signature of doping $0.12 < n_h < 0.20$.

We interpret this as fluctuations of charge stripes, i.e. the stripe degrees of freedom mentioned above. Following the logic from before, this then suggests that charge fluctuations are a necessary but not sufficient condition for optimal superconductivity. In addition, the anomaly persists to high temperatures, so the phenomenon must be intrinsic to the doped samples in a large temperature range.

Very recently, resonant X-ray methods were used to determine 'charge density fluctuations' (CDF) in samples of $YBa_2Cu_3O_{7-\delta}$ and $Nd_{1+x}Ba_{2-x}Cu_3O_{7-\delta}$ over a large doping range. Similar to what has been observed in the phonon anomaly, the CDF's are constrained in the phase diagram, but persists well above the pseudogap temperature T^*. Figure 10.2 shows a summary of their results and a schematic of where one finds the phonon anomaly. The similarity of these phenomena strongly supports the suggested [188] connection between the phonon anomaly and dynamic stripes.

Finally, we discovered that the electronic structure as observed by ARPES in $La_2CuO_{4+\delta}$ is remarkably similar to that of overdoped $La_{1.77}Sr_{0.23}CuO_4$. Since $La_2CuO_{4+\delta}$ is known to phase separate into stripe ordered and superconducting phases, this is interpreted as a superposition of the two phenomena in the ARPES spectrum in chapter 9

Appendix A

PhononNeutron

During the thesis, a selection of Python classes were developed with the intention of generalizing some of the tasks required to get the correct neutron weights out of simulations. While software such as MDANSE [211] does a good job with respect to molecular dynamics, I wanted something focussed on analyzing phonons specifically from different levels of theory (MD and 'Frozen Phonons'). The code be found at https://github.com/tejsner/phonon_neutron and features two modules

1. md_tools.py
2. phonopy_tools.py

md_tools.py

This module is used to perform various task on molecular dynamics trajectories as obtained from VASP. VASP trajectories are saved in `XDATCAR` files, which can be analysed, for example, in the following way:

```
1 from md_tools import VaspMD
2 md_data = VaspMD('XDATCAR', dt=1)
3 md_data.compute_velocity()
4 md_data.compute_temperature()
5 md_data.compute_pdf()
6 md_data.compute_dos(sigma=0.5)
```

Line 1 simply imports the module, line 2 reads the VASP trajectory and lines 3-6 computes velocity, temperature, the pair distribution function and the phonon density of states with a Gaussian smearing width of $\sigma = 0.5\,\text{meV}$. Everything is now saved in the `md_data` object, and can be plotted, for example, using matplotlib in the following way:

```
1  import matplotlib.pytplot as plt
2  # temperature
3  plt.figure()
4  plt.plot(md_data.vtime, md_data.temperature)
5  # PDF
6  plt.figure()
7  plt.plot(md_data.pdf_x, md_data.pdf)
8  # DOS
9  plt.figure()
10 plt.plot(md_data.omega, md_data.dos)
```

Many additional features are present in this module and can be found by inspecting the code. A current limitation is that it only contains neutron cross sections for the atomic species used in this thesis (La, Sr, Cu, O), but it is a fairly simple procedure to add scattering lengths at the top of `md_tools.py`.

phonopy_tools.py

This module contains a number of helper functions used to manipulate output from a Phonopy [126, 131] calculation. In particular, I wanted easy access to neutron-weighted band structure plotted in different ways as shown throughout this thesis (in particular chapter 6). In order for the code to load Phonopy data, we require two files

1. `phonopy_disp.yaml`: Contains information about the input structure and phonon calculation.
2. `FORCE_SETS`: Contains the force constants obtained from DFT calculations.

With those files, neutron weighted band structure plots can be generated in the following way

```
1 from phonopy_tools import PhonopyNeutron
2 import matplotlib.pyplot as plt
3 f, ax = plt.subplots()
4 ph_data = PhonopyNeutron('phonopy_disp.yaml', 'FORCE_SETS')
5 ph_data.set_path([[0,0,0],[0.5,0.5,0],[1,0,0],[0,0,0]])
6 ph_data.set_labels(['$\Gamma$', 'X', 'M', '$\Gamma$'])
7 ph_data.compute_bands()
8 ph_data.compute_neutron_bands()
9 ph_data.plot_neutron_bands(ax, plotype='lines', sigma=0.2)
```

Line 1 imports the module, and line 4 imports the Phonopy data. In order to get the band structure, it is necessary to set the path in reciprocal space that you want to plot as shown in line 5. The coordinates are here with respect to the input cell, so not necessarily the primitive cell. Line 5 simply labels these paths, line 6 and 7 computes the bands and line 8 plots them. A different option is to plot in 2 dimensions of $\boldsymbol{Q}$ at a selected energy as we also saw in chapter 6. An example of how to get this plot is:

```
1 from phonopy_tools import PhonopyNeutron, get_xy_colormap
2 import matplotlib.pyplot as plt
3 ph_data = PhonopyNeutron('phonopy_disp.yaml', 'FORCE_SETS')
4 cmap_data = lco.get_sqw_xy([1,5,-1,3], 100, 100)
5 x, y, I = get_xy_colormap(cmap_data, 9, sigma=1)
6 plt.pcolor(x, y, I)
```

We load the modules in line 1, and the Phonopy data in line 3. In line 4, we generate the $S(\boldsymbol{Q}, \omega)$ in a grid where Q_x ranges from 1 to 5 and Q_y ranges from -1 to 3 with a grid size of 100 in each direction. The evaluation of this can be quite slow, so start with a small grid size. Finally, the `get_xy_colormap()` function uses this data to generate a colormap at a certain energy with some fixed resolution σ (in meV).

Appendix B

Low energy phonons, additional plots

This appendix contains the plot and fits used to compare low energy phonons with simulation data in chapter 6. Figures B.1, B.2, B.3 and B.4 is data obtained from interpolation of FlatCone data in various directions. Figures B.5, B.6, B.7, B.8 and B.9 show the comparison of this data with simulations in various structural and electonic phases.

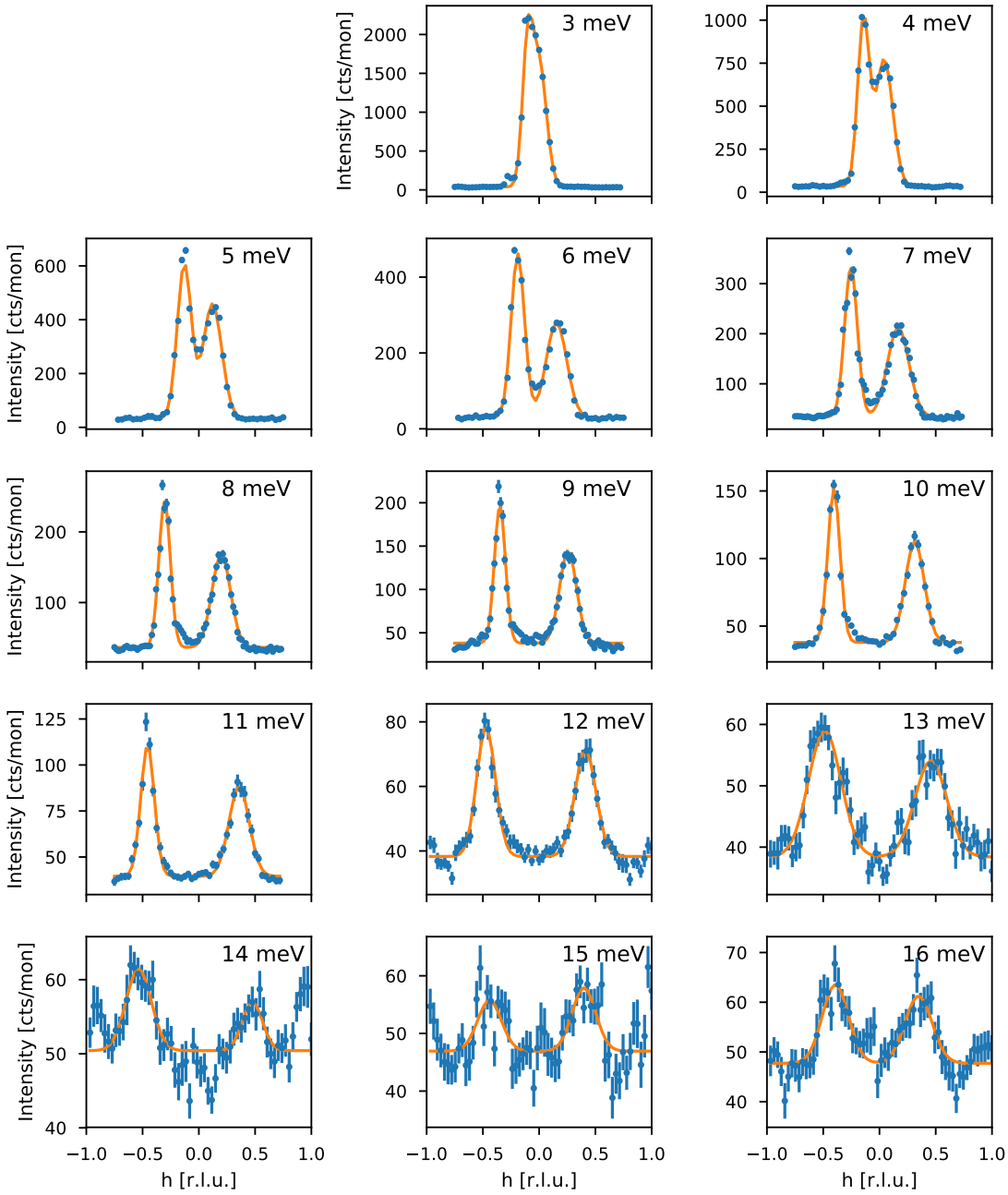

Figure B.1: Interpolated data from FlatCone measurements of $La_{1.94}Sr_{0.06}CuO_{4+\delta}$ taken around the (400) peak in the transverse direction. Fits are two Gaussians.

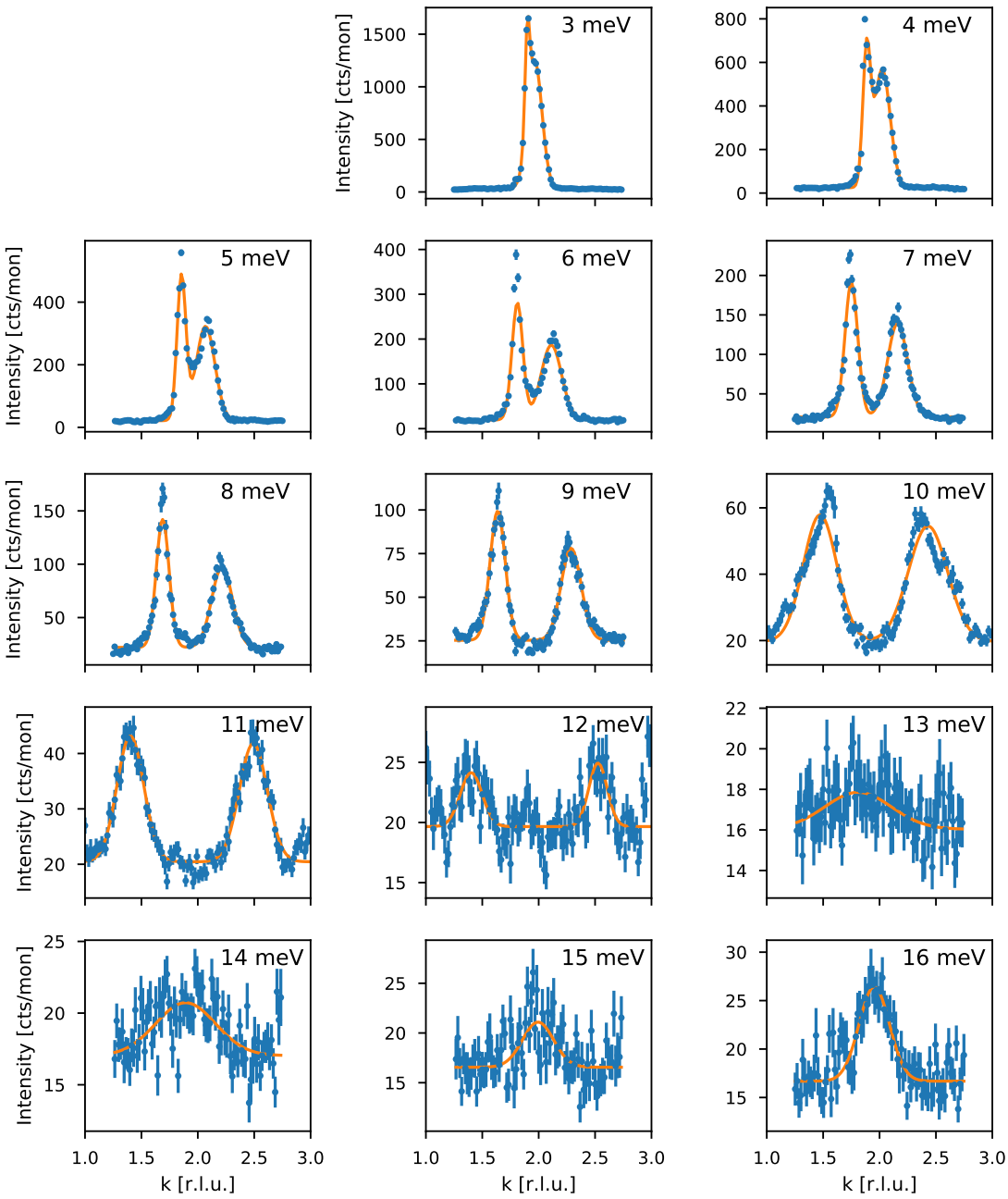

Figure B.2: Interpolated data from FlatCone measurements of $La_{1.94}Sr_{0.06}CuO_{4+\delta}$ taken around the (200) peak in the transverse direction. Fits are two Gaussians.

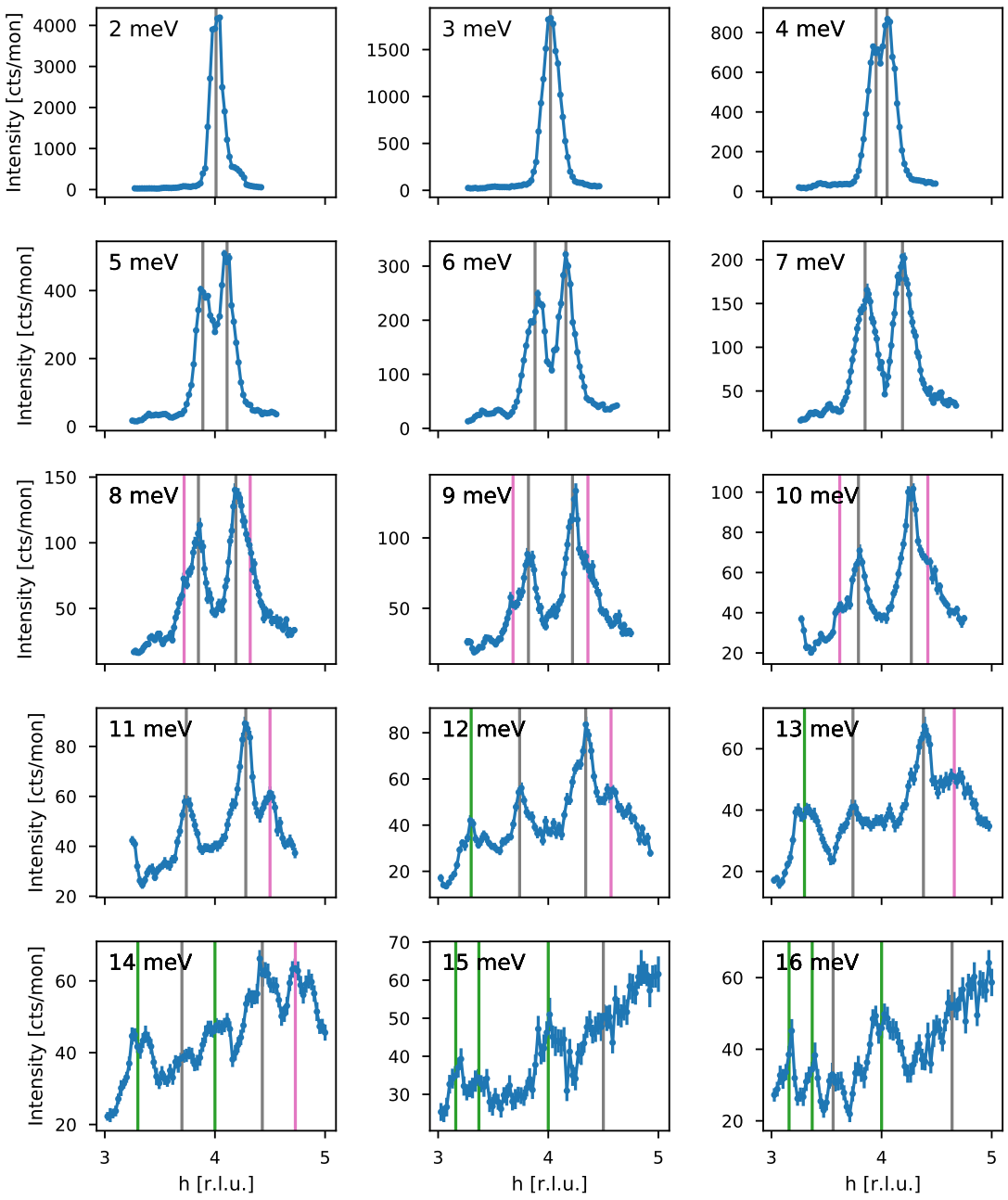

Figure B.3: Interpolated data from FlatCone measurements of $La_{1.94}Sr_{0.06}CuO_{4+\delta}$ taken around the (400) peak in the longitudinal direction.

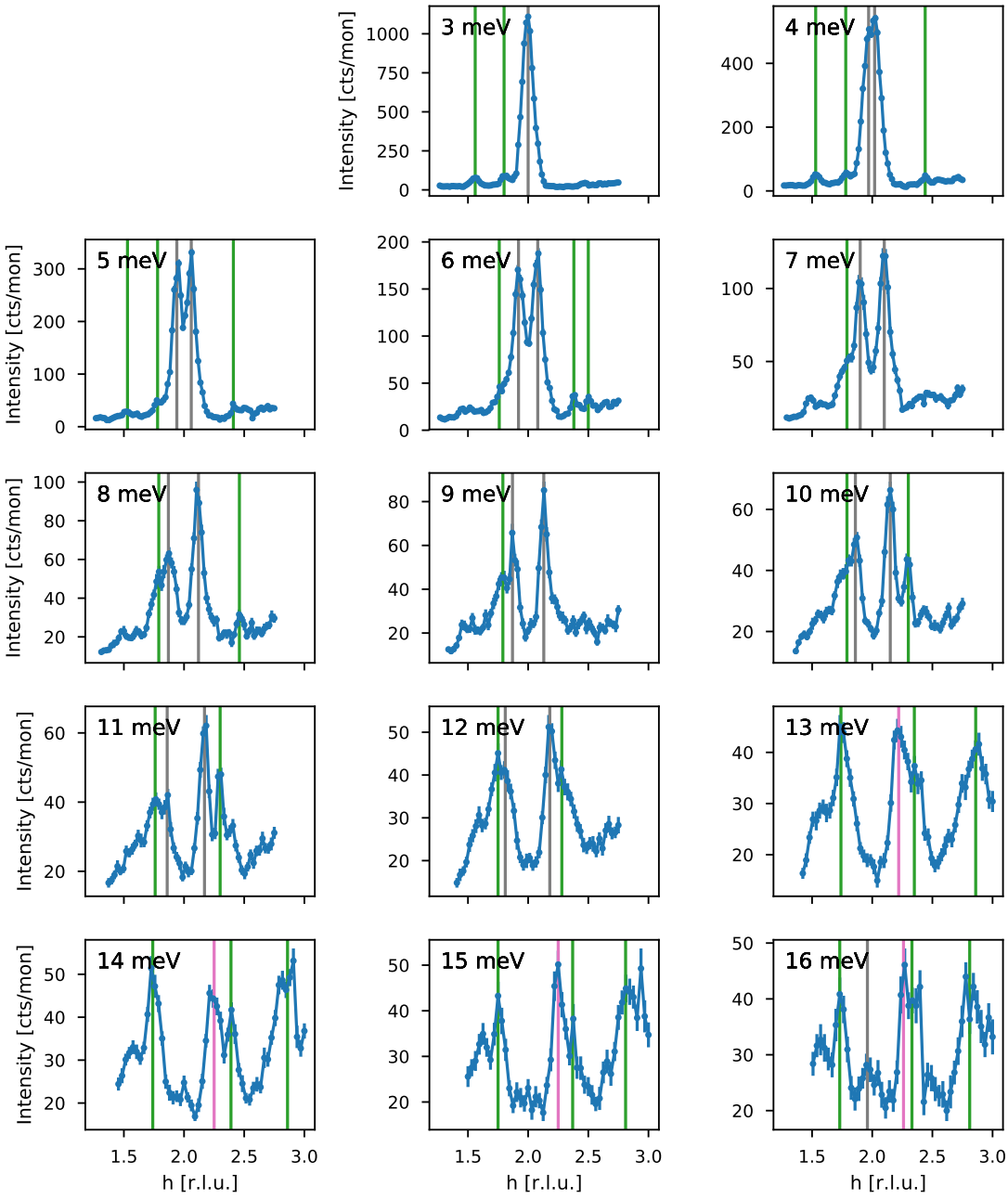

Figure B.4: Interpolated data from FlatCone measurements of $La_{1.94}Sr_{0.06}CuO_{4+\delta}$ taken around the (220) peak in the longitudinal direction.

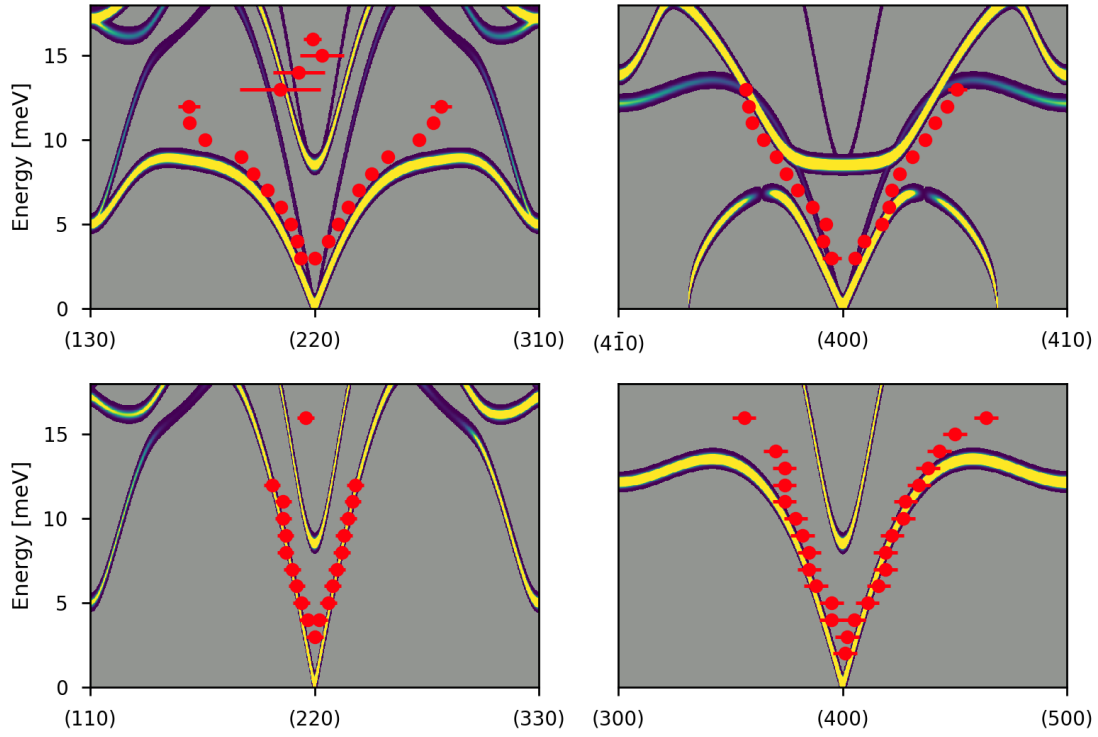

Figure B.5: Red datapoints are measured by neutron spectroscopy using a Flatcone analyser and lines are neutron weighted simulation data. HTT AFM simulation data.

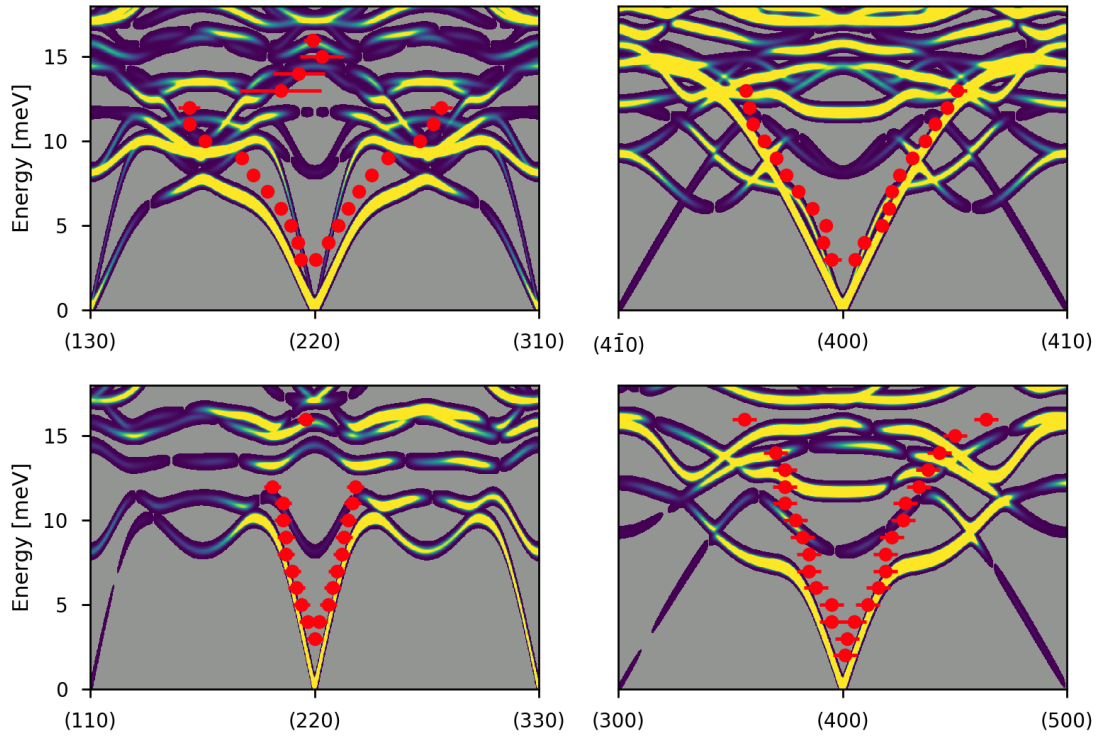

Figure B.6: Flatcone dispersion and neutron weighted simulation data. LTT AFM simulation data.

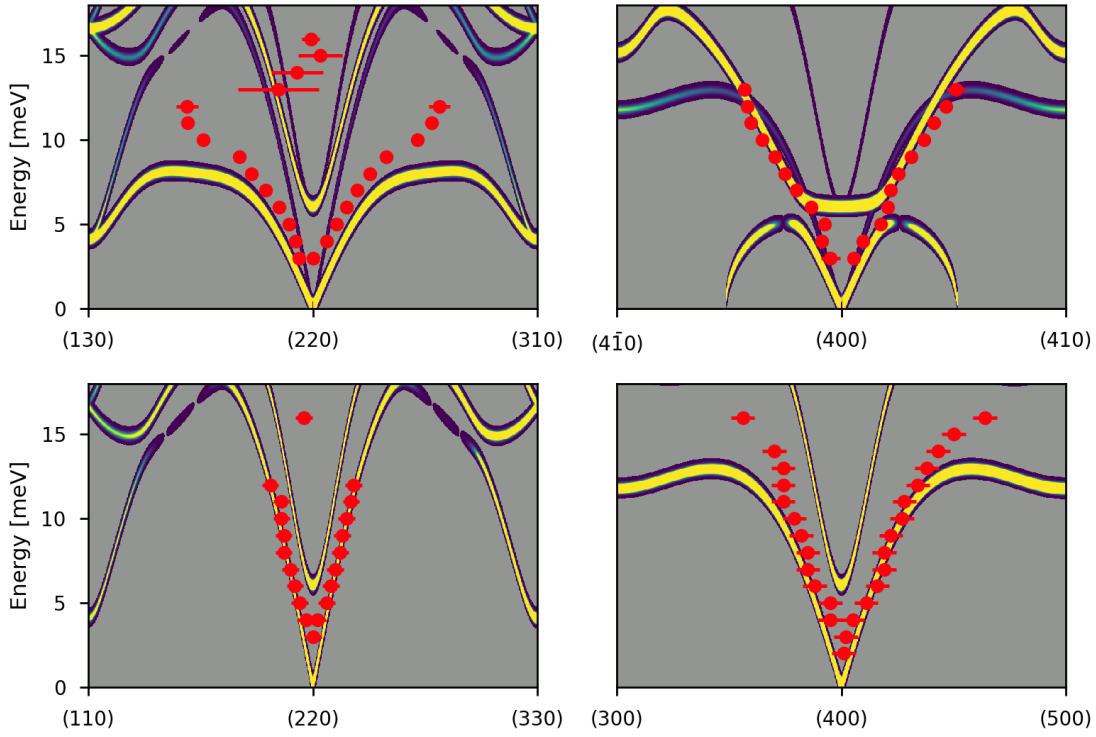

Figure B.7: Flatcone dispersion and neutron weighted simulation data. LTT AFM simulation data.

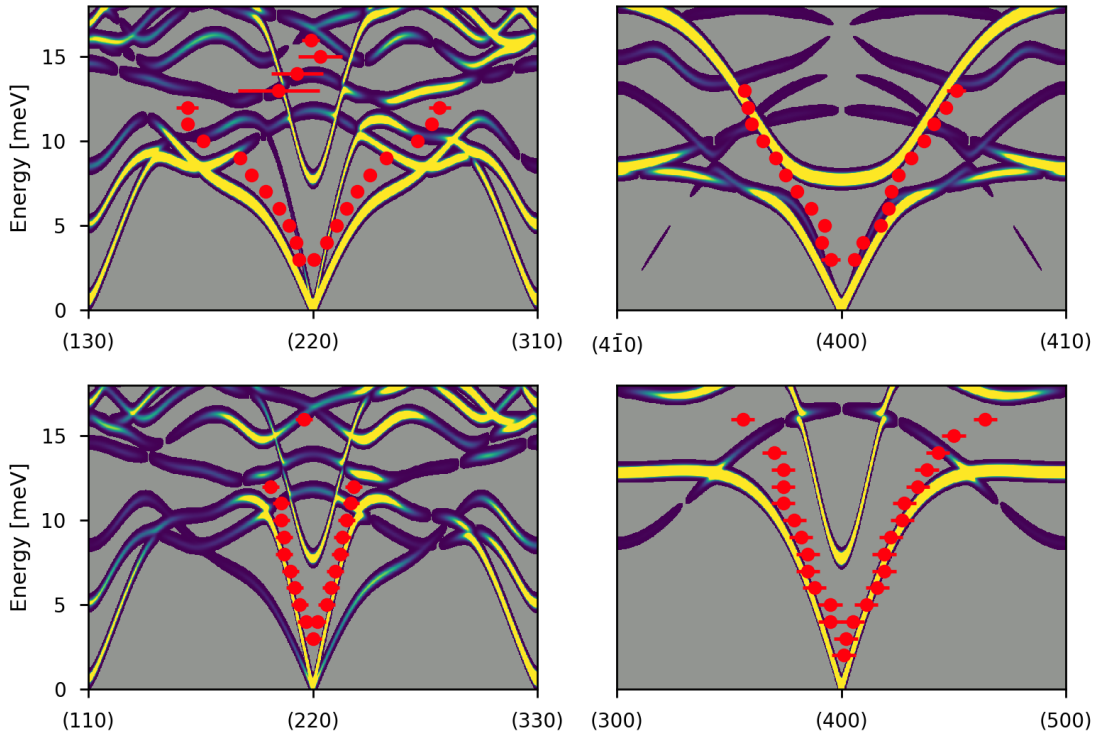

Figure B.8: Flatcone dispersion and neutron weighted simulation data. LTO metal simulation data.

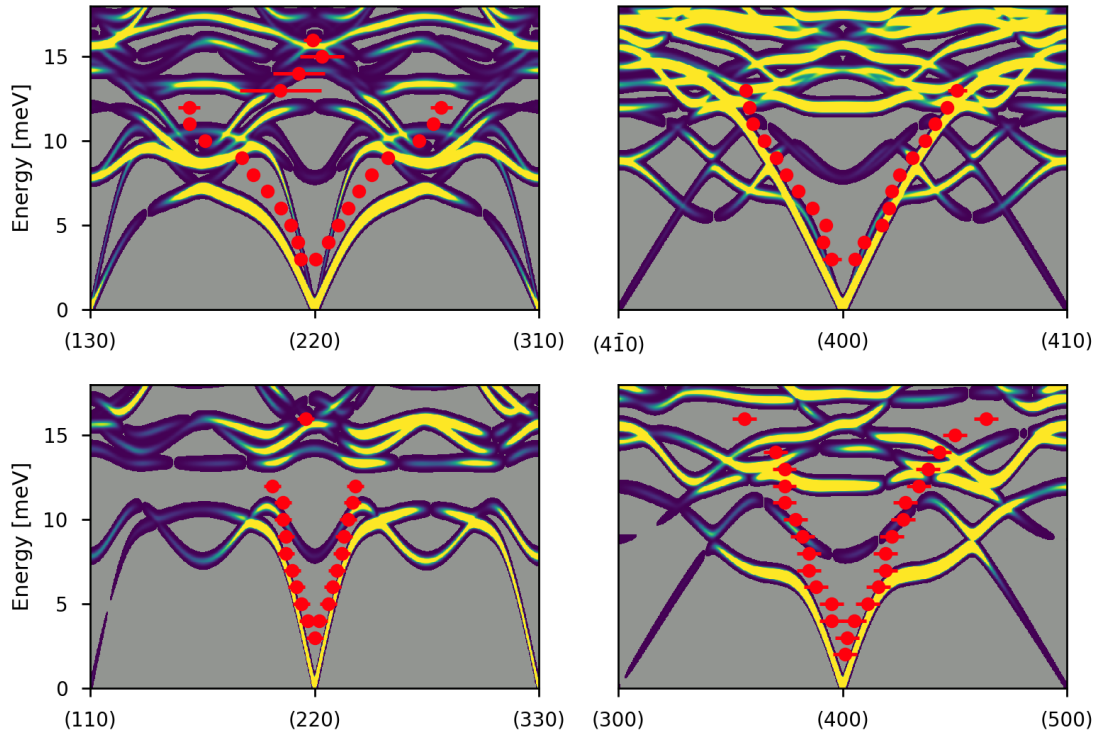

Figure B.9: Flatcone dispersion and neutron weighted simulation data. LTT Metal simulation data.

Appendix C

Phonon DOS, additional plots

This appendix contains additional temperatures of the density of states measurements performed in chapter 7. Figure C.1 contains data for 60 K and C.2 contains data for 300 K

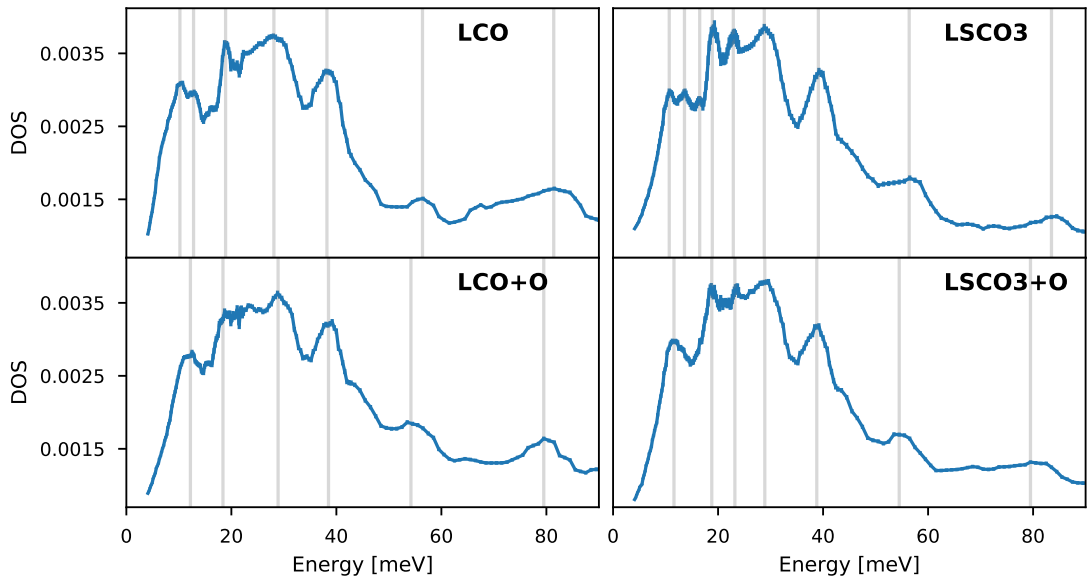

Figure C.1: Phonon density of states of all four samples at at 60 K

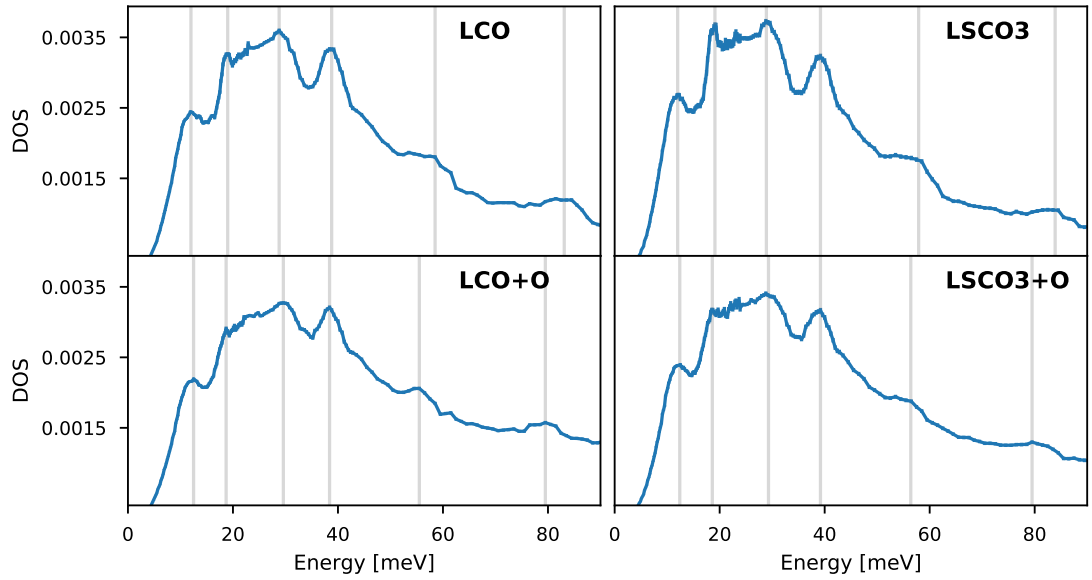

Figure C.2: Phonon density of states of all four samples at at 300 K

Bibliography

[1] J. File and R. G. Mills, Phys. Rev. Lett. **10**, 93–96 (1963).

[2] D. van Delft and P. Kes, Physics Today **63**, 38–43 (2010).

[3] *File:efektmeisnera.svg*, https://commons.wikimedia.org/wiki/File:EfektMeisnera.svg (visited on 06/12/2019).

[4] W. Meissner and R. Ochsenfeld, Naturwissenschaften **21**, 787–788 (1933).

[5] F. London and H. London, Proceedings of the Royal Society of London. Series A, Mathematical and Physical Sciences **149**, 71–88 (1935).

[6] C. Kittel, *Introduction to solid state physics*, 8th ed. (Wiley, 2005).

[7] V. L. Ginzburg and L. D. Landau, 'On the Theory of Superconductivity', in *On Superconductivity and Superfluidity: A Scientific Autobiography*, edited by V. L. Ginzburg (Springer, Berlin, Heidelberg, 2009), pp. 113–137.

[8] A. A. Abrikosov, Journal of Physics and Chemistry of Solids **2**, 199–208 (1957).

[9] K. Tomimoto, I. Terasaki, A. I. Rykov, T. Mimura and S. Tajima, Phys. Rev. B **60**, 114–117 (1999).

[10] F. S. Wells, A. V. Pan, X. R. Wang, S. A. Fedoseev and H. Hilgenkamp, Scientific Reports **5**, 8677 (2015).

[11] R. Doll and M. Näbauer, Phys. Rev. Lett. **7**, 51–52 (1961).

[12] B. S. Deaver and W. M. Fairbank, Phys. Rev. Lett. **7**, 43–46 (1961).

[13] J. Bardeen, L. N. Cooper and J. R. Schrieffer, Phys. Rev. **108**, 1175–1204 (1957).

[14] I. Giaever, Phys. Rev. Lett. **5**, 147–148 (1960).

[15] I. Giaever, Phys. Rev. Lett. **5**, 464–466 (1960).

[16] B. D. Josephson, Physics Letters **1**, 251–253 (1962).

[17] R. C. Jaklevic, J. Lambe, J. E. Mercereau and A. H. Silver, Phys. Rev. **140**, A1628–A1637 (1965).

[18] E. Maxwell, Phys. Rev. **78**, 477 (1950).

[19] C. A. Reynolds, B. Serin, W. H. Wright and L. B. Nesbitt, Phys. Rev. **78**, 487–487 (1950).

[20] J. de Launay, Phys. Rev. **93**, 661–665 (1954).

[21] A. P. Drozdov, M. I. Eremets, I. A. Troyan, V. Ksenofontov and S. I. Shylin, Nature **525**, 73–76 (2015).

[22] J. Nagamatsu, N. Nakagawa, T. Muranaka, Y. Zenitani and J. Akimitsu, Nature **410**, 63–64 (2001).

[23] J. G. Bednorz and K. A. Müller, en, Z. Physik B - Condensed Matter **64**, 189–193 (1986).

[24] M. K. Wu, J. R. Ashburn, C. J. Torng, P. H. Hor, R. L. Meng, L. Gao, Z. J. Huang, Y. Q. Wang and C. W. Chu, Phys. Rev. Lett. **58**, 908–910 (1987).

[25] R. M. Hazen, C. T. Prewitt, R. J. Angel, N. L. Ross, L. W. Finger, C. G. Hadidiacos, D. R. Veblen, P. J. Heaney, P. H. Hor, R. L. Meng, Y. Y. Sun, Y. Q. Wang, Y. Y. Xue, Z. J. Huang, L. Gao, J. Bechtold and C. W. Chu, Phys. Rev. Lett. **60**, 1174–1177 (1988).

[26] Z. Z. Sheng, A. M. Hermann, A. El Ali, C. Almasan, J. Estrada, T. Datta and R. J. Matson, Phys. Rev. Lett. **60**, 937–940 (1988).

[27] R. M. Hazen, L. W. Finger, R. J. Angel, C. T. Prewitt, N. L. Ross, C. G. Hadidiacos, P. J. Heaney, D. R. Veblen, Z. Z. Sheng, A. El Ali and A. M. Hermann, Phys. Rev. Lett. **60**, 1657–1660 (1988).

[28] S. S. P. Parkin, V. Y. Lee, E. M. Engler, A. I. Nazzal, T. C. Huang, G. Gorman, R. Savoy and R. Beyers, Phys. Rev. Lett. **60**, 2539–2542 (1988).

[29] T. Kaneko, H. Yamauchi and S. Tanaka, en, Physica C: Superconductivity **178**, 377–382 (1991).

[30] S. N. Putilin, E. V. Antipov, O. Chmaissem and M. Marezio, en, Nature **362**, 226–228 (1993).

[31] A. Schilling, M. Cantoni, J. D. Guo and H. R. Ott, en, Nature **363**, 56–58 (1993).

[32] Suryadijaya, T. Sasagawa and H. Takagi, Physica C: Superconductivity, Proceedings of the 17th International Symposium on Superconductivity (ISS 2004) **426-431**, 402–406 (2005).

[33] W. Ruan, X. Li, C. Hu, Z. Hao, H. Li, P. Cai, X. Zhou, D.-H. Lee and Y. Wang, Nature Physics **14**, 1178 (2018).

[34] S. Chakravarty, H.-Y. Kee and K. Völker, en, Nature **428**, 53–55 (2004).

[35] M. Hücker, Physica C: Superconductivity, Stripes and Electronic Liquid Crystals in Strongly Correlated Materials **481**, 3–14 (2012).

[36] D. C. Peets, J. D. F. Mottershead, B. Wu, I. S. Elfimov, R. Liang, W. N. Hardy, D. A. Bonn, M. Raudsepp, N. J. C. Ingle and A. Damascelli, New J. Phys. **9**, 28–28 (2007).

[37] B. Keimer, S. A. Kivelson, M. R. Norman, S. Uchida and J. Zaanen, Nature **518**, 179–186 (2015).

[38] H. Alloul, T. Ohno and P. Mendels, Phys. Rev. Lett. **63**, 1700–1703 (1989).

[39] C. C. Homes, T. Timusk, R. Liang, D. A. Bonn and W. N. Hardy, Phys. Rev. Lett. **71**, 1645–1648 (1993).

[40] J. W. Loram, K. A. Mirza, J. R. Cooper and W. Y. Liang, Phys. Rev. Lett. **71**, 1740–1743 (1993).

[41] V. J. Emery and S. A. Kivelson, Nature **374**, 434–437 (1995).

[42] P. Curty and H. Beck, Phys. Rev. Lett. **91**, 257002 (2003).

[43] S. Martin, A. T. Fiory, R. M. Fleming, L. F. Schneemeyer and J. V. Waszczak, Phys. Rev. B **41**, 846–849 (1990).

[44] A. Legros, S. Benhabib, W. Tabis, F. Laliberté, M. Dion, M. Lizaire, B. Vignolle, D. Vignolles, H. Raffy, Z. Z. Li, P. Auban-Senzier, N. Doiron-Leyraud, P. Fournier, D. Colson, L. Taillefer and C. Proust, Nature Physics, 1 (2018).

[45] A. Damascelli, Z. Hussain and Z.-X. Shen, Rev. Mod. Phys. **75**, 473–541 (2003).

[46] J. Osterwalder, 'Electron Based Methods: 3.2.2 Photoelectron Spectroscopy and Diffraction', in *Surface and Interface Science* (John Wiley & Sons, Ltd, 2014), pp. 151–214.

[47] C. E. Matt, D. Sutter, A. M. Cook, Y. Sassa, M. Månsson, O. Tjernberg, L. Das, M. Horio, D. Destraz, C. G. Fatuzzo, K. Hauser, M. Shi, M. Kobayashi, V. N. Strocov, T. Schmitt, P. Dudin, M. Hoesch, S. Pyon, T. Takayama, H. Takagi, O. J. Lipscombe, S. M. Hayden, T. Kurosawa, N. Momono, M. Oda, T. Neupert and J. Chang, Nature Communications **9**, 972 (2018).

[48] T. Yoshida, M. Hashimoto, I. M. Vishik, Z.-X. Shen and A. Fujimori, J. Phys. Soc. Jpn. **81**, 011006 (2011).

[49] D. L. Feng, A. Damascelli, K. M. Shen, N. Motoyama, D. H. Lu, H. Eisaki, K. Shimizu, J.-i. Shimoyama, K. Kishio, N. Kaneko, M. Greven, G. D. Gu, X. J. Zhou, C. Kim, F. Ronning, N. P. Armitage and Z.-X Shen, Phys. Rev. Lett. **88**, 107001 (2002).

[50] C. C. Tsuei and J. R. Kirtley, Rev. Mod. Phys. **72**, 969–1016 (2000).

[51] A. P. Mackenzie and Y. Maeno, Rev. Mod. Phys. **75**, 657–712 (2003).

[52] R. Joynt and L. Taillefer, Rev. Mod. Phys. **74**, 235–294 (2002).

[53] N. S. Headings, S. M. Hayden, R. Coldea and T. G. Perring, Phys. Rev. Lett. **105**, 247001 (2010).

[54] K. Yamada, C. H. Lee, K. Kurahashi, J. Wada, S. Wakimoto, S. Ueki, H. Kimura, Y. Endoh, S. Hosoya, G. Shirane, R. J. Birgeneau, M. Greven, M. A. Kastner and Y. J. Kim, Phys. Rev. B **57**, 6165–6172 (1998).

[55] M. Enoki, M. Fujita, T. Nishizaki, S. Iikubo, D. K. Singh, S. Chang, J. M. Tranquada and K. Yamada, Phys. Rev. Lett. **110**, 017004 (2013).

[56] Y. Drees, D. Lamago, A. Piovano and A. C. Komarek, en, Nature Communications **4**, 2449 (2013).

[57] Y. Drees, Z. W. Li, A. Ricci, M. Rotter, W. Schmidt, D. Lamago, O. Sobolev, U. Rütt, O. Gutowski, M. Sprung, A. Piovano, J. P. Castellan and A. C. Komarek, en, Nature Communications **5**, 5731 (2014).

[58] E. Demler, S. Sachdev and Y. Zhang, Phys. Rev. Lett. **87**, 067202 (2001).

[59] Y. Zhang, E. Demler and S. Sachdev, Phys. Rev. B **66**, 094501 (2002).

[60] J. Chang, C. Niedermayer, R. Gilardi, N. B. Christensen, H. M. Rønnow, D. F. McMorrow, M. Ay, J. Stahn, O. Sobolev, A. Hiess, S. Pailhes, C. Baines, N. Momono, M. Oda, M. Ido and J. Mesot, Phys. Rev. B **78**, 104525 (2008).

[61] R. J. Birgeneau, C. Stock, J. M. Tranquada and K. Yamada, J. Phys. Soc. Jpn. **75**, 111003 (2006).

[62] H. Jacobsen, S. L. Holm, M.-E. Lăcătuşu, A. T. Rømer, M. Bertelsen, M. Boehm, R. Toft-Petersen, J.-C. Grivel, S. B. Emery, L. Udby, B. O. Wells and K. Lefmann, Phys. Rev. Lett. **120**, 037003 (2018).

[63] M. Kofu, S.-H. Lee, M. Fujita, H.-J. Kang, H. Eisaki and K. Yamada, Phys. Rev. Lett. **102**, 047001 (2009).

[64] D. J. Scalapino, Rev. Mod. Phys. **84**, 1383–1417 (2012).

[65] P. W. Anderson, en, Science **316**, 1705–1707 (2007).

[66] N. E. Bickers, D. J. Scalapino and S. R. White, Phys. Rev. Lett. **62**, 961–964 (1989).

[67] J. D. Axe, A. H. Moudden, D. Hohlwein, D. E. Cox, K. M. Mohanty, A. R. Moodenbaugh and Y. Xu, Phys. Rev. Lett. **62**, 2751–2754 (1989).

[68] M. Braden, G. Heger, P. Schweiss, Z. Fisk, K. Gamayunov, I. Tanaka and H. Kojima, Physica C: Superconductivity **191**, 455–468 (1992).

[69] T. C. Huang, E. Moran, A. I. Nazzal, J. B. Torrance and P. W. Wang, en, Physica C: Superconductivity **159**, 625–628 (1989).

[70] R. D. Shannon, en, Acta Cryst A **32**, 751–767 (1976).

[71] P. G. Radaelli, D. G. Hinks, A. W. Mitchell, B. A. Hunter, J. L. Wagner, B. Dabrowski, K. G. Vandervoort, H. K. Viswanathan and J. D. Jorgensen, Phys. Rev. B **49**, 4163–4175 (1994).

[72] J. M. Tranquada, B. J. Sternlieb, J. D. Axe, Y. Nakamura and S. Uchida, Nature **375**, 561–563 (1995).

[73] N. B. Christensen, J. Chang, J. Larsen, M. Fujita, M. Oda, M. Ido, N. Momono, E. M. Forgan, A. T. Holmes, J. Mesot, M. Huecker and M. v Zimmermann, arXiv:1404.3192 [cond-mat] (2014).

[74] T. P. Croft, C. Lester, M. S. Senn, A. Bombardi and S. M. Hayden, Phys. Rev. B **89**, 224513 (2014).

[75] V. Thampy, M. P. M. Dean, N. B. Christensen, L. Steinke, Z. Islam, M. Oda, M. Ido, N. Momono, S. B. Wilkins and J. P. Hill, Phys. Rev. B **90**, 100510 (2014).

[76] M. H. Julien, Physica B: Condensed Matter, Proceedings of the 23rd International Conference on Low Temperature Physics **329-333**, 693–696 (2003).

[77] J. M. Tranquada, H. Woo, T. G. Perring, H. Goka, G. D. Gu, G. Xu, M. Fujita and K. Yamada, en, Nature **429**, 534–538 (2004).

[78] P. Blakeslee, R. J. Birgeneau, F. C. Chou, R. Christianson, M. A. Kastner, Y. S. Lee and B. O. Wells, Phys. Rev. B **57**, 13915–13921 (1998).

[79] M. Ahmad, 'Property investigation of the high Tc superconductors La2CuO4+y and La2−xSrxCuO4+y', MA thesis (University of Copenhagen, 2019).

[80] M. Karppinen, L. Niinistö and H. Yamauchi, en, Journal of Thermal Analysis **48**, 1123–1141 (1997).

[81] L. H. Liu, G. C. Che, J. Zhao and Z. X. Zhao, Physica C: Superconductivity **425**, 37–43 (2005).

[82] B. Lorenz, Z. G. Li, T. Honma and P.-H. Hor, Phys. Rev. B **65**, 144522 (2002).

[83] M. Fratini, N. Poccia, A. Ricci, G. Campi, M. Burghammer, G. Aeppli and A. Bianconi, en, Nature **466**, 841–844 (2010).

[84] B. O. Wells, Y. S. Lee, M. A. Kastner, R. J. Christianson, R. J. Birgeneau, K. Yamada, Y. Endoh and G. Shirane, en, Science **277**, 1067–1071 (1997).

[85] N. Poccia, A. Ricci, G. Campi, M. Fratini, A. Puri, D. D. Gioacchino, A. Marcelli, M. Reynolds, M. Burghammer, N. L. Saini, G. Aeppli and A. Bianconi, PNAS **109**, 15685–15690 (2012).

[86] B. O. Wells, R. J. Birgeneau, F. C. Chou, Y. Endoh, D. C. Johnston, M. A. Kastner, Y. S. Lee, G. Shirane, J. M. Tranquada and K. Yamada, en, Zeitschrift für Physik B Condensed Matter **100**, 535–545 (1996).

[87] J. M. Tranquada, Y. Kong, J. E. Lorenzo, D. J. Buttrey, D. E. Rice and V. Sachan, Phys. Rev. B **50**, 6340–6351 (1994).

[88] P. J. Ray, N. H. Andersen, T. B. S. Jensen, H. E. Mohottala, C. Niedermayer, K. Lefmann, B. O. Wells, M. v. Zimmermann and L. Udby, Phys. Rev. B **96**, 174106 (2017).

[89] Y. S. Lee, F. C. Chou, A. Tewary, M. A. Kastner, S. H. Lee and R. J. Birgeneau, Phys. Rev. B **69**, 020502 (2004).

[90] A. Bianconi, International Journal of Modern Physics B **14**, 3289–3297 (2000).

[91] H. E. Mohottala, B. O. Wells, J. I. Budnick, W. A. Hines, C. Niedermayer, L. Udby, C. Bernhard, A. R. Moodenbaugh and F.-C. Chou, Nature Materials **5**, 377–382 (2006).

[92] L. Udby, J. Larsen, N. B. Christensen, M. Boehm, C. Niedermayer, H. E. Mohottala, T. B. S. Jensen, R. Toft-Petersen, F. C. Chou, N. H. Andersen, K. Lefmann and B. O. Wells, Phys. Rev. Lett. **111**, 227001 (2013).

[93] Y. Y. Peng, G. Dellea, M. Minola, M. Conni, A. Amorese, D. Di Castro, G. M. De Luca, K. Kummer, M. Salluzzo, X. Sun, X. J. Zhou, G. Balestrino, M. Le Tacon, B. Keimer, L. Braicovich, N. B. Brookes and G. Ghiringhelli, Nature Physics **13**, 1201–1206 (2017).

[94] O. Ivashko, M. Horio, W. Wan, N. B. Christensen, D. E. McNally, E. Paris, Y. Tseng, N. E. Shaik, H. M. Rønnow, H. I. Wei, C. Adamo, C. Lichtensteiger, M. Gibert, M. R. Beasley, K. M. Shen, J. M. Tomczak, T. Schmitt and J. Chang, Nature Communications **10**, 786 (2019).

[95] E. S. Božin, G. H. Kwei, H. Takagi and S. J. L. Billinge, Phys. Rev. Lett. **84**, 5856–5859 (2000).

[96] S. W. Lovesey, *Theory of Neutron Scattering from Condensed Matter*, en (Clarendon Press, 1984).

[97] G. L. Squires, *Introduction to the Theory of Thermal Neutron Scattering*, en (Cambridge University Press, Mar. 2012).

[98] H. Schober, Journal of Neutron Research **17**, 109–357 (2014).

[99] G. Shirane, S. M. Shapiro and J. M. Tranquada, *Neutron Scattering with a Triple-Axis Spectrometer: Basic Techniques* (Cambridge University Press, Feb. 2002).

[100] L. Van Hove, Phys. Rev. **95**, 249–262 (1954).

[101] *Neutron scattering lengths and cross sections*, `https://www.ncnr.nist.gov/resources/n-lengths/` (visited on 21/11/2019).

[102] J. Jensen and A. R. Mackintosh, *Rare earth magnetism: structures and excitations*, en (Clarendon Press, Aug. 1991).

[103] B. Fåk and B. Dorner, Physica B: Condensed Matter, Proceedings of the First European Conference on Neutron Scattering **234-236**, 1107–1108 (1997).

[104] T. Weber, R. Georgii and P. Böni, SoftwareX **5**, 121–126 (2016).

[105] J. Šaroun and J. Kulda, Physica B: Condensed Matter, Proceedings of the First European Conference on Neutron Scattering **234-236**, 1102–1104 (1997).

[106] *Thermal neutron three-axis spectrometer in8*, `https://www.ill.eu/users/instruments/instruments-list/in8/description/instrument-layout/` (visited on 22/11/2019).

[107] *Thermal neutron time-of-flight spectrometer in4c*, `https://www.ill.eu/users/instruments/instruments-list/in4c/description/instrument-layout/` (visited on 22/11/2019).

[108] J. M. Carpenter and D. L. Price, Phys. Rev. Lett. **54**, 441–443 (1985).

[109] *Disordered materials diffractometer*, https://www.ill.eu/users/instruments/instruments-list/d4/description/instrument-layout/ (visited on 22/11/2019).

[110] D. A. Keen, en, J Appl Cryst **34**, 172–177 (2001).

[111] F. Giustino, *Materials Modelling using Density Functional Theory: Properties and Predictions*, en (OUP Oxford, May 2014).

[112] R. M. Martin, *Electronic Structure: Basic Theory and Practical Methods*, en (Cambridge University Press, Apr. 2004).

[113] R. M. Martin, L. Reining and D. M. Ceperley, *Interacting Electrons*, en (Cambridge University Press, June 2016).

[114] R. Hoffmann, en, Angewandte Chemie International Edition in English **26**, 846–878 (1987).

[115] S. Lloyd, Phys. Rev. Lett. **88**, 237901 (2002).

[116] P. Hohenberg and W. Kohn, Phys. Rev. **136**, B864–B871 (1964).

[117] N. Mardirossian and M. Head-Gordon, Molecular Physics **115**, 2315–2372 (2017).

[118] W. Kohn and L. J. Sham, Phys. Rev. **140**, A1133–A1138 (1965).

[119] D. M. Ceperley and B. J. Alder, Phys. Rev. Lett. **45**, 566–569 (1980).

[120] J. P. Perdew and A. Zunger, Phys. Rev. B **23**, 5048–5079 (1981).

[121] J. P. Perdew and K. Schmidt, AIP Conference Proceedings **577**, 1–20 (2001).

[122] J. Tao, J. P. Perdew, V. N. Staroverov and G. E. Scuseria, Phys. Rev. Lett. **91**, 146401 (2003).

[123] V. I. Anisimov, F. Aryasetiawan and A. I. Lichtenstein, J. Phys.: Condens. Matter **9**, 767 (1997).

[124] R. P. Feynman, Phys. Rev. **56**, 340–343 (1939).

[125] K. Parlinski, Z. Q. Li and Y. Kawazoe, Phys. Rev. Lett. **78**, 4063–4066 (1997).

[126] A. Togo and I. Tanaka, Scripta Materialia **108**, 1–5 (2015).

[127] L. Verlet, Phys. Rev. **159**, 98–103 (1967).

[128] S. Nosé, J. Chem. Phys. **81**, 511–519 (1984).

[129] M. T. Dove, *Introduction to Lattice Dynamics*, en (Cambridge University Press, Oct. 1993).

[130] *The radial distribution functions: definitions*, http://isaacs.sourceforge.net/phys/rdfs.html (visited on 07/12/2019).

[131] *Phonopy website*, https://atztogo.github.io/phonopy/ (visited on 25/11/2019).

[132] H. E. Fischer, A. C. Barnes and P. S. Salmon, en, Rep. Prog. Phys. **69**, 233–299 (2005).

[133] G. Kresse and J. Hafner, Phys. Rev. B **47**, 558–561 (1993).

[134] G. Kresse and J. Hafner, Phys. Rev. B **49**, 14251–14269 (1994).

[135] G. Kresse and J. Furthmüller, Phys. Rev. B **54**, 11169–11186 (1996).

[136] G. Kresse and J. Furthmüller, Computational Materials Science **6**, 15–50 (1996).

[137] P. E. Blöchl, Phys. Rev. B **50**, 17953–17979 (1994).

[138] G. Kresse and D. Joubert, Phys. Rev. B **59**, 1758–1775 (1999).

[139] *The VASP Manual - Vaspwiki*, https://cms.mpi.univie.ac.at/wiki/index.php/The_VASP_Manual (visited on 14/11/2019).

[140] E. L. da Silva, J. M. Skelton, S. C. Parker and A. Walsh, Phys. Rev. B **91**, 144107 (2015).

[141] J. P. Perdew, K. Burke and M. Ernzerhof, Phys. Rev. Lett. **77**, 3865–3868 (1996).

[142] L. K. Wagner and D. M. Ceperley, Rep. Prog. Phys. **79**, 094501 (2016).

[143] W. E. Pickett, Rev. Mod. Phys. **61**, 433–512 (1989).

[144] C. Lane, J. W. Furness, I. G. Buda, Y. Zhang, R. S. Markiewicz, B. Barbiellini, J. Sun and A. Bansil, Phys. Rev. B **98**, 125140 (2018).

[145] F. Giustino, M. L. Cohen and S. G. Louie, Nature **452**, 975–978 (2008).

[146] S. L. Dudarev, G. A. Botton, S. Y. Savrasov, C. J. Humphreys and A. P. Sutton, Phys. Rev. B **57**, 1505–1509 (1998).

[147] V. I. Anisimov, M. A. Korotin, A. S. Mylnikova, A. V. Kozhevnikov, D. M. Korotin and J. Lorenzana, Phys. Rev. B **70**, 172501 (2004).

[148] S. Pesant and M. Côté, Phys. Rev. B **84**, 085104 (2011).

[149] *Energy vs volume Volume relaxations and Pulay stress - Vaspwiki*, https://cms.mpi.univie.ac.at/wiki/index.php/Energy_vs_volume_Volume_relaxations_and_Pulay_stress (visited on 14/11/2019).

[150] A. H. Larsen, J. J. Jørgen Mortensen, J. Blomqvist, I. E. Castelli, R. Christensen, M. Dułak, J. Friis, M. N. Groves, B. Hammer, C. Hargus, E. D. Hermes, P. C. Jennings, P. Bjerre Jensen, J. Kermode, J. R. Kitchin, E. L. Kolsbjerg, J. Kubal, K. Kaasbjerg, S. Lysgaard, J. Bergmann Maronsson, T. Maxson, T. Olsen, L. Pastewka, A. Peterson, C. Rostgaard, J. Schiøtz, O. Schütt, M. Strange, K. S. Thygesen, T. Vegge, L. Vilhelmsen, M. Walter, Z. Zeng and K. W. Jacobsen, J Phys Condens Matter **29**, 273002 (2017).

[151] K. Momma and F. Izumi, J Appl Cryst **41**, 653–658 (2008).

[152] Y. Hinuma, G. Pizzi, Y. Kumagai, F. Oba and I. Tanaka, Computational Materials Science **128**, 140–184 (2017).

[153] D. Vaknin, S. K. Sinha, D. E. Moncton, D. C. Johnston, J. M. Newsam, C. R. Safinya and H. E. King, Phys. Rev. Lett. **58**, 2802–2805 (1987).

[154] S. Uchida, T. Ido, H. Takagi, T. Arima, Y. Tokura and S. Tajima, Phys. Rev. B **43**, 7942–7954 (1991).

[155] V. I. Anisimov and O. Gunnarsson, Phys. Rev. B **43**, 7570–7574 (1991).

[156] M. Horio, C. E. Matt, K. Kramer, D. Sutter, A. M. Cook, Y. Sassa, K. Hauser, M. Månsson, N. C. Plumb, M. Shi, O. J. Lipscombe, S. M. Hayden, T. Neupert and J. Chang, Nature Communications **9**, 3252 (2018).

[157] P. Vinet, J. R. Smith, J. Ferrante and J. H. Rose, Phys. Rev. B **35**, 1945–1953 (1987).

[158] F. D. Murnaghan, PNAS **30**, 244–247 (1944).

[159] F. Birch, Phys. Rev. **71**, 809–824 (1947).

[160] J. P Poirier and A Tarantola, Physics of the Earth and Planetary Interiors **109**, 1–8 (1998).

[161] H. Takahashi, H. Shaked, B. A. Hunter, P. G. Radaelli, R. L. Hitterman, D. G. Hinks and J. D. Jorgensen, Phys. Rev. B **50**, 3221–3229 (1994).

[162] G. I. Csonka, J. P. Perdew, A. Ruzsinszky, P. H. T. Philipsen, S. Lebègue, J. Paier, O. A. Vydrov and J. G. Ángyán, Phys. Rev. B **79**, 155107 (2009).

[163] R. J. McQueeney, Y. Petrov, T. Egami, M. Yethiraj, G. Shirane and Y. Endoh, Phys. Rev. Lett. **82**, 628–631 (1999).

[164] S. R. Park, T. Fukuda, A. Hamann, D. Lamago, L. Pintschovius, M. Fujita, K. Yamada and D. Reznik, Phys. Rev. B **89**, 020506 (2014).

[165] A. Piovano, A. Perrichon, M. Boehm, M. R. Johnson and W. Paulus, en, Phys. Chem. Chem. Phys. **18**, 17398–17403 (2016).

[166] A. Perrichon, A. Piovano, M. Boehm, M. Zbiri, M. Johnson, H. Schober, M. Ceretti and W. Paulus, J. Phys. Chem. C **119**, 1557–1564 (2015).

[167] C. Rial, E. Morán, M. A. Alario-Franco, U. Amador and N. H. Andersen, Physica C: Superconductivity **278**, 122–134 (1997).

[168] J. Hickman and Y. Mishin, Phys. Rev. B **94**, 184311 (2016).

[169] N. Poccia, M. Fratini, A. Ricci, G. Campi, L. Barba, A. Vittorini-Orgeas, G. Bianconi, G. Aeppli and A. Bianconi, en, Nature Mater **10**, 733–736 (2011).

[170] F. V. Kusmartsev, D. Di Castro, G. Bianconi and A. Bianconi, en, Physics Letters A **275**, 118–123 (2000).

[171] *Flatcone*, https://www.ill.eu/users/instruments/instruments-list/flatcone/ (visited on 27/11/2019).

[172] P. J. Ray, 'Master's thesis: Structural investigation of La(2-x)Sr(x)CuO(4+y) - Following staging as a function of temperature', MA thesis (University of Copenhagen, 2016).

[173] *Nplot*, https://github.com/nplot/nplot (visited on 28/11/2019).

[174] S. Wakimoto, S. Lee, P. M. Gehring, R. J. Birgeneau and G. Shirane, J. Phys. Soc. Jpn. **73**, 3413–3417 (2004).

[175] C.-H. Lee, K. Yamada, M. Arai, S. Wakimoto, S. Hosoya and Y. Endoh, Physica C: Superconductivity and its Applications **257**, 264–270 (1996).

[176] O. Arnold, J. C. Bilheux, J. M. Borreguero, A. Buts, S. I. Campbell, L. Chapon, M. Doucet, N. Draper, R. Ferraz Leal, M. A. Gigg, V. E. Lynch, A. Markvardsen, D. J. Mikkelson, R. L. Mikkelson, R. Miller, K. Palmen, P. Parker, G. Passos, T. G. Perring, P. F. Peterson, S. Ren, M. A. Reuter, A. T. Savici, J. W. Taylor, R. J. Taylor, R. Tolchenov, W. Zhou and J. Zikovsky, Nuclear Instruments and Methods in Physics Research Section A: Accelerators, Spectrometers, Detectors and Associated Equipment **764**, 156–166 (2014).

[177] *Computeincoherentdos v1*, `https://docs.mantidproject.org/v3.11.0/algorithms/ComputeIncoherentDOS-v1.html` (visited on 30/11/2019).

[178] P. S. Häfliger, S. Gerber, R. Pramod, V. I. Schnells, B. dalla Piazza, R. Chati, V. Pomjakushin, K. Conder, E. Pomjakushina, L. Le Dreau, N. B. Christensen, O. F. Syljuåsen, B. Normand and H. M. Rønnow, Phys. Rev. B **89**, 085113 (2014).

[179] J. M. Tranquada, J. D. Axe, N. Ichikawa, Y. Nakamura, S. Uchida and B. Nachumi, Phys. Rev. B **54**, 7489–7499 (1996).

[180] S. Anissimova, D. Parshall, G. D. Gu, K. Marty, M. D. Lumsden, S. Chi, J. A. Fernandez-Baca, D. L. Abernathy, D. Lamago, J. M. Tranquada and D. Reznik, en, Nature Communications **5**, 3467 (2014).

[181] S. A. Kivelson, I. P. Bindloss, E. Fradkin, V. Oganesyan, J. M. Tranquada, A. Kapitulnik and C. Howald, Rev. Mod. Phys. **75**, 1201–1241 (2003).

[182] R. Arpaia, S. Caprara, R. Fumagalli, G. D. Vecchi, Y. Y. Peng, E. Andersson, D. Betto, G. M. D. Luca, N. B. Brookes, F. Lombardi, M. Salluzzo, L. Braicovich, C. D. Castro, M. Grilli and G. Ghiringhelli, en, Science **365**, 906–910 (2019).

[183] M. Mitrano, S. Lee, A. A. Husain, L. Delacretaz, M. Zhu, G. d. l. P. Munoz, S. X.-L. Sun, Y. I. Joe, A. H. Reid, S. F. Wandel, G. Coslovich, W. Schlotter, T. van Driel, J. Schneeloch, G. D. Gu, S. Hartnoll, N. Goldenfeld and P. Abbamonte, en, Science Advances **5**, eaax3346 (2019).

[184] D. Reznik, L. Pintschovius, M. Fujita, K. Yamada, G. D. Gu and J. M. Tranquada, en, J Low Temp Phys **147**, 353–364 (2007).

[185] L. Chaix, G. Ghiringhelli, Y. Y. Peng, M. Hashimoto, B. Moritz, K. Kummer, N. B. Brookes, Y. He, S. Chen, S. Ishida, Y. Yoshida, H. Eisaki, M. Salluzzo, L. Braicovich, Z.-X. Shen, T. P. Devereaux and W.-S. Lee, en, Nature Physics **13**, 952–956 (2017).

[186] D. Reznik, L. Pintschovius, M. Ito, S. Iikubo, M. Sato, H. Goka, M. Fujita, K. Yamada, G. D. Gu and J. M. Tranquada, Nature **440**, 1170–1173 (2006).

[187] M. Le Tacon, A. Bosak, S. M. Souliou, G. Dellea, T. Loew, R. Heid, K.-P. Bohnen, G. Ghiringhelli, M. Krisch and B. Keimer, en, Nature Physics **10**, 52–58 (2014).

[188] D. Reznik, Physica C: Superconductivity, Stripes and Electronic Liquid Crystals in Strongly Correlated Materials **481**, 75–92 (2012).

[189] E. Kaneshita, M. Ichioka and K. Machida, Phys. Rev. Lett. **88**, 115501 (2002).

[190] A. T. Rømer, J. Chang, N. B. Christensen, B. M. Andersen, K. Lefmann, L. Mähler, J. Gavilano, R. Gilardi, C. Niedermayer, H. M. Rønnow, A. Schneidewind, P. Link, M. Oda, M. Ido, N. Momono and J. Mesot, Phys. Rev. B **87**, 144513 (2013).

[191] J. M. Tranquada, C. H. Lee, K. Yamada, Y. S. Lee, L. P. Regnault and H. M. Rønnow, Phys. Rev. B **69**, 174507 (2004).

[192] B. Lake, G. Aeppli, K. N. Clausen, D. F. McMorrow, K. Lefmann, N. E. Hussey, N. Mangkorntong, M. Nohara, H. Takagi, T. E. Mason and A. Schröder, en, Science **291**, 1759–1762 (2001).

[193] J. M. Tranquada, AIP Conference Proceedings **1550**, 114–187 (2013).

[194] G. Aeppli, T. E. Mason, S. M. Hayden, H. A. Mook and J. Kulda, en, Science **278**, 1432–1435 (1997).

[195] D. Reznik, T. Fukuda, D. Lamago, A. Q. R. Baron, S. Tsutsui, M. Fujita and K. Yamada, Journal of Physics and Chemistry of Solids, SNS2007 **69**, 3103–3107 (2008).

[196] S. R. Park, Y. Cao, Q. Wang, M. Fujita, K. Yamada, S.-K. Mo, D. S. Dessau and D. Reznik, Phys. Rev. B **88**, 220503 (2013).

[197] D. R. Garcia and A Lanzara, Advances in Condensed Matter Physics **2010** (2010).

[198] Z. Zhang, R. Sutarto, F. He, F. C. Chou, L. Udby, S. L. Holm, Z. H. Zhu, W. A. Hines, J. I. Budnick and B. O. Wells, Phys. Rev. Lett. **121**, 067602 (2018).

[199] S. Holm-Dahlin, J. Larsen, H. Jacobsen, A. T. Rømer, A.-E. Ţuţueanu, M. Ahmad, J.-C. Grivel, T. Goko, R. Scheuermann, M. v Zimmermann, M. Boehm, P. Steffens, K. Conder, C. Niedermayer, K. S. Pedersen, N. B. Christensen, S. B. Emery, B. O Wells, K. Lefmann and L. Udby, Manuscript in preparation (2019).

[200] D. Reznik, D. Parshall, S. R. Park, J. W. Lynn and T. Wolf, en, J Supercond Nov Magn **29**, 643–644 (2016).

[201] M. Fujita, H. Goka, K. Yamada, J. M. Tranquada and L. P. Regnault, Phys. Rev. B **70**, 104517 (2004).

[202] E. Fradkin, S. A. Kivelson and J. M. Tranquada, Rev. Mod. Phys. **87**, 457–482 (2015).

[203] S. A. Kivelson, E. Fradkin and V. J. Emery, en, Nature **393**, 550–553 (1998).

[204] A. Ino, C. Kim, M. Nakamura, T. Yoshida, T. Mizokawa, A. Fujimori, Z.-X. Shen, T. Kakeshita, H. Eisaki and S. Uchida, Phys. Rev. B **65**, 094504 (2002).

[205] X. J. Zhou, T. Yoshida, S. A. Kellar, P. V. Bogdanov, E. D. Lu, A. Lanzara, M. Nakamura, T. Noda, T. Kakeshita, H. Eisaki, S. Uchida, A. Fujimori, Z. Hussain and Z.-X. Shen, Phys. Rev. Lett. **86**, 5578–5581 (2001).

[206] Q. Li, M. Hücker, G. D. Gu, A. M. Tsvelik and J. M. Tranquada, Phys. Rev. Lett. **99**, 067001 (2007).

[207] Y.-S. Su, T. A. Kaplan, S. D. Mahanti and J. F. Harrison, Phys. Rev. B **59**, 10521–10529 (1999).

[208] P. Lazić and D. K. Sunko, en, EPL **112**, 37011 (2015).

[209] P. Lazić, D. Pelc, M. Požek, V. Despoja and D. K. Sunko, en, J Supercond Nov Magn **28**, 1299–1303 (2015).

[210] N. Poccia, A. Ricci, G. Campi and A. Bianconi, en, Supercond. Sci. Technol. **30**, 035016 (2017).

[211] G. Goret, B. Aoun and E. Pellegrini, J. Chem. Inf. Model. **57**, 1–5 (2017).